UNIVERSITÀ DEGLI STUDI DI PADOVA

FACOLTÀ DI SCIENZE MM.FF.NN.

DIPARTIMENTO DI SCIENZE CHIMICHE

Tesi di Dottorato in Chimica

SCUOLA DI DOTTORATO IN SCIENZE CHIMICHE

INDIRIZZO SCIENZE MOLECOLARI

CICLO XXI

ADVANCED COMPUTATIONAL TOOLS FOR THE INTERPRETATION OF MAGNETIC RESONANCE SPECTROSCOPIES

Direttore della Scuola: Ch.mo Prof. Maurizio Casarin

Supervisore: Prof. Antonino Polimeno

Dottorando: Mirco Zerbetto

Anno accademico 2008 - 2009

ADVANCED COMPUTATIONAL TOOLS FOR THE INTERPRETATION OF MAGNETIC RESONANCE SPECTROSCOPIES

Mirco Zerbetto

Scuola di Dottorato in Scienze Chimiche
Indirizzo Scienze Molecolare
Ciclo XXI

February 2nd, 2009

Abstract

Electron and nuclear magnetic spectroscopies are powerful tools for studying molecular dynamics, being particularly sensitive to motions with relaxation times in the range of 10^{-9} - 10^{-6} s. This time window includes rigid body motions in fluids and "soft" internal motions of molecules. Moreover, dynamics in this range comprehend proteins internal motions responsible for relevant chemical-physical properties, like substrate recognition, activity and folding.

In a typical electron spin resonance (ESR) experiment molecular motions affect considerably the shape of the spectral line. In a nuclear magnetic resonance (NMR) experiment characteristic relaxations times of the spin magnetization, i.e. T_1, T_2 and NOE, are directly affected by internal mobility.

The aim of this Ph.D. work is the implementation of integrated theoretical / computational methodologies for characterization of dynamical properties of molecules gathered from ESR and NMR measurements. The starting point is a "time coarse-graining" procedure that leads to simplified models in which we introduce only dynamical characteristics that are relevant to the physical observables considered. In particular, stochastic models are employed, based on a number of structural parameters which are calculated. The idea is to treat these parameters at atomistic and / or mesoscopic level depending on their nature.

Software packages have been developed, comprehending E-SpiReS (Electron Spin Resonance Simulation) for cw-ESR simulations, C^{++}OPPS (COupled Probe Protein Smoluchowski) for NMR simulations and DITE (DIffusion TEnsor) for the evaluation of dissipative properties of molecules. These programs have been built as user-friendly tools targeted for use by experimentalists, as a kind of *in silico* extension of the laboratory equipment.

Supervisor: Prof. Antonino Polimeno

ADVANCED COMPUTATIONAL TOOLS FOR THE INTERPRETATION OF MAGNETIC RESONANCE SPECTROSCOPIES

Mirco Zerbetto

Scuola di Dottorato in Scienze Chimiche
Indirizzo Scienze Molecolare
Ciclo XXI

2 Febbraio 2009

Sommario

Tecniche efficaci nello studio della dinamica molecolare sono le spettroscopie di risonanza elettronica e nucleare, essendo particolarmente sensibili a moti caratterizzati da scale dei tempi nell'intervallo da 10^{-9} a 10^{-6} s, nel quale rientrano sia i moti globali (di corpo rigido), sia le dinamiche interne di molecole in soluzione. È da notare che questa finestra comprende anche la dinamica delle proteine, responsabile di proprietà chimico-fisiche molto importanti, quali il riconoscimento del substrato, l'attività ed il *folding*.
Tipicamente, in un esperimento di risonanza di spin elettronico (RSE) i moti molecolari sono responsabili dell'allargamento inomogeneo delle righe spettrali. Per quanto riguarda la risonanza magnetica nucleare (RMN), invece, la dinamica molecolare influisce sui rilassamenti T_1, T_2 e NOE.
Lo scopo di questo lavoro è l'implementazione di metodologie integrate teorico / computazionali per la caratterizzazione della dinamica molecolare a partire da misure RSE e RMN. In particolare, si proiettano i moti non importanti (*"time coarse-graining"*), ottenendo modelli per la dinamica relativamente semplici, che descrivono esclusivamente i moti rilevanti rispetto all'osservabile fisico in esame. In particolare, si impiegano modelli stocastici nei quali intervengono anche parametri strutturali che devono essere calcolati. Questi ultimi sono descritti a livello atomistico e / o mesoscopico in base alla loro natura.
Sono stati sviluppati tre nuovi programmi: E-SpiReS (*Electron Spin Resonance Simulation*) per la simulazione di spettri RSE in onda continua, C^{++}OPPS (*COupled Protein Probe Smoluchowski*) per simulazioni di misure di RMN e DITE (*DIffusion TEnsor*) per il calcolo di proprietà dissipative di molecole con gradi di libertà interni. Nell'implementazione dei programmi si è fatto attenzione alla semplicità d'uso, occupandosi anche dello sviluppo di interfacce grafiche, con l'obiettivo di affiancare i programmi alla strumentazione di laboratorio, come una sorta di estensione *in silico* della stessa.

Supervisore: Prof. Antonino Polimeno

Acknowledgements

First, I would like to thank my supervisor, prof. Antonino Polimeno, for his continuous support in my Ph.D. work and for taking care of my scientific growth, aiming on both the increase of my researcher skills and on my preparation in chemistry.

A huge collaboration with many chemists, from Universities inside and outside of Italy, is a centrepiece of this doctoral work. Among people in the University of Padova I particularly thank dr. Silvia Carlotto, profs. Carlo Corvaja, Michele Maggini, Claudio Toniolo, Marina Brustolon and dr. Lorenzo Franco, with whom I carried out most of the work on electron spin resonance simulations. I, also, say thank you to ing. Gianpietro Sella for his great support in the development of web versions of the software that I implemented.

A strong collaboration with the theoretical chemistry group of the University "Federico II" of Napoli has been really profitable, especially for their expertise in the field of quantum mechanics applied to the calculation of magnetic properties of molecules. I'm very grateful to prof. Vincenzo Barone, for his significant contribution to the Ph.D. project. Also, I show gratitude to drs. Paola Cimino, Pasquale Caruso and Carmine Garzillo: we worked together to some parts of the research project, in simulations and algorithm generation.

A short but very productive collaboration with the University of Madrid led to interesting results in the field of ESR of polymerization of radical species. I thank profs. Carlos S. del Nido and Paloma Calle, and I'm especially obligated to dr. Laura Hermosilla, who worked with me during her stay in Italy.

A fundamental contribution, regarding the part of the work dedicated to NMR, came from the strict collaboration with prof. Eva Meirovitch, from the Bar-Ilan university in Israel, to who I'm especially grateful. And I say thank you also to her collaborator dr. Benny Shomer for his fine collaboration and help in advancement of the development of the algorithms.

Science is not the only aspect of academic life. Working in a nice and peaceful environment is very important. I really enjoyed these years in Padova and I thank my colleagues, but first of all friends: Silvia, Giulia, Barbara, Cristina, Mirko, Andrea, Fabio, Marzio, Roberto and Diego.

Finally, a very special thank goes to my family. They provided me support, help, financial relief, they tolerated my mood changes. In substance, they simplified a lot my life outside the university, giving me the possibility to stay more concentrated on my work. So, even if not for strictly scientific reasons, my family contributed to this Ph.D. work and I'm really grateful to them.

Contents

List of Figures

List of Tables

Chapter 1

Methodology: experiments and theory

It should be natural for a chemist to think about molecules as dynamical systems. Thermal effects and interaction with other molecules cause both internal and global dynamics. As a consequence, macroscopic chemical and physical properties of molecules depend on their dynamics, in varying degrees depending on the physical observable considered. Modern physical-chemistry presents several examples: collision theory is built on the assumption that molecules move (in order to collide) to react; temperature is a macroscopic physical observable which is related to the average square velocity of particles; osmotic pressure in biological cells is a macroscopic observable and it is kept at a set point value by the action of Na / K pumps, which are molecular machines that carry out their function thanks to internal dynamics; many enzymes can react and transform a substrate because of change of conformation occurs in bonding and serve to create the right chemical environment around the substrate.

If the role of theoretical chemistry is to interpret macroscopic observations in terms of physico-chemical properties of molecules, dynamics is therefore a fundamental ingredient, together with structural properties, that needs to be taken into account. Moreover, any theoretical chemistry approach aimed at some degree of predictivity needs to include dynamics, especially in models targeted to the interpretation of processes occurring in large biomolecules or complex (”soft”) materials.

In this work our main purpose is the development of integrated theoretical / computational approaches for interpreting slow motions[1] in complex molecular systems. The ideal final target is the application to the study of dynamics (mobility) of proteins, or rather the interpretation of spectroscopic data for gathering information on their dynamics.

Indeed, information on dynamics can be gathered only indirectly from experiments. A theoretical framework is therefore required to link macroscopic observations to molecular dynamics. A sensible plan of action is then *i)* choose a reference experimental technique which is particularly sensible to the kind of motions we are interested in; *ii)* set up a framework for describing dynamics and its influence on the chosen physical observable; *iii)* make a selection of model systems, which serve to build and test theoretical models.

1.1 Experiments: using magnetic resonance to unravel molecular motions

Interpretation of structural properties and dynamic behaviour of molecules in solution is of fundamental importance to understand their stability, chemical reactivity and catalytic action. High interest is especially on the development of new materials and study of biological macromolecules. In general one has to treat complex systems in which motions are present in a wide range of time scales encompassing global dynamics (μs), domains dynamics (ns), localized fluctuations involving selected chemical groups (ps and fs).

Experimental determination of dynamical properties of molecular systems is based on sophisticated spectroscopic techniques, which are employed to investigate the dynamic behaviour of molecules and macromolecules in solutions and to understand their reactivity. Physico-chemical properties of molecules in solution depend on the action of different motions at several time and length scales, and information on multiscale dynamics can be gained, in principle, by a variety of spectroscopic techniques, magnetic (nuclear magnetic resonance, NMR, and electron spin resonance, ESR) and optic (fluorescence polarization anisotropy, FPA, dynamic light scattering, DLS, and time resolved Stokes shift, TRSS). In this work we are interested in the investigation of slow motions, such as solvent cage effects in liquid crystals, collective dynamics in proteins, fluctuations of membranes, etc. The most sensible

---

[1] i.e. for all practical purposes in the range $10^{-9} - 10^{-6}$ s

spectroscopic techniques to such motions are magnetic spectroscopies, both electron spin resonance (ESR) and nuclear magnetic resonance (NMR). This means that slow motional processes have characteristic time scales that are comparable to that of spin (electronic or nuclear) relaxation.

ESR

ESR and theoretical chemistry have been entangled since the beginning of ESR studies. On one hand the rich and detailed information hidden in ESR spectra has been a challenge for physico-chemical interpretations and computational models. On the other hand ESR spectroscopists have been always looking for better tools helping in interpreting the spectra. The intrinsic resolution of ESR spectra, together with the unique role played by paramagnetic probes in providing information on their environment, make in principle ESR one of the most powerful methods of investigation on the electron distribution in molecules, and on the properties of their environments. The tools needed by ESR spectroscopists are from the world of quantum mechanics calculations, as far as the parameters of the spin Hamiltonian are concerned, and from the world of molecular dynamics and statistical thermodynamics for the spectral line shapes.

Because of its favourable time scale, ESR experiments can be highly sensitive to the details of the rotational and internal dynamics. In particular, with the advent of very high field ESR corresponding to frequencies above 140 GHz, the rotational dynamics of spin-labeled molecules observed by ESR is more commonly found to be in the so-called *slow motional regime* than is the case at conventional ESR frequencies (e.g., 9.5 GHz). For this regime, the spectral line shapes take on a complex form which is found to be sensitive to the microscopic details of the motional process. This is to be contrasted with the *fast motional regime*, where simple Lorentzian line shapes are observed, and only estimates of molecular parameters (e.g., diffusion tensor values) are obtained independently from the microscopic details of the molecular dynamics. The interpretation of slow motional spectra requires an analysis based upon sophisticated theory, as it will be underlined in the next section.

ESR spectroscopy is applied extensively to material science and biochemistry. An example is given in the search of new materials with tailored magnetic properties, which has intensified in recent years. Here ESR can be employed profitably for characterizing novel stable radicalic systems, and a currently studied case is given, for instance, by nitronylnitroxide free radicals [2, 3, 4].

High interest is focused on the study of the dynamics of biological molecules, like proteins and, in particular, electron spin resonance measurements performed on proteins via site directed spin labelling (SDSL) is highly informative [5, 6, 7]. The wealth of dynamic information which can be extracted from a continuous wave electron spin resonance (cw-ESR) or electron - nuclei double resonance (ENDOR) spectrum in SDSL measured is, at present limited experimentally by the difficulty of obtaining extensive multi frequency data on spin-labelled protein and theoretically by the necessity of employing computationally efficient dynamic models. Nitroxide radicals are widely employed as spin probes. Nitroxide spin-label studies with high-frequency ESR and two-dimensional Fourier transform ESR, due to sensitivity of the spin label to its surroundings, enable one to monitor the details of the complex molecular dynamics. These studies can, for instance, provide time resolution to studies of functional dynamics of proteins.

NMR

NMR spectroscopy is nowadays considered "the" most important experimental technique in the interpretation of molecular dynamics of proteins [8, 9]. The most relevant physical observables in standard NMR measurements are the T_1, T_2 and NOE relaxations of ^{15}N, ^{2}H and ^{13}C nuclei, which are very sensitive to local dynamics. Usually, ^{15}N relaxation is employed in the study of backbone dynamics of the protein [10, 11, 12]. ^{13}C relaxation allows to investigate both backbone and lateral chain dynamics [10, 12, 13, 14]. Finally, deuterium relaxation is mainly informative for motions of lateral chains, especially via dynamical relaxation of methyl groups [13, 14].

The large amount of potential information, which can be extracted from NMR observations, comes from the fact that isotopic enrichment can be targeted to single residues of the protein, leading to the possibility to understand localized dynamics (e.g. studying conformational motions specifically in the active site of the protein). Moreover, comparison of data coming from different residues of the same protein permits to make spatial (structural) considerations.

NMR relaxation data depends on dipolar (^{15}N and ^{13}C) and quadrupolar (^{2}H) interactions, chemical shift anisotropy and cross-correlation effects. It is well known from Bloch theory [15] that NMR observables can be described as the spectral densities of the magnetic interactions. This is the conjunction point between macroscopic and molecular descriptions: the spectral densities are calculated within the theoretical framework describing the dynamics of the system.

1.2 Theory: stochastic modelling

It is convenient to clarify some assumptions that will be used in this work for both electronic and nuclear spectroscopies.

We shall treat only diluted solutions, for which we can say that every probe in solution is independent (”isolated”) and the total spin magnetization is simply the sum of the spin magnetizations of all the molecules. So we concentrate our attention only on single probe systems unless more paramagnetic centres are present on the same probe. In dilute solutions we can treat independently the dynamics of the probes. So, instead of averaging the physical observable, i.e. the spin magnetization, over the instantaneous positions of all the probes we simply average over the trajectory of only one representative probe.

A second assumption is that spin relaxation occurs without disturbing the equilibrium distribution of the dynamical coordinates. This means that the average of a physical observable is done over a macroscopic system at equilibrium.

Finally, we consider only linear responses, i.e. no intense fields causing saturation and no presence of oscillating fields are accounted for. We are indeed interested in systems in which at a time $t < 0$ a field disturbs the spin steady state, causing a deviation from equilibrium linear with the field. Then at $t = 0$ the perturbation is turned off and we describe the spin relaxation back to the steady state. Treatment of non-linear responses is well known [16], but it goes beyond the purposes of this work.

In general, the physical observable that gives the instantaneous spin state is the spin magnetization $M(t)$. Following the spin relaxation means following the decay of the magnetization back to its steady state value $M(0)$ determined by the static external field. When the magnetization decays to its equilibrium value, it dissipates the effect induced by the perturbation. In magnetic resonance, we say that the dynamics of the molecule induces relaxation. On the basis of standard linear response theory we are interested in the evaluation of the autocorrelation function

$$G(t) = \langle M(t)M(0)\rangle \tag{1.1}$$

which describes how the spin magnetization relaxes to the steady state.

The calculation of ESR and NMR observables can be in principle based on the complete solution of Schrödinger equation for the system made of paramagnetic probe + explicit solvent molecules. Given the Hamiltonian $\hat{\mathcal{H}}(\{\boldsymbol{r}_i\},\{\boldsymbol{R}_k\},\{\boldsymbol{q}_\alpha\})$, we can write the general expression

$$\begin{aligned}\hat{\mathcal{H}}(\{\boldsymbol{r}_i\},\{\boldsymbol{R}_k\},\{\boldsymbol{q}_\alpha\}) &= \hat{\mathcal{H}}_{probe}(\{\boldsymbol{r}_i\},\{\boldsymbol{R}_k\}) + \hat{\mathcal{H}}_{probe-solvent}(\{\boldsymbol{r}_i\},\{\boldsymbol{R}_k\},\{\boldsymbol{q}_\alpha\}) + \\ &\quad +\hat{\mathcal{H}}_{solvent}(\{\boldsymbol{q}_\alpha\})\end{aligned} \tag{1.2}$$

where probe and solvent terms are separated. Here we are explicitly considering *i)* electronic coordinates $\{\boldsymbol{r}_i\}$ of the paramagnetic probe (where index i runs on all probe electrons), *ii)* nuclear coordinates $\{\boldsymbol{R}_k\}$ (where index k runs on all ρ-vibrational nuclear coordinates) and *iii)* coordinates $\{\boldsymbol{q}_\alpha\}$, in which we include all degrees of freedom of all solvent molecules, each labelled by index α. The basic object of study, to which any spectroscopic observable can be linked, is given by the density matrix $\hat{\rho}(\{\boldsymbol{r}_i\},\{\boldsymbol{R}_k\},\{\boldsymbol{q}_\alpha\},t)$, which in turn is obtained from the Liouville equation

$$\begin{aligned}\frac{\partial}{\partial t}\hat{\rho}(\{\boldsymbol{r}_i\},\{\boldsymbol{R}_k\},\{\boldsymbol{q}_\alpha\},t) &= -i\left[\hat{\mathcal{H}}(\{\boldsymbol{r}_i\},\{\boldsymbol{R}_k\},\{\boldsymbol{q}_\alpha\}),\hat{\rho}(\{\boldsymbol{r}_i\},\{\boldsymbol{R}_k\},\{\boldsymbol{q}_\alpha\},t)\right] \\ &= -\hat{\mathcal{L}}(\{\boldsymbol{r}_i\},\{\boldsymbol{R}_k\},\{\boldsymbol{q}_\alpha\})\hat{\rho}(\{\boldsymbol{r}_i\},\{\boldsymbol{R}_k\},\{\boldsymbol{q}_\alpha\},t)\end{aligned} \tag{1.3}$$

Solving eq. 1.3 in time - for instance via an *ab initio* molecular dynamics scheme - allows in principle the direct evaluation of $\hat{\rho}(\{\boldsymbol{r}_i\},\{\boldsymbol{R}_k\},\{\boldsymbol{q}_\alpha\},t)$ and hence calculation of any molecular property. However, significant approximations are possible, which are basically rooted in time-scale separation.

Averaging a probe Hamiltonian with respect to femtoseconds and sub-picoseconds dynamics, pertaining to probe electronic coordinates, leaves us with only nuclear coordinates of probe and solvent molecules. Averaging on the electron coordinates is the usual implicit procedure for obtaining a spin Hamiltonian from the complete Hamiltonian of the radical. This system can be treated within the framework of classical molecular dynamics (MD), where the effect of the electrons is introduced in the classical potential terms describing the interactions among nuclei. Time evolution of the system is calculated solving the Newton's equations of motion. Given the shape of the Hamiltonian function, it is possible solve the Liouville equation for the density matrix of the system

$$\frac{\partial}{\partial t}\rho(\{\boldsymbol{R}_k\},\{\boldsymbol{q}_\alpha\},t) = -i\,[H(\{\boldsymbol{R}_k\},\{\boldsymbol{q}_\alpha\}),\rho(\{\boldsymbol{R}_k\},\{\boldsymbol{q}_\alpha\},t)] \tag{1.4}$$

and from the density matrix, the spin magnetization is given as

$$M_{XY}(t) = Tr\left\{(M_X + iM_Y)\,\rho(\{\boldsymbol{R}_k\},\{\boldsymbol{q}_\alpha\},t)\right\} \tag{1.5}$$

To follow this approach it is important to ensure that the MD trajectory is at equilibrium, allowing to sample the whole phase space of conformations. This requirement implies that the trajectory covers all the time scales of the dynamics of the system.

Our main purpose is to apply the modelling of magnetic resonance to complex systems with many degrees of freedom. The overall mobility of these systems is characterized by time scales ranging from fs - ps motions of small groups of atoms to ns - μs motions (e.g. of proteins domains). Magnetic relaxation is mostly affected by slow motions, so the trajectory should be of length of μs. Also, fast motions may, in general, be coupled to the relaxation of slow motions, implying that the time steps in the MD simulation have to be kept on the order of fs. At present it is not possible to perform such simulations in large molecular systems (say above 20 - 30 kDalton). An alternative strategy is based on the explicit introduction of a modellistic approach. The main idea is that given a physical observable, we can identify a subset of the coordinates of the system which we refer to as *relevant coordinates*, that are strongly coupled to the observable. In other words, only part of the dynamics of the system influences in a relevant way the physical observable of interest. A usual way to proceed is to separate the nuclear coordinates of the probe into two main sets: fast probe vibrational coordinates $\boldsymbol{R}_{fast}$ and slow probe coordinates, i.e. intermolecular rotation degrees of freedom and, if required, intra molecular "soft" torsional degrees of freedom, $\boldsymbol{R}_{slow}$, relaxing at least in a picoseconds time scale. Then the probe Hamiltonian is averaged with respect to picoseconds dynamics, pertaining to probe internal vibrational degrees of freedom. In the frame of a Born-Oppenheimer approximation, the averaging on the picosecond dynamics of nuclear coordinates allows to introduce in the calculation of magnetic parameters the effect of the vibrational motions, that can be very relevant in some cases [17, 18, 19]. In this way a probe Hamiltonian is obtained characterized by magnetic tensors:

$$\hat{\mathcal{H}}(\boldsymbol{R}_{slow}, \{\boldsymbol{q}_\alpha\}) = \hat{\mathcal{H}}_{spin}(\boldsymbol{R}_{slow}, \{\boldsymbol{q}_\alpha\}) + \hat{\mathcal{H}}_{probe-solvent}(\boldsymbol{R}_{slow}, \{\boldsymbol{q}_\alpha\}) + \hat{\mathcal{H}}_{solvent}(\{\boldsymbol{q}_\alpha\}) \quad (1.6)$$

The first term is the probe spin Hamiltonian. In ESR spectroscopy it will contain terms as Zeeman interaction of the unpaired electron with the field, hyperfine interactions of the unpaired electron with spin-active nuclei, electron dipolar and exchange terms in case of bi-radicals. In NMR, $\hat{\mathcal{H}}_{spin}$ will be written in terms of Zeeman interaction of nuclei with the external field, chemical shifts, hyperfine interactions among nuclei. Additional terms in eq. 1.6 may account for interactions between the probe and the medium which do not affect directly the magnetic properties (e.g. solvation energy); $\hat{\mathcal{H}}_{solvent}(\{\boldsymbol{q}_\alpha\})$ accounts for solvent-related terms. An explicit dependence is left in the magnetic tensor definition from slow probe coordinates (e.g. geometrical dependence upon rotation), and solvent coordinates. The averaged density matrix becomes $\hat{\rho}(\boldsymbol{R}_{slow}, \{\boldsymbol{q}_\alpha\}, t) = \langle \hat{\rho}(\{\boldsymbol{r}_i\}, \{\boldsymbol{R}_k\}, \{\boldsymbol{q}_\alpha\}, t)\rangle_{\{\boldsymbol{r}_i\}, \boldsymbol{R}_{fast}}$ and the corresponding Liouville equation, in the hypothesis of no residual dynamic effect of averaging with respect to sub-picoseconds processes, can be simply written as in eq. 1.3 with $\hat{\mathcal{H}}(\boldsymbol{R}_{slow}, \{\boldsymbol{q}_\alpha\})$ instead of $\hat{\mathcal{H}}(\{\boldsymbol{r}_i\}, \{\boldsymbol{R}_k\}, \{\boldsymbol{q}_\alpha\})$.

Finally, the dependence upon solvent or bath coordinates can be treated at a classical mechanical level, either by solving explicitly the Newtonian dynamics of the explicit set $\{\boldsymbol{q}_\alpha\}$ or by adopting standard statistical thermodynamics argument. This is formally equivalent to averaging the density matrix with respect to solvent variables
$\hat{\rho}(\boldsymbol{R}_{slow}, t) = \langle \hat{\rho}(\boldsymbol{R}_{slow}, \{\boldsymbol{q}_\alpha\}, t)\rangle_{\{\boldsymbol{q}_\alpha\}}$.

The modified time evolution equation for $\hat{\rho}(\boldsymbol{R}_{slow}, t)$ can be interpreted within the framework of explicit stochastic modelling according to the so-called stochastic Liouville equation (SLE) formalism, defined by the direct inclusion of motional dynamics in the form of stochastic (Fokker-Planck / diffusive) operators in the Liouvillean governing the time evolution of the system [16, 20]

$$\frac{\partial}{\partial t}\hat{\rho}(\boldsymbol{R}_{slow}, t) = -i\left[\hat{\mathcal{H}}(\boldsymbol{R}_{slow}), \hat{\rho}(\boldsymbol{R}_{slow}, t)\right] - \hat{\Gamma}\hat{\rho}(\boldsymbol{R}_{slow}, t) = -\hat{\boldsymbol{\mathcal{L}}}\hat{\rho}(\boldsymbol{R}_{slow}, t) \quad (1.7)$$

where the effective Hamiltonian, averaged with respect to the solvent coordinates, is only the probe spin Hamiltonian, i.e. $\hat{\mathcal{H}}(\boldsymbol{R}_{slow}) \equiv \hat{\mathcal{H}}_{spin}(\boldsymbol{R}_{slow})$, while $\hat{\Gamma}$ is the stochastic (Fokker-Planck or Smoluchowski) operator modelling the dependence of the reduced density matrix on relaxing processes described by stochastic coordinates $\boldsymbol{R}_{slow}$.

This is a general scheme, which can allow for additional considerations and further approximations. First, the average with respect to picoseconds dynamic processes is carried on, in practice, together with the average with respect to solvent coordinates to allow the evaluation at quantum mechanical level of magnetic tensors corrected for solvent effects. Secondly, time-separation techniques can be applied to treat approximately relatively faster relaxing coordinates included in the relevant set $\boldsymbol{R}_{slow}$, like restricted (local) torsional motions. Thirdly complex solvent environments like e.g. highly viscous fluids, can be described by an augmented set of stochastic coordinates, to be included in $\boldsymbol{R}_{slow}$, which describes slow relaxing local solvent structures [21].

Time dependence of slow coordinates is usually assumed to be a stationary Markov process, and the density probability of finding the system in configuration $\boldsymbol{R}_{slow}(t)$ at some time t if its configuration was $\boldsymbol{R}_{slow}(t-\Delta t)$ at time $t-\Delta t$ is given by

$$\frac{\partial}{\partial t}P(\boldsymbol{R}_{slow},t) = -\hat{\Gamma}(\boldsymbol{R}_{slow})P(\boldsymbol{R}_{slow},t) \tag{1.8}$$

being $\hat{\Gamma}(\boldsymbol{R}_{slow})$ a diffusive / Fokker-Planck operator [22, 23, 24, 25, 26, 27, 28, 29]. It is assumed that the stochastic process has a unique time-independent equilibrium distribution of the kind of a Boltzmann equation

$$P_{eq}(\boldsymbol{R}_{slow}) = \exp\left[-V(\boldsymbol{R}_{slow}/\mathrm{k_B}T\right]/\langle\exp\left[-V(\boldsymbol{R}_{slow}/\mathrm{k_B}T\right]\rangle_{\boldsymbol{R}_{slow}} \tag{1.9}$$

with $V(\boldsymbol{R}_{slow})$ the potential acting on the slow coordinates, $\mathrm{k_B}$ the Boltzmann constant, T the absolute temperature and $\langle\ldots\rangle_{\boldsymbol{R}_{slow}}$ means averaging over $\boldsymbol{R}_{slow}$.

Once that the set of coordinates $\boldsymbol{R}_{slow}$ and the stochastic Liouville operator $\hat{\mathcal{L}}$ have been defined, the correlation function of the magnetization can be calculated as

$$G(t) = \langle M(t)|e^{-\hat{\mathcal{L}}t}|M(t)P_{eq}(\boldsymbol{R}_{slow})\rangle \tag{1.10}$$

where now $\langle\ldots\rangle$ means average over $\boldsymbol{R}_{slow}$ and trace over spin states.

The shape of the stochastic operator $\hat{\Gamma}$ is defined accordingly to the physical interpretation of the system under exam.

The selection of the relevant coordinates $\boldsymbol{R}_{slow}$ is tantamount to introduction of a ”time coarse-graining” procedure. For large rigid molecules in isotropic media, time coarse graining is quite simple: fast coordinates are essentially the ”solvent” degrees of freedom, where we may define as the solvent the bath generating random noise affecting the rigid body coordinates (global rotation) of the molecule. Notice that, in the case of magnetic resonance, translations have no effect on the spin relaxation if the molecule is moving in a region of constant external static field, so for rigid molecules we can identify $\boldsymbol{R}_{slow} \equiv \boldsymbol{\Omega}$, and the only relevant coordinates are the Euler angles giving the global orientation of the molecule with respect to the laboratory inertial frame [2] .

In case of ordered media and / or glasses it is necessary to preserve some information about the dynamics of solvent [30, 31, 32]. The leading idea is that in such systems, the solvent molecules around the probe constitute a cage with a slow relaxation rotational dynamics coupled to the rotational motion of the probe. This is the so-called slowly relaxing local structure (SRLS) model, which has also been extended conveniently to the interpretation of NMR spectroscopy of biomolecules, as discussed in the following chapters.

When the probe molecule has internal degrees of freedom, time coarse graining procedure is more difficult. For relatively small molecular systems, as it will be shown in Chapter 3, it is often possible to use mainly chemical insight to identify the relevant coordinates. In case of complex molecules (biomolecular systems), the definition of relevant dynamics is an open problem. At present there are no satisfactory methodologies to clearly detect relevant coordinates in large molecules and this fundamental topic will be pointed out at the end of this work. In this work we shall concentrate only on the application of simple, but essentially phenomenological approaches (e.g. SRLS).

1.3 Work plan

Most of the research activities during this Ph.D. work were related to ESR spectroscopy and in particular to the development and validation of an integrated computational approach (ICA) aimed to the *ab initio* calculation of continuous wave (cw) ESR spectra. The protocol merges *ad hoc* theoretical / computational methodologies for the evaluation of structural

---

[2] in principle, inertial effects related to the relaxation of conjugate generalized momenta $\boldsymbol{V}_{slow} = \dot{\boldsymbol{R}}_{slow}$ should also be taken into account. However, in this work we assume that momenta have a smaller relaxation time compared to their conjugate generalized coordinates, i.e. that a high friction regime is always achieved. Practically, this means the system relaxation is observed only when momenta have already reached an equilibrium distribution, and therefore only the probability density depending on the coordinates is needed, governed by diffusion (or Smoluchowski) operators [22, 23, 24, 25, 26, 27, 28, 29].

parameters of the molecule (magnetic tensors, dissipative properties, etc.) with the modelling of dynamics in slow-motion regime coupled to spin relaxation based on the stochastic Liouville equation formalism. A description is provided in Chapter 3. A number of model systems have been taken into account, with the dual aim of developing and testing the theoretical models / computational approaches included in the ICA protocol. The case-studies considered are quite different in nature and include rigid and flexible (one internal degree of freedom) molecules in both isotropic and ordered phases. As a main outcome, the new software E-SpiReS (Electron Spin Resonance Simulation) [33] has been developed, which includes and automatically interfaces the different theoretical / computational methodologies scheduled in the ICA protocol. In principle, E-SpiReS is meant to be useful to both theoreticians, interested in further development of new models, and experimentalists as a tool to be coupled to a spectrometer in the laboratory. The presence of a graphical user interface makes the program simple to use and it should free users from being concerned about boring input / output operations. Moreover, E-SpiReS is based on a parallelized algorithm and runs on computer clusters. A Java web interface has been developed for remote usage, which runs on the user's computer (from any web browser) and automatically handles the communications with the remote computer.

As part of the development process of E-SpiReS, a tool for the investigation of dissipative properties of rigid and flexible molecules has been implemented. The stand alone program DITE (DIffusion TEnsor) [34] is based on the methodology introduced by Moro [35, 36] for the hydrodynamic calculation of the full friction / diffusion tensor of molecules with internal degrees of freedom represented by torsional angles. The methodology has been generalized and implemented in such a way it can in principle automatically handle molecular topology. Finally, a first attempt to tackle to the study of nuclear magnetic spectroscopy, and in particular to its application in the field of proteins, has been carried on in the final semester of activity. This preliminary work consists in the development of a new software for the interpretation of NMR data based on the SRLS model for the description of the dynamics of the system. The software, C^{++}OPPS (COupled Protein Probe Smoluchowski) [37] implements the SRLS model for the dynamics of the system and includes the cores of the DITE program for the evaluation of the diffusion tensor of the protein. Like DITE and E-SpiReS, it has a graphical user interface to simplify its usage, it is parallelized and has a web interface for remote access to a cluster. Because C++ is an object-oriented language, C^{++}OPPS is highly modular, allowing in a near future, to introduce easily new advanced models for the description of relevant dynamics in proteins.

This work is organized as follows: in Chapter 2 we discuss the calculation of dissipative properties of rigid and flexible molecules in which internal degrees of freedom are represented by torsional angles; Chapter 3 is dedicated to the presentation of the ICA for ESR spectroscopy; in Chapter 4 the C^{++}OPPS approach and code is described; finally in Chapter 5 some perspectives for further advancements are provided. The three central chapters (2, 3 and 4) have purposely the same organization with an introductory part recalling the theoretical methodology, a section describing the software and a final part presenting the application to selected case-studies.

Chapter 2

Friction tensor of flexible molecules

Experimental data from magnetic and optical spectroscopic measurements provide rich structural and dynamic information on molecular systems. However, deriving information from the experiments requires proper theoretical models in which molecular motions are carefully taken into account [38, 39, 40]. In many cases motions of the whole molecule (e.g. the global tumbling of a molecule in a fluid) and internal degrees of freedom (e.g. rotation of two molecular fragments around a bond) can be defined as a diffusive process, which depends, in turn, on a tensorial quantity, the diffusion tensor.

Evaluation of translational and rotational diffusion tensors of molecules can be based either on molecular dynamics (MD) simulations [41] or on mesoscopic, hydrodynamics-based approaches [42, 43]. In the former set of methods, explicit microscopic definition of diffusion coefficients in term of velocity correlation functions are computed from MD trajectories. In the latter set of treatments the molecular system under investigation is assimilated to a collection of elementary rigid bodies (usually spherical beads) or to a generic triaxial ellipsoid, immersed in a low-Reynolds number fluid. While methods based on MD simulations are time consuming, but apt to describe even small molecules with a minimum usage of free parameters, mesoscopic treatments are suited to the treatment of large molecules (e.g. globular proteins), although they usually require some adjustable parameters. Several authors have described the principles and applications of hydrodynamic approaches, starting with the seminal work of Bloomfield [43, 44]. Basically, the molecule is partitioned into a collection of beads, which are chosen to describe the overall shape of the molecule as closely as possible. In the classical bead approximation each atom or group of atoms is represented by a single bead; the overall rotational diffusion tensor is obtained by classic arguments [45, 46]. A remarkable implementation of these principles is provided by the HYDRONMR code [46]. In a further development beads can be chosen in order to describe only the external surface of the molecule (i.e. the part of the molecule "exposed" to the solvent); this method has been implemented in both the HYDRONMR and FAST-HYDRONMR codes [47, 48]. An alternative route, which has been the subject of recent investigation, is the definition of an equivalent triaxial ellipsoid description of the molecular shape [1]. Current implementations available as organized software tools share the partial inability of accounting for non-rigid molecules [36], and they are unrelated to current continuum solvent models also relying on solvent accessible surfaces [49].

Therefore, we would like to present here the implementation and validation of a new hydrodynamic model for direct evaluation of diffusion (friction) tensorial properties, applicable to flexible molecules for which the internal degrees of freedom are represented by torsional angles, and coupled to evaluation of solvent accessible surfaces by the same linear scaling algorithms developed for the last implementations of the so called polarizable continuum model (PCM) [50]. In particular we discuss an effective computational procedure for evaluating the diffusion tensor for a generic molecule in the presence of internal degrees of freedom: a comparison with existing literature data is also presented to show the effectiveness of the approach for a large range of molecular dimensions and solvent environments.

2.1 Computational methodology

Let us consider a molecule made of N_A atoms, which has been partitioned into N_F fragments. The i-th fragment is composed of N_i atoms and its orientation relative to the $i+1$-th fragment is defined by the torsional angle θ_i. We limit our discussion to non-cyclic molecules, so that a generic molecular systems is considered in general as a sequence of N_F fragments, and the total number of torsional angles is $N_T = N_F - 1$. Notice that $\sum_{i=1}^{N_F} N_i = N_A$. Figures 2-1 and 2-2 show schematic representations of linear and branched molecular systems in which sequences of fragments are highlighted. We define a molecular frame (MF) fixed on a chosen fragment ν (hereafter referred to as *main fragment*), which is placed for convenience in the centre of mass of the main fragment itself. The atoms in the main fragment are characterized

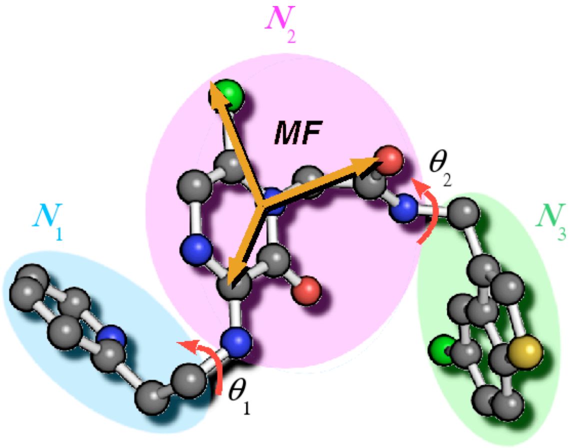

Figure 2-1: Example of molecule partitioning into a linear chain of fragments: three fragments, two torsional angles; MF is set on the second fragment.

by translational and rotational motions, while atoms belonging to the other fragments have also additional internal motions. We define the set of generalized coordinates $\boldsymbol{\mathcal{R}} = [\boldsymbol{r}, \boldsymbol{\Omega}, \boldsymbol{\theta}]$ for describing the translational and rotational coordinates of the main fragment and internal torsional motions. Associated to $\boldsymbol{\mathcal{R}}$ is the set of velocities $\boldsymbol{\mathcal{V}} = \left[\boldsymbol{v}, \boldsymbol{\omega}, \dot{\boldsymbol{\theta}}\right]$ (where the dot stands for time derivative) and also the total force consists of three contributions $\boldsymbol{\mathcal{F}} = [\boldsymbol{f}, \boldsymbol{\tau}, \boldsymbol{\tau}_i]$ corresponding, respectively, to the translational force and the global torque and internal torque moments. Forces and velocities are related by the friction tensor $\boldsymbol{\xi}$ which is defined as a $(6 + N_T) \times (6 + N_T)$ matrix

$$\begin{pmatrix} \boldsymbol{f} \\ \boldsymbol{\tau} \\ \boldsymbol{\tau}_i \end{pmatrix} = -\boldsymbol{\xi} \begin{pmatrix} \boldsymbol{v} \\ \boldsymbol{\omega} \\ \dot{\boldsymbol{\theta}} \end{pmatrix} \tag{2.1}$$

or simply $\boldsymbol{\mathcal{F}} = -\boldsymbol{\xi}\boldsymbol{\mathcal{V}}$. If one considers the system without constraints (bonds), i.e. the position of each atom is independent by the positions of the other atoms, the friction tensor $\boldsymbol{\Xi}$ of the N_A independent atoms is represented as a $3N_A \times 3N_A$ matrix. If $\boldsymbol{F}_i$ and $\boldsymbol{V}_i$ are, respectively, the translational force and velocity of the i-th atom, we can write

$$\begin{pmatrix} \boldsymbol{F}_1 \\ \vdots \\ \boldsymbol{F}_{N_A} \end{pmatrix} = -\boldsymbol{\Xi} \begin{pmatrix} \boldsymbol{V}_1 \\ \vdots \\ \boldsymbol{V}_{N_A} \end{pmatrix} \tag{2.2}$$

or $\boldsymbol{F} = -\boldsymbol{\Xi}\boldsymbol{V}$. Following standard geometrical arguments [36] one can show that $\boldsymbol{\mathcal{F}} = \boldsymbol{A}\boldsymbol{F}$ and $\boldsymbol{V} = \boldsymbol{B}\boldsymbol{\mathcal{V}}$, where $\boldsymbol{A}$ and $\boldsymbol{B}$ are $(6 + N_T) \times 3N_A$ and $3N_A \times (6 + N_T)$ matrices which

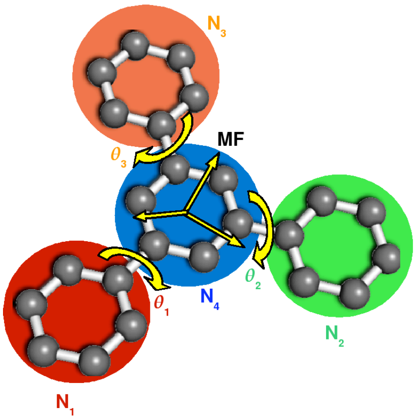

Figure 2-2: Example of molecule partitioning into a branched chain of fragments: four fragments, three torsional angles; MF is set on the central fragment.

depend on the molecular geometry; additionally, $\boldsymbol{B} = \boldsymbol{A}^{\mathrm{tr}}$. It follows that

$$\boldsymbol{\xi} = \boldsymbol{B}^{\mathrm{tr}}\boldsymbol{\Xi}\boldsymbol{B} = \begin{pmatrix} \boldsymbol{\xi}_{TT} & \boldsymbol{\xi}_{TR} & \boldsymbol{\xi}_{TI} \\ \boldsymbol{\xi}_{RT} & \boldsymbol{\xi}_{RR} & \boldsymbol{\xi}_{RI} \\ \boldsymbol{\xi}_{IT} & \boldsymbol{\xi}_{IR} & \boldsymbol{\xi}_{II} \end{pmatrix} \tag{2.3}$$

where the subscripts stand for T = translational, R = rotational and I = internal. The diffusion tensor is obtained from Einstein relation, as the inverse of $\boldsymbol{\xi}$

$$\boldsymbol{D} = k_B T \boldsymbol{\xi}^{-1} = \begin{pmatrix} \boldsymbol{D}_{TT} & \boldsymbol{D}_{TR} & \boldsymbol{D}_{TI} \\ \boldsymbol{D}_{RT} & \boldsymbol{D}_{RR} & \boldsymbol{D}_{RI} \\ \boldsymbol{D}_{IT} & \boldsymbol{D}_{IR} & \boldsymbol{D}_{II} \end{pmatrix} \tag{2.4}$$

where k_B is the Boltzmann constant and T the absolute temperature. The friction tensors are linked to the diffusion tensors $\boldsymbol{D}$ (constrained spheres) and $\boldsymbol{d}$ (unconstrained spheres) via the generalized Einstein relations $\boldsymbol{D} = k_B T \boldsymbol{\xi}^{-1}$ and $\boldsymbol{d} = k_B T \boldsymbol{\Xi}^{-1}$. It follows that the molecular diffusion tensor for the joint translation, rotation and internal conformational motion for the molecule, i.e. $\boldsymbol{D}$, is obtained as

$$\boldsymbol{D} = (\boldsymbol{B}^{\mathrm{tr}}\boldsymbol{d}^{-1}\boldsymbol{B})^{-1} \tag{2.5}$$

Main ingredients for the calculation of the diffusion tensor are the geometric matrix $\boldsymbol{B}$ and the unconstrained diffusion tensor $\boldsymbol{d}$. Let us first consider the calculation of the geometric matrix. We define $\boldsymbol{r}_j^i$ as the vector of the i-th atom in the j-th fragment, $\boldsymbol{u}_n$ as the unitary vector defining the rotation θ_n, taken to be parallel to the n-th torsional angle and pointing away from the main fragment, and $\boldsymbol{r}^i_{j,k}$ the distance vector between the j-th atom of i-th fragment and the atom at the origin of the unitary vector $\boldsymbol{u}_k$. Atoms in the main fragment are characterized only by translational and global rotational velocity

$$\boldsymbol{v}^{\nu}_j = \boldsymbol{v} + \boldsymbol{\omega} \times \boldsymbol{r}^{\nu}_j \tag{2.6}$$

while for the remaining fragments ($i \neq \nu$) torsional contributions must be included

$$\boldsymbol{v}^{i}_j = \boldsymbol{v} + \boldsymbol{\omega} \times \boldsymbol{r}^{i}_j + \sum_k \dot{\theta}_k \boldsymbol{u}_k \times \boldsymbol{r}^i_{j,k} \tag{2.7}$$

where the summation is taken over the angles that link the main fragment to the i-th fragment. Equations (2.6) and (2.7) can be rewritten in matrix form

$$\boldsymbol{v}^{i}_j = {}^T\boldsymbol{B}^i_j \boldsymbol{v} + {}^R\boldsymbol{B}^i_j \boldsymbol{\omega} + \sum_k {}^I\boldsymbol{B}^i_{j,k} \dot{\theta}_k \tag{2.8}$$

where ${}^T\boldsymbol{B}^i_j = \mathbf{1}_3$, ${}^R\boldsymbol{B}^i_j = \boldsymbol{r}^{i\,\times}_j$ and ${}^I\boldsymbol{B}^i_{j,k} = \boldsymbol{r}^{i\,\times}_{j,k}\boldsymbol{u}_k$ or $\mathbf{0}$ depending on k and i, and $r^{\times}_{\alpha\beta} = r_k \xi_{\alpha\beta\gamma}$, where $\xi_{\alpha\beta\gamma}$ is the Levi-Civita tensor with $\alpha, \beta, \gamma = 1, 2, 3$. For a linear chain of fragments, numbered sequentially from the first to the last one, the general form of the $\boldsymbol{B}$ matrix is

$$\boldsymbol{B} = \begin{pmatrix}
\mathbf{1}_3 & \boldsymbol{r}^{1\,\times}_j & \boldsymbol{r}^{1\,\times}_{j,1}\boldsymbol{u}_1 & \cdots & \boldsymbol{r}^{1\,\times}_{j,\nu-1}\boldsymbol{u}_{\nu-1} & \mathbf{0} & \mathbf{0} & \cdots & \mathbf{0} \\
\mathbf{1}_3 & \boldsymbol{r}^{2\,\times}_j & \mathbf{0} & \cdots & \boldsymbol{r}^{2\,\times}_{j,\nu-1}\boldsymbol{u}_{\nu-1} & \mathbf{0} & \mathbf{0} & \cdots & \mathbf{0} \\
\vdots & \vdots & \vdots & & \vdots & \vdots & \vdots & & \vdots \\
\mathbf{1}_3 & \boldsymbol{r}^{\nu-1\,\times}_j & \mathbf{0} & \cdots & \boldsymbol{r}^{\nu-1\,\times}_{j,\nu-1}\boldsymbol{u}_{\nu-1} & \mathbf{0} & \mathbf{0} & \cdots & \mathbf{0} \\
\mathbf{1}_3 & \boldsymbol{r}^{\nu\,\times}_j & \mathbf{0} & \cdots & \mathbf{0} & \mathbf{0} & \mathbf{0} & \cdots & \mathbf{0} \\
\mathbf{1}_3 & \boldsymbol{r}^{\nu+1\,\times}_j & \mathbf{0} & \cdots & \mathbf{0} & \boldsymbol{r}^{\nu+1\,\times}_{j,\nu}\boldsymbol{u}_{\nu} & \mathbf{0} & \cdots & \mathbf{0} \\
\vdots & \vdots & \vdots & & \vdots & \vdots & \vdots & & \vdots \\
\mathbf{1}_3 & \boldsymbol{r}^{N_F-1\,\times}_j & \mathbf{0} & \cdots & \mathbf{0} & \boldsymbol{r}^{N_F-1\,\times}_{j,\nu}\boldsymbol{u}_{\nu} & \boldsymbol{r}^{N_F-1\,\times}_{j,\nu+1}\boldsymbol{u}_{\nu+1} & \cdots & \mathbf{0} \\
\mathbf{1}_3 & \boldsymbol{r}^{N_F\,\times}_j & \mathbf{0} & \cdots & \mathbf{0} & \boldsymbol{r}^{N_F\,\times}_{j,\nu}\boldsymbol{u}_{\nu} & \boldsymbol{r}^{N_F\,\times}_{j,\nu+1}\boldsymbol{u}_{\nu+1} & \cdots & \boldsymbol{r}^{N_F\,\times}_{j,N_F-1}\boldsymbol{u}_{N_F-1}
\end{pmatrix} \tag{2.9}$$

The form of the geometric matrix $\boldsymbol{B}$ is dependent on the topology and also on the numbering scheme chosen for the fragments. While for a linear chain of fragments it is quite natural to number the fragments sequentially, finding a simple and generalized scheme for branched systems is not straightforward. However, in the software developed by us (see next section), users need not to be concerned with the topological problem. The numbering scheme is decided by an automatic procedure, following a very simple algorithm, implemented in our code. Users need only to supply information on the pairs of atoms which define the rotating bonds: this information is used by the program to recognize the fragments and to compute the correct form of the geometric matrix. The algorithm is completely general for systems partitionable in a non-cyclic sequence of fragments, while cyclic structures are not included in the present implementation.

Evaluation of $\boldsymbol{d}$ can be carried out at the simplest possible level assuming the model of non-interacting spheres in a fluid, or one can include hydrodynamic interactions. We have followed the second route, based on the Rotne-Prager (RP) approach [51, 52], which ensures a satisfactory albeit not too cumbersome treatment of sphere-sphere hydrodynamic interactions. The resulting elements of $\boldsymbol{D}$ depend upon a purely geometrical tensorial component $\overline{\boldsymbol{D}}$ and the translational diffusion coefficient for an isolated sphere D_0, i.e.

$$\boldsymbol{D} = D_0 \overline{\boldsymbol{D}} \tag{2.10}$$

where $D_0 = k_B T / C R_e \eta \pi = k_B T / \Xi_0$: here C is a constant depending upon hydrodynamic boundary conditions, R_e is the average radius for the spheres, η is the local viscosity. The RP unconstrained diffusion tensor is given as

$$d_{ii} = \frac{k_B T}{\Xi_0} \mathbf{1}_3$$

$$\begin{cases} d_{ij} = \dfrac{k_B T}{\Xi_0} \dfrac{3R_e}{4r_{ij}^3} \left[\left(r_{ij}^2 + \dfrac{2}{3} R_e^2 \right) \mathbf{1}_3 + \left(1 - 2 \dfrac{R_e^2}{r_{ij}^2} \right) \boldsymbol{r}_{ij} \otimes \boldsymbol{r}_{ij} \right] & \text{, if } r_{ij} > 2R_e \\ d_{ij} = \dfrac{k_B T}{\Xi_0} \left[\left(1 - \dfrac{9}{32} \dfrac{r_{ij}}{R_e} \right) \mathbf{1}_3 + \dfrac{3}{32} \dfrac{\boldsymbol{r}_{ij} \otimes \boldsymbol{r}_{ij}}{r_{ij}^2} \right] & \text{, if } r_{ij} < 2R_e \end{cases} \tag{2.11}$$

where i and j are two generic atoms, $\boldsymbol{r}_{ij} = \boldsymbol{r}_i - \boldsymbol{r}_j$ and with the symbol $\otimes$ we intend the dyadic product. Notice that the general methodology reported above can be applied with minor changes to other types of internal motions, like stretching of bonds, bending of bond angles, domain and loop motions.

2.2 DITE software

DITE (DIffusion TEnsor) is the newly developed package for the calculation of dissipative parameters (friction and / or diffusion tensors) of small and large molecular systems, in the presence of internal (conformational) degrees of freedom. DITE is based on a computational approach which combines PCM-based calculations of molecular shape and hydrodynamic modelling described in the previous section. As it will be shown in Section 2.3.1 this approach is able to reproduce accurately experimental diffusion coefficients, both translational and rotational, for molecules of diverse extensions ranging from a few atoms to proteins. In

Cut-off	Beads	τ / ns	D_{XX} / 10^{-7} Hz	D_{YY} / 10^{-7} Hz	D_{ZZ} / 10^{-7} Hz	t / s
0%	563	5.0	3.11	3.27	3.55	2.30
5%	558	5.028	3.12	3.37	3.56	2.25
10%	518	5.011	3.12	3.29	3.57	1.87
15%	411	4.9380	3.17	3.34	3.62	1.06
20%	351	4.8091	3.23	3.40	3.76	0.73
25%	315	4.7425	3.29	3.45	3.80	0.56
Experiment		5.0	3.12	3.21	3.67	

Table 2.1: Rotational diffusion tensor and correlation time of ubiquitin calculated at different cut-offs.

particular, successful application to the interpretation of spectroscopical observables, like for instance continuous-wave electron spin resonance measurements has been demonstrated, for spin-labelled systems ranging from 20 to 200 atoms. Comparison with other current methodologies has also been carried out. DITE computational times are comparable with existing established software in the field, due to the combination of the fast determination of the molecular surface and the optimization of the linear algebra operations required to evaluate the friction tensors. Moreover, the direct inclusion of conformational degrees of freedom is made possible, at negligible additional computational cost, at least when compared to the evaluation of friction / diffusion tensors of rigid molecular systems of similar dimensions, which are the only ones treated by approaches like HYDRONMR [46] and the triaxial ellipsoid method [1].

Implementation

Our purposes in the course of this study have been *i)* the testing and validation of an efficient version of the standard hydrodynamic model which is expected to perform effectively both for large and relatively small molecular systems and *ii)* an implementation of the aforementioned model compatible with the evaluation of solvent accessible surfaces developed in the framework of the PCM [50]. In particular, the new code post-processes a modified version of the G03 code providing the exposed atoms and their surfaces by very effective linear scaling algorithms [53].

A fast and reliable implementation of the procedure, briefly sketched in Section 2.1, is based on the availability of efficient routines for matrix inversion (in order to evaluate eq. (2.5)).

Our strategy is based on two very simple choices: first of all optimized open-source code (LAPACK) is employed [54]; next, we introduce the possibility to exclude from the calculation atoms that are not ”wetted” by the solvent, assuming that they give vanishing contribution to the total friction. Thus only the (non-hydrogen) atoms with a solvent exposed surface above a suitable threshold are taken into account in the contracted or pruned molecule used to calculate the unconstrained diffusion tensor and geometric matrix.

DITE consists of a graphical user interface (GUI) written in Java in which the user is able, by a simple point-and-click procedure, to *i)* model the partitioning into fragments of flexible molecules, *ii)* set the physical parameters and also *iii)* launch an automatically generated input for the G03 program [53] if geometry optimization and/or PCM analysis is required in the calculation of the diffusion tensor. The core of DITE that performs all the calculations is, instead, written in the C language because a Java program is only interpreted (not compiled in machine code) and so it should result in too slow computations.

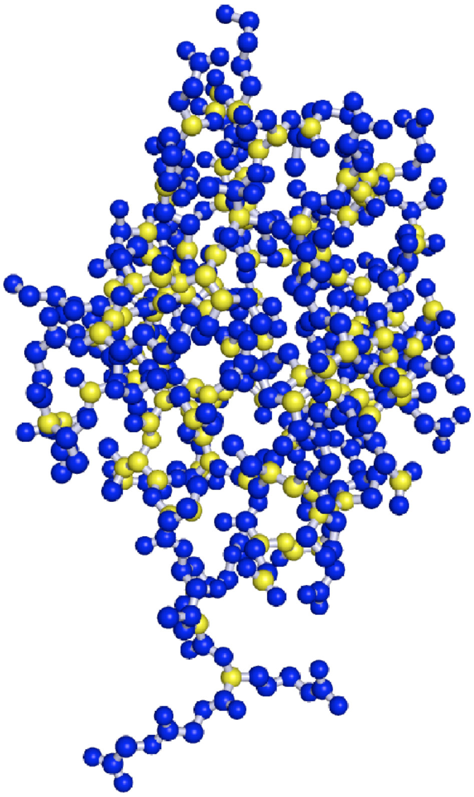

Figure 2-3: Representation of wetted (blue) and unwetted (yellow) extended atoms of Ubiquitin, based on the threshold of 10% of area per atom outside of the effective molecular surface calculated by Gaussian 03.

We tested the effect of the cut-off on the ubiquitin protein. Calculations were performed with $R_e = 4.1$ Å and $C = 6$, parameters that give the best agreement with experimental data obtained at 300 K in aqueous solution [55]. The last five residues have been clipped off from the PDB file because of the flexibility of the C-terminus. This procedure was followed also in references [1, 46] to compare calculated and experimental diffusion tensors. Also, experimental data has been scaled to 293 K in order to further compare our results with that reported in Ref. [1]. Table 2.1 sketches the changes of the diffusion tensor with the cut-off, together with the number of ”wetted” beads and the calculation time. As can be seen, a 10% exposed surface per extended atom can be considered a safe cut-off for considering an atom wetted. In Figure 2-3 the selection procedure results are shown for Ubiquitin: blue atoms expose more than 10% of their area to the solvent, i.e. they extend themselves of this amount outside the effective molecular surface, while yellow atoms are below this threshold. If a cut-off larger than 10% is chosen, a higher percentage of atoms could be excluded to improve calculation time but, of course, introducing some error.

Notice that in all the cases presented here, no geometry optimization has been performed, but one can easily use the whole procedure to obtain at once both structural information (from QM, MM or mixed methods including PCM for taking into account bulk solvent effects) and diffusion properties. As a matter of fact, this approach has been adopted in the *ab initio* integrated approach to the simulation of electron spin resonance (ESR) spectroscopy of different systems [56, 57, 58, 59] as will be pointed out in the next chapter.

2.3 Applications

2.3.1 Case studies

We compare our results with available experimental values for a number of model systems. We present in this Section some of our results both for linear and branched flexible molecules. To check the code performance and capabilities we compare our findings, for rigid molecules only, with an established paradigm software in the field, the well-known HYDRONMR program by Josè Garcia de la Torre et al. [46]. Table 2.2 summarizes our first set of results, for rigid molecules of increasing size, chosen on the basis of available experimental data in the literature. Parameters are chosen as follows: the temperature is 298.15 K for all small molecules and BPTI, and 293.15 K for Ubiquitin and lysozyme. The boundary constant C has been always taken equal to 6 (stick boundary conditions). The sphere effective radius is chosen first according to the following expression:

$$R_e = \sum_{\alpha} n_\alpha R_\alpha / \sum_{\alpha} n_\alpha \tag{2.12}$$

where n_α is the number of atoms of type α and R_α is the associated VdW radius (we employ the standard UA0 set of van der Waals radii, used in the latest PCM implementations [50]). The overall agreement of calculated results (column 3) with experimental data is satisfactory, even for small molecules. Theoretical calculations over-estimate diffusion parameters for the proteins BPTI and Ubiquitin. Adjustment of the effective radius in different solvents reduces significantly this discrepancy (column 5). Notice that results are in good agreement with HYDRONMR predictions, and that the computational effort required, even for the largest system considered here (lysozyme in water) is about 11 seconds on a standard Intel Dualcore 2.16 GHz processor.

We then performed calculations over the five globular proteins of different dimensions reported in Table 2 of ref. [1] to compare our results with the ones obtained with HYDRONMR and with the method of the triaxial ellipsoid. Results are given in Table 2.3. For all the proteins an augmented effective radius is needed to fit experimental data due to the presence of a layer of hydration water which increases the exposed surface, which leads, in turn, to a larger friction. With our model we needed an effective radius of 3.7 Å and stick boundary conditions, while for HYDRONMR the atomic effective radius (AER) is set to 3.2 Å (keeping the default settings for the minibeads) and for the triaxial ellipsoid method the value for the hydration layer thickness (HLT) is set to 2.8 Å . Differences in the adjustable parameter of the three methods are related to the different approximations used for the solvent exposed surface of the molecule, which is responsible of the friction. As mentioned above, the calculation time for our program increases with the cubic power of the number of effective atoms, since the algorithm involves inversion of a $3N \times 3N$ matrix.

Molecule	Experimental	DITE (fixed R_e)		DITE (fitted R_e)		HYDRONMR (fixed R_e)		HYDRONMR (fitted R_e)	
Acetylcholine in water / D_{TT}[60]	$6.1 \cdot 10^{-10}$ m^2/s	2.00 Å	$6.7 \cdot 10^{-10}$ m^2/s	2.55 Å	$6.1 \cdot 10^{-10}$ m^2/s	2.00 Å	$6.3 \cdot 10^{-10}$ m^2/s	2.25 Å	$6.1 \cdot 10^{-10}$ m^2/s
PDT in n-hexane / D_{TT}[61]	$2.9 \cdot 10^{-9}$ m^2/s	2.23 Å	$2.1 \cdot 10^{-9}$ m^2/s	1.05 Å	$2.9 \cdot 10^{-9}$ m^2/s	2.23 Å	$1.9 \cdot 10^{-9}$ m^2/s	1.30 Å	$2.9 \cdot 10^{-9}$ m^2/s
Coumarin 153 in methanol / D_{RR}[62]	$4.0 \cdot 10^{9}$ Hz	2.01 Å	$3.2 \cdot 10^{9}$ Hz	1.65 Å	$4.1 \cdot 10^{9}$ Hz	2.01 Å	$2.0 \cdot 10^{9}$ Hz	1.30 Å	$3.2 \cdot 10^{9}$ Hz
Sucrose in water / D_{TT}[61]	$5.2 \cdot 10^{-10}$ m^2/s	2.00 Å	$5.3 \cdot 10^{-10}$ m^2/s	2.00 Å	$5.2 \cdot 10^{-10}$ m^2/s	2.00 Å	$4.6 \cdot 10^{-10}$ m^2/s	1.80 Å	$5.2 \cdot 10^{-10}$ m^2/s
Tetrapeptide in water / D_{TT}[63]	$4.7 \cdot 10^{-10}$ m^2/s	2.06 Å	$4.5 \cdot 10^{-10}$ m^2/s	1.80 Å	$4.7 \cdot 10^{-10}$ m^2/s	2.06 Å	$4.1 \cdot 10^{-10}$ m^2/s	1.55 Å	$4.7 \cdot 10^{-10}$ m^2/s
BPTI in water / D_{TT}[47]	$1.3 \cdot 10^{-10}$ m^2/s	2.01 Å	$1.7 \cdot 10^{-10}$ m^2/s	3.20 Å	$1.4 \cdot 10^{-10}$ m^2/s	2.01 Å	$1.6 \cdot 10^{-10}$ m^2/s	3.20 Å	$1.5 \cdot 10^{-10}$ m^2/s
BPTI in water / D_{RR}[47]	$4.2 \cdot 10^{7}$ Hz	2.01 Å	$5.9 \cdot 10^{7}$ Hz	3.20 Å	$4.2 \cdot 10^{7}$ Hz	2.01 Å	$5.0 \cdot 10^{7}$ Hz	3.20 Å	$4.2 \cdot 10^{7}$ Hz
Ubiquitin in water / D_{RR}^{XX}[1]	$3.1 \cdot 10^{7}$ Hz	2.06 Å	$3.4 \cdot 10^{7}$ Hz	4.10 Å	$3.1 \cdot 10^{7}$ Hz	2.06 Å	$4.2 \cdot 10^{7}$ Hz	3.20 Å	$3.1 \cdot 10^{7}$ Hz
Ubiquitin in water / D_{RR}^{YY}[1]	$3.2 \cdot 10^{7}$ Hz	2.06 Å	$3.5 \cdot 10^{7}$ Hz	4.10 Å	$3.3 \cdot 10^{7}$ Hz	2.06 Å	$4.3 \cdot 10^{7}$ Hz	3.20 Å	$3.3 \cdot 10^{7}$ Hz
Ubiquitin in water / D_{RR}^{ZZ}[1]	$3.7 \cdot 10^{7}$ Hz	2.06 Å	$5.0 \cdot 10^{7}$ Hz	4.10 Å	$3.6 \cdot 10^{7}$ Hz	2.06 Å	$6.6 \cdot 10^{7}$ Hz	3.20 Å	$3.6 \cdot 10^{7}$ Hz
Lysozyme in water / D_{TT}[47]	$1.1 \cdot 10^{-10}$ m^2/s	2.00 Å	$1.2 \cdot 10^{-10}$ m^2/s	2.10 Å	$1.2 \cdot 10^{-10}$ m^2/s	2.00 Å	$1.2 \cdot 10^{-10}$ m^2/s	2.60 Å	$1.2 \cdot 10^{-10}$ m^2/s
Lysozyme in water / D_{RR}[47]	$2.6 \cdot 10^{7}$ Hz	2.00 Å	$2.7 \cdot 10^{7}$ Hz	2.10 Å	$2.6 \cdot 10^{7}$ Hz	2.00 Å	$2.5 \cdot 10^{7}$ Hz	2.60 Å	$2.8 \cdot 10^{7}$ Hz

Table 2.2: Translational and rotational diffusion coefficients for a selection of rigid molecular systems of increasing size. Fixed-radius calculations were performed by choosing, for each molecule, R_e as defined in eq. 2.12, while for fitted-radius calculations R_e was adjusted for best agreement with experimental data. Here D_{TT} and D_{RR} are one third of the traces of the translational and rotational parts of the diffusion tensor, while $D_{RR}^{\alpha\alpha}$. with $\alpha = X, Y, Z$ represent the diagonal components of the rotational diffusion tensor in the molecular frame.

We decided to avoid further approximations, beyond the mesoscopic approach to the problem, even if the resulting algorithm is slower than other existing methods.

FAST-HYDRONMR employs the so-called double summation approximation (DSA) [48] which is based on the truncation to the second term of the expansion formula for the inversion of a matrix. With this approximation the computational cost becomes proportional to N^2 instead than N^3. De La Torre and co-workers found that the "exact" diffusion tensor is just the approximated one scaled by a factor. The method is very fast, but at the price of the introduction of a new parameter.

	τ / ns	D_{XX} / 10^{-7} Hz	D_{YY} / 10^{-7} Hz	D_{ZZ} / 10^{-7} Hz	N beads	time / s
			Protein G, 1igd.pdb			
experiment	3.7	3.73	4.15	5.63		
HYDRONMR	3.9	3.67	3.81	5.19		
PCA	3.9	3.89	4.05	4.83		
DITE	3.9	3.71	3.86	5.26	434	1.2
			Ubiquitin, 1ubq.pdb			
experiment	5.0	3.12	3.21	3.67		
HYDRONMR	5.0	3.14	3.28	3.61		
PCA	4.9	3.24	3.37	3.61		
DITE	4.7	3.33	3.50	3.82	563	2.3
			Cytochrome c2, 1c2n.pdb			
experiment	10.4	1.42	1.62	1.77		
HYDRONMR	7.9	1.81	1.98	2.52		
PCA	7.7	1.95	2.09	2.44		
DITE	7.7	1.86	2.02	2.62	907	8.0
			Ribonuclease H, 2rn2.pdb			
experiment	11.7	1.34	1.34	1.59		
HYDRONMR	11.6	1.28	1.38	1.64		
PCA	10.4	1.45	1.56	1.78		
DITE	11.5	1.29	1.39	1.65	1238	18.6
			HIV-1 protease, 1bvg.pdb			
experiment	13.0	1.11	1.18	1.55		
HYDRONMR	13.8	1.02	1.05	1.56		
PCA	13.0	1.12	1.17	1.67		
DITE	13.2	1.07	1.10	1.63	1554	35.0

Table 2.3: Rotational correlation time and diffusion tensor for a selection of five globular proteins. Calculations were performed by choosing, $AER = 3.2$ Å for HYDRONMR, $HLT = 2.8$ Å for the ellipsoid model and $R_e = 3.7$ Å for our program. As in ref. [1]: protein G has the first five residues from the PDB file clipped off; ubiquitin has the last five residues from the PDB file clipped off due to the mobility of the C-terminus; of the 20 structures in the PDB file of Cytochrome c2 the second was taken into account. All experimental data are normalized to 293 K and the rotational correlation time is calculated as $\tau = 1/\left(6tr\{\boldsymbol{D}_{RR}\}\right)$.

Also the triaxial ellipsoid method involves a very fast algorithm, which takes fractions of seconds even for very large molecules (10^4 atoms), but it is based on the assumption that a molecule can be approximated by an ellipsoid. While this assumption is reasonable for globular proteins it can break down for molecules of complex shapes. We preferred to keep generality and lowest number of free parameters as possible, even if this places a limit on the dimensions of the molecules that can be treated, and to concentrate on the aspect of flexibility which represents in our opinion an important advancement for a tool intended to supply a molecular property for the interpretation of experimental measurements. As mentioned above, our program is able to post-process the output of codes including solvent accessible surface evaluation and, with a cut-off of 10%, molecules of medium-large size can be treated quite reasonably in terms of computer resources and time.

Next, we report the calculation of the diffusion tensor for the $FeCo_2(CO)_9(\mu_3\text{-}PPh)$ system, represented in Figure 2-4, in which the single bond between the phenyl group and the cobalt atom can rotate. Data for global and internal diffusion parameters are available [64]. To proceed, we partition the molecule into two fragments, i.e. the metal cluster (fragment 1) and the phenyl ring (fragment 2). The reference fragment is chosen on the cluster and the molecular frame is located for convenience on the P atom. Global tumbling diffusion is defined by two coefficients $D_\perp$ and $D_\parallel$, as indicated in Figure 2-4, internal diffusion is described by D_{II}. Experimental data, obtained from ^{13}C NMR spin-lattice relaxation measures are available for $D_\perp = 4.9 \cdot 10^9$ Hz and $D_S = D_\parallel + D_{II} = 4.8 \cdot 10^{10}$ Hz.

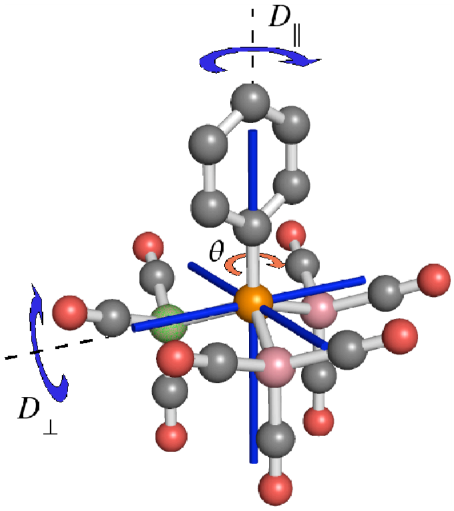

Figure 2-4: Representation of $FeCo_2(CO)_9(\mu_3\text{-}PPh)$ complex.

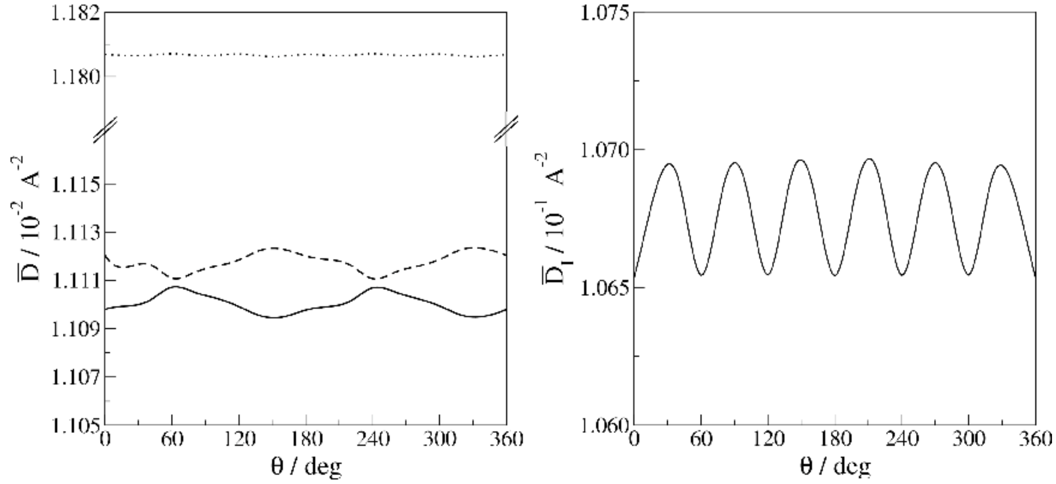

Figure 2-5: Dependence upon internal angle of scaled rotational components (above: D_{XX} full line, D_{YY} dashed line, D_{ZZ} dotted line) and scaled internal component (below) of the diffusion tensor of the $FeCo_2(CO)_9(\mu_3\text{-PPh})$ complex in $CDCl_3$ at 330 K.

The best agreement with experimental data in chloroform at 298.15 K is obtained by choosing $R_e = 1.03$ Å (with stick boundary conditions, $C = 6$): calculated values are $D_\perp = 4.3 \cdot 10^9$ Hz and $D_S = D_\parallel + D_{II} = 4.7 \cdot 10^{10}$ Hz. Strictly speaking these are values averaged with respect to the torsional angle. The weak dependence of all the theoretical diffusion tensor components on the internal torsional angle is shown in Figure 2-5, where the scaled values of calculated diffusion tensor are represented. Absolute values can be obtained multiplying by $D_0 = 3.9 \cdot 10^{11} \text{Å}^2 \text{s}^{-1}$. In this example, internal rotation can be safely assumed to be essentially free from steric hindrance (no internal torsional potential), so that one can compare directly the measured internal diffusion parameter $D_S = D_\parallel + D_{II}$, obtained as the inverse of correlation times of the motion obtained by NMR relaxation measures [65] with the calculated diffusion coefficients. It has to be noticed that in the presence of an internal potential acting on the torsional angles, diffusion coefficients are not simply the inverse of correlation times of the motion. It is a common practice to interpret correlation times as the inverse of diffusion coefficients even in such situations, leading to the conclusion that diffusion (so friction) is a quantity that depends on the steric hindrance. In our formalism, the molecule is considered as a flexible ”mechanical” body made by discrete masses joined by constraints and hubs and moving in a continuum fluid. Friction acting on such a body moving in the fluid is independent on obstacles that it could encounter along its trajectory; it only depends on the geometry of the body and on the macroscopic characteristics of the fluid. The

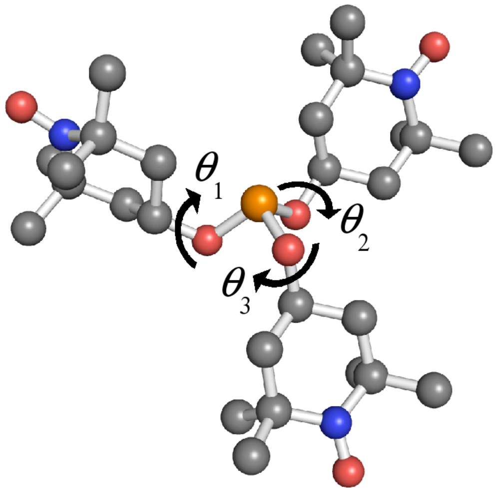

Figure 2-6: Structure of tris(2,2,6,6 tetramethyl - 1 - oxyl -4 - piperidyl) phosphite (TMP) with minimum energy. Rotations about the P-O bonds have a high energy barriers so those angles were fixed, giving only the three torsional angles indicated ad θ_1, θ_2 and θ_3.

interpretation of experimental data in the presence of a torsional potential can be done by introducing *ad hoc* models for the dynamics of the molecule, in which the diffusion tensor and the torsional potential are two ingredients which both act on the relaxation of the motion. An example of this approach is the slowly relaxing local structure (SRLS) model where two bodies rotate one with respect to the other under the influence of an internal potential. A large literature is available concerning the use of the SRLS model in the interpretation of magnetic resonance data, both electronic and nuclear [16, 32, 56, 57, 58, 59, 66, 67]. Diffusion coefficients can also be obtained from the analysis of electron spin resonance (ESR) spectra as will be discussed in detail in the next chapter.

Finally we performed calculations on two molecules involving three significant internal rotations which define four fragments connected in such a way to lead to a branched topology, i.e. a central fragment with the other three fragments attached to it. We analysed the small Tris(2,2,6,6 tetramethyl-1-oxyl-4-piperidyl) phosphite (TTP), Figure 2-6, and a hypothetical tri-labeled T4 lysozyme (3R2T4), Figure 2-7, with the 1-oxyl-2,2,5,5-tetramethyl-3-pyrrolidine-3-(methyl)-mathanethiosulfonate spin label, known as R2 spin label and represented in Figure 2-8. We chose spin labelled molecules because, experimentally, diffusion tensors could be extracted from the analysis of their cw-ESR spectra.

In both cases we generated 1000 conformations by taking ten points from 0 to 2π for each torsional angle to study the dependence of the different parts of the diffusion tensor on the internal dynamics. Calculations have been performed with a standard effective radius of 2.0 Å and slip boundary conditions. In all cases we will present the reduced form of the diffusion tensor, i.e. the tensor divided by the quantity $k_BT/\pi R_e C\eta$, which depends only on geometric properties of the molecule and not on physical properties of the fluid.

For the TTP molecule we found that the rotational part of the diffusion tensor is strongly dependent on the values of the internal angles obtaining an overall variation of about 10% for the trace of the rotational part and variations of 9% for the D_{XX} component, 13% for the D_{YY} component, and 23% for the D_{ZZ} component. We also found that the internal part of the diffusion tensor shows off-diagonal terms of the same order, or at most one order smaller, of the diagonal part, leading to a strong coupling between the three internal motions. Furthermore, the dependence of the tensor coefficients on the θ_3 angle is higher than the variation given by the rotation of the two angles θ_1 and θ_2. The X-band ESR spectrum of the 3R2T4 molecule would be affected mainly by the angle indicated in Figure 2-8 of the three spin probes (and of course on global tumbling), while the other four internal angles can be considered frozen [67].

Figure 2-7: T4 lysozyme mutant with three R2 spin labels placed on residues 65, 82 and 131. Also torsional angles are indicated which correspond to the three χ_4 angles.

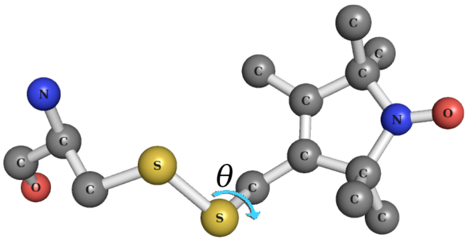

Figure 2-8: T4 lysozyme mutant with three R2 spin labels placed on residues 65, 82 and 131. Also torsional angles are indicated which correspond to the three χ_4 angles.

Analysis of the diffusion tensor for each conformation shows that the global rotational diffusion tensor is negligibly affected by the internal rotations (deviations under 5%) due to the very small size of the three rotating frames with respect to the overall extension of the molecule. Moreover, the internal part of the diffusion tensor reveals that the three motions are practically decoupled, with the off-diagonal terms 2 - 3 orders of magnitude smaller than the diagonal values: this can be attributed to both the small dimensions of the rotating fragments and to their large distances. In Figure 2-10 the dependence is shown of the trace of the rotational part and the three diagonal components of the internal part of the diffusion tensor on the three internal angles.

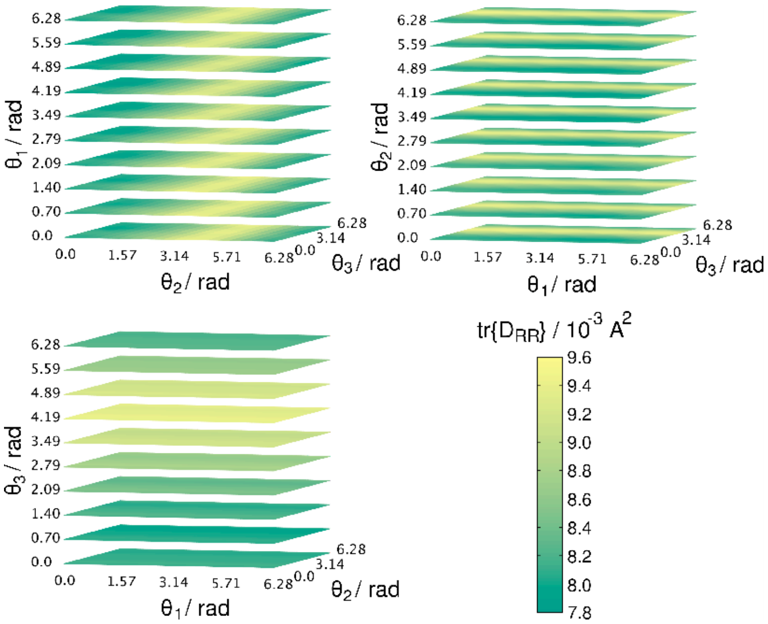

Figure 2-9: Representation of the trend of the trace of the rotational part of the diffusion tensor of tris(2,2,6,6 tetramethyl-1-oxyl-4-piperidyl) phosphite as function of the three internal angles.

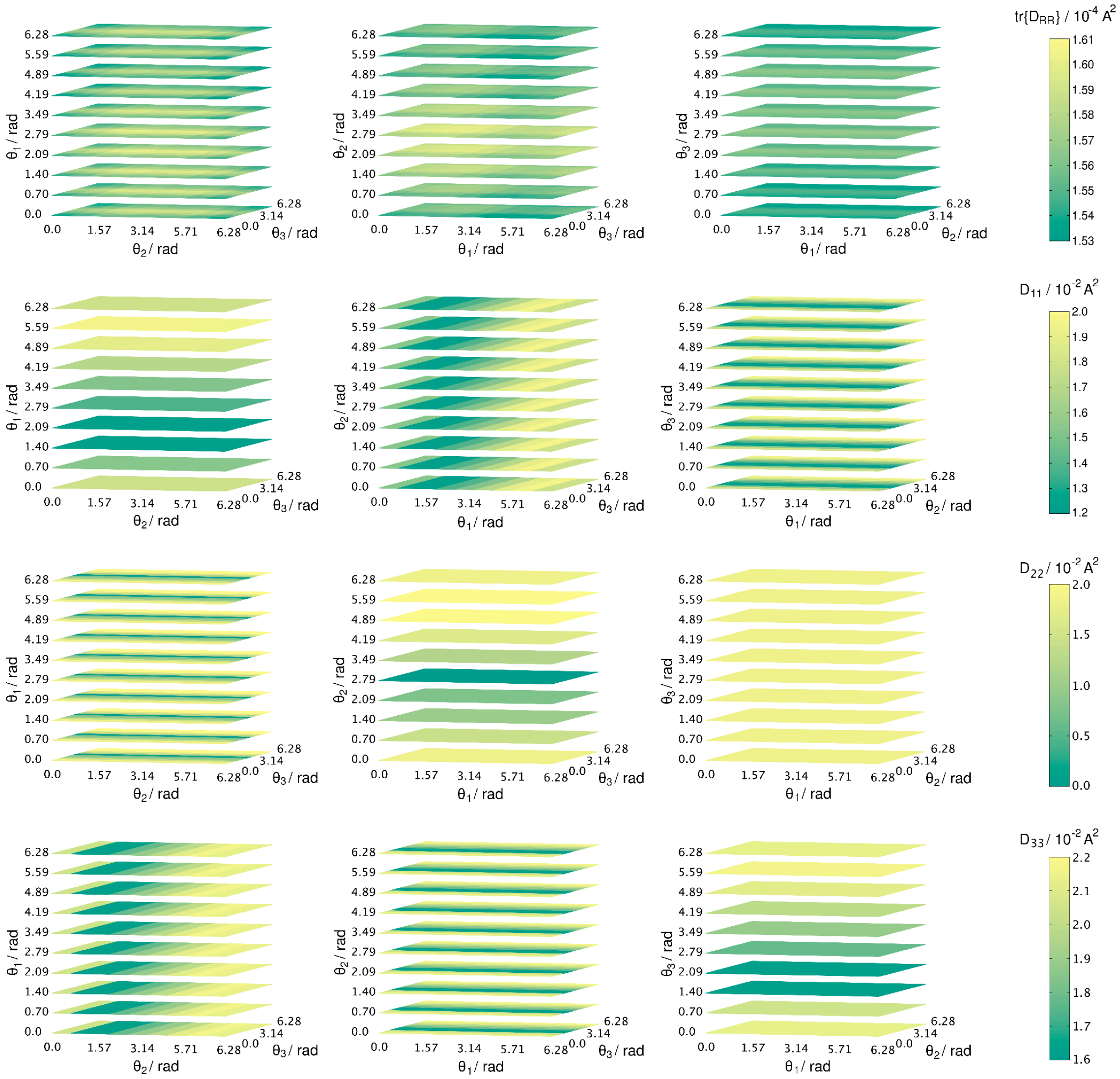

Figure 2-10: Representation of the trend of, from the top, the trace of the rotational part of the diffusion tensor and the D_{11}, D_{22} and D_{33} components of the internal part of the diffusion tensor of the tri-labeled T4 lysozyme as function of the three internal angles.

Finally we performed some additional calculations on a singly labelled T4 lysozyme: Figures 2-11 and 2-12 show the dependence of the internal diffusion coefficient and of its trace of the rotational part as a function of the internal angle. The average value of the trace of the rotational part of the diffusion tensor for the singly and tri labelled proteins are, respectively, $1.56 \cdot 10^{-4}$ Å^2 and $1.62 \cdot 10^{-4}$ Å^2, a small difference being possibly attributed to the fact that the two structures have 22 beads of difference. Another interesting result is that the internal diffusion coefficient of the singly labelled lysozyme shows the same value and behaviour of the corresponding angle in the 3R2T4 (the D_{33} coefficient), which can be taken as a confirmation of the independence of the three internal motions in the 3R2T4 molecule.

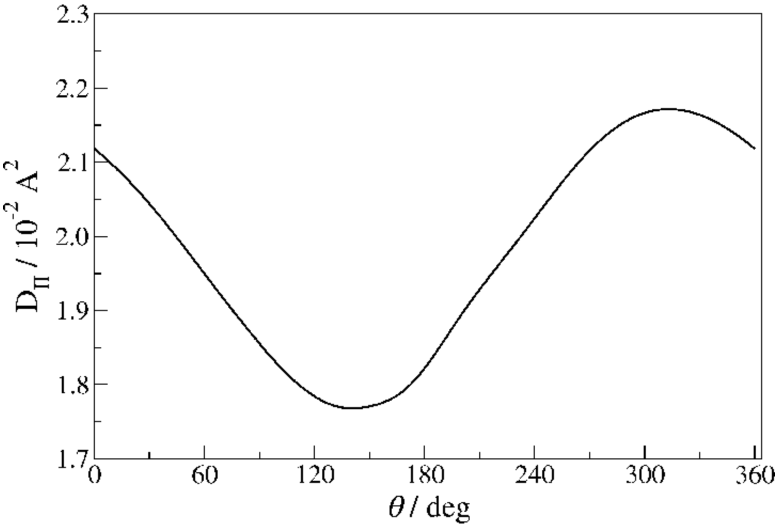

Figure 2-11: Trend of the internal coefficient of the diffusion tensor of the singly labelled T4 lysozyme vs. the internal angle.

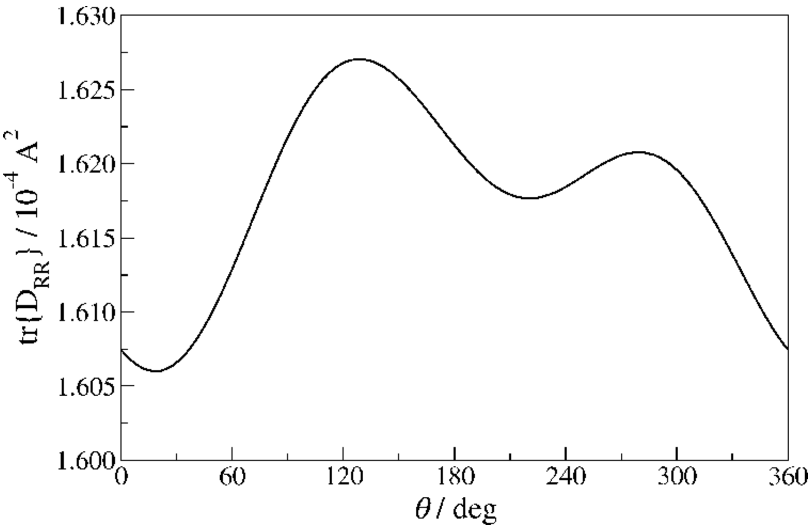

Figure 2-12: Trend of the trace of the rotational part of the diffusion tensor of the singly labelled T4 lysozyme vs. the internal angle.

2.3.2 Mobility of proteins

Describing the internal mobility of proteins is a very important task in order to understand their physical and chemical properties, the way they explicate their functions, interact with other molecules and fold. Such big molecules are characterized by very complex dynamics, including all time scales ranging from fs to μs. Once the relevant coordinates have been identified it is possible to define stochastic models that take into account only the relevant dynamical relaxation processes in a sort of ”time coarse-graining” procedure. Specific models for proteins however are still lacking, mostly for the difficulty to define relevant coordinates. A secondary aspect which limits the modellization of internal mobility of macromolecules is the lack of a convenient tool to define friction / diffusion properties in the presence of internal degrees of freedom. Introducing internal mobility without a proper tool signifies increasing the number of free parameters in the calculation, procedure that could cause a number of problems, i.e. technical difficulties in the simulations, more uncertainty in the physical interpretation of fitted parameters, the need of getting more experimental data to avoid correlations among parameters that emerge when their number is comparable to that of data points to be fitted (this is a very important issue especially in NMR).

DITE is therefore a potentially useful tool to start, at least, to define the basic internal / external diffusion processes of proteins. Here we present a report on the evaluation of diffusion properties of proteins with large-amplitude internal motional degrees of freedom of domains. Our results are preliminary and concerning roto-translational and internal diffusion tensorial parameters of two case studies: calmodulin and E. Coli adenylate kynase (AKeco) proteins.

The case of calmodulin

Two domains, connected by a flexible linker, characterize the structure of calmodulin. Figure 2-13 shows the system, evidencing the two fragments.

The linker flexibility is described in terms of the torsional angles of its constitutive residues. We select the two angles θ_1 and θ_2 as main degrees of freedom (dof) describing the molecular geometry, as shown in Figure 2-14. One should notice that no fundamental reason stands for selecting only two relevant dof, and that the whole set of torsional angles defining the

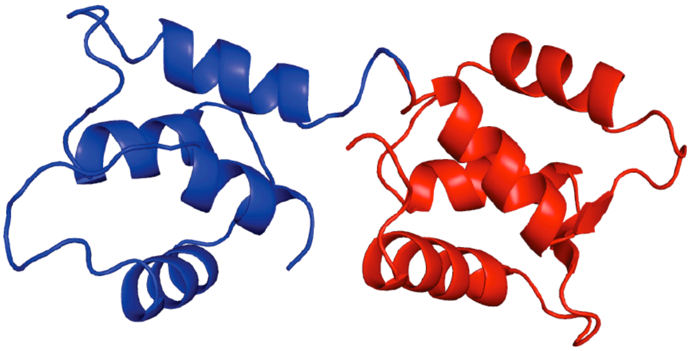

Figure 2-13: Linked domains of calmodulin.

linker should be considered; however, this choice is a reasonable compromise between having a manageable dynamic model for the system and assuring at least at coarse grained level the introduction of flexibility in the system.

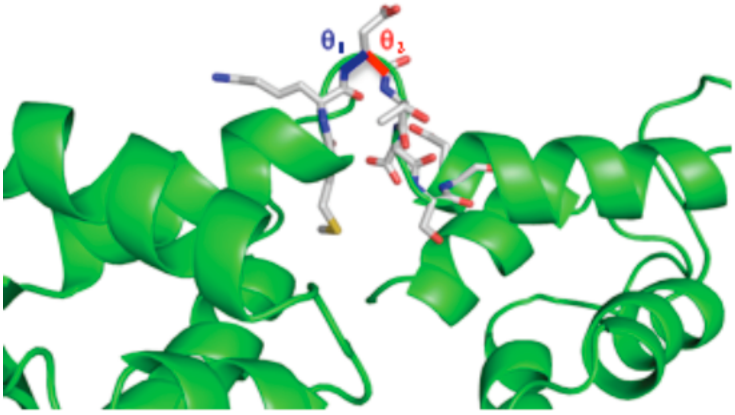

Figure 2-14: Torsional angles selected as main dof in calmodulin flexible linker.

DITE allows defining the domains, selecting the relevant dof and set-up and solving expressions, based on standard hydrodynamic theory, for evaluating the roto-translational and internal diffusion tensor. In Appendix A a brief tutorial is provided for this system, with a step-by-step description of operations.

Results can be summarized as follows. The physical parameters (requested by the hydrodynamic approach employed by DITE) have been set to: $R_e = 2.0$ Å, $C = 6$, $\eta = 1.0$ cP, $T =$

293 K. The general structure of the diffusion tensor is

$$\boldsymbol{D} = \begin{bmatrix} \boldsymbol{D}_{TT} & \boldsymbol{D}_{TR} & \boldsymbol{D}_{TI} \\ \boldsymbol{D}_{TR}^{tr} & \boldsymbol{D}_{RR} & \boldsymbol{D}_{RI} \\ \boldsymbol{D}_{TI}^{tr} & \boldsymbol{D}_{RI}^{tr} & \boldsymbol{D}_{II} \end{bmatrix} \tag{2.13}$$

where $\boldsymbol{D}_{TT}$, $\boldsymbol{D}_{RR}$ are the 3×3 translation and rotation blocks; $\boldsymbol{D}_{TR} = \boldsymbol{D}_{RT}^{tr}$ are the 3×3 roto-translational coupling blocks; $\boldsymbol{D}_{TI} = \boldsymbol{D}_{IT}^{tr}$, $\boldsymbol{D}_{RI} = \boldsymbol{D}_{IR}^{tr}$ are the 3×2 internal-translation and 2×3 internal-rotation coupling blocks; $\boldsymbol{D}_{II}$ is the 2×2 internal block. Naturally all blocks elements are functions of the internal and orientational angles. One can define an instantaneous geometry (i.e. set of values for torsional angles) and define a reference frame (Molecular Frame, MF) based on one of the protein residues; finally one can choose the orientation of the MF either to minimize some of the coupling blocks or to diagonalize one of the diagonal blocks. Our choice is to put the MF on the central residue of the flexible linker, with an orientation such that $\boldsymbol{D}_{RR}$ is diagonal. For the geometry characterized by both torsional angles equal to zero, the full diffusion tensor assumes for instance the form

$$\boldsymbol{D} = \left[\begin{array}{ccc|ccc|cc}
1.63{\cdot}10^{-10} & -2.80{\cdot}10^{-12} & -1.95{\cdot}10^{-11} & -1.32{\cdot}10^{-3} & 2.82{\cdot}10^{-3} & 4.65{\cdot}10^{-2} & 2.39{\cdot}10^{-2} & -1.43{\cdot}10^{-2} \\
-2.80{\cdot}10^{-12} & 1.14{\cdot}10^{-10} & -1.28{\cdot}10^{-11} & -1.51{\cdot}10^{-3} & -1.18{\cdot}10^{-2} & 1.84{\cdot}10^{-3} & 6.03{\cdot}10^{-3} & 9.84{\cdot}10^{-3} \\
-1.95{\cdot}10^{-11} & -1.28{\cdot}10^{-11} & 1.42{\cdot}10^{-10} & -6.37{\cdot}10^{-4} & 1.55{\cdot}10^{-2} & -2.34{\cdot}10^{-2} & -1.08{\cdot}10^{-2} & 1.34{\cdot}10^{-2} \\
\hline
-1.32{\cdot}10^{-3} & -1.51{\cdot}10^{-3} & -6.37{\cdot}10^{-4} & 1.27{\cdot}10^{7} & 0.00 & 0.00 & 1.07{\cdot}10^{7} & -1.12{\cdot}10^{7} \\
2.8{\cdot}10^{-3} & -1.18{\cdot}10^{-2} & 1.55{\cdot}10^{-2} & 0.00 & 1.61{\cdot}10^{7} & 0.00 & -9.36{\cdot}10^{6} & 2.42{\cdot}10^{6} \\
4.65{\cdot}10^{-2} & 1.84{\cdot}10^{-3} & -2.34{\cdot}10^{-2} & 0.00 & 0.00 & 3.58{\cdot}10^{7} & 1.36{\cdot}10^{7} & -1.13{\cdot}10^{7} \\
\hline
2.39{\cdot}10^{-2} & 6.03{\cdot}10^{-3} & -1.08{\cdot}10^{-2} & 1.07{\cdot}10^{7} & -9.36{\cdot}10^{6} & 1.36{\cdot}10^{7} & 3.71{\cdot}10^{7} & -1.15{\cdot}10^{7} \\
-1.43{\cdot}10^{-2} & 9.84{\cdot}10^{-3} & 1.34{\cdot}10^{-2} & -1.12{\cdot}10^{7} & 2.42{\cdot}10^{6} & -1.13{\cdot}10^{7} & -1.15{\cdot}10^{7} & 2.64{\cdot}10^{7}
\end{array}\right]$$

where the translation-translation (TT, red box) block elements are in $\mathrm{m^2 s^{-1}}$, the translation-rotation (TR, green box) and translation-internal (TI, brown box) blocks in $\mathrm{ms^{-1}}$ and the rotation-rotation (RR, orange box), rotation-internal (RI, blue box), internal-internal (II, magenta box) blocks in Hz. General characteristics can be observed such as the weak coupling between translations and rotation plus conformational dof. We report in Table 2.4 a summary of values for the diagonal elements of $\boldsymbol{D}$ for the rotational and internal blocks, for a range of values of conformational angles. It should be stressed that a different choice of the MF would have lead, naturally, to different values in the above table; the relevant dynamics should always be discussed in terms of a complete model for the roto-translational plus internal dof (i.e. for instance of a properly defined diffusive operator) [36].

The case of AKeco

The LID domain of AKeco is a rigid body moving with respect to the rest of the molecule through two hinges (H5 and H6) located at residues 115 and 158 [68]. Figure 2-15 shows the cartoon of the AKeco protein evidencing the LID domain (in blue).

Figure 2-15: Cartoon structure of AKeco.

The internal mobility of AKeco can be described choosing the two torsional angles between residues 114-115 and 158-159, respectively, as relevant dof, as depicted in Figure 2-16.
The procedure for choosing the torsional angles and evaluating the diffusion tensor, which is formally equivalent to the one obtained for calmodulin, leads to the equivalent expression for the full diffusion tensor in the case of both angles

$$\boldsymbol{D} = \begin{bmatrix} 1.28{\cdot}10^{-10} & -1.29{\cdot}10^{-11} & 2.43{\cdot}10^{-12} & 1.42{\cdot}10^{-3} & -1.99{\cdot}10^{-2} & -1.43{\cdot}10^{-3} & 7.01{\cdot}10^{-5} & -5.06{\cdot}10^{-4} \\ -1.29{\cdot}10^{-11} & 1.03{\cdot}10^{-10} & 5.44{\cdot}10^{-12} & 2.41{\cdot}10^{-3} & 8.56{\cdot}10^{-3} & 4.86{\cdot}10^{-4} & 4.49{\cdot}10^{-4} & -1.01{\cdot}10^{-3} \\ 2.43{\cdot}10^{-12} & 5.44{\cdot}10^{-12} & 1.31{\cdot}10^{-10} & 1.96{\cdot}10^{-2} & 4.93{\cdot}10^{-4} & 1.71{\cdot}10^{-3} & 8.36{\cdot}10^{-5} & 1.22{\cdot}10^{-4} \\ 1.42{\cdot}10^{-3} & 2.41{\cdot}10^{-3} & 1.96{\cdot}10^{-2} & 1.00{\cdot}10^{7} & 0.00 & 0.00 & 1.79{\cdot}10^{5} & 3.23{\cdot}10^{5} \\ -1.99{\cdot}10^{-2} & 8.56{\cdot}10^{-3} & 4.93{\cdot}10^{-4} & 0.00 & 1.06{\cdot}10^{7} & 0.00 & 3.97{\cdot}10^{5} & -3.13{\cdot}10^{5} \\ -1.43{\cdot}10^{-3} & 4.86{\cdot}10^{-4} & 1.71{\cdot}10^{-3} & 0.00 & 0.00 & 1.48{\cdot}10^{7} & 4.13{\cdot}10^{5} & -6.33{\cdot}10^{5} \\ 7.01{\cdot}10^{-5} & 4.49{\cdot}10^{-4} & 8.36{\cdot}10^{-5} & 1.79{\cdot}10^{5} & 3.97{\cdot}10^{5} & 4.13{\cdot}10^{5} & 1.28{\cdot}10^{6} & -4.03{\cdot}10^{5} \\ -5.06{\cdot}10^{-4} & -1.01{\cdot}10^{-3} & 1.22{\cdot}10^{-4} & 3.23{\cdot}10^{5} & -3.13{\cdot}10^{5} & -6.33{\cdot}10^{5} & -4.03{\cdot}10^{5} & 1.18{\cdot}10^{6} \end{bmatrix}$$

while Table 2.5 shows the variation of rotational and internal diagonal coefficient with torsional angles.

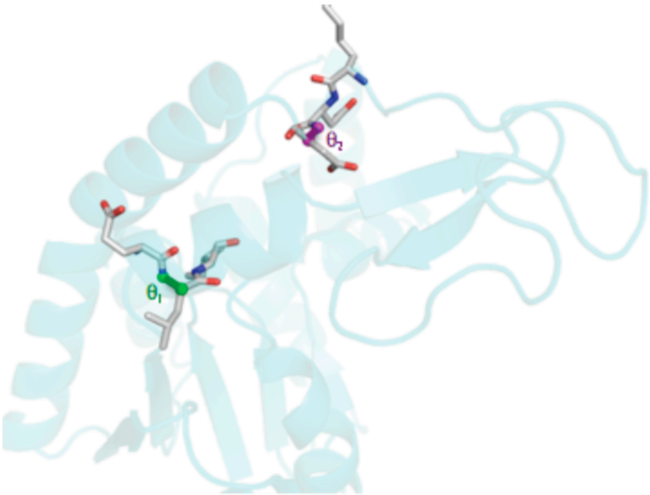

Figure 2-16: Relevant dof chosen for describing AKeco mobility.

2.3.3 Discussion

Combination of cost-effective PCM-based calculations of molecular shape and hydrodynamic modelling for the evaluation of diffusion (friction) tensors of molecules (both rigid and with internal torsional degrees of freedom) is able to reproduce accurately experimental diffusion coefficients, both translational and rotational, for molecules of diverse extensions ranging from a few atoms to proteins, with two adjustable parameters. The most important free parameter is the average radius for all extended atoms (beads). This parameter governs the effective shape of the molecule and, therefore, the friction tensor of the unconstrained system of beads. The other parameter is the threshold on the exposed area, which determines if a given bead is wetted and therefore included in the computation of the total friction: this has to be considered as a ”computational” rather than a physical parameter of the method. As shown in the implementation section, a threshold of 10% can be safely employed to boost the computational performances without introducing important errors in the calculated diffusion tensor.

Computational times are comparable with existing established software in the field, due to the combination of the fast determination of the molecular surface and the optimization of the linear-algebra operations required to evaluate the friction tensors.

θ_1 / deg	θ_2 / deg	${}^{RR}D_{11}$ / 10^7 Hz	${}^{RR}D_{22}$ / 10^7 Hz	${}^{RR}D_{33}$ / 10^7 Hz	${}^{II}D_{11}$ / 10^7 Hz	${}^{II}D_{22}$ / 10^7 Hz
-20	-20	1.31	1.48	2.84	1.10	0.716
-20	-10	1.26	1.50	3.13	2.28	1.46
-20	0	1.23	1.52	3.51	3.34	2.48
-20	10	1.19	1.54	3.87	4.05	3.48
-20	20	1.15	1.55	4.15	4.65	4.21
-10	-20	1.35	1.57	2.93	1.42	1.02
-10	-10	1.29	1.53	3.12	2.34	1.37
-10	0	1.25	1.56	3.52	3.49	2.54
-10	10	1.20	1.58	3.91	4.32	3.53
-10	20	1.16	1.60	4.24	4.95	4.35
0	-20	1.40	1.65	3.08	1.96	1.33
0	-10	1.33	1.60	3.14	2.32	1.74
0	0	1.27	1.61	3.58	3.71	2.64
0	10	1.21	1.62	3.97	4.54	3.57
0	20	1.16	1.64	4.31	5.16	4.38
10	-20	1.43	1.67	3.01	1.76	1.19
10	-10	1.36	1.66	3.33	2.94	1.92
10	0	1.29	1.65	3.67	3.94	2.73
10	10	1.23	1.66	4.04	4.72	3.59
10	20	1.17	1.67	4.38	5.30	4.39
20	-20	1.47	1.69	3.01	1.77	1.21
20	-10	1.39	1.68	3.39	2.98	1.92
20	0	1.31	1.67	3.78	4.10	2.77
20	10	1.24	1.67	4.12	4.84	3.59
20	20	1.18	1.69	4.44	5.40	4.38

Table 2.4: Values of diagonal elements of $\boldsymbol{D}^{RR}$, $\boldsymbol{D}^{II}$ for calmodulin.

θ_1 / deg	θ_2 / deg	${}^{RR}D_{11}$ / 10^7 Hz	${}^{RR}D_{22}$ / 10^7 Hz	${}^{RR}D_{33}$ / 10^7 Hz	${}^{II}D_{11}$ / 10^7 Hz	${}^{II}D_{22}$ / 10^7 Hz
-20	-20	1.01	1.19	1.28	0.114	0.131
-20	-10	0.996	1.14	1.36	0.0522	0.0619
-20	0	0.996	1.09	1.47	0.0249	0.0337
-20	10	0.989	1.05	1.57	0.0181	0.0267
-20	20	0.961	1.00	1.62	0.0136	0.0217
-10	-20	1.03	1.19	1.30	0.261	0.275
-10	-10	1.01	1.13	1.38	0.109	0.139
-10	0	1.00	1.08	1.48	0.0390	0.0499
-10	10	0.997	1.04	1.60	0.0203	0.0313
-10	20	0.969	1.00	1.67	0.0142	0.0206
0	-20	1.03	1.19	1.34	0.466	0.404
0	-10	1.02	1.11	1.42	0.319	0.276
0	0	1.00	1.06	1.48	0.128	0.118
0	10	0.991	1.02	1.56	0.0300	0.0399
0	20	0.964	0.983	1.63	0.0178	0.0238
10	-20	1.01	1.21	1.40	0.766	0.571
10	-10	1.00	1.11	1.44	0.542	0.384
10	0	0.979	1.03	1.43	0.202	0.146
10	10	0.965	0.984	1.47	0.0469	0.0569
10	20	0.936	0.950	1.53	0.0216	0.0321
20	-20	0.966	1.22	1.47	1.02	0.722
20	-10	0.966	1.11	1.47	0.731	0.547
20	0	0.949	1.03	1.39	0.324	0.272
20	10	0.918	0.976	1.37	0.100	0.116
20	20	0.886	0.940	1.40	0.0437	0.0647

Table 2.5: Values of diagonal elements of $\boldsymbol{D}^{RR}$, $\boldsymbol{D}_{II}$ for AKeco.

Chapter 3

Electron Spin Resonance

Electron spin resonance (ESR) is one of the most powerful tools in the interpretation of structural properties and dynamic processes of molecules in fluids. Because of their favourable time scale, ESR experiments can be highly sensitive to the details of global and internal dynamics. In the so-called slow motional regime, the spectral line shapes take on complex forms, which are found to be sensitive to the microscopic details of motional processes. Hence, the interpretation of slow motional spectra requires an analysis based upon sophisticated theory, and it is usually carried out via explicit modelling of the dynamics of radicalic species.

ESR spectroscopy is applied extensively to material science. An example is given in the search of new materials with tailored magnetic properties, which has intensified in recent years. Here ESR can be employed profitably for characterizing novel stable radicalic systems, and a currently studied case is given, for instance, by nitronylnitroxide free radicals [2, 3, 4]. Highly valuable information can also be gathered from ESR studies of complex biomolecules. Studying the dynamical relaxation processes in proteins and enzymes is of fundamental importance in order to understand their chemical and physical properties, such as substrate recognition, reactivity, folding [6, 7, 69, 70]. Thanks to the development of the so called site directed spin labelling (SDSL) technique [5, 6], which consists of attaching a small molecule with an unpaired electron to a molecule which is not natively a radical, ESR is beginning to be accepted as a comprehensive way to study proteins, encompassing both structural and dynamic information. The SDSL technique allows to add one or more spin probes to the protein with a minimal effect on its original dynamics / structure.

In a typical standard continuous wave ESR (cw-ESR) experiment the molecular information of interest is hidden in the line shape of the spectrum. It is important to employ a fast, reasonably accurate theoretical approach for the interpretation of the experimental spectra which allows a correct link between the macroscopic observables and the microscopic parameters of the molecule.

An advanced theoretical approach to the interpretation of ESR spectra is based on the definition and solution of the stochastic Liouville equation (SLE) [16] of the system. This is essentially a semi-classical approach based on the Liouville equation for the magnetic probability density of the molecule augmented by a stochastic operator which describes the relevant relaxation processes that occur in the system, responsible of the broadening of the spectral lines [15]. The SLE approach can be linked profitably to advanced density functional theory (DFT) evaluation of geometry and magnetic parameters of the radical in its environment [57]. Dissipative parameters, such as rotational diffusion tensors, can in turn be determined at a coarse-grained level by using standard hydrodynamic arguments. The combination of the evaluation of structural properties, based on quantum mechanical advanced methods, with hydrodynamic modelling for dissipative properties and, in the case of multilabeled systems, determination of dipolar interaction based on the molecular structures beyond the point approximation are the fundamental ingredients needed by the SLE to provide a fully integrated computational approach (ICA) that gives the spectral profile [57]. As it will become clear in the next sections, a number of parameters enter in the definition of the SLE and customarily a multi-component fitting procedure is employed. ICA attempts to replace fitting procedures as much as possible with the *ab initio* evaluation of parameters in order to give them a sound physical interpretation and fitting may be retained as a ”refining” step.

The ICA protocol has been implemented in the new software E-SpiReS (Electron Spin Resonance Simulation), which includes and automatically interfaces the different theoretical / computational methodologies in a transparent way to the user. The graphical user interface (GUI), which renders the program very user-friendly, has been thought in such a way that the work flow of the calculation is clearly pointed out. Users are asked to define input by point-and-click, i.e. indicating the magnetic probes on the molecule and setting some physical data like frequency of the spectrometer, temperature, viscosity of the fluid. Then, to obtain the cw-ESR spectrum it is sufficient to follow a number of guided steps that require as little intervention as possible from the user because most of the work (especially input / output operations) is handled by the computational tool.

3.1 Integrated Computational Approach

The integrated computational approach (ICA) to the interpretation of electron magnetic resonance merges a number of theoretical / computational methodologies that, starting from the geometry of the molecule, permit to evaluate, in principle, all the molecular properties that enter as parameters in the equations describing the time evolution of the system. In order to realize this *ab initio* approach it is important to include in the computational protocol *ad hoc* methodologies that treat the molecule at different coarse-grained levels, depending on the physical nature of the parameter to be evaluated. The ICA is effectively a multi-scale approach to ESR spectroscopy [57].

As was underlined in the introduction of this chapter, the theoretical methodology that we employ is based on the definition and numerical solution of the stochastic Liouville equation, which describes the time evolution of the density probability of the system [16, 21, 32]. Given the set of spin variables, $\boldsymbol{\sigma}$, and the set of stochastic variables, $\boldsymbol{X}$, the SLE is written as [16]

$$\begin{aligned}\frac{\partial \rho(\boldsymbol{\sigma},\boldsymbol{X},t)}{\partial t} &= -i\left[\hat{H}(\boldsymbol{\sigma},\boldsymbol{X}),\rho(\boldsymbol{\sigma},\boldsymbol{X},t)\right] - \hat{\Gamma}(\boldsymbol{X})\rho(\boldsymbol{\sigma},\boldsymbol{X},t)\\ &= -\left[i\hat{H}^{\times}(\boldsymbol{\sigma},\boldsymbol{X}) + \hat{\Gamma}(\boldsymbol{X})\right]\rho(\boldsymbol{\sigma},\boldsymbol{X},t)\\ &= -\hat{\mathcal{L}}(\boldsymbol{\sigma},\boldsymbol{X},t)\rho(\boldsymbol{\sigma},\boldsymbol{X},t) \qquad (3.1)\end{aligned}$$

where the Liouvillean $\hat{\mathcal{L}} = i\hat{H}^{\times} + \hat{\Gamma}$ is given by the sum of the stochastic operator $\hat{\Gamma}$, describing the time evolution of the stochastic variables $\boldsymbol{X}$, and the commutator $\hat{H}^{\times}$ which is the quantum Liouville operator, that is, the super-operator defined with respect to the magnetic Hamiltonian of the system, $\hat{H}$. It depends on both spin and stochastic coordinates so spin relaxation is coupled to the dynamics of the molecule. In particular, the dependence of the magnetic part on dynamical variables can be separated in *i)* a contribution that comes from the anisotropy of that magnetic tensors that enter the spin Hamiltonian, e.g. the tumbling of the molecule changes the orientation of the magnetic tensors relative to the laboratory frame (where both the magnetic field and the spin operators are defined); *ii)* a contribution from internal variables via changes on the electronic distribution, e.g. motion around a torsional angle leads to modifications on the geometry that may imply important changes in electron structure so affecting the principal values of the magnetic tensors.

In the present implementation of the ICA protocol within the code E-SpiReS (see next section), it is possible to treat singly and doubly spin-labelled molecules. For each probe a maximum of two nuclei can be coupled with each electron. In case of biradicals, the dipolar and exchange terms appear in the Hamiltonian, together with the electron Zeeman and nucleus - electron hyperfine interaction terms. So, the general form of the spin Hamiltonian is

$$\hat{\mathcal{H}}/\hbar = \sum_{i=1}^{2} \left(\omega_{g,i} \boldsymbol{Z} \Delta \boldsymbol{g}_i \hat{\boldsymbol{S}}_i + \sum_{j=1}^{2} \omega_{A,ij} \hat{\boldsymbol{I}}_{ij} \Delta \boldsymbol{A}_{ij} \hat{\boldsymbol{S}}_i \right) + \hat{\boldsymbol{S}}_1 \boldsymbol{T} \hat{\boldsymbol{S}}_2 \tag{3.2}$$

where i is the summation index over the electrons and j over the nuclei. For every electron three terms are present, i.e. the Zeeman interaction of the electron with the magnetic field and the two hyperfine interactions of the electron with the two nuclei of spin I_{ij}. In the equation, $\Delta \boldsymbol{g}_i$ is the traceless Zeeman interaction tensor of i-th atom, $\omega_{g,i} = \beta_e B_0 Tr\{\boldsymbol{g_i}\}/3\hbar$, $\boldsymbol{Z}$ is the axis of the laboratory inertial frame parallel to the magnetic field, $\hat{\boldsymbol{S}}_i$ is the spin operator for the i-th electron; $\Delta \boldsymbol{A}_{ij}$ is the traceless hyperfine coupling tensor of i-th electron with j-th nucleus, $\omega_{A,ij} = \gamma_e Tr\{\boldsymbol{A}_{ij}\}/3$, $\hat{\boldsymbol{I}}_{ij}$ is the spin operator of j-th nucleus coupled to the i-th electron. The last term in the expression of the Hamiltonian is the interaction term coupling the two electrons

$$\boldsymbol{T} = \boldsymbol{T}^J + \boldsymbol{T}^{DD} = -2\gamma_e J \mathbf{1}_3 + \boldsymbol{T}^{DD} \tag{3.3}$$

where J is the exchange interaction energy between the two electrons and $\boldsymbol{T}^{DD}$ is the dipolar interaction tensor. If the two unpaired electrons are localized in sufficiently distant orbitals, it is possible to introduce the point dipole approximation, so

$$\boldsymbol{T}^{DD} = \frac{\mu_0}{4\pi} \frac{g_e^2 \beta_e^2}{\hbar r^3} \left(\mathbf{1}_3 - \frac{3}{r^2} \boldsymbol{r} \otimes \boldsymbol{r} \right) \tag{3.4}$$

with $\boldsymbol{r}$ the distance vector between the two electrons and $\otimes$ the dyadic product. On the other hand, if the two orbitals containing the unpaired electrons are close one to the other, it becomes necessary to consider the delocalization of the electrons and the tensor is given as

$$\boldsymbol{T}^{DD} \propto \langle \Psi_1(\boldsymbol{r}_1)\Psi_2(\boldsymbol{r}_2) - \Psi_1(\boldsymbol{r}_2)\Psi_2(\boldsymbol{r}_1) \, | \hat{\boldsymbol{T}}^{DD} | \, \Psi_1(\boldsymbol{r}_1)\Psi_2(\boldsymbol{r}_2) - \Psi_1(\boldsymbol{r}_2)\Psi_2(\boldsymbol{r}_1) \rangle \tag{3.5}$$

where the wave functions Ψ_1 and Ψ_2 are the two singly occupied molecular orbitals (SOMO) containing the unpaired electrons. The components of the tensorial operator $\hat{T}^{DD}_{\alpha,\beta}$ $(\alpha, \beta = X, Y, Z)$ are

$$\hat{T}^{DD}_{\alpha,\beta} = \frac{r^2 \delta_{\alpha,\beta} - 3(\boldsymbol{r})_\alpha (\boldsymbol{r})_\beta}{r^5} \tag{3.6}$$

with $(\boldsymbol{r})_\alpha$ being the α component of vector $\boldsymbol{r}$.

Depending on the radical under study only the needed terms of the spin Hamiltonian 3.2 are taken into account. From the general equation of the spin Hamiltonian it is evident that a number of parameters are required, i.e. the $\boldsymbol{g}$ tensors of the electrons, the $\boldsymbol{A}$ hyperfine coupling tensors for all considered nuclei, the exchange interaction energy J and the dipolar interaction tensor $\boldsymbol{T}^{DD}$. All these quantities are purely quantum mechanical properties and their evaluation requires a first principles treatment. The ICA protocol schedules quantum mechanical calculations based on the most advanced DFT techniques. More details are given in Section 3.1.1.

The stochastic operator, $\hat{\Gamma}$, is a very important ingredient in the methodology because depending on how we describe the time behaviour of the relaxation processes in the system we influence the inhomogeneous broadening of the spectral lines. In Chapter 1 we have just discussed about the importance of choosing the relevant dynamics of the system. The next step is determining their time evolution, depending on their physical origin. Usually Fokker Planck / diffusive operators are employed and this choice for the relaxation of dynamics is presently implemented in the ICA protocol. In particular, two dynamical models are implemented which are *i)* a rigid body model, where the molecule is seen as a rigid rotator diffusing in the fluid and the stochastic variables are $\boldsymbol{X} = \boldsymbol{\Omega}$, the set of Euler angles which give the relative orientation of the molecule with respect to the inertial laboratory frame; *ii)* a "flexible" body model, where the molecule is described as a rotator with one internal degree of freedom represented by a torsional angle, so the stochastic variables, $\boldsymbol{X} = (\boldsymbol{\Omega}, \theta)$, are the set of angles $\boldsymbol{\Omega}$ (for the global rotation) and the torsional angle θ. In both models the stochastic variables are considered as diffusive processes and the stochastic operator has the general form

$$\hat{\Gamma} = -\hat{\nabla}^{tr}_{\boldsymbol{X}} \boldsymbol{D}(\boldsymbol{X}) P_{eq}(\boldsymbol{X}) \hat{\nabla}_{\boldsymbol{X}} P^{-1}_{eq}(\boldsymbol{X}) \tag{3.7}$$

where $\hat{\nabla}_{\boldsymbol{X}}$ is the vector operator of partial derivatives over the stochastic variables, $\boldsymbol{D}(\boldsymbol{X})$ is the full diffusion tensor of the system (which in general depends on the stochastic variables) and $P_{eq}(\boldsymbol{X})$ is the equilibrium distribution probability of the system for which a Boltzmann form is considered

$$P_{eq}(\boldsymbol{X}) = \exp\left[-V(\boldsymbol{X})/kT\right]/\langle \exp\left[-V(\boldsymbol{X})/kT\right]\rangle \tag{3.8}$$

Here, $V(\boldsymbol{X})$ is the potential acting on the stochastic coordinates and $\langle \ldots \rangle$ represents the integration over $\boldsymbol{X}$. We make the assumption that the potential has two separated contributions, an "external" term acting on the global orientation (e.g. ordering effects in liquid crystals) and an internal term acting on the torsional angle (if present) which is the torsional potential, i.e.

$$V(\boldsymbol{X}) = V_{ext}(\boldsymbol{\Omega}) + V_{int}(\theta) + V_{coupling}(\boldsymbol{X}) \approx V_{ext}(\boldsymbol{\Omega}) + V_{int}(\theta) \tag{3.9}$$

Once that the shape of the stochastic operator has been decided, new parameters enter in the SLE, being the full diffusion tensor of the system and the terms of the orienting potential acting on the stochastic coordinates. The evaluation of the diffusive properties is fully described in Chapter 2 and it is based on a mesosopic coarse-grained description of the molecule. The internal potential can be evaluated from a potential energy surface scan over the torsional angle θ. For small molecules this operation can be easily conducted ad QM level, while for big molecules, such as proteins, mixed quantum mechanical / molecular mechanics (QM/MM) methodologies can be employed. Finally, for the orienting potential we usually adopt a phenomenological shape based on "chemical insight". As an example: in considering a molecule of cylindrical shape in a nematic environment it is reasonable to model the orienting potential with a second order Legendre polynomial.

Just to summarize, several parameters are needed to properly define the SLE, which are quite different in their nature. For each a different *ad hoc* computational methodology is however generally available which attempts, in controlled conditions, a determination in terms of the molecular topology and shape and solvent macroscopic properties. A picture of the full ICA methodology is given in Figure 3-1 and all the mentioned techniques are implemented within the new software E-SpiReS (Electron Spin Resonance Simulation - see Section 3.2.3) which integrates quantum mechanical (QM) methods for magnetic and structural properties

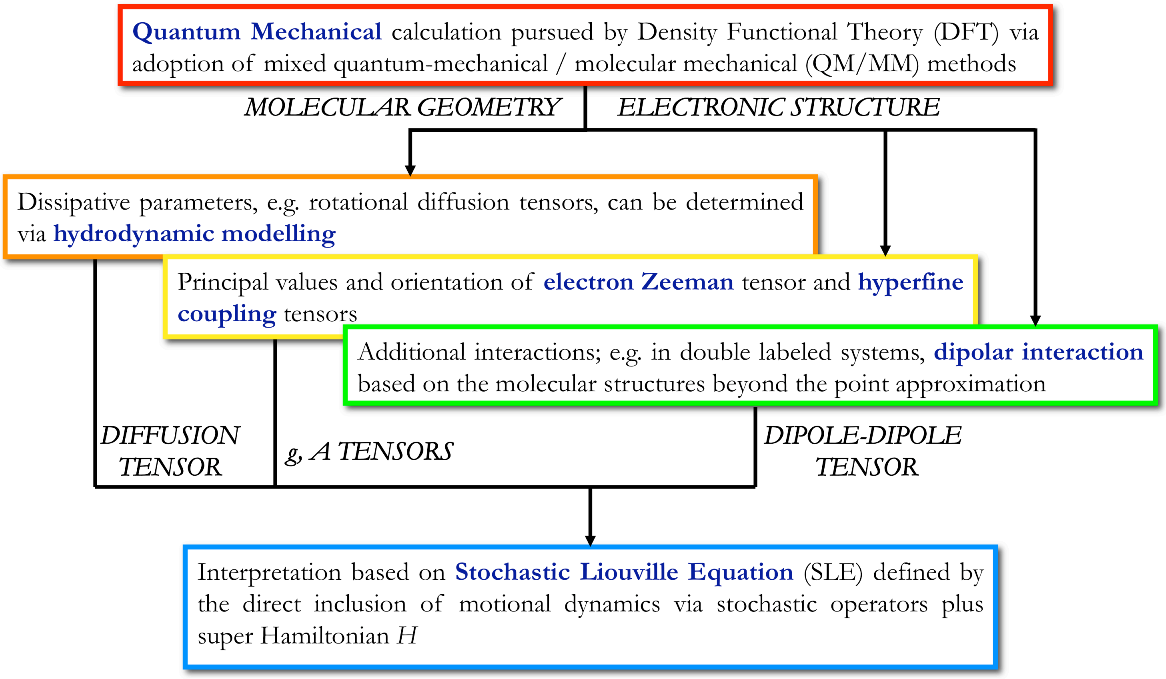

Figure 3-1: Chart of the ICA for the simulation of cw-ESR spectra in solution. Steps (2) and (3) are based on the optimized geometry and electronic structure obtained in step (1).

and a hydrodynamic approach to the diffusive properties, and finally takes care of the numerical solution of the SLE. Some details on the different approaches are given in the next subsections.

3.1.1 Quantum mechanical properties

The introduction of the Density Functional Theory (DFT) is a turning point for the calculations of the spin Hamiltonian parameters [38, 71, 72, 73]. Before DFT, *ab initio* calculations of the magnetic parameters of spin Hamiltonians were either prohibitively expensive already for medium size radicals [74, 75, 76, 77] or less reliable than semiempirical methods. These latter were based on the approaches introduced by McConnell [78, 79] and Stone [80, 81] for the calculations of the hyperfine coupling and the $\boldsymbol{g}$ tensors respectively. Based on semiempirical parameters taking into account separately the spin density on the SOMO and that due to spin polarization [82], the method for the evaluation of hyperfine tensors has been an invaluable tool for understanding the correlation between the magnetic parameters of the spin Hamiltonian, the spin distribution, the conformation of radicals, the molecular properties in general. However the reliability of the method was very restricted, as limited to predictions inside groups of similar radicals for which the same set of semiempirical parameters were sound, and the parameters to be calculated were only the SOMO spin densities [82]. Within these limits the calculated hyperfine tensors were quite reliable. On the other hand, the agreement between calculated and experimental values for $\boldsymbol{g}$ tensors used to be in general much worse. To this end, it should be noted that the recently achieved chances of calculating reliable $\boldsymbol{g}$ tensors principal values by DFT on one hand [83, 84, 85, 86, 87], and to measure them by High Frequency ESR on the other one, has provided a new largely unexplored source of information on molecular properties attainable by ESR analysis.

Today, the agreement between experimental and calculated parameters of the spin Hamiltonian by DFT is outstanding [38, 71, 72, 73, 83, 87]. Both the vibrational averaging of the parameters [17, 18, 19] and the interactions of the probe with the environment [88, 89, 90, 91, 92, 93] is taken into account, therefore providing a set of tailored parameters that can be used confidently for further calculations. It should be noted that this approach is a step forward with respect to the traditional starting point, i.e. the use of a set of experimental hyperfine and $\boldsymbol{g}$ tensors generally obtained for a different system, and extrapolated to the case of interest.

The $\boldsymbol{g}$ tensor can be dissected into three main contributions [83, 84, 85, 86, 87]

$$\boldsymbol{g} = g_e \mathbf{1}_3 + \Delta\boldsymbol{g}^{RMC} + \Delta\boldsymbol{g}^{GC} + \Delta\boldsymbol{g}^{OZ/SOC} \tag{3.10}$$

where g_e is the free electron value ($g_e = 2.002319$) and $\mathbf{1}_3$ is the 3 unit matrix. $\Delta\boldsymbol{g}^{RMC}$ and $\Delta\boldsymbol{g}^{GC}$ are first order contributions, which take into account relativistic mass (RMC) and gauge (GC) corrections, respectively. The last term, $\Delta\boldsymbol{g}^{OZ/SOC}$, is a second-order contribution arising from the coupling of the Orbital Zeeman (OZ) and the Spin-Orbit Coupling (SOC) operators. The SOC term is a true two-electron operator, but here it will be approximated by a one-electron operator involving adjusted effective nuclear charges [94]. This approximation has been proven to work fairly well in the case of light atoms, providing results close to those obtained using more refined expressions for the SOC operator [83, 84, 85]. In our general procedure, spin-unrestricted calculations provide the zero-order Kohn-Sham (KS) orbitals and the magnetic field dependence is taken into account using the coupled-perturbed KS formalism described by Neese, but including the GIAO approach [83, 84, 85].

Solution of the coupled perturbed KS equation (CP-KS) leads to the determination of the OZ/SOC contribution.

The second term is the hyperfine interaction contribution, which, in turn, contains the so-called Fermi-contact interaction (an isotropic term), which is related to the spin density at the corresponding nucleus n by [95]

$$A_{n,0} = \frac{8\pi}{3}\frac{g_e}{g_0} g_n \beta_n \sum_{\mu,\nu} P_{\mu,\nu}^{\alpha-\beta} \langle \varphi_\mu \left| \delta\left(r_{kn}\right) \right| \varphi_\nu \rangle \tag{3.11}$$

and an anisotropic contribution, which can be derived from the classical expression of interacting dipoles [96]

$$A_{n,ij} = \frac{g_e}{g_0} g_n \beta_n \sum_{\mu,\nu} P_{\mu,\nu}^{\alpha-\beta} \langle \varphi_\mu \left| r_{kn}^{-5} \left(r_{kn}^2 \delta_{ij} - 3 r_{kn,i} r_{kn,j} \right) \right| \varphi_\nu \rangle \tag{3.12}$$

$\boldsymbol{A}$ tensor components are usually given in Gauss (1 G = 0.1 mT); to convert data to MHz one has to multiply by 2.8025.

Magnetic tensors evaluated at this level do not give sufficiently accurate estimates of experimental values, especially if one considers a molecule in a solvent with high polarity and / or a solvent that can form hydrogen bonds. Environmental effects (e.g. solvent) need to be taken into account and the most promising general approach to the problem can be based on a system-bath decomposition. Calculations can be performed on the system including the part of the solute where the essential part of the process to be investigated is localized together with, possibly, the few solvent molecules strongly and specifically interacting with it. This part is treated at the electronic level of resolution, and is immersed in a polarizable continuum, mimicking the macroscopic properties of the solvent. So, the solution process can then be dissected into the creation of a cavity in the solute, process requiring an energy E_{cav}, and the successive switching on of dispersion-repulsion, with energy $E_{dis-rep}$, and electrostatic, with energy E_{el}, interactions with surrounding solvent molecules. All of these contributions, for both isotropic and anisotropic solutions, are included into the so-called polarizable continuum model (PCM) [97, 98, 99, 100]. Taking into account solvent effects gives the corrections required in order to predict values of the tensors very close to the experimental ones (see Tables 2 and 7 of ref. [57]).

While in some cases considering the environment is sufficient to reproduce experimental values of the $\boldsymbol{g}$ and hyperfine tensors, there are molecules presenting fast motions in the neighbours of the unpaired electron. Dependence of the magnetic parameters on these small geometry variations can be very significative [17, 101, 102, 103]. These motions are usually too fast with respect to ESR time scales window so the effective contribution is a correction that can be calculated as an average over short time dynamics calculated at QM level [104, 105]. Quantum mechanical calculations are also important when there is the need of calculating the electrons dipolar interaction, in bi-radicals, as given in equation 3.5, that we rewrite here

$$\boldsymbol{T}^{DD} \propto \langle \Psi_1(\boldsymbol{r}_1)\Psi_2(\boldsymbol{r}_2) - \Psi_1(\boldsymbol{r}_1)\Psi_2(\boldsymbol{r}_2)\, |\hat{\boldsymbol{T}}^{DD}|\, \Psi_1(\boldsymbol{r}_1)\Psi_2(\boldsymbol{r}_2) - \Psi_1(\boldsymbol{r}_1)\Psi_2(\boldsymbol{r}_2) \rangle \tag{3.13}$$

To evaluate tensor $\boldsymbol{T}^{DD}$ one needs to know information about the two singly occupied molecular orbitals (SOMO) containing the unpaired electrons. In the current implementation of the ICA methodology we included only the approximated formula for the evaluation of the dipolar interaction (eq. 3.4). However in one of the case studies that were treated in the validation of the ICA (cfr. Section 3.3.4) we needed to use the correct formula. To this purpose we have just introduced a calculation routine, but it still presents some limitations and further work is going to be done in the next future in order to include this feature in our software. Details on the present implementation are given in Appendix B.

Finally, in the case of flexible molecules it is important to evaluate also the torsional potential, i.e. the potential acting on the torsional angle which, together with the diffusion coefficient, determines the relaxation properties of the internal dynamics. Evaluation of the potential is performed at a QM or quantum mechanical/molecular mechanics (QM/MM) level, by calculating the energy of the molecule at different values of the free internal torsional angle between 0° and 360°.

3.1.2 Diffusive properties

We just stressed in the previous sections that dissipative properties are very important parameters. The diffusion tensor is one of the two ingredients determining the time scales of the relaxation processes in the system. The other ingredient is the potential, if present.

The general methodology to the evaluation of diffusive properties has just been presented and discussed in Chapter 2. The approach is fully implemented into the ICA protocol giving the possibility of treating both rigid molecules and molecules that present internal flexibility in terms of a torsional angle.

In the particular case of a rigid molecule only six coordinates completely describe the configuration of the system (the position of the centre of mass and the global orientation) and the full diffusion tensor is represented by a 6×6 matrix containing only translational, rotational and coupling terms. When we consider an internal torsional angle, together with the six degrees of freedom of the rigid body, another coordinate has to be taken into account and in this case the diffusion tensor is represented by a 7×7 matrix containing, now, also an internal coefficient and coupling terms among the internal part and the translational and rotational parts.

Usually translational motion is poorly coupled to rotational and internal motions so it is easy to project the translational part, which has no effect on the spectrum if the molecule is supposed to move in a region of space where the applied magnetic field is uniform.

Generally the diffusion tensor depends on all the stochastic coordinates. To simplify the formalism we express the diffusion tensor on a frame fixed on the molecule, that we call molecular frame (MF), so that the tensor does not depend more on the orientation. Dependence on the internal torsional angle, instead, is not generally negligible so in principle it has to be taken into account. This dependence could be omitted as a further approximation based on a preliminary study of the molecule that is going to be studied. In the present implementation of the ICA, however, we assume that the dependence of the diffusion tensor on the internal angle can be always neglected. This approximation gives some restrictions on the molecules that can be treated to those that do not change significantly their shape with a change of the internal angle.

3.1.3 Solution of the SLE

Once magnetic, structural and dissipative parameters have been estimated the SLE is completely defined. At this point, physical properties can be calculated, with the knowledge of $\hat{\Gamma}$ and P_{eq}, either directly from the conditional probability $P(\boldsymbol{X}, t)$ or in terms of time correlation functions, which are defined, for two correlated observables $f(\boldsymbol{X}, t)$ and $g(\boldsymbol{X}, t)$

as

$$G(t) = \langle f(\boldsymbol{X},t) \,|\, \exp{(-\hat{\Gamma}t)} |\, g(\boldsymbol{X},t) P_{eq}(\boldsymbol{X}) \rangle \tag{3.14}$$

from which it is possible to calculate the spectral density, i.e. the Fourier-Laplace transform of $G(t)$ as

$$J(\omega) = \frac{1}{\pi} \int_0^\infty d\omega G(t) e^{-i\omega t} = \frac{1}{\pi} \langle f(\boldsymbol{X},t) \,|\, \left(i\omega + \hat{\Gamma}\right)^{-1} |\, g(\boldsymbol{X},t) P_{eq}(\boldsymbol{X}) \rangle \tag{3.15}$$

The formalism for evaluating cw-ESR spectra is now easily interpreted in terms of spectral densities. In the SLE framework, the stochastic operator $\hat{\Gamma}$ is part of the generic stochastic Liouvillean $\hat{\mathcal{L}}$ (eq. 3.1) and the cw-ESR spectrum given by

$$I(\omega - \omega_0) = \frac{1}{\pi} \mathcal{R}e \left\{ \langle\langle v \,|\, \left[i(\omega - \omega_0) + \hat{\mathcal{L}} \right]^{-1} |\, v P_{eq} \rangle\rangle \right\} \tag{3.16}$$

i.e., as the real part of the spectral density for the auto-correlation function for the observable, usually called "starting" vector corresponding to the X-component of the magnetization. It is usual to transform the Liouvillean with the symmetrization

$$\tilde{\mathcal{L}} = P_{eq}^{-1/2} \hat{\mathcal{L}} P_{eq}^{1/2} = i\hat{\mathcal{H}}^\times + P_{eq}^{-1/2} \hat{\Gamma} P_{eq}^{1/2} = i\hat{\mathcal{H}}^\times + \tilde{\Gamma} \tag{3.17}$$

and now we are following the time evolution of the density matrix $\tilde{\rho}(\boldsymbol{Q},t) = \rho(\boldsymbol{Q},t)/\rho_{eq}(\boldsymbol{Q})$ and the equilibrium probability density of the stochastic coordinates is $\tilde{P}_{eq}(\boldsymbol{X}) = P_{eq}^{1/2}(\boldsymbol{X})$. The spectral density becomes now:

$$I(\omega - \omega_0) = \frac{1}{\pi} \mathcal{R}e \left\{ \langle\langle v P_{eq}^{1/2} \,|\, \left[i(\omega - \omega_0) + i\hat{\mathcal{H}}^\times + \tilde{\Gamma} \right]^{-1} |\, v P_{eq}^{1/2} \rangle\rangle \right\} \tag{3.18}$$

Definition of the starting vector depends on the radical that is going to be studied. Consider as an example the case of a monoradical in which the unpaired electron is coupled to a nucleus of spin I: the starting vector takes the form

$$|\, v P_{eq}^{1/2} \rangle\rangle = (2I+1)^{-1/2} |\, \hat{S}_X \times \mathbf{1}_I \times P_{eq}^{1/2} \rangle\rangle \tag{3.19}$$

The cw-ESR spectrum is obtained by numerically evaluating the spectral density defined in eq 3.18 and here we adopt the standard methodology of spanning the Liouvillean over a proper basis set defined by the direct product

$$|\, \Sigma \rangle\rangle = |\, \sigma \rangle\rangle \otimes |\, \Lambda \rangle \tag{3.20}$$

The basis set for the spin coordinates, $|\,\sigma\rangle\rangle$, is the space of spin transitions and is defined elsewhere [16, 21, 32]. For the stochastic part we make the standard choice of employing Wigner rotation matrices for the global rotation and complex exponentials for the internal torsional angle, i.e. $|\,\Lambda\rangle = |\,LMK\rangle \otimes |\,n\rangle$ with

$$|\,LMK\rangle = \sqrt{\frac{2L+1}{8\pi^2}}\mathcal{D}^{L}_{M\,K}\left(\boldsymbol{\Omega}\right) \tag{3.21}$$

$$|\,n\rangle = \frac{1}{\sqrt{2\pi}}e^{-in\theta} \tag{3.22}$$

To obtain the spectral density usually iterative algorithms, like Lanczos [20, 106] or conjugate gradients [107] are employed. In particular we make use of the Lanczos algorithm, a recursive procedure to generate orthonormal functions which allows a tridiagonal matrix representation of the system Liouvillean. Assuming as a first function the normalized zero-average observable, $|\,1\rangle\rangle = |\,vP_{eq}^{1/2}\rangle\rangle/\langle\langle v\,|P_{eq}|\,v\rangle\rangle^{1/2}$, the following functions are obtained recursively

$$\beta_{n+1}|\,n+1\rangle\rangle = \left(\tilde{\mathcal{L}} - \alpha_n\right)|\,n\rangle\rangle - \beta_n|\,n-1\rangle\rangle \tag{3.23}$$

$$\alpha_n = \langle\langle n\,|\tilde{\mathcal{L}}|\,n\rangle\rangle \tag{3.24}$$

$$\beta_n = \langle\langle n\,|\tilde{\mathcal{L}}|\,n-1\rangle\rangle \tag{3.25}$$

Coefficients α_n and β_n actually form the first and second diagonal of the tridiagonal (complex) symmetric matrix representation of the symmetrized Liouvillean, and the spectrum can be written in the form of a continued fraction [20]

$$I(\omega) = \cfrac{1}{i\omega - \alpha_1 - \cfrac{\beta_2^2}{i\omega - \alpha_2 - \cfrac{\beta_3^2}{i\omega - \alpha_3 - \ldots}}} \tag{3.26}$$

Evaluation of eqs. 3.23-3.25 is carried on in finite arithmetic by projecting the symmetrized Liouvillean and the the starting vector on the basis set 3.20, defining the matrix operator and starting vector elements

$$\boldsymbol{\mathcal{L}} = \langle\langle \Sigma\,|\tilde{\mathcal{L}}|\,\Sigma'\rangle\rangle \tag{3.27}$$

$$\boldsymbol{v} = \langle\langle \Sigma\,|1\rangle\rangle \tag{3.28}$$

so that the matrix-vector counterparts of eqs. 3.23-3.25 become

$$\beta_{n+1}\boldsymbol{v}_{n+1} = (\boldsymbol{\mathcal{L}} - \alpha_n)\,\boldsymbol{v}_n - \beta_n\boldsymbol{v}_{n-1} \tag{3.29}$$

$$\alpha_n = \boldsymbol{v}_n \cdot \boldsymbol{\mathcal{L}} \cdot \boldsymbol{v}_n \tag{3.30}$$

$$\beta_n = \boldsymbol{v}_n \cdot \boldsymbol{\mathcal{L}} \cdot \boldsymbol{v}_{n-1} \tag{3.31}$$

Symmetry arguments can be employed to significantly reduce the number of basis function sets required to achieve convergence, together with numerical selection of a reduced basis set of functions based on ”pruning” of basis elements with negligible contributions to the spectrum [16].

3.2 E-SpiReS software

We present in this section a new software tool, named E-SpiReS (Electron Spin Resonance Simulation), aimed at the interpretation of dynamical properties of molecules in fluids from electron spin resonance (ESR) measurements. The code implements the integrated computational approach, described in the previous section, for the calculation of relevant molecular properties that are needed in order to obtain spectral lines. The protocol encompasses information from atomistic level (quantum mechanical) to coarse-grained level (hydrodynamical), and evaluates ESR spectra for rigid or flexible single or multi-labelled paramagnetic molecules in isotropic and ordered phases, based on a numerical solution of a stochastic Liouville equation.

E-SpiReS automatically interfaces all the computational methodologies scheduled in the ICA in a way completely transparent to the user, who controls the whole calculation flow via a graphical interface.

Parallelized algorithms are employed in order to allow running on calculation clusters, and a web applet Java has been developed with which it is possible to work from any operating system, avoiding the problems of recompilation.

Due to the modular nature of the ICA protocol, E-SpiReS is not a single program, but rather a package of many applications. The main distinction is from the calculation core programs which work from the command line and the graphical user interface (GUI) which is the high

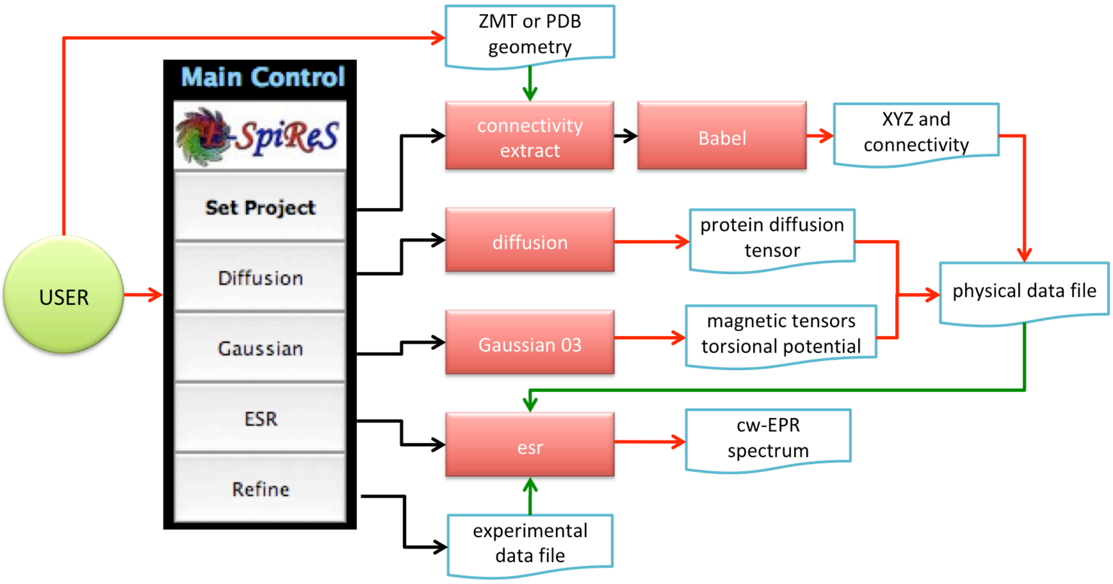

Figure 3-2: Schematic representation of all the operations handled by the graphical user interface of E-SpiReS in function of user's actions. Red arrows represent output, green arrows input data and red boxes the core programs

level wrapper that interfaces all the core applications and also other external programs like Gaussian 03 [53], for QM calculations, and Babel [108], for translating among molecular file formats. Figure 3-2 shows a scheme illustrating the work flow that the graphical interface automatically handles for each specific request of the user.

Simulations are organized in projects. The first and only permitted operation when using the program is the specification of the molecular geometry. Once the user has feeded E-SpiReS with the geometry file, in Z-matrix (ZMT) or protein data bank (PDB) format, E-SpiReS sets as project directory the one where the geometry file is located. In this folder all the input / output and supporting files are stored. It is possible to keep more projects in the same folder without making confusion because E-SpiReS appends the name of the geometry file as a prefix to the names of all the produced files. As an example, if one puts in the same directory the two geometry files, say "tempol.pdb" and "toac.pdb", all files related to the first project will start with "tempol_" and those related to the second project will start with "toac_". In any case, a lot of files are created during a simulation so it is recommended to work in separate folders.

Users which feel at ease working with command line can perform a simulation completely by calling the calculation core programs in sequence. This can be a tedious process, however, and the GUI is really helpful in managing the different operations, especially for I/O.

In the subsections below some details on the implementation and usage of E-SpiReS are given.

3.2.1 Graphical user interface

The GUI of E-SpiReS is written in Java. The choice of writing the interface in such a language came in part from the relative simplicity of developing graphical applications and for the possibility of creating, with a minimal effort, a web applet that works on internet browsers. This aspect will be discussed in the "Web interface" subsection.

As it can be seen in Figure 3-3, the interface has a very simple outlook. It is made of a window representing the 3D space where the molecule is plotted and some point-and-click input is done when preparing a simulation, and a small control panel with five buttons, which stand for the guided work flow that users should follow in order to complete the simulation and obtain the cw-ESR spectrum. Every button represents a procedure in the simulation work flow where some decisions need to be taken by the user. Unfortunately, the intrinsic complexity of the methodology does not permit to write a "single button" or black-box program: users have freedom of choice in several crucial steps, e.g. in deciding which parameters to evaluate theoretically or fix or fit, changing the defaults settings for the calculations and so on. This fact implies that the work flow to follow is not predetermined, but changes depending on user's knowledge, expertise and so on. As an example, suppose that a user is dealing with a flexible molecule and wants to focus only on the internal potential. There are two possibilities: calculating the potential via QM or setting a custom shape. The difference between the two choices is that the first case implies that the user enters the "Gaussian" environment in order to calculate the torsional potential, while in the second case he / she can avoid completely the "Gaussian" step following a different work flow.

In the next subsections a description of the five steps (or environments) of a typical calculation is given. Each environment collects a number of correlated numerical and physical aspects.

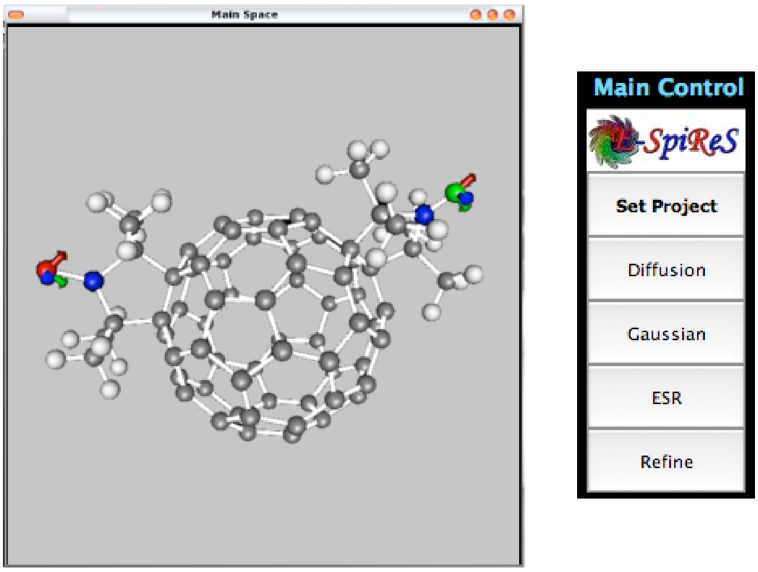

Figure 3-3: Graphical User Interface of E-SpiReS. It consists of a window (on the left) which is the 3D space where the molecules are plotted and a control panel (on the right) with which setting and running the calculations.

Set Project

The "Set Project" environment is the starting step of a simulation. Here the user configures the system and makes basic choices about the calculation strategy. The initialization of a new calculation is automatically handled by E-SpiReS once a molecular geometry file (either in ZMT of PDB formats) is loaded. Once the molecule is displayed in the 3D space window, a number of decisions have to be taken. Firstly it is necessary to select the dynamical model for the molecule. At present, there are only two models implemented: the first is the "rigid body model" (RBM) in which the molecule is seen as a rigid rotator reorienting in the fluid. The second is the "flexible body model" (FBM) where, together with the global tumbling, also internal degrees of freedom are taken under consideration. In this case, the user has to specify the two atoms bonded by the torsional angle and this definition can be done directly on the molecule by clicking the two atoms. In the near future more complex motional models will be added as complementary modules to E-SpiRes (two and three body diffusive models, membrane environments and locally vibrating motions). After the selection of the dynamical model it is fundamental to give to E-SpiReS some basic information on the magnetic probe, which is tantamount to defining the effective spin Hamiltonian. The user can again select

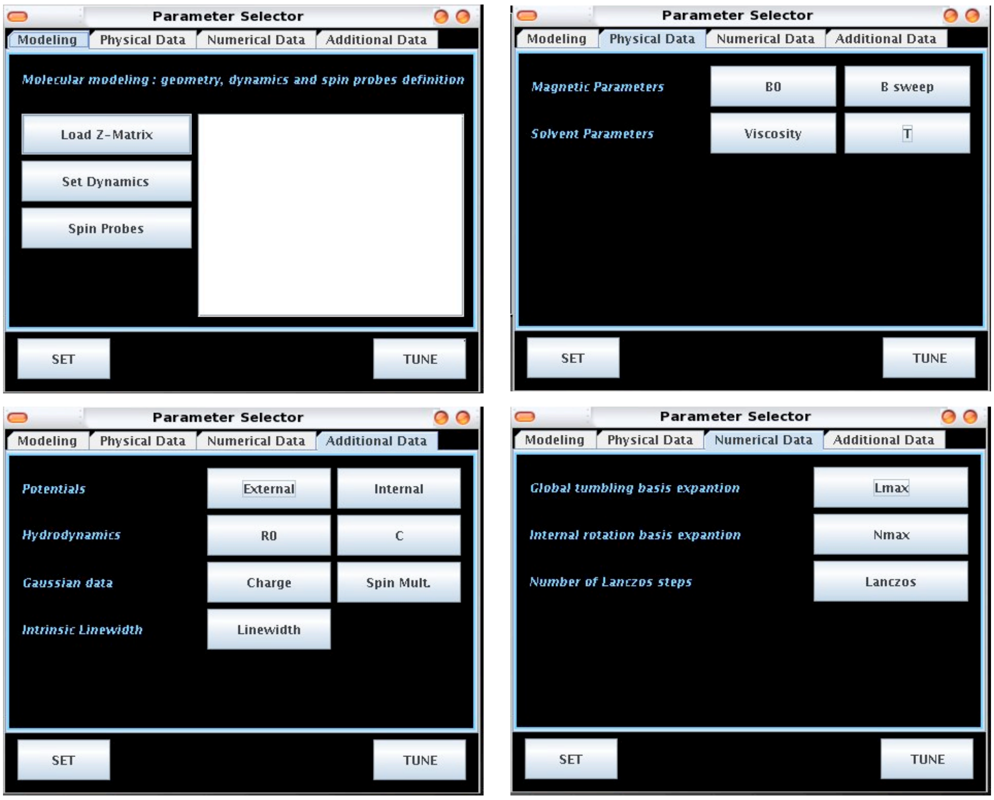

Figure 3-4: Representation of the panels aimed to the definition of the physics of the system. The Modelling Panel (up, left) is aimed to the point-and-click definition of the spin Hamiltonian and the diffusive operator; in the Physical Data Panel (up, right) users introduce important experimental data (field, field sweep, temperature and viscosity); the Numerical Data panel (bottom right) contains the information about numerical parameters (basis truncation numbers, Lanczos iterations); finally, the Additional Data panel (bottom left) serves to optionally introduce some more information on the system (the shape and strength of applied potentials, hydrodynamic properties, molecular charge, spin multiplicity and intrinsic linewidth).

directly on the molecule the atoms bearing the unpaired electrons and the nuclei coupled to the electrons. At present, it is possible to define up to two spin probes on the molecule and two nuclei per spin probe. E-SpiReS takes a default set of magnetic properties (principal values of tensors, orientations, nuclear spin, etc.) which can be modified by the user in a further step (the ”Diffusion” environment, see below).

At this stage the user has decided the Liouvillean shape and the ensemble of physical parameters is well defined. Some of these parameters are chosen initially with default values by E-SpiReS, but they can be modified by the user if needed; four important parameters must be inserted because they represent the experimental conditions and these are the frequency of the spectrometer, the field sweep (i.e. the range of fields of acquisition of the signal), the temperature and the viscosity of the solution. All the parameters that enter the SLE are collected into three different panels, as shown in Figure 3-4. The first panel includes the four most relevant parameters reported before. The second panel shows generic information like the truncation limit of the basis. Finally, the third panel collects the remaining data, such as potentials, radius of the spheres, intrinsic linewidth etc.

Diffusion

The "Diffusion" environment is the next step in the simulation. When it is entered, E-SpiReS automatically launches the calculation of the diffusion tensor. The atoms of the molecule are highlighted with a different colour in order to show clearly different fragment of the molecules. As it can be seen in Figure 3-5a in the case of RBM the molecule is a unique rigid fragment, so all the atoms have the same colour (blue). Figure 3-5b shows the case of FBM, for which the atoms are coloured blue or red depending on which fragment they belong to. Atoms in the reference fragment, which is the fragment which defines the global orientation of the molecule with respect to the inertial laboratory frame, are blue.

The output of the diffusion tensor calculation reports the rotation matrix that transforms from the laboratory to the instantaneous local molecular frame (MF), so E-SpiReS uses this information to transform the position vectors of the atoms in the MF and then plots the diffusion tensor, i.e. a right-handed system of coordinates collinear to the principal axes of the diffusion tensor and with the three axes of length proportional to the principal values. Users have the possibility to adjust the single eigenvalues and / or the trace of the diffusion tensor simply in the "diffusion tensor editor" window that appears after clicking on the diffusion tensor. The orientation of the tensor, instead, cannot be changed; all the variations in the orientation will be reflected in adjustments of the orientation of the magnetic tensors. Due to the fact that the orientations of the magnetic tensors are relative to the MF, the "diffusion" environment gives the users the possibility to modify the magnetic tensors, i.e. the orientation relative to MF and also the principal values of all $\boldsymbol{g}$ and $\boldsymbol{A}$ tensors, via a simple point-and-click procedure. Figure 3-6 shows the mask that appears when a magnetic tensor is clicked.

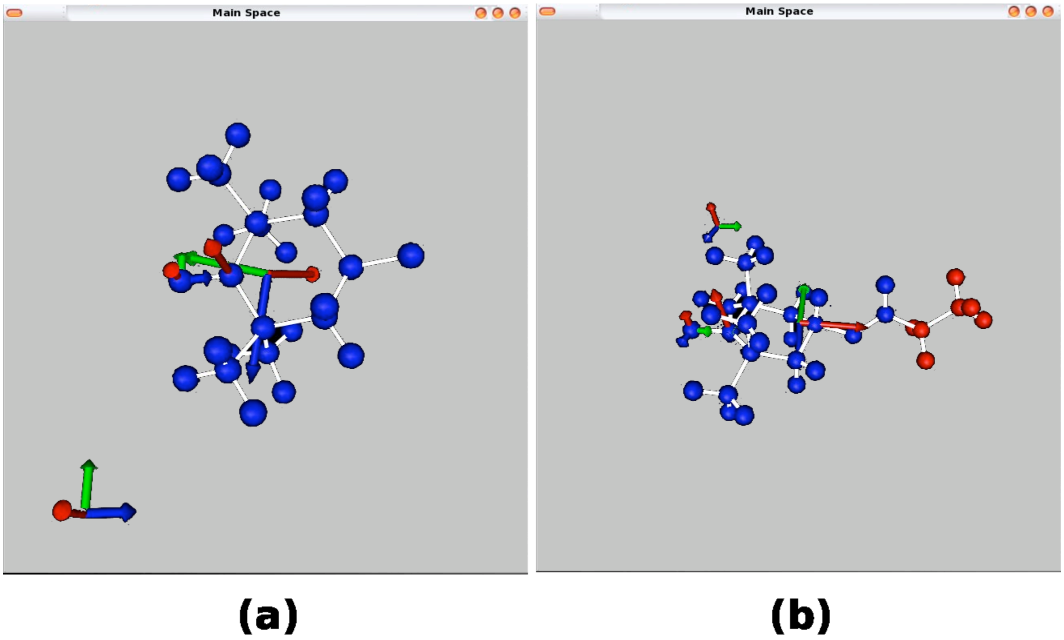

Figure 3-5: In the "diffusion" environment the atoms of the molecule are coloured depending on the fragments to which they belong: (a) in a rigid molecule there is only one fragment and all the atoms have the same colour; (b) in a molecule with one internal degree of freedom there are two fragments and the colours of the atoms clarify the partitioning of the molecule. The diffusion tensor is always referred to a frame fixed on the blue fragment.

Gaussian

The "Gaussian" environment is dedicated to the calculation of structural parameters, i.e. the magnetic tensors and / or the internal torsional potential in the case of FBM model. E-SpiReS is programmed to interface with the Gaussian 03 package for QM calculations [53]. The program automatically writes an input file for Gaussian starting from the geometry file given by the user and the modelling of the magnetic part. This input file is prepared using a standard basis set and DFT functional for what concerns magnetic calculations [73] and also the PCM (polarizable continuum model) flag is added in order to perform the calculation with implicit solvent [50]. In case of a flexible molecule, E-SpiReS appends to the Gaussian input file also the directives to perform a scan of the torsional angle so to evaluate the potential energy surface (PES). This input file can be edited at will directly from the GUI, via a simple internal text editor of E-SpiReS as Figure 3-7 shows, and then the file can be submitted to the Gaussian program right from E-SpiReS. At the end of the calculation, E-SpiReS automatically reads the output of Gaussian and updates the principal values and

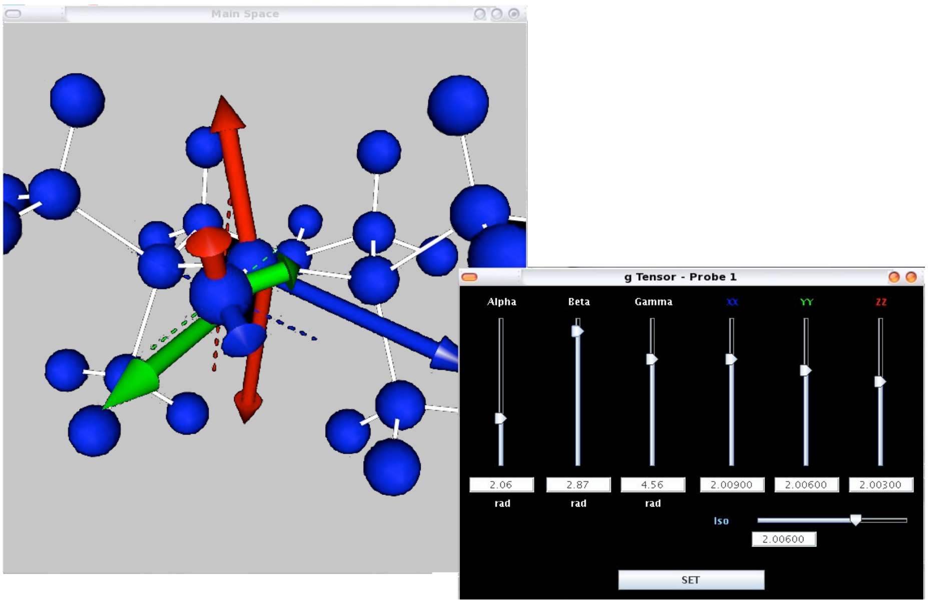

Alpha 2.06 rad
Beta 2.87 rad
Gamma 4.56 rad
XX 2.00900
YY 2.00600
ZZ 2.00300
Iso 2.00600

Figure 3-6: Each magnetic tensor can be edited by the user in the "diffusion" environment. With a simple mask, users can change the three Euler angles giving the orientation with respect to the molecular frame, the three principal values and the trace of the tensor.

orientations of the magnetic tensors. In case of flexible molecules, E-SpiReS reads the PES and spans the calculated potential over complex exponentials $e^{-in\theta}$ which is the same basis set over which the diffusive operator of the internal angle is spanned. All these operations are completely automatic and transparent to the user. It is also possible to import a precalculated QM calculation, but attention must be payed to the fact that the atoms numbering must be the same of the geometry file feeded to E-SpiReS in the "Set Project" environment. Checking or un-checking the "use Gaussian out" box in this environment makes E-SpiReS entering in the "Diffusion" environment and automatically adjusting the orientations and principal values of the magnetic tensors and then back to the "Gaussian" environment.

Esr

The "Esr" environment launches the calculation of the spectrum and plots, directly from the GUI, the result. The SLE is solved following a standard variational approach (see Section 3.1.3), by spanning the Liouville operator over a proper basis set, obtained as the direct product of the space of spin transitions and the rotational space defined by stochastic variables. The spectrum is evaluated by standard algebraic methods [16]. Matrix dimensions

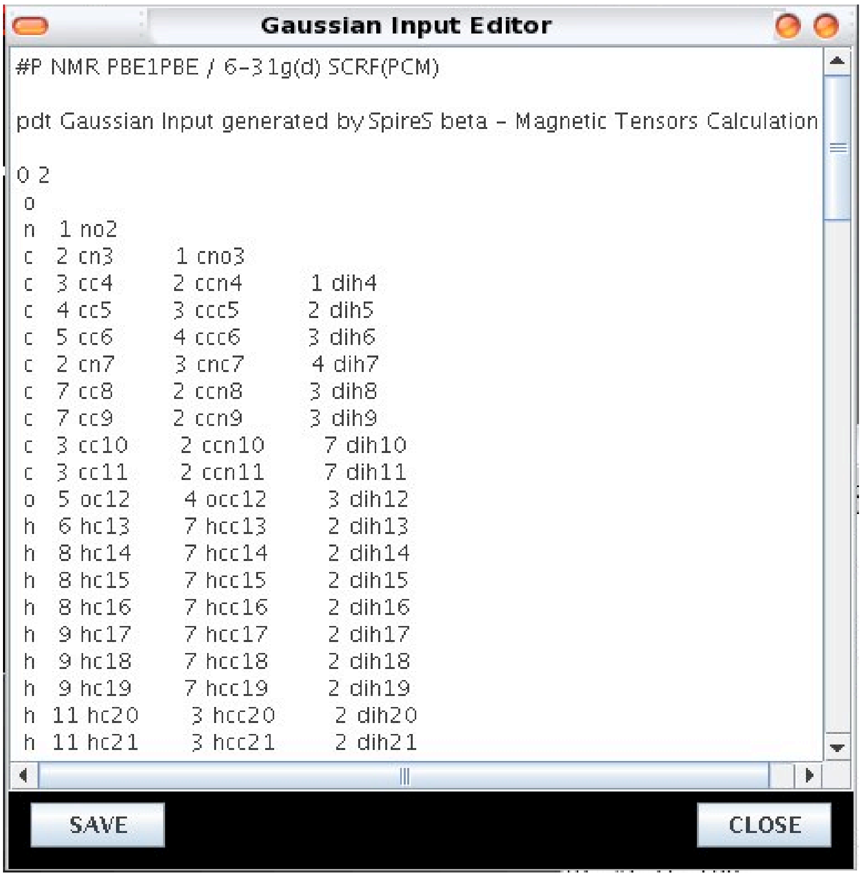

```
#P NMR PBE1PBE / 6-31g(d) SCRF(PCM)

pdt Gaussian Input generated by SpireS beta - Magnetic Tensors Calculation

0 2
 o
 n   1 no2
 c   2 cn3       1 cno3
 c   3 cc4       2 ccn4       1 dih4
 c   4 cc5       3 ccc5       2 dih5
 c   5 cc6       4 ccc6       3 dih6
 c   2 cn7       3 cnc7       4 dih7
 c   7 cc8       2 ccn8       3 dih8
 c   7 cc9       2 ccn9       3 dih9
 c   3 cc10      2 ccn10      7 dih10
 c   3 cc11      2 ccn11      7 dih11
 o   5 oc12      4 occ12      3 dih12
 h   6 hc13      7 hcc13      2 dih13
 h   8 hc14      7 hcc14      2 dih14
 h   8 hc15      7 hcc15      2 dih15
 h   8 hc16      7 hcc16      2 dih16
 h   9 hc17      7 hcc17      2 dih17
 h   9 hc18      7 hcc18      2 dih18
 h   9 hc19      7 hcc19      2 dih19
 h  11 hc20      3 hcc20      2 dih20
 h  11 hc21      3 hcc21      2 dih21
```

Figure 3-7: The Gaussian Editor window is a very basic text editor where users can modify the standard Gaussian 03 input file produced by E-SpiReS before to submit the QM calculation.

in a typical cw-ESR simulation can be quite large. As an example, the simplest case of a rigid nitroxide probe with one electron interacting with a nitrogen nucleus and subject to free fast rotation needs roughly 1260 basis functions, while adding a second equal probe the dimension makes this number grow to 45360, i.e. simply adding another electron and another coupled nitrogen nucleus the dimension of the basis grows of one order of magnitude. This makes it impossible to use the simple techniques for solving algebraic problems, even if the matrix associated to the Liouvillean is sparse. Symmetry arguments can be taken into account in order to reduce the dimensions, but in many cases the number of basis functions required remains high. Handling big matrices does not imply only large calculation times, a problem which is in part solved by using iterative algorithms. It also carries problems with storage. Even if the Liouvillean matrix is very sparse and only non-zero elements are kept in memory, the situation becomes critical when the dimensions reach orders of magnitudes of

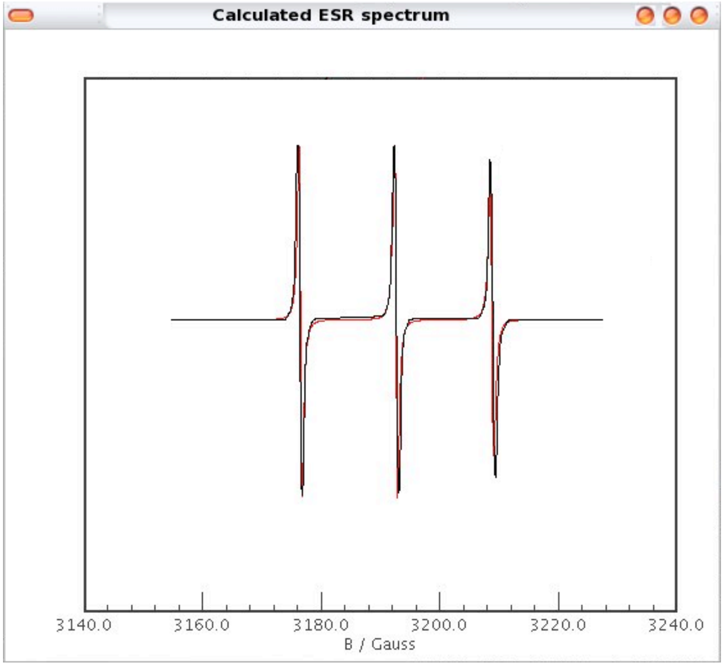

Figure 3-8: Snapshot of the plotter window that appears when the "Plot" button is clicked in the "ESR" environment. Here the last calculated spectrum is represented.

millions. If one considers a basis with dimensions of 10^6, and only 1% of non-zero elements, if each element occupies 16 bytes (numbers are complex, so we need to store two floating point numbers per element) and considering that only half of the out-of-diagonal elements have to be stored (matrices are in general complex symmetric), the memory required is about 80 Gbytes and it cannot be handled by a single computer (at the present, computers usually have less than 16 GB of RAM memory). To deal with both time and memory problems, the "esr" core routine of E-SpiReS has been parallelized. In particular two parts of the program are parallel, the construction of the matrix associated to the Liouvillean and the matrix vector product in the Lanczos tridiagonalization. Parallelization of the code is done under the message passing interface (MPI) [109, 110] paradigm which is a non-shared memory methodology. The code is written in such a way that it is scalable with the number of processors given by the user at run time so it can take advantage of running on a cluster of computers. In the "Esr" environment it is also possible to run a fitting of an experimental spectrum, but the choice of the fitting parameters is placed in a dedicated environment and the reasons will be given in the next subsection. At every fit step two files are produced, one with the values of the free parameters at that step and one containing the theoretical spectrum calculated with that values of the parameters.

At the end of the calculation, the "Plot" button, as shown in Figure 3-8, opens a window where the calculated spectrum is plotted. In case of fitting, clicking on "Plot" shows the last calculated spectrum superposed to the experimental one.

Refining

Fitting in E-SpiReS is considered an operation to be used as sparingly as possible; the main idea is the *ab initio* calculation of all the physical parameters. In this context, fitting is seen more as a "refinement" operation, i.e. it is considered a step where parameters are smoothed to overcome little discrepancies from the "real" values due to approximations of the calculation methodologies. This means that the initial guess passed to the fitting routine are supposed to be in a region of the phase-space of the free parameters near the global minimum of the surface, so avoiding problems of getting stuck in local and / or non-physical minima.

As shown in Figure 3-9, in the "refining" environment the user have to decide which parameters are to be fitted just by checking the relative check-boxes; the experimental spectrum in (field, signal) double column ASCII format must be supplied. Once the free parameters have been set, the calculation is launched from the "Esr" environment. The fitting algorithm is based on the Levenberg-Marquardt method of non linear least squares minimization, i.e. the routine searches for the set of parameters $\boldsymbol{p}$ that minimizes the function

$$\chi^2 = \sum_i \left[y_{exp}\left(x_i\right) - y_{theo}\left(x_i, \boldsymbol{p}\right)\right]^2 \tag{3.32}$$

where $y_{exp}(x_i)$ is the i-th experimental data point and $y_{theo}(x_i, \boldsymbol{p})$ is the theoretical approximating data point calculated for a certain set of values of the parameters $\boldsymbol{p}$.

At every n-th step of the fitting the program dumps a file containing the values of the fitting parameters at that step, $\boldsymbol{p}_n$, and a file containing the theoretical spectrum calculated with those parameters. While the fitting routine is running, users have the possibility to see the progress by clicking the "Plot" button in the "Esr" environment which puts in graph both the experimental spectrum and the last theoretical spectrum calculated.

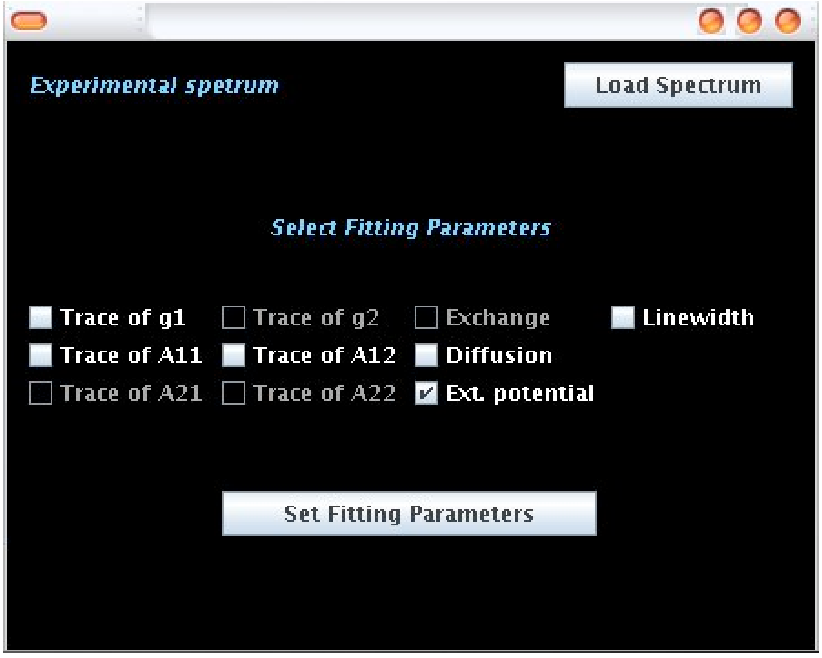

☐ Trace of g1 ☐ Trace of g2 ☐ Exchange ☐ Linewidth
☐ Trace of A11 ☐ Trace of A12 ☐ Diffusion
☐ Trace of A21 ☐ Trace of A22 ☑ Ext. potential

Figure 3-9: In the refinement mask users can decide which parameters are to be fitted and supply the experimental spectrum file to E-SpiReS.

3.2.2 Calculation core

Figure 3-2 shows how E-SpiReS works, i.e. how the GUI responds to the requests of the user. The GUI handles a number of core programs, represented by red boxes in the figure. The core programs, written in C, are:

- *connectivity_extract*: aimed to call the Babel [108] program to convert from the ZMT or PDB format to the Cartesian XYZ coordinates and also to extract the atoms connectivity matrix;

- *diffusion*: is the core program of the DITE package and its task is to calculate the diffusion tensor of the molecule; if a Gaussian calculation has been performed, it reads the output of Gaussian to get the geometry and also updates orientations of the magnetic tensors;

- *esr*: is the program that solves the stochastic Liouville equation producing the spectrum, for both single calculation of fitting procedure.

Two other programs are involved, which are the Babel program for the conversions among molecular file formats and, optionally, the Gaussian 03 package for the quantum mechanical calculations.

The three core programs *connectivity_extract*, *diffusion* and *esr* were developed introducing a number of libraries, summarized in Appendix D, in order to handle different base tasks, like fitting, linear algebra operations, numerical integration and so on.

3.2.3 Web interface

The choice of employing the Java programming language to build the graphical interface stems from the fact that with a minimal effort it is possible to transform an application to an applet that runs on a web browser. The program is configured to work under the applet - servlet paradigm, i.e. the applet runs locally on the user's browser and every request of calculation or upload / download of files is sent by the applet to a servlet running on the cluster. The communications between applet and servlet are handled with the standard Apache Web Server program.

Interfacing users and calculation cluster through a Java web interface present a number of advantages, i.e. no installation is required (the Java virtual machine is a standard), the same version works on every browser and on every operating system and users do not need to be concerned about questions of remote access, graphics forwarding etc. because the Apache Web Server does automatically all that is needed.

3.3 Case-study calculations

We present in this section studies conducted over a number of different model systems. The selected cases were used for the purpose of setting up, implementing and testing our integrated computational approach and E-SpiReS. In particular we considered the following systems:

- [C60]fulleropyttolidine bisadducts with nitroxide probes in toluene [111]: a paradigm of rigid bi-radical species. Rigidity of the fullerene structure permits to study spatial effects on the electrons exchange interaction energy;

- p-(methylthio)phenyl nitronylnitroxide molecule in toluene [58]: an important molecule in material sciences. It is a rigid small radical in which the unpaired electron has important hyperfine coupling with two ^{14}N atoms;

- bi-labeled small peptides in different solvents [56, 59, 112]: due to the sensitivity of cw-ESR spectra on both dynamics and structure and the quality of quantum mechanical and hydrodynamic evaluation of molecular parameters, the integrated computational approach show to be promising in the possibility of assigning secondary structure to biological molecules;

- tempo-palmitate in 5-cyanobiphenyl [113]: an example of flexible molecule in orienting environments. This study underline the importance of taking into account relevant dynamical processes and to introduce dynamical models based on a detailed atomistic description of the internal motions of molecules;

- polymerization of methyl methacrylate radical in toluene [114]: an example of how modelling based on the interpretation of relevant dynamical and structural details of the molecule give the possibility of well describing the behaviour of complex systems with relatively simple models.

This systematic study, which took most of the doctoral work, led to the present version of E-SpiReS that is able to handle rigid and flexible (with one torsional angle) molecules, with one or two spin probes, in both isotropic and oriented phases.

3.3.1 [60]fulleropyrrolidine bisadducts with nitroxide probes

We address the interpretation of continuous wave electron spin resonance (cw-ESR) spectra of fulleropyrrolidine bisadducts with nitroxide addends. The approach is based on the definition of the spin Hamiltonian which includes exchange and dipolar interactions and on the complete numerical solution of the resulting stochastic Liouville equation, with inclusion of diffusive rotational dynamics. Cw-ESR spectra are simulated for a series of C_{60} bisadducts made up of four trans isomers and the equatorial isomer. A non-linear least square fitting procedure allows to extract directly from the available experimental spectra a wide range of parameters, namely inter-probes relative distances, diffusion tensors and values of exchange parameter J. Results are in good agreement with previous more phenomenological estimates, proving that the combination of sensitive ESR spectroscopy based on multiple spin labelling with nitroxide radicals and sophisticate modelling can be highly helpful in providing structural and dynamic information on molecular systems.

Introduction

Most of the available studies are concentrated on mono-nitroxides derivatives, although nitroxide biradicals and polyradicals have been used in the past for liquid crystal studies [115, 116] and are being employed as spin labels in biopolymer and peptide model systems [117]. Biradicals are characterized by anisotropic tensor $\boldsymbol{g}$ and ^{14}N hyperfine coupling tensor $\boldsymbol{A}$ like monoradicals, but contain additional interaction terms in the spin Hamiltonian, namely the exchange interaction and the dipolar interaction between the unpaired electrons. The distance between the radicals is inferred from the measurement of the dipolar interaction [118], but structural information can be gained also from measuring the exchange constant J between radicals. Conformations of macromolecules have been studied in this way [119, 120]. Measurements of the exchange interaction are somewhat difficult to interpret, because of the lack of knowledge of its dependence on relative distance and orientation of the radicals. Theoretical calculations have been conducted to evaluate the exchange interaction in different molecular geometries [121, 122], which however can hardly be tested by comparison with controlled experimental findings, given the difficulty of preparing binitroxides model systems with defined relative distance and orientation in rigid molecular structures.

As a rigid template, C_{60} has been shown to be an ideal candidate to support nitroxide groups placed at fixed distances and orientations. An ESR study was recently presented [123] for a series of C_{60} bisadducts, which provides a good example of geometrically-controlled molecular system where the relative positions of the unpaired electron couple is exactly determined. As such, it is amenable to an advanced theoretical modelling which includes explicitly the molecular rotational dynamics based on the SLE formalism, employed extensively for the interpretation of ESR spectra of monoradicals [16].

In this work we propose to apply the standard SLE approach to interpret experimental ESR observables for this series of bisadducts, elucidating the formal aspects and summarizing the necessary computational steps, with an emphasis on the general strategy more than on the technical details.

Molecular system and modelling

The series of biradicals studied in [123] are C_{60} bisadducts containing the C_{2v} symmetric tetramethylpyrrolidine-1-oxyl group. The bisadducts series includes all four trans-isomers **1**-**4** and the equatorial isomer **5**, and they are shown in Figure 3-10. Notice that for isomers **1**-**4** the exchange magnitude, J, is of the same order of magnitude of the hyperfine coupling; the measured ESR spectra are complex and showing the presence of several transitions. A description of the synthetic procedures, together with ESR sample preparation and magnetic resonance measurements are provided in ref. [123].

We start by defining the magnetic Hamiltonian of the system which includes Zeeman, hyperfine, exchange and dipolar interaction for the two nitroxides labelled 1 and 2

$$\begin{aligned}\hat{\mathcal{H}}/\hbar &= \frac{\beta_e}{\hbar}\sum_i \boldsymbol{B}_0 \boldsymbol{g}_i \hat{\boldsymbol{S}}_i + \gamma_e \sum_i \hat{\boldsymbol{I}}_i \boldsymbol{A}_i \hat{\boldsymbol{S}}_i - 2\gamma_e J \hat{\boldsymbol{S}}_1 \hat{\boldsymbol{S}}_2 + \\ &+ \frac{\mu_0}{4\pi}\frac{g_e^2 \beta_e^2}{\hbar r^3}\left[\hat{\boldsymbol{S}}_1 \hat{\boldsymbol{S}}_2 - \frac{3}{r^2}\left(\hat{\boldsymbol{S}}_1 \cdot \boldsymbol{r}\right)\left(\hat{\boldsymbol{S}}_2 \cdot \boldsymbol{r}\right)\right] \qquad (3.33)\end{aligned}$$

where the first term is the Zeeman interaction of each electron spin with magnetic field $\boldsymbol{B}_0$, depending on the $\boldsymbol{g}_i$ tensor; the second term is the hyperfine interaction of each couple ^{14}N / unpaired electron, defined with respect to hyperfine tensor $\boldsymbol{A}_i$; the third and fourth term represent the exchange and dipolar term, respectively. Here tensors $\boldsymbol{g}_i$, $\boldsymbol{A}_i$ are diagonal in the local frame N_iF rigidly fixed on the i-th nitroxide (we assume here for simplicity

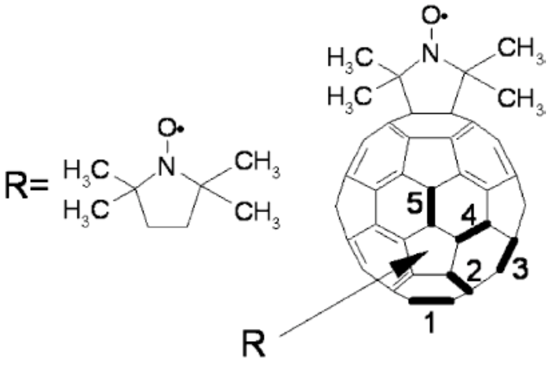

Figure 3-10: Structures of biradicals **1-4** (trans isomers) and **5** (equatorial isomer).

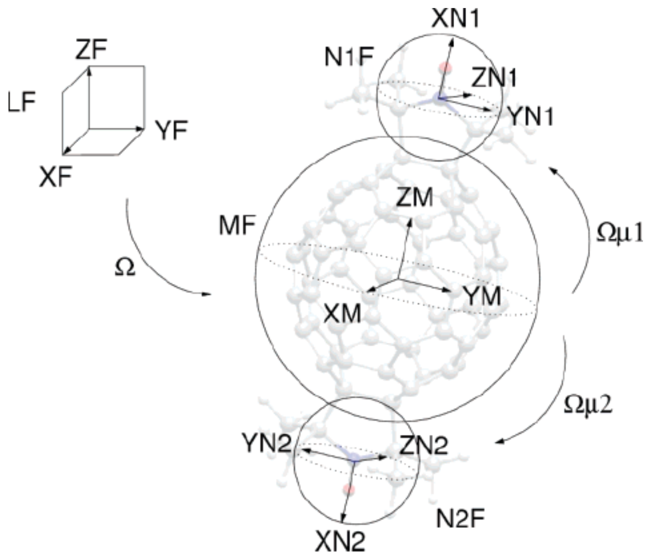

Figure 3-11: Reference frames employed in the stochastic Liouville equation.

that both tensors are diagonal in the same local frame); operators $\hat{\boldsymbol{I}}_i$, $\hat{\boldsymbol{S}}_i$ are defined in the laboratory or inertial frame (LF); finally $\boldsymbol{r}$ is the distance between the two nitroxides. The system geometry is summarized in Figure 3-11. The set of Euler angles $\boldsymbol{\Omega}$ defines the relative orientation of the generic molecular frame (MF), fixed rigidly on the fullerene backbone, with respect to the LF; the local frames N$_i$F are in turn defined with respect to MF by a set of angles $\boldsymbol{\Omega}_i$. Each nitroxide is finally identified by a set of polar coordinates $\boldsymbol{r}_i = (r_i, \phi_i, \theta_i)$, where we take the centre of the fullerene backbone as origin and we assume that the centre of the N-O bond represents the nitroxide effective position, and $\boldsymbol{r} = \boldsymbol{r}_2 - \boldsymbol{r}_1$.

The Hamiltonian in eq. (3.33) can be also written in the compact form

$$\hat{\mathcal{H}} = \frac{\beta_e}{\hbar}\sum_i \boldsymbol{B}_0 \boldsymbol{g}_i \hat{\boldsymbol{S}}_i + \gamma_e \sum_i \hat{\boldsymbol{I}}_i \boldsymbol{A}_i \hat{\boldsymbol{S}}_i + \hat{\boldsymbol{S}}_1 \boldsymbol{T} \hat{\boldsymbol{S}}_2 \tag{3.34}$$

with

$$\boldsymbol{T} = \left(-2\gamma_e J + \frac{\mu_0}{4\pi}\frac{g_e^2\beta_e^2}{\hbar r^3}\right)\mathbf{1} - \frac{\mu_0}{4\pi}\frac{g_e^2\beta_e^2}{\hbar r^5}\begin{pmatrix} r_X^2 & r_X r_Y & r_X r_Z \\ r_Y r_X & r_Y^2 & r_Y r_Z \\ r_Z r_X & r_Z r_Y & r_Z^2 \end{pmatrix} \tag{3.35}$$

being the interaction tensor summarizing both exchange and dipolar interaction. Following the standard approach of description of ESR signals in liquids, we define the SLE given in eq. 3.1.

$$\frac{\partial}{\partial t}\rho(\boldsymbol{Q}, t) = -\left[i\hat{\mathcal{H}}^{\times}(\boldsymbol{Q}) + \hat{\Gamma}(\boldsymbol{\Omega})\right]\rho(\boldsymbol{Q}, t) \tag{3.36}$$

Here we adopt the simple choice of considering as only relevant variables the orientation of MF in the LF, i.e. the Euler angles set, $\boldsymbol{Q} = \boldsymbol{\Omega}$. We shall also assume that the system reorients freely in space, subject to a simple diffusive motional regime, i.e.

$$\hat{\Gamma} = D_{XX}\hat{J}_X^2 + D_{YY}\hat{J}_Y^2 + D_{ZZ}\hat{J}_Z^2 \tag{3.37}$$

where $\hat{J}_i$ is the i-th component of the angular momentum operator in the molecular frame. The ESR spectrum is obtained as the Fourier-Laplace transform of the correlation function for the X-component of the magnetization, defined as $|\,v\rangle\rangle = (2I+1)^{-1}|\,\hat{S}_{X,1} + \hat{S}_{X,2}\rangle\rangle$, where I is the nuclear spin. Following standard definitions [16] we obtain

$$I\left(\omega - \omega_0\right) = \frac{1}{\pi}\mathcal{R}e\left\{\langle\langle v\,|\left[i\left(\omega-\omega_0\right)\mathbf{1} - \left(i\hat{\mathcal{H}}^{\times} + \hat{\Gamma}\right)\right]^{-1}|\,vP_{eq}\rangle\rangle\right\} \tag{3.38}$$

where $P_{eq} = 1/8\pi^2$ is the (isotropic) distribution in the $\boldsymbol{\Omega}$ space. Here ω is the sweep frequency and $\omega_0 = g_0\beta_e B_0/\hbar$, and g_0 is one third of the trace of each $\boldsymbol{g}_i$ tensor, which is the same for the two electrons. The starting vector $|\,v\rangle\rangle$, with respect to which the resolvent in eq. (3.38) is evaluated, is related to the allowed ESR transitions, and it is actually an operator acting on the electron spin degrees of freedom [32].

To summarize, a bisadduct is described as a diffusive rotator, bearing two spin probes rigidly fixed. Parameters are *i)* the principal values of the diffusion tensor D_{XX}, D_{YY} and D_{ZZ}; *ii)* the principal values of $\boldsymbol{g}$ and $\boldsymbol{A}$ tensors, and Euler angles $\boldsymbol{\Omega}_\mu$ ($\mu = g, A$) specifying the orientation of magnetic local tensors with respect to MF, and finally *iii)* the exchange interaction J. The computational implementation of eq. (3.38) is accomplished by converting the problem to a standard linear algebraic formulation of the resolvent in terms of matrices / vectors by projecting the Liouvillean $\hat{\mathcal{L}}$ and the starting vector $|\,v\rangle\rangle$ on a suitable basis set that in our case can be initially defined as

$$|\,\Sigma\rangle\rangle = |\,p_1^S q_1^S, p_1^I q_1^I\rangle\rangle \otimes |\,p_2^S q_2^S, p_2^I q_2^I\rangle\rangle \otimes |\,LMK\rangle = |\,\sigma_1, \sigma_2, LMK\rangle\rangle \tag{3.39}$$

where the same notation of ref. [16] is used: the basis set is given by the direct product of spin operators of nitroxides 1 and 2, defined by electron and nuclear spin quantum numbers p_i^S, q_i^S, p_i^I, q_i^I [16, 32], globally indicated as σ_i, and of normalised Wigner rotation matrices $|\,LMK\rangle$, which correspond to the rotational degrees of freedom, with $L > 0$, $-L \leq M, K \leq L$. It is convenient to introduce a symmetrized basis set, which allows exploiting symmetry properties of the Liouville operator [16, 21]

$$|\,\Sigma\rangle\rangle_K = |\,\sigma_1, \sigma_2, LMK, j^K\rangle\rangle = \left[2\left(1+\delta_{K,0}\right)\right]^{-1/2} e^{-i\pi\left(j^K-1\right)/4}\left(|+\rangle\rangle + j^K s^K|-\rangle\rangle\right) \tag{3.40}$$

where $s^K = (-)^{L+K}$, with $K \geq 0$, and $j^K = \pm 1$ for $K > 0$, $(-)^L$ for $K = 0$; ket symbol $|+\rangle\rangle$, $|-\rangle\rangle$ stand for $|\Sigma\rangle\rangle$ and $|\Sigma\rangle\rangle$ with $K \to -K$. Matrix elements of the stochastic Liouvillean in the symmetrized basis set are real. A symmetric matrix representation of the Liouville operator is given as:

$$\begin{aligned}\langle\langle \Sigma\,|\hat{\mathcal{L}}|\,\Sigma'\rangle\rangle &= \frac{1}{2}\left[(1+\delta_{K,0})\,(1+\delta_{K',0})\right]^{-1/2} \times \\ &\Big[\delta_{j^K,j^{K'}}\mathcal{R}e\left\{\langle\langle + |\hat{\mathcal{L}}|+\rangle\rangle + j^{K'}s^{K'}\langle\langle + |\hat{\mathcal{L}}|-\rangle\rangle\right\} + \\ &+\delta_{j^K,-j^{K'}}\mathcal{I}m\left\{\langle\langle + |\hat{\mathcal{L}}|+\rangle\rangle + j^{K'}s^{K'}\langle\langle + |\hat{\mathcal{L}}|-\rangle\rangle\right\}\Big] \end{aligned} \tag{3.41}$$

The basis set has twelve indexes, leading to very large matrices that need to be treated in order to evaluate each spectrum. Fortunately, a number of established techniques profitably exploited in the past for the study of many-body stochastic Liouville and Fokker-Planck operators can be employed to reduce the computational burden. Exact procedures can be used to reduce the basis dimension invoking rotational symmetries and approximate techniques, based on pruning schemes of the complete basis set, can be employed. First however, in order to evaluate explicitly symmetrized or unsymmetrized matrix elements, one needs to make explicit the dependence of the super-hamiltonian $i\hat{\mathcal{H}}^{\times}$ from magnetic and orientational parameters. Following the established route used for monoradicals [16, 32] we adopt a spherical irreducible tensorial representation

$$\hat{\mathcal{H}}^{\times} = \sum_{\mu}\sum_{l=0,2}\sum_{m,m'=-l}^{l} \mathcal{D}^{l}_{m\,m'}(\mathbf{\Omega})\,F^{(l,\,m')\,*}_{\mu,\,MF}\,\hat{A}^{(l,\,m)\,\times}_{\mu,\,LF} \tag{3.42}$$

where μ runs over all possible interactions, $\mathcal{D}^{l}_{m\,m'}(\mathbf{\Omega})$ is a generic Wigner matrix, $F^{(l,m)\,*}_{\mu,\,MF}$ is built from elements of $\boldsymbol{g}_i$, $\boldsymbol{A}_i$, $\boldsymbol{T}$ in the MF, $\hat{A}^{(l,\,m)\,\times}_{\mu,\,MF}$ is obtained from spin operators. Next the Liouvillean matrix elements are straightforwardly calculated in the unsymmetrized basis set and the symmetrized matrix is built. The starting vector is also easily calculated, since $\langle\langle \Sigma\,|v\rangle\rangle_K \propto \delta_{j^K,1}\langle\langle \Sigma\,|v\rangle\rangle$. Explicit matrix element in the unsymmetrized set are obtained following standard arguments reported elsewhere [16, 21]. Finally, eq. (3.38) can be converted in matrix / vector and standard algorithms for tridiagonalization and direct evaluation of spectral densities in continuous fraction form can be employed, like Lanczos or conjugate gradient [16]. The basis set dimension is given by the product of the number of possible magnetic transitions for each spin (electrons and nuclei) and the number of normalized

Wigner rotation matrices up to a given truncation value L_{max}. In our case, with two electrons and two ^{14}N nuclei, the total number of magnetic basis functions is $4 \times 4 \times 9 \times 9 = 1296$, while for a given L_{max} the number of Wigner functions is given by $(L_{max}+1)(2L_{max}+1)(2L_{max}+3)/3$, for instance for $L_{max} = 2$, which has been employed throughout this work, the number of rotational basis functions is 35, leading to a basis set dimension of 45360.

These are the typical dimensions matrices that need to be employed for evaluating the ESR spectrum. Albeit relatively large, this is not a prohibitive dimension. On a desktop Pentium IV PC, a C program based on Lanczos algorithm is able to calculate a spectrum, for a given set of parameters, in less than 15 minutes. Furthermore, it is possible to reduce significantly the computational burden by selecting relevant basis set elements, adopting the so-called pruning scheme which has been extensively used by Freed and co-workers for mono-radicals. Details on the pruning scheme are given elsewhere [124], and we give here, for sake of completeness, just a general description. The pruning scheme is based on the conjugate gradient algorithm, and it looks at the spectrum, at a given frequency, as obtained in the form $I(\omega) = \langle\langle v \,| u(\omega)\rangle\rangle$; the vector $|\, u(\omega)\rangle\rangle$ is found solving, via conjugate gradient algorithm, a linear system of equations. Basis elements can be classified in term of their projection on $|\, u(\omega)\rangle\rangle$. Sampling the spectrum in a representative range of frequencies, one can find a reduced basis set made only of elements whose projection is higher that a given tolerance. Our extensive tests have shown that even adopting rather conservative criterion in determining the relevant basis element based on the pruning scheme, in the system studied here we are often left with an effective dimension less than 10 - 20 % of the original one, without any significant loss of accuracy in the spectrum evaluation. This fact allows us to determine accurately and quickly the overall spectrum (less than 30 seconds per spectrum), and a systematic fitting procedure of parameters becomes feasible.

Results

The following fitting strategy has been adopted. Principal values of the magnetic tensors have been chosen in accordance with previous knowledge [125]; for both nitroxides we have therefore $g_{XX} = 2.009$, $g_{YY} = 2.006$, $g_{ZZ} = 2.003$ and $A_{XX} = 5.0$, $A_{YY} = 5.0$, $A_{ZZ} = 34.5$ Gauss. Geometry has been also chosen according to molecular structure of each isomer. Finally, the following dissipative and magnetic parameters have been left freely changing, and

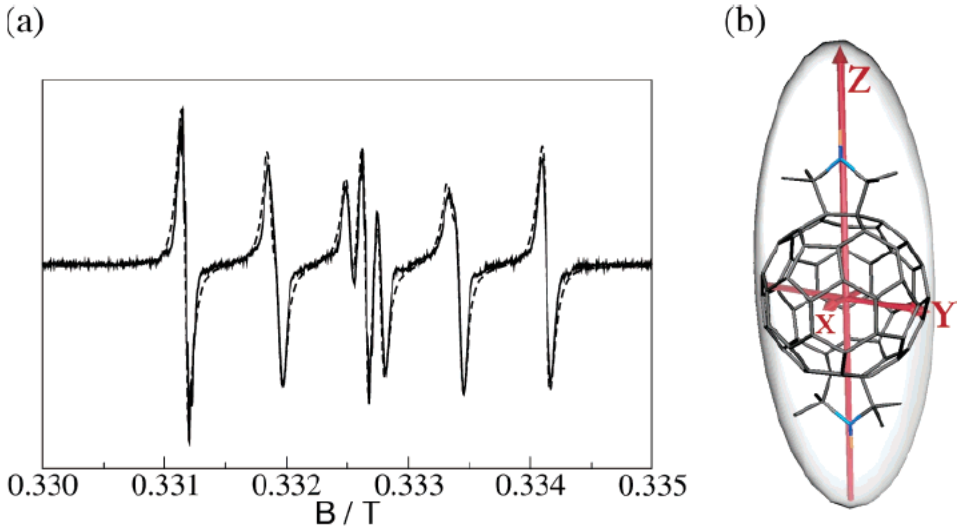

Figure 3-12: (a) Experimental (full line) and simulated (dashed line) ESR spectrum of isomer **1**; (b) principal axis of diffusion tensor of isomer **1**.

therefore determined via a least-square fitting of simulated spectra to experimental data: the principal values of the diffusion tensor D_{XX}, D_{YY}, D_{ZZ} and the exchange coupling constant J. As far as geometrical parameters are concerned, Euler angle set $\mathbf{\Omega}_i$ specifying the relative orientation of the magnetic tensors, i.e. local frames $\mathrm{N}_i\mathrm{F}$, with respect to MF have been inferred from molecular geometry, as shown in Figure 3-10. Similarly, both spin probes and polar angles θ_i, ϕ_i have been estimated from the conformer geometry. Fitting has been employed explicitly instead, only to determine the effective value of the distance from centre for the two nitroxides, $r_1 = r_2 = R$.

A well established search algorithm based on Levenberg-Marquardt approach has been employed [16]. However, a preliminary analysis has shown that in all cases the experimental spectra could not be fit to a single component, i.e. a single simulated ESR result. Essentially, in all cases the intensity of the hyperfine components corresponding to $I_{z,1} \neq I_{z,2}$ were shown to be rather overemphasized in the simulated spectra. By accepting as a working hypothesis that the molecules are essentially rigid objects, without additional degrees of freedom such as fast local libration of the nitroxide residues, we have attempted to add to the simulated one a second component corresponding to a monoradical, which is calculated with standard SLE [16, 21]. For the monoradical the same diffusion tensor of the biradical was assumed:

$$I(\omega) = (1-p)\, I_{mono}(\omega) + p I_{bi}(\omega) \tag{3.43}$$

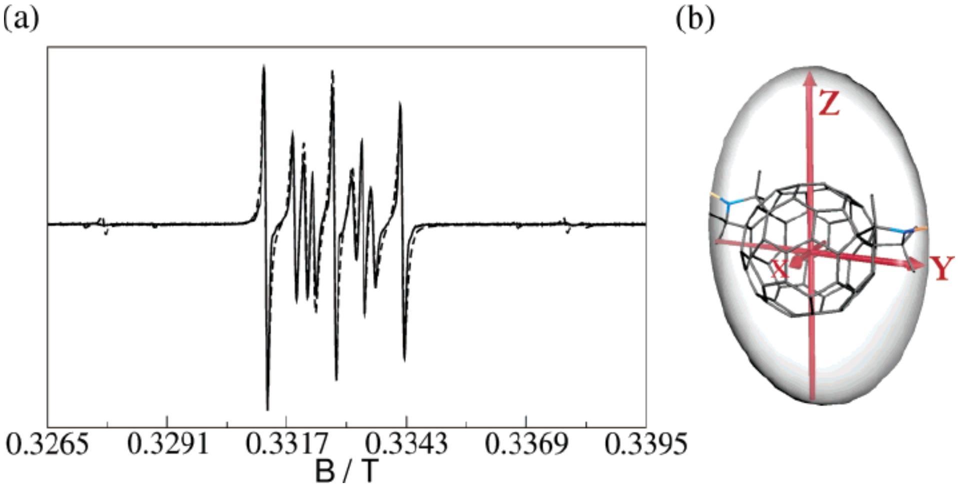

Figure 3-13: (a) Experimental (full line) and simulated (dashed line) ESR spectrum of isomer **2**; (b) principal axis of diffusion tensor of isomer **2**.

The additional parameter p was considered free to change. Although the analytical data for **1-5** are fully in agreement with the proposed structures, we cannot exclude the presence, in the samples of the bisadducts, of traces of a monoradical species. The synthesis of binitroxides **1-5** is in fact based on the oxidation, with chloroperbenzoic acid, of the corresponding bisamines [123], through a postulated intermediary of an hydroxylamine species [126], so it is reasonable to assume an incomplete oxidation and the presence of a monoradical hydroxylamine component. This derivative cannot be easily distinguished from the corresponding biradical by, for example, UV-Vis spectroscopy. Although UV-Vis spectra of C_{60} derivatives have been extensively used for the discrimination between mono- and bisadducts and among isomeric bisadducts, they cannot be employed to characterize fullerene bisadducts with the same addition pattern but different functionalities. Also mass spectrometry failed to reveal the mentioned impurity, whose molecular mass coincides with that of the ^{13}C containing biradical.

After allowing for the presence of the monoradical component, the overall agreement with experimental data was found to be rather good. The overall procedure was proven to be very stable, and the full set of parameters (D_{XX}, D_{YY}, D_{ZZ} and J; distance R and weight p) described in the previous Section was fitted together, i.e. in a single search. In all cases convergence to a unique set of optimized parameters required less than 100 spectrum evaluations, indicating the existence of a relatively sharp region of validity of the model in the parameter space, or in other words, that the model is sensitive in its discrimination of struc-

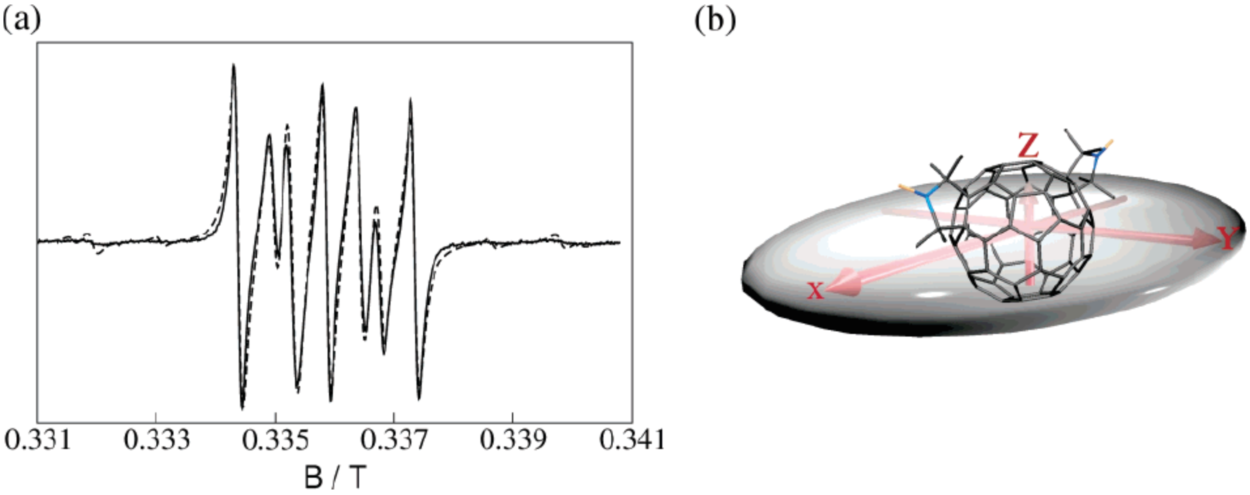

Figure 3-14: (a) Experimental (full line) and simulated (dashed line) ESR spectrum of isomer **3**; (b) principal axis of diffusion tensor of isomer **3**.

tural changes. This is in fact due to several reasons: *i)* the five isomers present very different values of the constant J and four of these values fall in a region where even small changes of J involve appreciable changes in the spectrum shape, and one therefore expects and finds relatively sharp minima with respect to the J parameter: *ii)* initial values employed in the fitting for inter-radical distance R is based on good estimates coming from molecular mechanics calculations of the overall geometry of each conformer (see below); and *iii)* finally the only effect of p on the spectrum is related to the intensity of the three principal lines, having no effect on their position or width. In this way, three of the six parameters (J, R and p) are limited to vary within a restricted range of values which is characteristic of each conformer.

Results are summarized in Table 3.1 and in Figures 3-12-3-16, in which the simulated and experimental spectra are accompanied by the molecular geometry to which an ellipsoid is superimposed, representing the principal values of diffusion tensor and the directions of principal axes of MF.

As an exercise, a comparison has also been carried between values of the nitroxide-nitroxide distance obtained from fitting of the experimental ESR spectra and estimates of the same quantities obtained by a standard molecular mechanics (MM) program, Tinker [127]. The values reported in Table 3.2 are in accord within 10% with the inter-radical distance taken from the mid points of the N-O bonds. This is an approximation based on the consideration that in nitroxide the spin density is equally distributed between the nitrogen and the

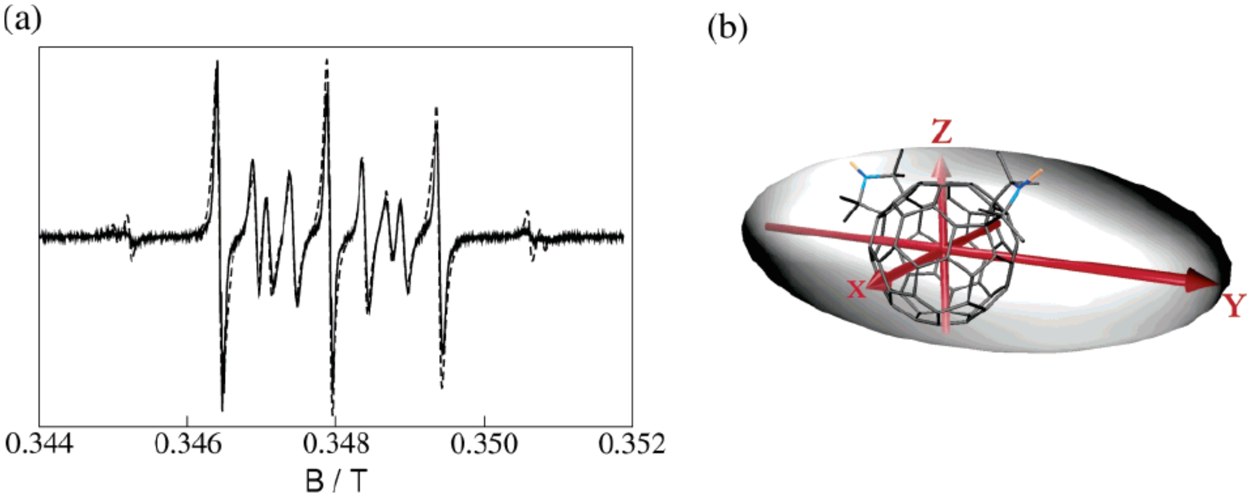

Figure 3-15: (a) Experimental (full line) and simulated (dashed line) ESR spectrum of isomer **4**; (b) principal axis of diffusion tensor of isomer **4**.

oxygen atoms [128, 129]. The rather good overall agreement of the model with experiments is best seen in Figures 3-12-3-16, where the experimental spectra of the biradicals **1-5** are shown together with the best fit spectra. Some small discrepancies in the line shape are present in the case of **2** (see Figure 3-13) for which a spectrum with very narrow lines has been recorded, showing additional small splittings caused by the hyperfine interaction of the methyl protons. For the other biradicals these splittings are unresolved, but contribute to the line shapes giving them a Gaussian contribution. ^{13}C satellites appearing in some of the spectra, particularly evident in those of isomers **1** and **2**, are not reproduced, since they are not included in the model. Moreover, the width of the small intensity lines due to singlet to triplet transitions [115, 116] occurring in the wings region of the spectra (see Figures 3-14 and 3-15) is poorly reproduced, but their position is properly obtained. This is not unexpected since these lines are severely affected by small-amplitude modulation of J interaction, which also is not included in the model [115, 116].

Isomer	R / nm	ϕ_1,θ_1	ϕ_2,θ_2	$\mathbf{\Omega}_1$	$\mathbf{\Omega}_2$	$\boldsymbol{D}$ / 10^9 Hz	J / mT	p
1	0.66	0, 0	180, 0	0, 90, 0	180, 90, 0	0.15, 2.5, 4.6	-8.94	0.83
2	0.58	-75, 0	75, 0	75, 45, 90	-75, 45, 90	0.31, 2.0, 2.2	2.29	0.85
3	0.61	-60, 0	60, 0	90, 72, 90	90, 60, -45	0.93, 0.95, 0.1	-1.70	0.84
4	0.66	-50, 0	50, 0	120, 135, 90	60, 55, 90	0.66, 4.9, 0.98	0.95	0.73
5	0.73	-45, 0	45, 0	-90, 135, 0	0, 90, -45	0.04, 1.0, 1.6	30.5	0.85

Table 3.1: Geometrical and rotational parameters obtained for conformers **1-5** (all angles are expressed in degrees).

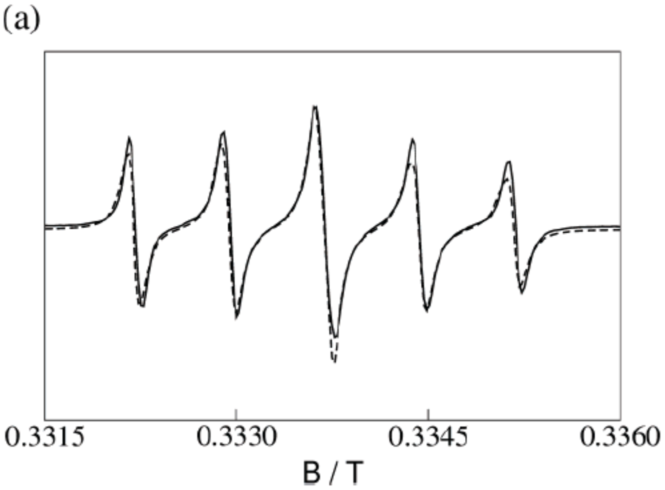

Figure 3-16: (a) Experimental (full line) and simulated (dashed line) ESR spectrum of isomer **5**; (b) principal axis of diffusion tensor of isomer **5**.

Cw-ESR spectrum shape is severely affected by the magnitude of J. To provide didactic illustration of the model flexibility, we have calculated a series of spectra for isomer **1**, maintaining constant all the magnetic and geometric parameters as obtained by the best fit, and varying the exchange interaction J. In Figure 3-17, we show the progression of simulated spectra obtained for decreasing values of the adimensional ratio J/a (where a is the trace of the $\boldsymbol{A}$ tensors) which takes the value of -5.387 in the experimental-related case. In principle all J/a ratios can be determined reliably, although the fitting procedure may become uncertain when $|J/a| >> 1$. In practice, in our case, simulated spectra are essentially independent from variation of $|J/a|$ for $|J/a| > 50$.

Isomer	r_{NN} / Å	r_{OO} / Å	$(r_{NN} + r_{OO})/2$ / Å	r_{fit}	% error
1	12.03	14.30	13.16	13.12	-0.3
2	11.65	14.04	12.84	11.31	-11.9
3	10.24	12.02	11.13	10.77	-3.2
4	9.72	11.57	10.64	10.34	-2.8
5	8.74	10.72	9.73	10.33	+6.2

Table 3.2: Comparison between probe-probe distances estimated by fitting SLE simulated spectra to experimental one (r_{fit}) and obtained by standard molecular mechanics calculation (r_{NN} = nitrogen-nitrogen distance, r_{OO} = oxygen-oxygen distance, obtained by Tinker MM program. Percentage errors are given to compare fitted values and calculated $(r_{NN}+r_{OO})/2$.

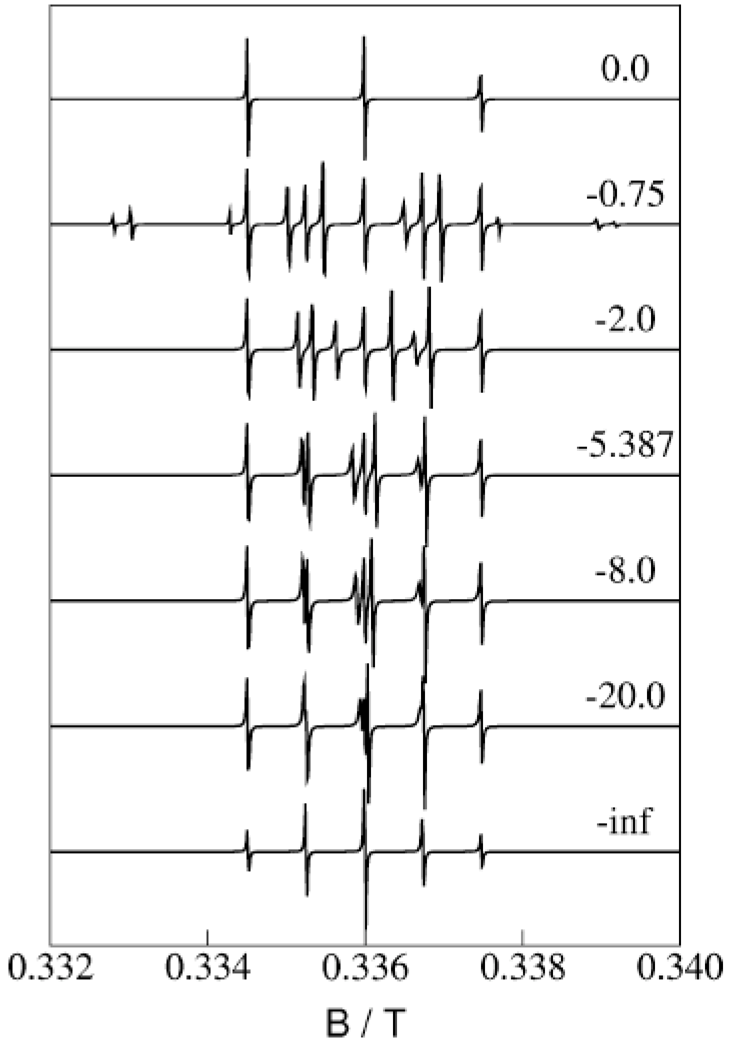

Figure 3-17: Variation of calculated ESR spectra (molecular geometry of isomer **1**) with respect to ratio J/a.

Conclusions

In this work, our main goal has been to show the potential usefulness of the stochastic Liouville approach in dealing with multi-probe systems by starting to analyse relative well-known, clearly defined chemical model systems. Our results are encouraging, since structural, energetic and dynamic parameters are promptly obtained by the SLE approach. Structural parameters are directly recovered in the form of inter-radicals distance.

Energy parameters, namely the exchange interaction constant J, are also evaluated. It is worth to mention that the fitted parameters include the exchange interaction constant J with its sign. For all the examined derivatives, the resulting signs coincide with those obtained

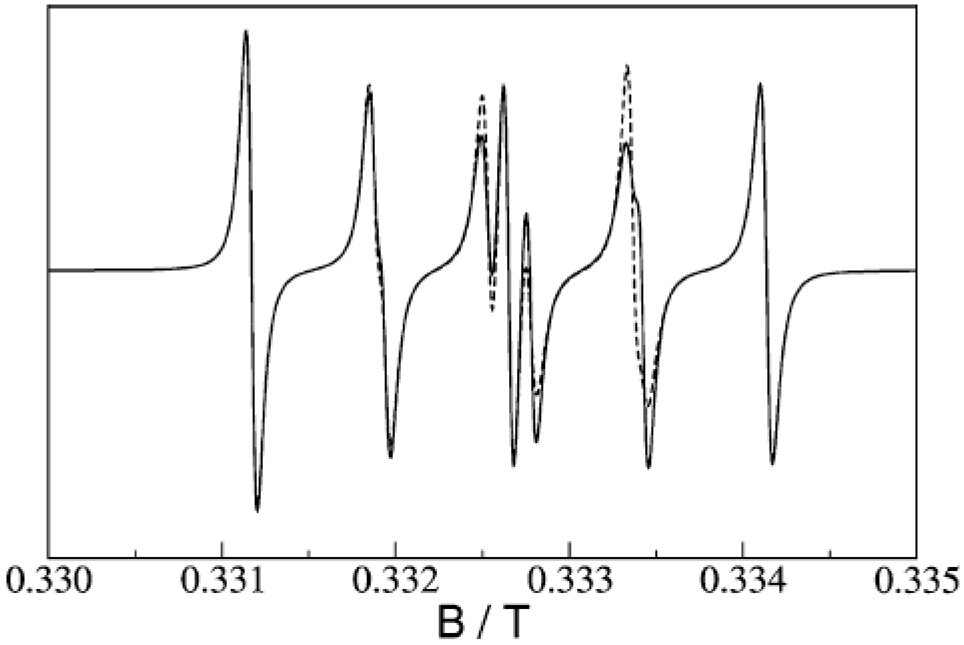

Figure 3-18: Variation of calculated ESR spectra with respect to the sign of J. Parameters for isomer **1** are considered, solid line (J/a = -5.387); opposite J sign, dashed line (J/a = +5.387).

by ENDOR spectroscopy [123]. This is worth to be pointed out since the sign of J does not influence the ESR line positions and its determination is not straightforward. However, for structural information it is important to take the sign into proper consideration, and any way to determine it is welcome, because the ENDOR technique is not always applicable. The dependence of the spectrum on the sign of J is shown in Figure 3-18. Finally, reasonable estimates of dynamic parameters, such as the rotation diffusion tensors, are directly obtained by the SLE solution, which is in accordance with the known molecular structure. Figure 3-19 shows the effect of altering the diffusion tensor values on the spectrum, moving away from the optimal set of parameters. The nice agreement between experimental and calculated spectra, verified for all biradicals in the examined series, confirms the idea that the described methodology can be applied with good confidence for investigating structural and dynamic properties of more complex systems, such as doubly labelled peptides and biopolymers. Of course, for such cases the model should be extended and modified. For a start, in the case of rigid systems of unknown structure, the necessary straightforward improvement consists in the inclusion among the fitting parameters of the angles specifying the nitroxide orientation relative to the diffusion tensor. For flexible systems the internal motions should be also

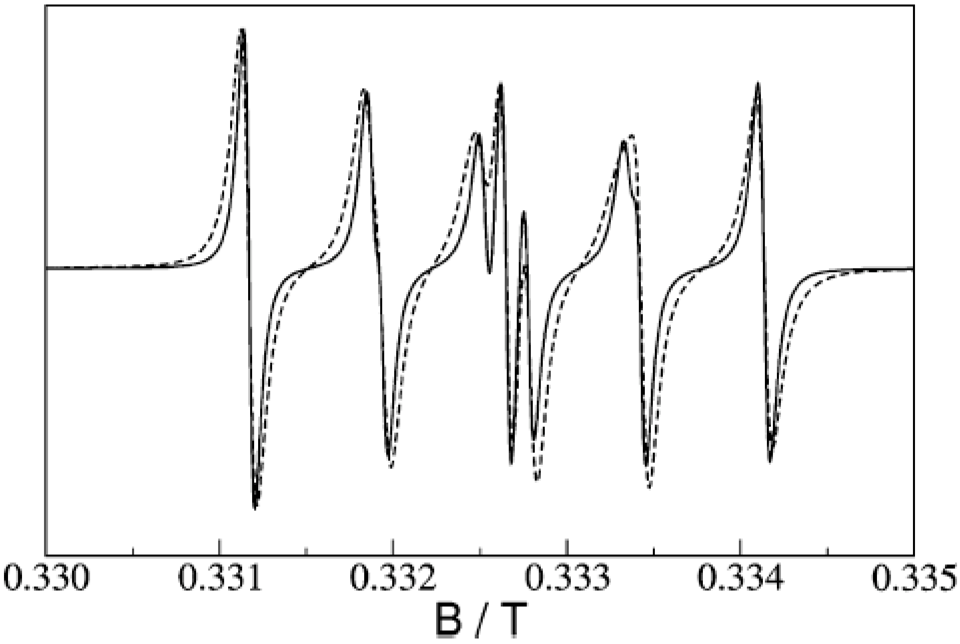

Figure 3-19: Variation of calculated ESR spectra with respect to diffusion. Parameters for isomer **1** are considered, solid line (values of $\boldsymbol{D}$ reported in Table 3.1); one-third of the values of $\boldsymbol{D}$, dashed line.

explicitly considered. Work in this direction require a careful definition of primary relaxation processes, i.e. motional contributions to the SLE, based on many-body stochastic formalism (e.g. N-body diffusive operators to allow the description of lateral and backbone motions).

3.3.2 On the interpretation of cw-ESR spectra of tempo-palmitate in 5-cyanobiphenyl

In this section we present the application of the ICA approach to the case of nematic liquid crystalline environments, by performing simulations of the ESR spectra of the prototypical nitroxide probe 4-(hexadecanoyloxy)-2,2,6,6-tetramethylpiperidine-1-oxy in isotropic and nematic phases of 5-cyanobiphenyl. We recall that the basic ingredients of the integrated approach are *i)* determination of geometric and local magnetic parameters by quantum mechanical calculations taking into account solvent and, when needed, vibrational averaging contributions; *ii)* numerical solution of the stochastic Liouville equation in the presence of diffusive rotational dynamics, based on *iii)* parametrization of diffusion rotational tensor provided by the hydrodynamic model discussed in Chapter 2. Next we shall present simulated spectra with minimal resorting to fitting procedures, proving that the combination of sensitive ESR spectroscopy and sophisticated modelling can be highly helpful in providing 3D-structural and dynamic information on molecular systems in anisotropic environments.

Introduction

Our main objective here is to apply integrated theoretical tools to the modelling of continuous wave electron spin resonance of a model system which combines two significant complications, namely the presence of internal dynamics, coupled with overall rotation and the effect of an anisotropic environment, i.e. a liquid crystalline nematic phase. These choices are meant to shed light on methodological aspects that will be needed to deal with complex macromolecular systems (proteins), and they are interesting *per se*, since they allow to extend the integrated computational approach to the case of flexible molecules and complex fluid environments.

Recent progresses were made by Ferrarini et al. [66, 67] in the introduction of internal dynamics of flexible spin probes, such as methanthiosulfonate (MTSSL), in the interpretation of cw-ESR spectra of spin labelled proteins. They assumed a jump model to treat transitions between probe conformations and made the hypothesis of fast dynamics. In this way they could obtain the conformational probability distribution for the internal dynamics, which is used to mediate the magnetic tensors that enter in the SLE.

Properties of liquid crystals as order parameters, dynamics and cage effects have been studied by several authors using ESR spectroscopy of dissolved spin probes and an SLE-based approach for interpretation. For instance, Sastry and co-workers [30, 130] studied two-dimensional Fourier transform (2D-FT) electron spin resonance (ESR) of the rigid rod-like cholestane (CSL) spin-label in the liquid crystal solvent butoxy benzylidene octylaniline (4O,8) and of the small globular spin probe perdeuterated tempone (PDT) in the same solvent. Experimental spectra are collected in a wide range of temperatures in such a way to include isotropic, nematic, smectic A and B and crystal phases of 4O,8. 2D-FT-ESR was chosen because it provides greatly enhanced sensitivity to rotational dynamics than cw-ESR analysis. For both the CSL and PDT spin probes, experimental spectra were interpreted via the Slowly Relaxing Local Structure (SRLS) model [32] in which dynamic of the system is described with two coupled relaxing processes which are interpreted as a fast global tumbling of the probe and a slow relaxation of the solvent cage collective motions. In [131] Zannoni and co-workers used the ESR spin-probe technique to study the changes in phase stability, orientational order and dynamics of the nematic 5-cyanobiphenyl (5CB) doped with different cis/trans *p*-azobenzene derivatives. CSL was again adopted as spin probe to monitor the order and the dynamics of the liquid crystal system, owing to its size, rigidity and rod-like shape analogous to that of the 5CB [132, 133]. In particular Zannoni et al. studied the variations induced by the 4-R-phenylazobenzenes on the order parameter $\langle P_2 \rangle$ and on the nematic-isotropic transition temperature T_{NI} of the 5CB, for different R (H, F, Br, CH_3, CF_3, O*n*-Bu, O*t*-Bu) and different mole fractions. Interpretation of the experimental spectra was carried out by simulations with the one body model implementation by Freed [134, 135, 136], by assuming the probe as a rigid rotator that reorients under the action of a potential of the type $-\epsilon \mathcal{D}^2_{0,0}(\boldsymbol{\Omega})$. A multicomponent fit procedure was employed to find the coefficient of the orienting potential, the diffusion tensor and an inhomogeneous line width. They found that only cis *p*-azobenzenes at high mole fraction have visible effects on the order parameter and on the transition temperature. Dynamics, instead, appears to be essentially independent of the nature, configuration and concentration of the different solutes and very similar to that observed in the pure 5CB. In [133] and [137] Zannoni and co-workers employed ESR spectroscopy to study, respectively, the effects of hydrophobic and hydrophilic aerosil nanoparticles on the order and dynamics of 5CB and the effects of hydrophobic aerosol nanoparticles on the order and dynamics of the nematic liquid crystal forming 4-*n*-octyl-4'-cyanobiphenyl (8CB). In the first case they used CSL as spin probe, while to study effects on 8CB they employed the 5-doxyl stearic acid probe. In both the works Zannoni et al. were interested in the changes of the order parameter of the liquid crystal and variations on the rotational dynamics of the probes. In the following we perform a complete *a priori* simulation of the ESR spectra of the prototypical nitroxide probe 4-(hexadecanoyloxy)-2,2,6,6-tetramethylpiperidine-1-oxy (usually referred to as Tempo-palmitate, TP), Figure 3-20, in isotropic and nematic phases

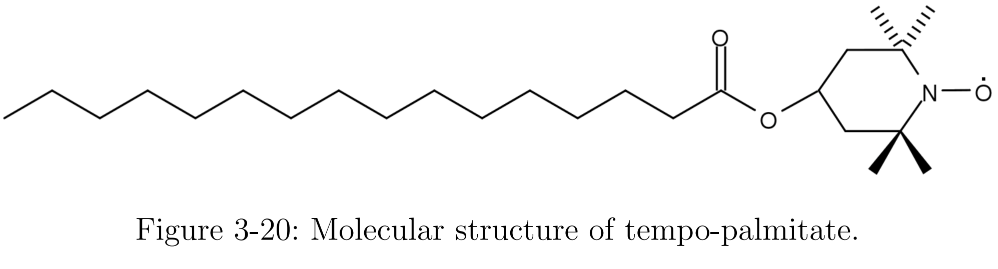

Figure 3-20: Molecular structure of tempo-palmitate.

of 5-cyanobiphenyl, for which detailed cw-ESR data are available in the literature [138]. We will show that our integrated approach provides remarkable results also in this more complex playground, provided that internal dynamics is taken into the proper account.

Method

We sketch here the principal points of the basic methodology described in Section 3.1.3. Simulation of the ESR spectra is based on the implementation of the stochastic Liouville equation (SLE) which was first applied to ESR by Freed, Moro, and other authors [16, 20, 21, 139]

$$\frac{\partial}{\partial t}\rho\left(\boldsymbol{Q},\, t\right) = -\hat{\mathcal{L}}\rho\left(\boldsymbol{Q},\, t\right) \tag{3.44}$$

describing the time evolution of the density matrix of the system, depending upon general stochastic coordinates $\boldsymbol{X}$, dynamically evolving under the action of the stochastic operator $\hat{\Gamma}$, and quantum coordinates $\boldsymbol{\sigma}$.

The magnetic Hamiltonian of the system includes the Zeeman and hyperfine interactions for the nitroxide probe

$$\hat{H}/\hbar = \frac{\beta_e}{\hbar}\boldsymbol{B}_0 \cdot \boldsymbol{g} \cdot \hat{\boldsymbol{S}} + \gamma_e \hat{\boldsymbol{I}} \cdot \boldsymbol{A} \cdot \hat{\boldsymbol{S}} \tag{3.45}$$

where β_e and γ_e are the Bohr magneton and gyromagnetic ratios; here the first term is the Zeeman interaction of the unpaired electron spin with magnetic field $\boldsymbol{B}_0$ depending on the $\boldsymbol{g}$ tensor; the second term is the hyperfine interaction ^{14}N / unpaired electron, defined with respect to hyperfine tensor $\boldsymbol{A}$. Here tensors $\boldsymbol{g}$ and $\boldsymbol{A}$ are diagonal in the same local frame rigidly fixed on the nitroxide fragment; spin operators are defined in the laboratory or inertial frame (see next Section). Notice that in general, several relaxation processes can be invoked, corresponding to different fast and slow degrees of freedom $\boldsymbol{X}$ subject to Brownian motions and described by many-body Fokker-Planck operators. In the next section we shall specialize our choice to the molecular system under investigation by choosing a form for the $\hat{\Gamma}$ operator and for the equilibrium probability $P_{eq}(\boldsymbol{X})$

The cw-ESR spectrum is obtained as the Fourier-Laplace transform of the correlation function for the X-component of the magnetization, defined as $|\, v\rangle\rangle = [I]^{-1/2} |\, \hat{S}_X \otimes \mathbf{1}_I\rangle\rangle$, where I is the nuclear spin. The cw-ESR signal is then defined as [16, 20]

$$I(\omega - \omega_0) = \frac{1}{\pi}\mathcal{R}e\left\{\langle\langle v\,|\left[i(\omega-\omega_0) + \hat{\mathcal{L}}\right]^{-1}|\, vP_{eq}\rangle\rangle\right\} \tag{3.46}$$

where ω is the sweep frequency, $\omega_0 = \beta_e B_0 Tr\{\boldsymbol{g}\}/3\hbar$. Here the double brackets $\langle\langle\ldots\rangle\rangle$ stand for integration on $\boldsymbol{X}$ and trace over spin states $\boldsymbol{\sigma}$. More conveniently, one usually adopts a symmetrized equivalent of the previous expression, given by

$$I(\omega-\omega_0) = \frac{1}{\pi}\mathcal{R}e\left\{\langle\langle vP_{eq}^{1/2}\,|\left[i(\omega-\omega_0)+\tilde{\mathcal{L}}\right]^{-1}|\,vP_{eq}^{1/2}\rangle\rangle\right\} \tag{3.47}$$

where $\tilde{\mathcal{L}} = i\hat{\mathcal{H}}^{\times} + \tilde{\Gamma}$ and $\tilde{\Gamma} = P_{eq}^{-1/2}\hat{\Gamma}P_{eq}^{1/2}$.

The spectrum is evaluated numerically by employing Lanczos algorithm [16, 20] assuming as a first vector the normalized zero-average observable, $|\,1\rangle\rangle = |\,vP_{eq}^{1/2}\rangle\rangle/\langle\langle v\,|P_{eq}|\,v\rangle\rangle$. Finally, the spectrum can be written in the form a continued fraction [20].

Model

According to Section 3.3.2, we need *i)* to define the molecular geometry and evaluate, via QM approaches, the structural and magnetic properties (magnetic tensors $\mathbf{g}$ and $\mathbf{A}$), *ii)* to identify the relevant set of stochastic coordinates which are next included explicitly in the SLE, *iii)* to estimate the system energetics, i.e. to define the dependence of the internal potential energy upon geometrical variations, *iv)* to evaluate the diffusion tensor $\boldsymbol{D}$ for the joint dynamics described by relevant set of coordinates. In the present case, the system is described as a flexible body re-orienting under the influence of an external field, which favours the orientation along the nematic director, which is assumed parallel to the external magnetic field along the Z-axis of the inertial laboratory frame (LF). Due to the intrinsic complexity of the system, we shall adopt a number of simplifying hypotheses, aimed at keeping the required computational effort at a reasonable level. The molecule is considered as split into two fragments, the alkyl chain and the paramagnetic probe (Tempo). Geometry and dynamics are described by two stochastic variables, as can be seen in Figure 3-21: *i)* the set of Euler angles ($\boldsymbol{\Omega}$) which describes the orientation between the LF and a molecule fixed frame (MF), and *ii)* an internal angle (θ) which defines the relative orientation between the Tempo fragment and the alkyl chain. Structural properties were obtained by means of quantum mechanical calculations, performed to find the minimum energy geometry of the molecule, evaluate the magnetic tensors and calculate the internal potential [38]. On the ground of a previous study [140], the alkyl chain of TP was replaced by an ethyl group. Internal torsional potentials and magnetic tensors were then evaluated by the PBE0 hybrid

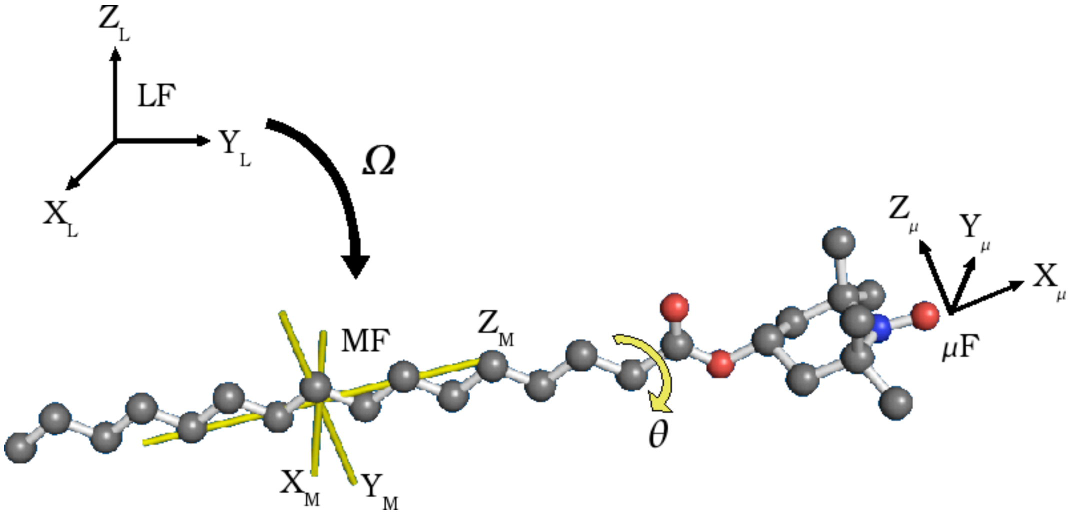

Figure 3-21: Relevant stochastic coordinates.

functional [141] and the purposely tailored N06 basis set. Solvent effects were taken into account by our anisotropic version of the polarizable continuum model [140]. Of course, the diffusion tensor was evaluated for the true TP radical using the geometry optimized for the all-trans conformer. The MF is fixed on the alkyl chain, which is considered as a rigid entity in all-trans conformation; the MF is chosen in such a way that the rotational part of the diffusion tensor (see below) is diagonal. Magnetic tensors are diagonal in the same reference frame (μF) fixed on paramagnetic probe, as shown in Figure 3-21.

The total potential energy of the system is defined according to the following expression

$$V\left(\boldsymbol{X}\right) = V_{\text{ext}}\left(\boldsymbol{\Omega}\right) + V_{\text{int}}\left(\theta\right) + V_{\text{coup}}\left(\boldsymbol{\Omega},\theta\right) \approx V_{\text{ext}}\left(\boldsymbol{\Omega}\right) + V_{\text{int}}\left(\theta\right) \tag{3.48}$$

i.e. we neglect potential coupling terms $V_{\text{coup}}\left(\boldsymbol{\Omega},\theta\right)$ between internal (θ) and external variables ($\boldsymbol{\Omega}$). A complete factorization of the distribution probability ensues from this choice, $P_{\text{eq}}\left(\boldsymbol{X}\right) \approx P_{\text{eq}}\left(\boldsymbol{\Omega}\right) P_{\text{eq}}\left(\theta\right)$, where $P_{\text{eq}}\left(\boldsymbol{\Omega}\right)$ and $P_{\text{eq}}\left(\theta\right)$ are the Boltzmann distributions with respect to $V_{\text{ext}}\left(\boldsymbol{\Omega}\right)$ and $V_{\text{int}}\left(\theta\right)$. The external potential is chosen according to a simple Maier-Saupe form [142, 143, 144]

$$U_{\text{ext}} = V_{\text{ext}}/k_B T = -\epsilon \mathcal{D}^2_{0,0}\left(\boldsymbol{\Omega}\right) \tag{3.49}$$

This is the simplest potential which assures the presence of an energy minimum when the alkyl chain is parallel to the nematic director.

An accurate evaluation of the internal potential is obtained directly by QM calculations. An energetic barrier is observed in correspondence of $\theta = 180°$. In general we may define the potential via the expansion $V_{\text{int}}/k_B T = -\sum \chi_n \, e^{-in\theta}$, where $\chi_n = \chi^*_{-n}$ is assumed to ensure that the potential is real. In practice terms up to $n = 1$ have been retained to fit the potential to the shifted cosine form

$$U_{\text{int}} = V_{\text{int}}/k_B T \approx A(1 - \cos\theta) \tag{3.50}$$

To summarize, energetics is defined by the following simplified expression

$$U = U_{\text{ext}} + U_{\text{int}} = -\epsilon \mathcal{D}^2_{0,0}(\boldsymbol{\Omega}) + A(1 - \cos\theta) \tag{3.51}$$

defined by parameters ϵ and A.

In the case under investigations, which includes, nematic (anisotropic) phase environments, we shall assume the usual approximation of considering isotropic local friction, and the macroscopic local viscosity is taken equal to half of the fourth Leslie-Ericksen coefficient η_4 [145, 146, 147, 148]. The diffusion tensor of the system is obtained, neglecting translational contributions, as a 4×4 matrix, i.e.

$$\boldsymbol{D} = \begin{bmatrix} \boldsymbol{D}_{RR} & \boldsymbol{D}_{RI} \\ \boldsymbol{D}_{IR} & D_{II} \end{bmatrix} \tag{3.52}$$

where the 3×3 $\boldsymbol{D}_{RR}$ block is the purely rotational contribution, the $\boldsymbol{D}_{IR} = \boldsymbol{D}^{\text{tr}}_{RI}$ blocks describe the roto-conformational interaction and D_{II} is the conformational diffusion coefficient. The general outcome of the elements of the 4×4 diffusion tensor shows, as expected a weak dependence upon the internal angles. We express the tensor as

$$\boldsymbol{D}(T) = D(T)\overline{\boldsymbol{d}} \tag{3.53}$$

in order to separate the purely geometrical tensorial component $\overline{\boldsymbol{d}}$ and the translational diffusion coefficient for an isolated sphere $D(T)$, i.e. $D(T) = k_B T / CR\pi\eta(T)$: here C is a constant depending on hydrodynamic boundary conditions, R is the average radius for the spheres, η is the local viscosity.

Selected tensor functions of the diffusion tensor, namely $Tr\{\boldsymbol{D}_{RR}\}$, $|\boldsymbol{D}_{RI}|$ and D_{II} are shown for $T = 316.92$ K in Figure 3-22 as function of θ: variation is indeed minimal, therefore we assume the diffusion tensor calculated for the minimum energy configuration ($\theta = 0$). A summary of the physical parameters and calculated coefficients is discussed in the next Section. As it can be seen in Figure 3-21, we chose the alkyl chain as the main fragment for

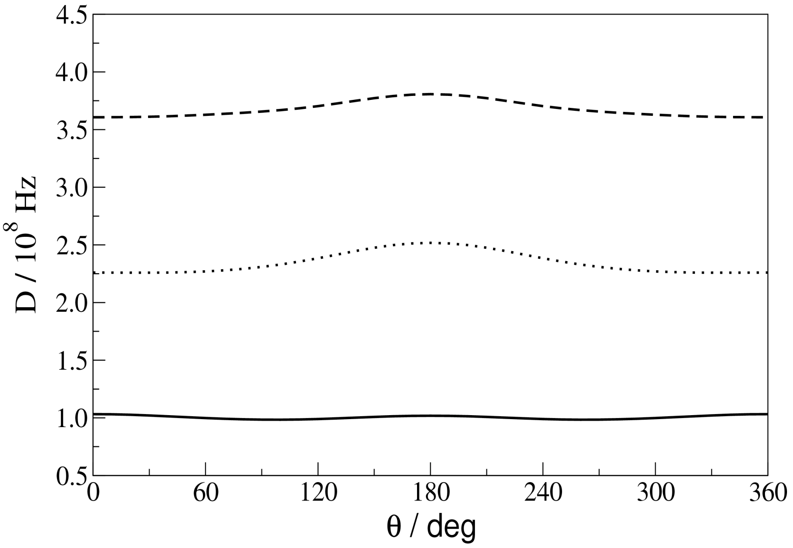

Figure 3-22: Values of Tr$\boldsymbol{D}_{RR} \times 10^{-7}$s (full line), $|\boldsymbol{D}_{RI}| \times 10^{-7}$s (dashed line) and $D_{II} \times 10^{-7}$s (dotted line) are shown for $T = 316.09$ K plotted vs. the conformation angle θ.

localizing the MF. The orientation of MF is such that the rotational part of the diffusion tensor is diagonal and practically the Z-axis of MF lies along the alkyl chain. This allows us to define the simple form (3.49) for U_{ext} without the need of introduction of tilt angles. Next we need to define the form of the time evolution operator (Liouvillean) for the density matrix described by the SLE. Before doing that, we wish to summarize and clarify the various reference frames explicitly employed to define the model, sketched in Figure 3-23. The molecule being partitioned in two fragments, as described above, we have *i)* two local frames respectively fixed on the palmitate chain (CF) and on the tempo probe (PB): these are chosen with their respective z-axes directed along the rotating bond, for convenience; *ii)* the molecular frame (MF), fixed on the palmitate chain: this is the frame which diagonalizes the rotational part of the diffusion tensor $\boldsymbol{D}_{RR}$; the magnetic frame, fixed on the probe (μF) where magnetic tensors are diagonal. Several set of Euler angles are defined: $\boldsymbol{\Omega}_{MC}$ is the set of Euler angles that transforms MF to CF, which has the z-axis parallel to the rotating bond, $\boldsymbol{\Omega}_{\mu}$ is the set of Euler angles that transforms from PF to μF; the set $(0, 0, \theta)$ is the rotation from CF to PF; finally $\boldsymbol{\Omega}$ transforms from the laboratory frame LF to MF. Following the estabilished methodology [16, 20, 21, 139] the general form of the spin super-Hamiltonian is cast in the contracted tensorial form

$$\hat{H}^{\times} = \sum_{\mu} \omega_{\mu} \sum_{l=0,2} \sum_{m=-l}^{l} F_{\mu,LF}^{(l,m)\,*} \hat{A}_{\mu,LF}^{(l,m)\,\times} \tag{3.54}$$

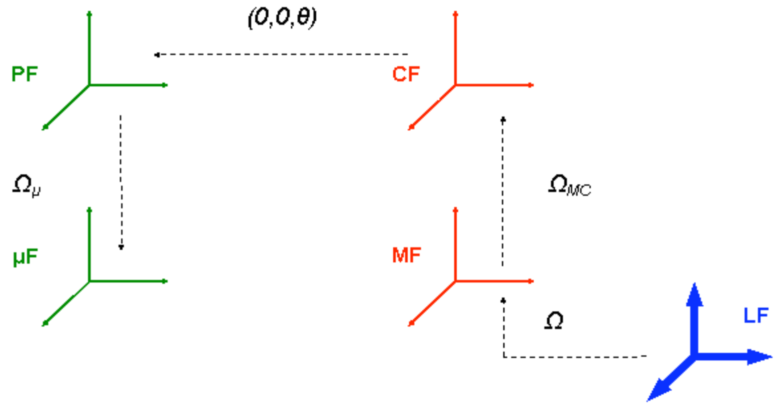

Figure 3-23: Molecular frames and Euler angle sets employed in the model.

where $\mu = g, A$ runs over the magnetic interactions, i.e. the Zeeman interaction between the electron and the external field (g) and the hyperfine interaction between the electron and the ^{14}N nucleus (A). Parameters ω_μ, with $\mu = g, A$ are defined as $\beta_e B_0 \mathrm{Tr}\boldsymbol{g}/3\hbar$ and $\gamma_e \mathrm{Tr}\boldsymbol{A}/3$ respectively. Notice that for the generic irreducible spherical tensor F one can write

$$F_{\mu,LF}^{(l,m)\,*} = \sum_{m',m''} \mathcal{D}^l_{m,m'}(\boldsymbol{\Omega})\, e^{-im''\theta} G_\mu^{(l,m',m'')} \tag{3.55}$$

with

$$G_\mu^{(l,m,m')} = \mathcal{D}^l_{m,m'}(\boldsymbol{\Omega}_{MC}) \sum_{m''} \mathcal{D}^l_{m',m''}(\boldsymbol{\Omega}_\mu)\, F_{\mu,\mu F}^{(l,m'')\,*} \tag{3.56}$$

Explicit forms for $F_{\mu,\mu F}^{(l,m)\,*}$ and superoperators $\hat{A}_{\mu,LF}^{(l,m)\,\times}$ are provided in the literature [21]. We turn now to define the form of the diffusion operator. In a symmetrized form we write

$$\tilde{\Gamma} = -P_{eq}^{-1/2} \begin{pmatrix} \hat{\boldsymbol{M}} \\ \dfrac{\partial}{\partial\theta} \end{pmatrix}^{\mathrm{tr}} \mathbf{D} P_{eq} \begin{pmatrix} \hat{\boldsymbol{M}} \\ \dfrac{\partial}{\partial\theta} \end{pmatrix} P_{eq}^{-1/2} = \tilde{\Gamma}_{RR} + \tilde{\Gamma}_{II} + \tilde{\Gamma}_{RI} \tag{3.57}$$

where $\tilde{\Gamma}$ acts on $\boldsymbol{X} = (\boldsymbol{\Omega}, \theta)$, the set of relevant variables; $\hat{\boldsymbol{M}}$ is the infinitesimal rotation operator. Finally, for the explicit evaluation of matrix elements, it is convenient to define

$$\begin{aligned} \tilde{\Gamma}_{RR} &= -P_{eq}^{-1/2} \hat{\boldsymbol{M}}^{\mathrm{tr}} \boldsymbol{D}_{RR} P_{eq} \hat{\boldsymbol{M}} P_{eq}^{-1/2} \\ \tilde{\Gamma}_{II} &= -D_{II} P_{eq}^{-1/2} \frac{\partial}{\partial\theta} P_{eq} \frac{\partial}{\partial\theta} P_{eq}^{-1/2} \\ \tilde{\Gamma}_{RI} &= -P_{eq}^{-1/2} \left(\hat{\boldsymbol{M}}^{\mathrm{tr}} \boldsymbol{D}_{RI} P_{eq} \frac{\partial}{\partial\theta} + \frac{\partial}{\partial\theta} \boldsymbol{D}_{IR} P_{eq} \hat{\boldsymbol{M}} \right) P_{eq}^{-1/2} \end{aligned} \tag{3.58}$$

The detailed form of the rotational, internal and rotational-internal operators is reported in Appendix E.2. Although rather cumbersome, the whole algebraic derivation is straightforward.

Results

The numerical solution is based on the standard methodology [16, 20, 139], by projecting the symmetrized time evolution operator and the starting vector on a suitable basis set that is defined as $|\Sigma\rangle\rangle = |p^S q^S p^I q^I\rangle\rangle \otimes |\Lambda\rangle$. The basis is given by the direct product of spin operators of the nitroxide and defined by electron and nuclear spin quantum numbers p^S, q^S, p^I, q^I [21], and of a complete, usually orthonormal for sake of simplicity, basis set in the $\boldsymbol{X}$ space, which is indicated here generically by

$$|\Lambda\rangle = |LMK, n\rangle = |LMK\rangle \times |n\rangle \tag{3.59}$$

where

$$\begin{aligned} |LMK\rangle &= \sqrt{\frac{[L]}{8\pi^2}}\mathcal{D}^L_{M,K}(\boldsymbol{\Omega}) && (3.60) \\ |n\rangle &= \frac{1}{\sqrt{2\pi}}e^{-in\theta} && (3.61) \end{aligned}$$

One needs to define the matrix operator and starting vector elements, $L_{\Sigma,\Sigma'} = \langle\langle\Sigma|\hat{\boldsymbol{\mathcal{L}}}|\Sigma'\rangle\rangle$ and $v_\Sigma = \langle\langle\Sigma|1\rangle\rangle$. Implementation of the Lanczos scheme, cfr. Section (3.1.3), follows along the lines presented for instance in [20]. Symmetry arguments can be employed to significantly reduce the number of basis function sets required to achieve convergence, together with numerical selection of a reduced basis set of functions based on "pruning" of basis elements with negligible contribution to the spectrum. A symmetrized basis set convenient for our systems is defined in Appendix E.2. In all the cases treated in this work, matrices of dimensions of order 10^4-10^5 before pruning have been treated, while after pruning dimensions of order 10^3 are usually found.

Let us first report the calculated set of parameters, obtained from the QM calculations for structural and magnetic properties and the hydrodynamic modelling for diffusion properties. The principal values of the magnetic tensors minus the isotropic part are $g_{xx} = 0.00221$, $g_{yy} = 0.00020$, $g_{zz} = -0.00240$, $A_{xx} = -9.19$ Gauss, $A_{yy} = -8.98$ Gauss and $A_{zz} = 18.18$

T / K	A_{iso} / Gauss	g_{iso}	ϵ	η / mPa s
316.09	15.5	2.00615	0.0	18.89
309.03	15.5	2.00629	0.0	23.80
308.72	15.7	2.00659	0.0	25.78
307.88	14.7	2.00679	0.9	26.80
299.02	13.5	2.00706	1.0	31.70

Table 3.3: Parameters employed in the simulations.

Gauss. Orientation of internal frames of references are specified by angles $\boldsymbol{\Omega_{MC}} = (90, 35, 0)$ degrees and $\boldsymbol{\Omega_{\mu}} = (0, 55, 180)$ degrees. The isotropic values of hyperfine and gyromagnetic tensors are significantly different for different phases and are taken from experiment (see Table 3.3). A comparison with QM computed values is discussed in the next section. The computed torsional barrier of 1.8 kcal/mol for the θ angle leads to a potential (adimensional) parameter $A = 453$ K/T. The diffusion tensor is expressed by eq. (3.53) with

$$\overline{\boldsymbol{d}} = \begin{pmatrix} 2.387 \cdot 10^{-3} & 0.0 & 0.0 & 1.560 \cdot 10^{-2} \\ 0.0 & 2.989 \cdot 10^{-3} & 0.0 & 1.313 \cdot 10^{-2} \\ 0.0 & 0.0 & 4.513 \cdot 10^{-2} & -3.071 \cdot 10^{-2} \\ 1.560 \cdot 10^{-2} & 1.313 \cdot 10^{-2} & -3.071 \cdot 10^{-2} & 5.884 \cdot 10^{-2} \end{pmatrix} \text{Å}^2 \tag{3.62}$$

and $D(T) = D(T_0)\dfrac{\eta(T_0)}{\eta(T)}\dfrac{T}{T_0}$, where $D(T_0)$ is the translational diffusion coefficient for a sphere of radius R at reference temperature T_0 given by $D(T_0) = \dfrac{k_B}{RC\pi}\dfrac{T_0}{\eta(T_0)}$. Choosing $R = 2.0$ Å, $C = 6$, $T_0 = 316.92$ K (as reference temperature) and $\eta(T_0) = 18.89 \cdot 10^{-3}$ Pa s one gets $D(T_0) = 6.12 \cdot 10^9$ Hz.

We can now simulate the cw-ESR spectra of the tempo-palmitate in 5-cyanobiphenyl in the range of temperatures from 316.92 K (isotropic phase) to 299.02 K (nematic phase). In Figure 3-24 five simulated spectra are reported, superimposed to experimental spectra taken from the literature [138].

Discussion

The results of the previous section show that our integrated approach to cw-ESR spectra performs a remarkable job also in the quite demanding playground represented by large nitroxides in nematic phases. In particular, the spectra at different temperatures and in

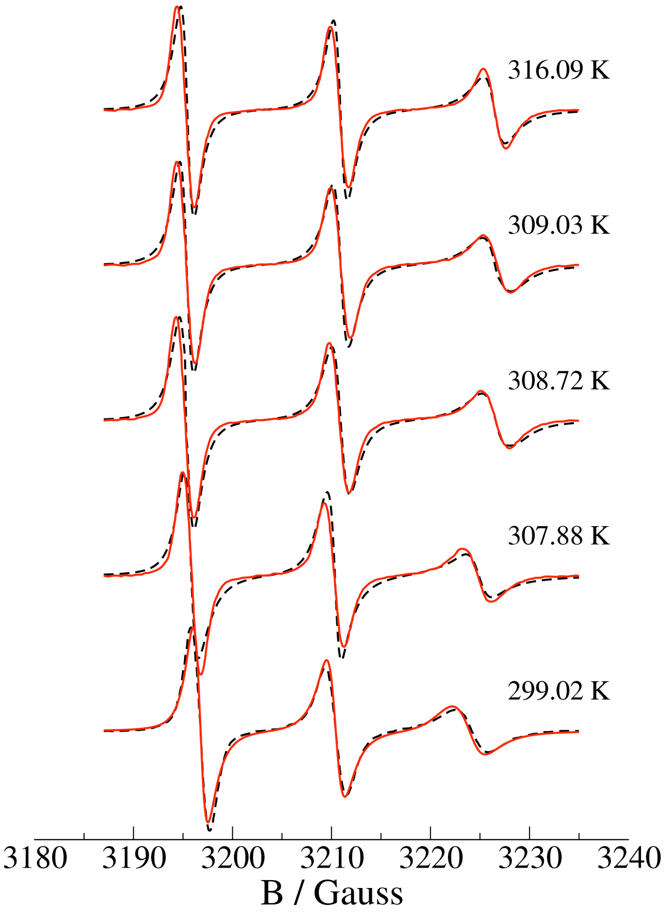

Figure 3-24: Experimental (full line) and simulated (dashed line) cw-ESR spectra of tempo-palmitate in 5-cianobiphenyl at 316.09, 309.03 K (isotropic phase), 308.72 K (isotropic-nematic transition), 307.88, 299.02 K (nematic phase).

different phases are reproduced with a very limited number of fitting parameters (ordering potential and isotropic parts of magnetic tensors), which could be possibly replaced by *a* priori computations in the near future. As a matter of fact, the computed value for the isotropic hyperfine splitting (15.3 G) nicely fits the experimental value in the isotropic phase. However, at lower temperature local effects come into play which cannot be reproduced by the continuum solvent model employed in our computations. Explicit dynamic simulations would be necessary to investigate the details of probe - solvent interactions, but they are out of the scope of the present work. In any case, already reduction of the number of fitting parameters, and definition of a limited range of variation represents, in our opinion, a remarkable result of QM computations. From another point of view, our results unequivocally show that a rigid model of the probe is not sufficient to reproduce experimental spectra

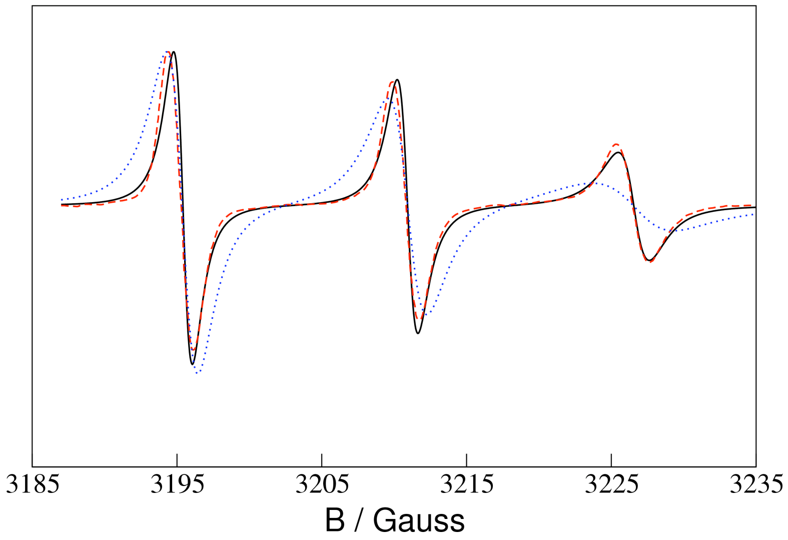

Figure 3-25: Experimental (full line) and simulated with internal dynamics (dashed line) and without internal dynamics (dotted line) cw-ESR spectra of tempo - palmitate in 5 - cianobiphenyl at 316.09 K.

and that, at least a moderately accurate description of internal dynamics is needed. The necessity of introducing an explicit description, albeit approximate, of the most important internal degrees of freedom is evidenced in Figure 3-25, where simulations with and without explicit description of internal dynamics are compared with the experimental spectra at a given temperature. Exclusion of other internal degrees of freedom was based on the analysis of QM calculated torsional potentials. The internal rotation shown in Figure 3-21 is the only (of the explored torsions) that present a barrier in the motion for which rotation is possible in the temperature range taken into account. Alternative treatments can be based on lattice description of the internal chain approximately coupled to overall molecular rotations; our approach has been, instead, based on the idea that relevant effects on the physical observable are mainly the consequence of a unique internal degree of freedom, described according to a fully off-lattice approach, exactly coupled with overall rotation. In summary, our results show that we have at our disposal a general computational tool for the *a priori* description of cw-ESR spectra of complex systems in different phases allowing the extension of magneto-structural relationships to different dynamical regimes.

3.3.3 Modeling of cw-ESR spectra p - (methyl - thio) phenyl - nitronyl - nitroxide in toluene

We discuss the interpretation, via our *ab initio* integrated computational approach, of continuous wave electron spin resonance (cw-ESR) spectra of p-(methyl-thio) phenyl-nitronyl-nitroxide (MTPNN) dissolved in toluene. In this case it is important to introduce averaging with respect to fast vibrational motions of magnetic tensor parameters (Zeeman and hyperfine tensors) in order to reproduce the experimental values and so the spectra. The stochastic Liouville equation is completed with inclusion of diffusive rotational dynamics by describing the molecule as a free Brownian rotator. Cw-ESR spectra of MTPNN are simulated for a wide range of temperatures (155-292 K) with minimal resorting to fitting procedures.

Introduction

ESR spectroscopy is an essential tool in material science. In particular, the search of new materials with tailored magnetic properties has intensified in recent years. In this field the most popular stable radicals are nitronyl nitroxide (NIT) free radicals. They exhibit a large variety of magnetic behaviour: paramagnetism down to very low temperature, ferromagnetism, antiferromagnetism [2]. Moreover, the nitronyl nitroxides have also been known as bidentate ligands for various transition and rare-earth metal ions. Ferromagnetic ground states have been observed also in these complexes [3, 4, 149, 150, 151]. For these particular magnetic properties NIT radicals are particularly appealing as molecular units for composite new materials. One of the driving forces of the present work was the demand for simulations of ESR spectra of NIT in any régime of motion, not available up today.

In the path towards new magnetic materials, the characterization of the electronic distributions and magnetic properties of isolated radicals is of primary interest. Theoretical predictions of the spin distribution on the radicals by DFT calculations are necessary in order to understand the radical-radical interactions in bulk and composite materials. On the other hand, the spin density depends strongly on the interaction with the environment that can be very complex in a composite material.

Here, we will show that for a prototypical nitronyl nitroxide radical (p-(methylthio)-phenyl-nitronyl-nitroxide, hereafter MTPNN) [152] in a simple environment as a toluene solution, starting simply from the formula of the radical and the physical parameters of the solvent, it is possible to calculate ESR spectra showing afterwards an exceptionally good agreement with the experimental ones, from room temperature to a temperature very near to the glassy transition.

Modeling and interpretation

Commonly employed paramagnetic probes in ESR studies are nitroxide derivatives, which have been extensively used for characterization of structural and dynamic behaviour of isotropic and ordered phases and complex molecular systems [21, 32, 107, 139, 153], with particular accent on biological macromolecules [115, 116, 153, 154]. They are widely employed in cw-ESR, pulsed ESR or ENDOR spectra. As probes or spin labels they are employed extensively to obtain information on structural and dynamic properties of biomolecules, micelles, and membranes [153]. In particular, measurements performed on proteins via site directed spin labelling (SDSL) are highly informative [115, 116, 154]. They are well characterized systems, both in terms of magnetic properties ($\boldsymbol{A}$ and $\boldsymbol{g}$ tensors) and dynamical properties (rotational diffusion). The development of simulation programs of their cw-ESR spectra in presence of several relaxation processes due to motions in different dynamical ranges (see for example the slowly relaxing local structure model, SRLS) has led to a number of applications in liquids, liquid crystalline phases, composite materials, and biological systems [21, 32, 107, 139, 153].

On the other side, the employment of NIT radicals in cw-ESR experiments is relatively recent, and it appears to be of relevance for their significant stability, and variety of magnetic behaviour, mostly in the context of materials science. NIT free radicals are particularly appealing as molecular units for composite new materials, and ESR is the tool of election to monitor structural and dynamic characteristics. However, the presence of the coupling of the unpaired electron with two nitrogen nuclei makes this probe different from nitroxides, and specific simulation programs of ESR spectra of NIT in any régime of motion are not available up today. They are approached in this work for the first time.

We shall consider p-(methyl-thio)-phenyl-nitroxyl-nitroxide (MTPNN) as a prototype NIT radical. A schematic overview of the molecule is shown in Figure 3-26, which illustrates the chemical structure of the paramagnetic probe stressing the coupling of the unpaired elec-

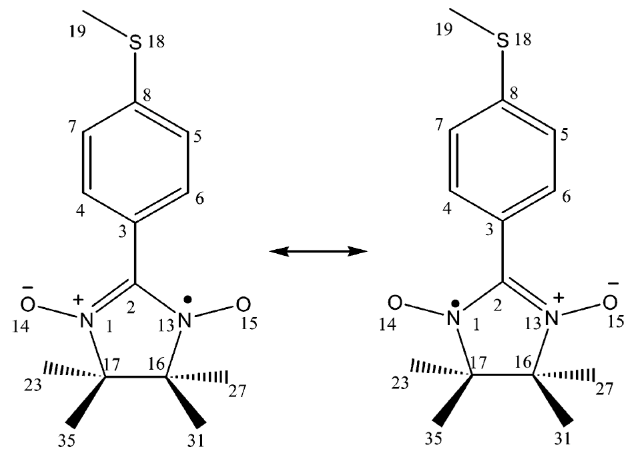

Figure 3-26: Structure of p-(methylthio)phenyl nitronylnitroxide (MTPNN).

tron with two ^{14}N. The molecule is characterized by a nitroxylnitroxide group linked to a methyl-thio-phenyl group.

In the case of MTPNN, we adopt the following hypotheses. We neglect explicit coupling with nuclei other than ^{14}N and we consider a planar geometry for the molecule. This is equivalent, in many cases, to renounce to describe accurately any super-hyperfine structure or inhomogeneous broadening in the spectra resulting from coupling with hydrogen nuclei. Estimates of inhomogeneous broadening line-widths can be obtained from calculated values of $\boldsymbol{A}_n$ tensors.

Although at least two relevant internal degrees of freedom i.e. dihedral angles can be identified, between the CH$_3$S- group and the phenyl ring and between the two rings; the former motion affects very slightly the magnetic parameters, and therefore it can be neglected, while we may assume that the second angle is affected by localized librations around the planar conformation (see next section). To simplify our methodology we shall not consider explicitly the coupling with this relatively soft degree of freedom which will be addressed elsewhere [155]. The final set of stochastic relevant coordinates is therefore restricted to the set of orientational coordinates $\boldsymbol{\Omega}$; these are described in terms of a simple formulation for a diffusive rotator, characterized by a diffusion tensor $\boldsymbol{D}$. The diffusion tensor is determined by the shape of the molecule, deriving from the minimum energy conformations obtained from the QM calculations. Our choice is formalized by adopting the following simple form for $\hat{\Gamma}$ [155]

$$\hat{\Gamma} = \hat{\boldsymbol{J}}^{tr}(\boldsymbol{\Omega})\,\boldsymbol{D}\hat{\boldsymbol{J}}(\boldsymbol{\Omega}) \tag{3.63}$$

where $\hat{\boldsymbol{J}}(\boldsymbol{\Omega})$ is the angular momentum operator for body rotation [156, 157, 158]. The Boltzmann distribution (equilibrium solution) is simply $P_{eq} = 1/8\pi^2$. By defining $\hat{\boldsymbol{J}}(\boldsymbol{\Omega})$ and $\boldsymbol{D}$ in the molecule-fixed frame where the diffusion tensor is diagonal (molecular frame, MF), a convenient form of eq. (3.63) is obtained which is directly written in terms of the diffusion tensor principal values.

Then we need to write the specific form of the spin Hamiltonian of the molecule. By taking into account only the electron Zeeman and the hyperfine interactions with ^{14}N nuclei, we can define

$$\hat{\mathcal{H}}/\hbar = \frac{\beta_e}{\hbar}\boldsymbol{B}_0\boldsymbol{g}\hat{\boldsymbol{S}} + \gamma_e\sum_{n=1}^{2}\hat{\boldsymbol{I}}_n\boldsymbol{A}_n\hat{\boldsymbol{S}} \tag{3.64}$$

The first term is the Zeeman interaction depending upon the $\boldsymbol{g}$ tensor, external magnetic field $\boldsymbol{B}_0$ and electron spin momentum operator $\hat{\boldsymbol{S}}$; the second term is the hyperfine interaction of the n-th ^{14}N nucleus and the unpaired electron, defined with respect to hyperfine tensor $\boldsymbol{A}_n$ and nuclear spin momentum operator $\hat{\boldsymbol{I}}_n$.

We can summarize the ICA applied to MTPNN as follows. Modelling based on the SLE approach requires the characterization of magnetic parameters (e.g. hyperfine for ^{14}N nuclei and Zeeman tensors). Integration among *i)* evaluation of magnetic tensor parameters via QM calculation, with corrections based on averaging of fast motions, *ii)* explicit modelling of slow motional processes via stochastic treatment and *iii)* evaluation of ESR spectra via SLE is the basic strategy behind a sound *ab initio* approach to interpretation of ESR data. Once the effective Liouvillean is defined, the direct calculation of the cw-ESR signal is possible without resorting to a complete solution of the SLE. Rather one can evaluate the spectral density from the expression [16, 20, 21]

$$I\left(\omega-\omega_0\right) = \frac{1}{\pi}\mathcal{R}e\left\{\langle\langle v\,|\left[i\left(\omega-\omega_0\right)+i\hat{\boldsymbol{\mathcal{L}}}\right]^{-1}|\,vP_{eq}\rangle\rangle\right\} \tag{3.65}$$

where the Liouvillean $\hat{\boldsymbol{\mathcal{L}}}$ acts on a starting vector which is defined as proportional to the X-component of the electron spin operator $\hat{S}_X$: in the present case one has $|\,vP_{eq}^{1/2}\rangle\rangle = \sqrt{(2I_1+1)(2I_2+2)}|\,\hat{S}_X\otimes\mathbf{1}_{I_1}\otimes\mathbf{1}_{I_2}\otimes P_{eq}^{1/2}\rangle\rangle$, where $I_1 = I_2 = 1$ in this case; here P_{eq} is the Boltzmann distribution in $\boldsymbol{\Omega}$-space, ω is the sweep frequency and $\omega_0 = g_0\beta_e B_0/\hbar$, where $g_0 = Tr\{\boldsymbol{g}\}/3$. Basic parameters for the direct evaluation of eq. (3.65) are therefore the following: principal values and orientation of hyperfine tensor for the two ^{14}N nuclei $\boldsymbol{A}_1$ and $\boldsymbol{A}_2$; principal values and orientation of Zeeman tensor $\boldsymbol{g}$; finally the knowledge of the rotational diffusion tensor $\boldsymbol{D}$ is required, for the specific solvent (toluene).

The system geometry is summarized in Figure 3-27. A set of Euler angles $\boldsymbol{\Omega}$ defines the relative orientation of a molecular frame (MF), fixed rigidly on the nitroxide ring, with respect to the LF; the local magnetic frames are in turn defined with respect to MF by proper sets of Euler angles.

Evaluation of structural parameters and magnetic tensors

All the computations have been performed by the G03 package [53] using the parameter-free PBE0 functional [141] and the 6-31+G(d,p) basis set [159]. Solvent effects on energies and magnetic tensors have been evaluated by the latest implementation of the so-called polarizable continuum model (PCM) [97, 100, 160]. This computational approach has been validated in a number of studies of magnetic properties of free radicals in non-protic solvents [103, 161, 162].

A full geometry optimization of MTPNN in the gas-phase leads to a nearly planar arrangement in which all the structural parameters are close to those reported in a previous study for related nitronylnitroxides [163, 164], except for a slight non planarity of the nitronyl-nitroxide ring, related to the steric hindrance of the four methyl groups. Since the general agreement with available experimental data [152] is satisfactory and no unexpected trends are found, we do not discuss in detail structural aspects. Then, a relaxed scan around the C7-C8-S18-C19 dihedral angle (Figure 3-26) results into a quite small energy barrier for the perpendicular orientation of the ring and the methyl group (about 2 kcal/mol in gas phase). In any case, the dependence of magnetic tensors on this dihedral angle is completely negligible. The situation is more involved for the N1-C2-C3-C4 dihedral angle (hereafter τ, which has an energy minimum for $\tau \approx 0°$ and a significant barrier for $\tau \approx 90°$ (about 7 and 5 kcal/mol in gas-phase and toluene, respectively). At the same time, the magnetic tensors show a significant dependence on this dihedral angle. For purposes of illustration the trend of the isotropic parts of hyperfine and $\boldsymbol{g}$ tensors are shown in Figures 3-28 and 3-29, respectively. It is noteworthy that the variation of $\boldsymbol{g}$ is dominated by its g_{XX} component directed along the N-O bond.

In view of the very low polarity of toluene we expect quite small solvent effects for both $\boldsymbol{g}$ and hyperfine tensors and this expectation is confirmed by explicit PCM computations,

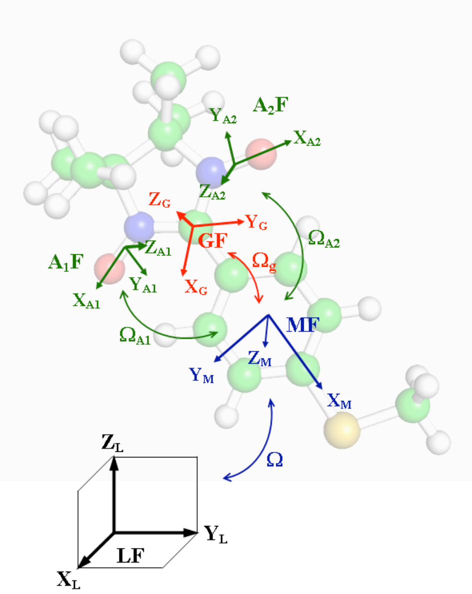

Figure 3-27: Reference frames employed in the stochastic Liouville equation.

which leads to differences between gas phase and toluene solution never exceeding 0.00004 ppm and 0.10 Gauss for $\boldsymbol{g}$ and hyperfine tensors, respectively. It seems, therefore, quite justified to use, in the following dynamical treatment, averaged values of magnetic tensors computed in the gas phase, i.e. $g_{XX} = 2.00683$, $g_{YY} = 2.01142$, $g_{ZZ} = 2.00226$ and $A_{1,XX} = A_{2,XX} = 18.2 \cdot 10^{-4}$, $A_{1,YY} = A_{2,YY} = 1.997 \cdot 10^{-4}$, $A_{1,ZZ} = A_{2,ZZ} = 1.743 \cdot 10^{-4}$. Euler angles specifying the relative orientation of magnetic tensors with respect to the molecular frame MF, which is chosen by definition as the molecule-fixed frame which diagonalize the rotational diffusion tensor are given in the next section.

Evaluation of rotation diffusion tensor

Calculations via hydrodynamic methodology described in Chapter 2 are performed in order to evaluate the full diffusion tensor. In the SLE the molecule is described as a rigid body, so the full diffusion tensor is

$$\boldsymbol{D}\left(\boldsymbol{q}_{int}\right) = \begin{bmatrix} \boldsymbol{D}_{TT} & \boldsymbol{D}_{TR} \\ \boldsymbol{D}_{TR}^{tr} & \boldsymbol{D}_{RR} \end{bmatrix} = \mathrm{k_B} T \boldsymbol{\xi}^{-1}\left(\boldsymbol{q}_{int}\right) \tag{3.66}$$

being $\boldsymbol{\xi}\left(\boldsymbol{q}_{int}\right)$ the friction tensor of the molecule calculated with eq. 2.3. Neglecting off-diagonal couplings, an estimate of the rotational diffusion tensor is given by $\boldsymbol{D}(\boldsymbol{q}_{int}) \equiv \boldsymbol{D}_{RR}(\boldsymbol{q}_{int})$, which depends directly from the atomic coordinates, temperature, and the sol-

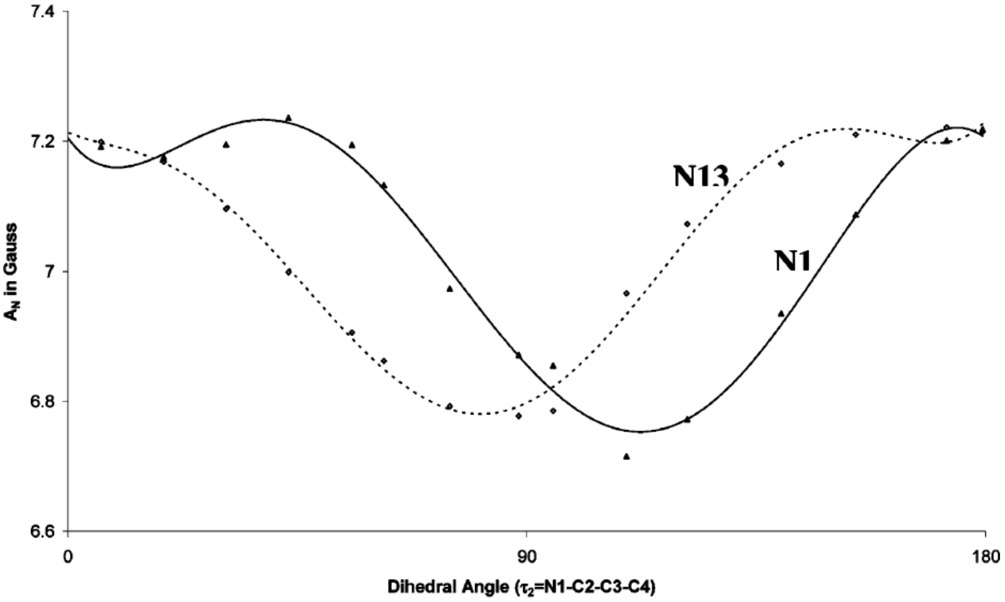

Figure 3-28: Dependence of the two nitrogen (N1 and N13) isotropic hyperfine coupling constants on the τ dihedral angle.

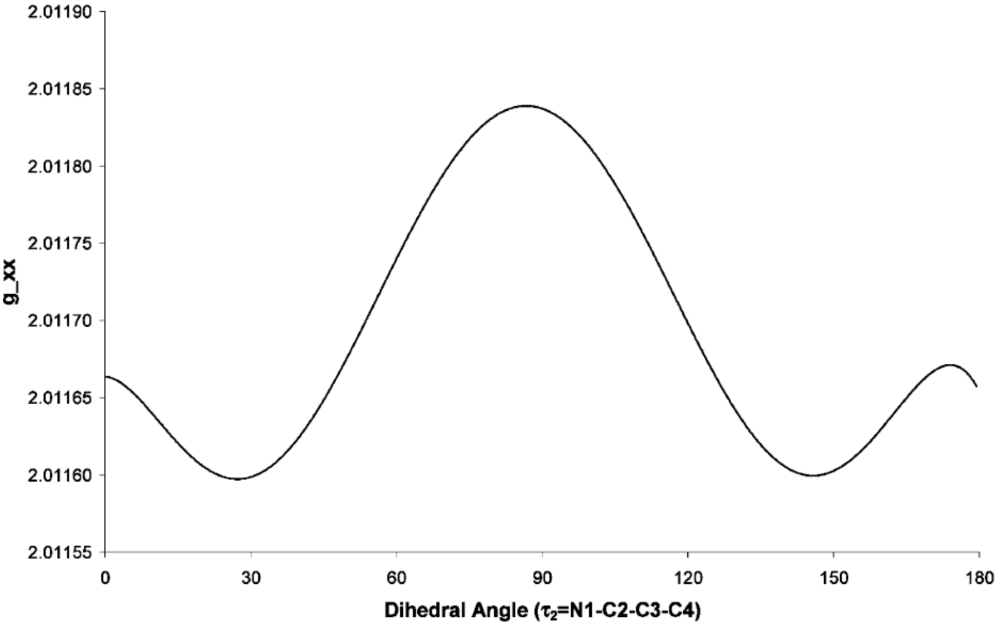

Figure 3-29: Dependence of the g_{XX} component on the τ dihedral angle.

vent viscosity.

The diffusion tensor generally is a function of the internal coordinates ($\boldsymbol{q}_{int}$), but in this case dependence of the molecular geometry upon the two most relevant torsional angles does not affect substantially the overall steric hindrance (cfr. Figure 3-30). Therefore, dependence of $\boldsymbol{D}$ upon internal degrees of freedom is neglected altogether.

Assuming a completely planar geometry, we can write the diffusional tensor (already diagonalized in the MF) in the form $\boldsymbol{D}(T) = D(T)\boldsymbol{d}$ where $D(T) = \mathrm{k_B}T/\xi(T)$ is the translational diffusional coefficient of a sphere or radius R_e at temperature T, and $\boldsymbol{d}$ is a diagonal tensor depending only on the molecular geometry, with values $d_{XX} = 0.1795 \cdot 10^{18}$, $d_{YY} = 0.2238 \cdot 10^{18}$ and $d_{ZZ} = 1.072 \cdot 10^{18}$ m^{-2}.

Absolute determination of the rotational diffusion tensor is difficult within the limitation of

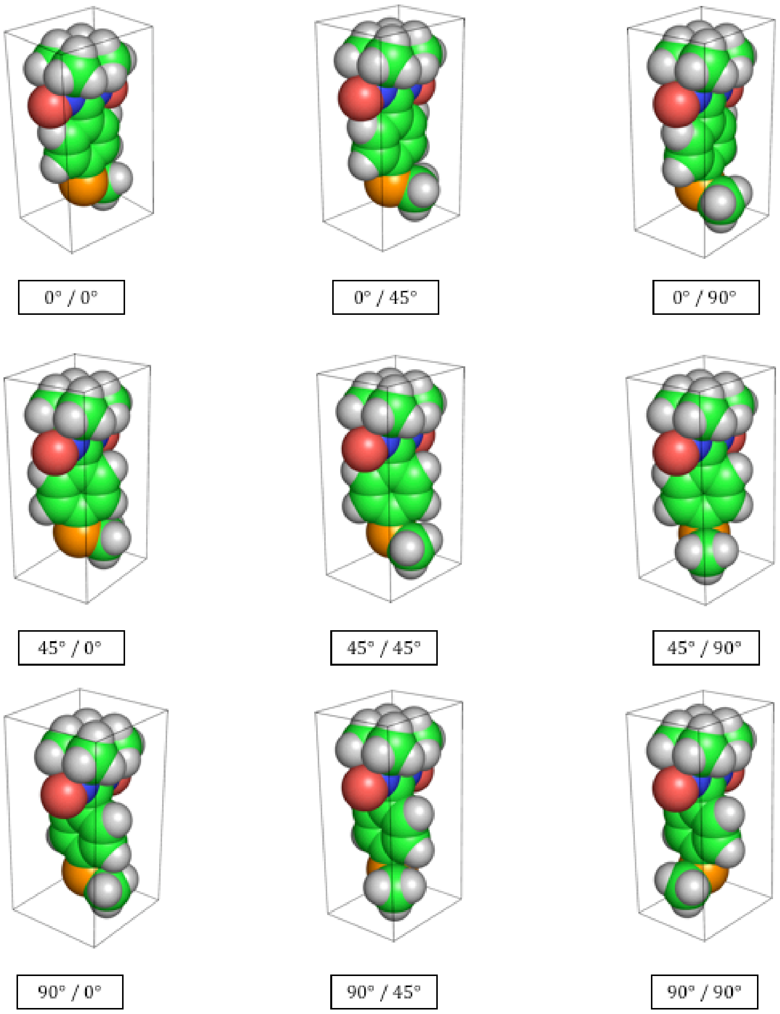

0° / 0°

0° / 45°

0° / 90°

45° / 0°

45° / 45°

45° / 90°

90° / 0°

90° / 45°

90° / 90°

Figure 3-30: Sterical hindrance of MTPNN upon variation of torsional angles.

the present coarse-grained approach, which describes the molecules as a macroscopic object immersed in a continuous fluid. Rather, it is convenient to refer the temperature dependence to a standard state by defining

$$D(T) = D(T_0)\frac{\eta(T_0)}{\eta T}\frac{T}{T_0}$$

where

$$D(T_0) = \frac{\mathrm{k_B}}{CR_e\pi}\frac{T_0}{\eta(T_0)}$$

is the translational diffusion coefficient for a sphere of radius R_e at reference temperature T_0. The number can be chosen once for all as an adjustable parameter. Taking as reference temperature $T_0 = 292$ K for which $\eta(T_0) = 595$ μPa s [165, 166], the best agreement (see below) with experimental data has been achieved by choosing $D(T_0) = 1.498$ m^2 s^{-1}.

The relative orientation of the magnetic frames GF, A$_i$F can now be given explicitly, in terms of sets of Euler angles; the relative orientation of GF with respect to MF is given by $\boldsymbol{\Omega}_g = (0°, 45°, 89°)$ while A$_1$F and A$_2$F are rotated of $\boldsymbol{\Omega}_{A1} = (17°, -84°, 81°)$ and $\boldsymbol{\Omega}_{A2} = (-164°, -81°, 66°)$, respectively. A slightly asymmetric disposition of A$_1$F and A$_2$F is due to molecular distortion of the minimized conformation from perfectly planar geometry and averaging.

Results and discussion

The series of experimental spectra is compared with the outcome of eq. 3.1. Magnetic and diffusion tensors principal values and orientation have been taken from QM calculations, according to the computational approaches described in the previous sections. The only adjustable parameters, valid for the entire set of spectra are the reference translational diffusion coefficient, $D(T_0)$, and an inhomogeneous broadening constant which has been taken equal to 4.7 Gauss for $T > 190$ K, 2.8 Gauss for 190 K $< T <$ 170 K and zero for $T < 170$ K. Inhomogeneous broadening is required in order to account for residual line-width resulting from super-hyperfine coupling with hydrogen nuclei, which are not accounted for explicitly in the simplified Hamiltonian defined in eq. 3.64. Notice that it is feasible *i)* on the basis of the evaluation of coupling constants resulting from the QM calculation, to estimate $\boldsymbol{A}$ coupling terms for all hydrogen atoms and *ii)* via a partial averaging of an extended SLE which include super-hyperfine coupling, to evaluate the inhomogeneous broadening constant and its weak temperature dependence [155].

T / K	g_0^{exp}	estimated error
292	2.00681	±0.0001
280	2.00727	±0.0002
230	2.00695	±0.0002
210	2.00720	±0.0002

Table 3.4: Measured values of g_0^{exp} for four temperatures.

The spectra are then calculated without further adjustments of temperature-dependent fitted parameters. In Figure 3-31, we compare the experimental (full line) and simulated (dashed line) cw-ESR spectra of MTPNN in toluene in the temperature range 155-292 K. Since experimental spectra at different temperatures have been measured at slightly varying frequencies ν_0, in Figure 3-31 spectra are reported relative to their respective central field B_0, for the readers convenience, i.e. implementing eq. 3.65 as such. Notice however that no adjustment is required in the absolute position of the spectra. In fact the measured value of g_0 at room temperature ($g_0 = 2.00681$) is matching perfectly the predicted theoretical value, obtained as 1/3 of the trace of the $\boldsymbol{g}$ tensor, $g_0^{calc} = 2.00686$. On the other hand the measured g_0 values are independent of the temperature inside the experimental error, see Table 3.4.

On the other side, the overall very satisfactory agreement of the spectra band-shape, particularly at low temperatures, is a convincing proof that the simplified dynamic modelling implemented in the SLE through the purely rotational stochastic diffusive operator $\hat{\Gamma}$, eq. 3.63, and the hydrodynamic calculation of the rotational diffusion tensor, is sufficient to describe the main slow relaxation processes. In our opinion, the above results show the potentialities of an integrated computational approach and the validity of the assumptions made in the specific application. In particular, the complete Hamiltonian of a radical interacting with the solvent molecules has been reduced by means of a series of approximations based on separations of motions taking advantage of their different time scale. In the two main steps of the calculation, first by a QM treatment the spin Hamiltonian of the paramagnetic probe is extracted, with magnetic parameters averaged on the electron and fast vibrational nuclear motions, and corrected for solvent effects. The minimum energy conformations of the molecule are evaluated. The motions in solution are then approached by a classical mechanical treatment within the framework of the stochastic Liouville equation. A stochastic operator $\hat{\Gamma}$ is built up in terms of the diffusion tensor principal values, based on

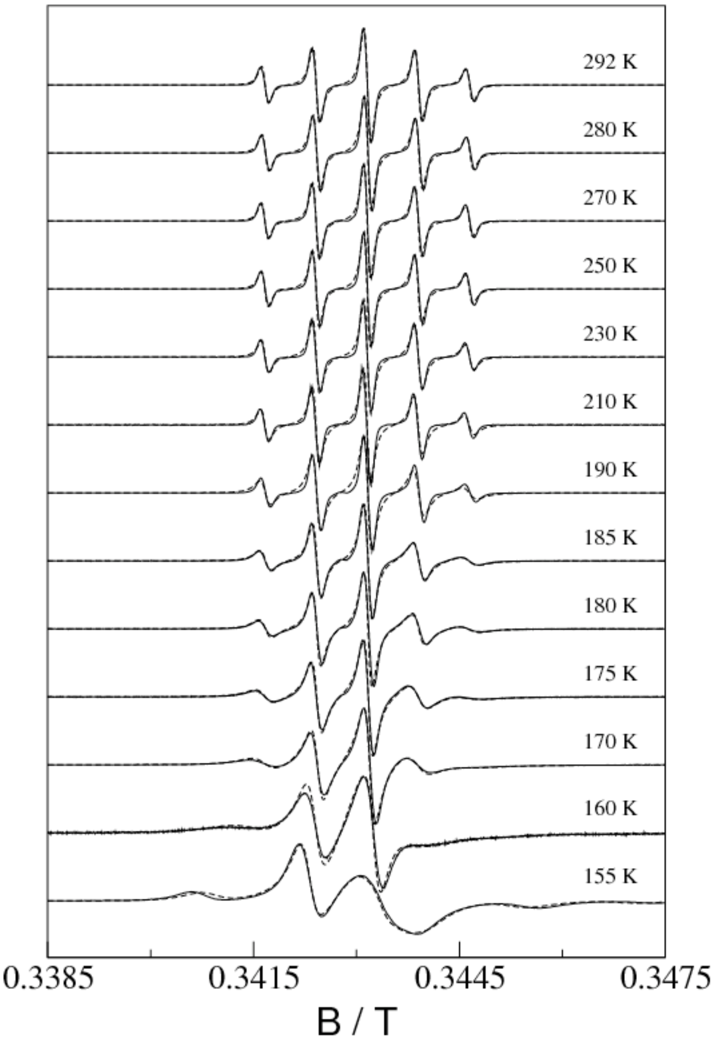

Figure 3-31: Experimental (full line) and simulated (dashed line) cw - ESR spectra of MTPNN in toluene in the temperature range 155 - 292 K.

the previously calculated molecular geometry and solvent thermodynamic properties. The spectral profile is then obtained by numerical integration of the Liouville equation.

The excellent agreement between calculated and experimental spectra shows that the ICA can start a new page in the field of ESR spectra interpretation. This procedure has been applied here to a radical in a single phase, but with magnetic interactions more complex than those typical of a nitroxide spin probe. The success of this method when applied to more challenging systems can be foreseen, as it is based on the link between sophisticated QM calculations of molecular properties giving amazingly reliable magnetic parameters tailored for each environment of the probes, and refined stochastic models for their reorientational motions in any dynamical régime and orienting potential symmetry.

As in the applications to complex systems (biological systems, composite materials) one must take into account different phases embedding the radical, or motions in different dynamical ranges, or both, the results obtained by the traditional simulation approach are doomed to a substantial ambiguity, as the number of adjustable parameters increases beyond the limit of a trustable unique set. On the other hand in the ICA, a self-consistent model for each molecular environment of the radical is used, where all the relevant parameters are entangled and no one can be changed independently. The larger reliability of this approach is evident.

3.3.4 Unraveling solvent-driven equilibria between α- and 3_{10}- helices

Site directed spin labelling (SDSL) of biological molecules coupled to advanced interpretation methodologies is able to give information about the dynamics of the system, but not only. Also structural aspects can be understood from the analysis of the spectra if the molecule is labelled with two radical probes. In particular, interest is about the possibility of determining the secondary structure. To this purpose it is required that the approach to the interpretation of the spectra must be very sensitive to molecular geometry changes. Here we present the work conducted on a small peptide. The usefulness and reliability of our ICA protocol are demonstrated on this very demanding playground, i.e. the tuning of the equilibrium between 3_{10}- and α-helices of polypeptides by different solvents. The starting point is the good agreement between computed and X-ray diffraction structures for the 3_{10}-helix adopted by the double spin labelled heptapeptide Fmoc-(Aib-Aib-TOAC)$_2$-Aib-OMe. Next, DFT computations, including dispersion interactions and bulk solvent effects, suggest another energy minimum corresponding to an α-helix in polar solvents, which, eventually, becomes the most stable structure. Computation of magnetic and diffusion tensors provides the basic ingredients for the building of complete spectra by methods rooted in the SLE. The remarkable agreement between computed and experimental spectra at different temperatures allowed us to identify helical structures in the various solvents. The generality of the computational strategy and its implementation in effective and user-friendly computer codes pave the route toward systematic applications in the field of biomolecules.

Introduction

In the specific field of proteins, it is well recognized that polypeptides represent suitable models for a number of properties, and several experimental techniques have been systematically applied to their study. Unfortunately, interpretation of experimental results is not without ambiguities either because of the role of different environmental effects (e.g. crystal state for X-ray diffraction) or because the relationship between spectroscopic and structural / dynamics characteristics is only indirect. Here, theoretical approaches come into play provided that they are able to couple reliability and feasibility for large systems.

Until quite recently, quantum mechanical (QM) computations of biomolecules were essentially restricted to the structural characteristics of relatively small models in the gas phase. However, the development of powerful methods, integrating the most recent models rooted into the density functional theory (DFT) [167] and discrete - continuum descriptions of solvent effects [97], is paving the route toward the description of more realistic systems in their natural (aqueous) environment [168, 169, 170]. Direct comparison with experimental results then calls for the concomitant computation of reliable structural and spectroscopic parameters taking dynamical effects into the proper account [39, 40, 171, 172]. Although this is, in general, a quite ambitious long-term target, under some favourable circumstances we can already obtain remarkable results. Extension and validation of ICA to labelled biomolecules would then provide access to information of unprecedented richness and reliability by combining experimental and computational methodologies. Since peptides are well recognized models for studying stability and folding of helical regions of proteins, we decided to tackle the complete task of characterizing the solvent-driven equilibrium between different helical forms of a nitroxide doubly labelled peptide by characterizing at the same time its 3D-structure and complete ESR spectrum in different solvents and at different temperatures. It should be pointed out that the ESR spectral features depend not only on the distance between the labels but also on the relative orientations of the principal axes of the electron dipolar interaction tensor, the nitroxide label $\boldsymbol{g}$ tensor, the ^{14}N hyperfine tensors, and the diffusion tensor. Thus, agreement between experimental spectra and their counterparts issuing from QM structures and magnetic tensors through solution of the SLE represents a convincing demonstration of the correctness of the predicted structure. This approach is particularly interesting when different peptide conformations with slightly diverging energies (like, e.g., 3_{10}- and α-helices) are available and the peptide can predominantly fold in one of them biased by temperature and / or solvent characteristics.

In the past decades, double spin labelling of peptides and proteins by stable nitroxide radicals has provided remarkable information: in particular, continuous wave (CW) and pulse [e.g. double quantum coherence (DQC) and PELDOR] ESR spectra of double spin labelled systems have been studied [6, 7, 118]. The sensitivity of DQC and PELDOR [173, 174] spectra allows the reliable determination of distances between labels in the range 1.6 - 6.0 nm in frozen solution, whereas shorter distances are not accessible because the electron dipolar interaction becomes too large and the presence of relevant scalar electron exchange interactions prevents the irradiation of a single electron spin, which is the prerequisite for their application [175].

On the other hand, when the spin labels are at short distances, the liquid solution cw-ESR spectrum could be very informative because its shape depends on several structural and dynamic parameters which characterize the double labelled peptide.

Here we present the results of a cw-ESR investigation of the double spin labelled, terminally protected, heptapeptide Fmoc-(AibAib-TOAC)$_2$-Aib-OMe (**1**) (Fmoc, fluorenyl-9-methoxycarbonyl; Aib, α-aminoisobutyrric acid; TOAC, 2,2,6,6-tetramethylpiperidine-1-oxyl-4-amino, 4-carboxylic acid; OMe, methoxy), which is characterized by the presence of two TOAC nitroxide free radicals at relative positions i, i+3 (Figure 3-32) in different solvents and at several temperatures. Aib [176, 177, 178] and TOAC [179, 180] are two strongly helicogenic, C$^{\alpha}$-tetrasubstituted, α-amino acids. The cw-ESR spectra have been compared with their theoretical counterparts pertaining to the deepest energy minima obtained by QM computations (3_{10}- and α-helix). It will be shown that in specific solvents the experimental spectra agree well with those expected for the 3_{10}-helix, in other solvents with those predicted for the α-helix, while for a final set of solvents with those associated with a mixture of α- and 3_{10}-helices with temperature-dependent relative percentages.

In the last part of this chapter we discuss the preliminary simulations of a similar system: a nonapeptide with formula Fmoc-Aib-TOAC-(Aib)$_5$-TOAC-Aib-OMe. The α- and 3_{10}-helices are two common polypeptide conformations [181, 182, 183, 184]. The former helix is a well-known secondary structural element in proteins. The 3_{10}-helix it not as widespread as the

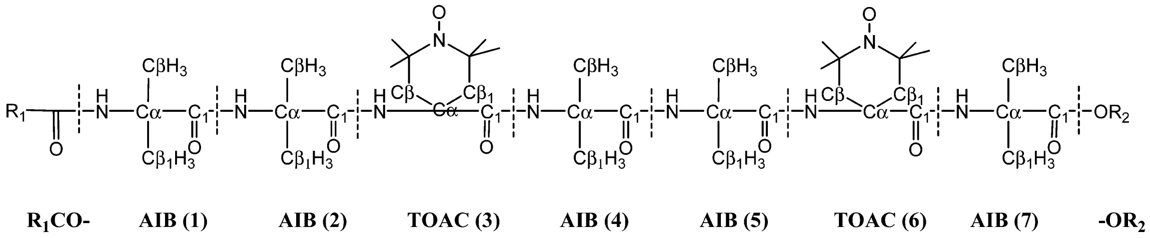

Figure 3-32: Chemical structure of Fmoc-(Aib-Aib-TOAC)$_2$-Aib-OMe (heptapeptide **1**). R$_1$ = 9-fluorenylmethoxy and R$_2$ = Me.

α-helix, but it is still rather frequently found in proteins, especially as a N- or C-terminal extension of an α-helix. The 3_{10}-helices are usually quite short (about four residues in length), although 3_{10}-helices of 712 residues [177, 182, 185, 186] in length have been authenticated in proteins. 3_{10}-Helices have been proposed as intermediates in the folding / unfolding processes of α-helices [119] because there is a lower entropic penalty for the onset of the bend required for the formation of the intramolecular $i \leftarrow i+3$ versus $i \leftarrow i+4$ hydrogen bonds. The relative stability in solution of these two ordered secondary structures depends on various factors. The major parameters are the peptide main-chain length, the amino acid sequence, the Aib content, and the solvent dielectric properties [177, 182, 185, 186, 187, 188, 189]. Relatively short oligopeptides rich in Aib have been observed to largely prefer 3_{10}-helical structures in nonaqueous solutions [178, 182, 190]. It has been also suggested that the asymmetric geometry adopted by the Aib residue can favour the 3_{10}- over the α-helix [191].

Modelling

From the cw-ESR spectra it is possible to obtain both dynamic and structural information. Our approach requires self-consistency between magnetic and diffusive parameters, which are both related to the geometrical structure issuing from a priori geometry optimization or short-time dynamics.

As in the previous cases, we have to firstly define the SLE of the system. One of the ingredients is spin Hamiltonian, which here takes the form

$$\hat{\mathcal{H}}/\hbar = \frac{\beta_e}{\hbar}\sum_i \boldsymbol{B}_0\boldsymbol{g}_i\hat{\boldsymbol{S}}_i + \gamma_e\sum_i \hat{\boldsymbol{I}}_i\boldsymbol{A}_i\hat{\boldsymbol{S}}_i - 2\gamma_e J\hat{\boldsymbol{S}}_1\hat{\boldsymbol{S}}_2 + \hat{\boldsymbol{S}}_1\boldsymbol{T}\hat{\boldsymbol{S}}_2 \qquad (3.67)$$

where the first term is the Zeeman interaction of each electron spin with magnetic field $\boldsymbol{B}_0$, depending on the $\boldsymbol{g}_i$ tensor; the second term is the hyperfine interaction of each ^{14}N/unpaired electron, defined with respect to the hyperfine tensor $\boldsymbol{A}_i$; the third and fourth terms are the electron exchange and spin-spin dipolar terms, respectively. Although all hyperfine tensors are available from our quantum mechanical (QM) computations, we neglect explicit coupling with nuclei other than ^{14}N since the small inhomogeneous broadening in the spectra resulting from coupling with hydrogen nuclei is essentially temperature and solvent independent. Notice, however, that hydrogen hyperfine tensors could be used to perform a partial averaging of an extended SLE equation leading to explicit evaluation of broadening constants and of their weak temperature dependence.

Several relaxation processes can be invoked and modelled accordingly within the SLE formalism by carefully choosing the time evolution operator $\hat{\Gamma}$. Here we shall limit our description to the case of a freely (and rigidly) orienting molecule in space, subjected to a simple diffusive motional regime. So the only stochastic variables are the Euler angles $\boldsymbol{\Omega}$ describing the overall orientation of the molecule with respect to the laboratory inertial frame. Due to the isotropy of the environment, the stochastic diffusive operator is simply the Smoluchowski operator

$$\hat{\Gamma} = \hat{\boldsymbol{J}}^{tr} \boldsymbol{D} \hat{\boldsymbol{J}} \tag{3.68}$$

being $\hat{\boldsymbol{J}}$ the angular momentum operator and $\boldsymbol{D}$ the rotational diffusion tensor of the molecule.

The ESR spectrum is obtained as the Fourier-Laplace transform of the correlation function for the X-components of the magnetizations which is dependent on the nuclear spin.

Results and discussion

The structure of heptapeptide **1**, as determined by single-crystal X-ray diffraction analysis, is illustrated in Figure 3-33. Relevant geometrical parameters are listed in Table 3.5. With the peptide being achiral and crystallizing in a centrosymmetric space group, molecules of both handedness are found in the crystals. A molecule of the right-handed screw sense has been chosen as the asymmetric unit. The peptide backbone is folded into a regular 3_{10}-helix, stabilized by five, consecutive, N-H. . .O=C intramolecular hydrogen bonds of the $i + 3 \rightarrow i$ type. The C-terminal Aib(7) residue, external to the H-bonding pattern, adopts a helical conformation with a screw sense opposite to that of the preceding residues. The piperidinyl

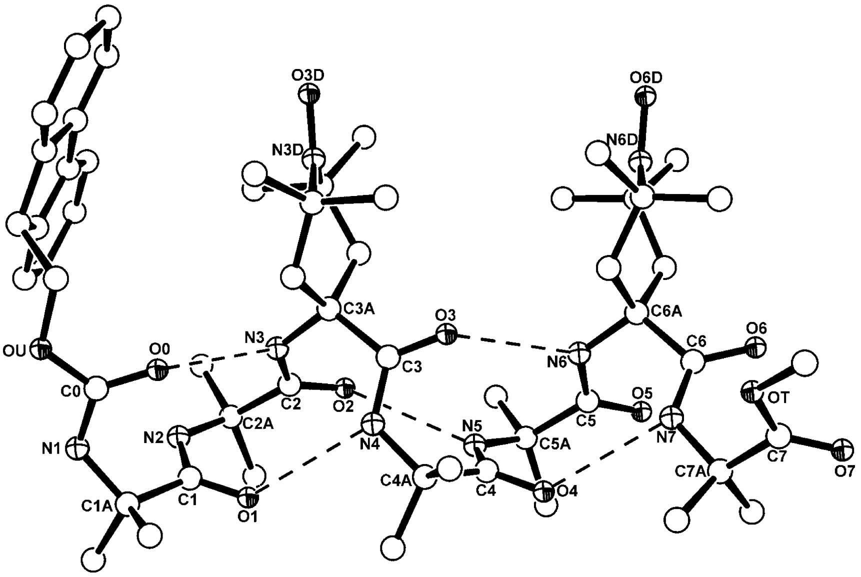

Figure 3-33: X-ray diffraction structure of heptapeptide **1**. Intramolecular H-bonds are represented by dashed lines.

rings of the two TOAC residues are oriented roughly perpendicular to the helix axis and parallel to each other, the angle between normals to their average planes being 4.5(1)°. The angle between the two N-O bonds is 10.9(4)°. The piperidinyl rings of both TOAC residues are found in the $^6T_2$ twist conformation (relative to the ring atom sequence N^{δ}-$C^{\gamma 2}$-$C^{\beta 2}$-C^{α}-$C^{\beta 1}$-$C^{\gamma 1}$, where $C^{\beta 1}$ refers to the *pro-S* C^{β} atom). For a statistical analysis of TOAC ring conformations in the crystal state, see ref [180]. The puckering parameters are the following: $Q_T = 0.595(4)$ Å, $\phi_2 = 92.3(4)°$, $\theta_2 = 86.2(4)°$ for TOAC(3), and $Q_T = 0.634(4)°$, $\phi_2 = 88.8(4)°$, $\theta_2 = 90.1(3)°$ for TOAC(6) [192]. The hydroxyl groups of the two cocrystallized TFE molecules are H-bonded to the nitroxide and to the carbonyl oxygen atoms, respectively, of TOAC(6) within the same asymmetric unit. In the packing mode, peptide molecules are linked head-to-tail through an intermolecular H-bond between the NH group of Aib(1) and the Aib(7) carbonyl oxygen atom of a (x, y - 1, z) symmetry related molecule, giving rise to rows of molecules along the *b* direction.

					TOAC3			TOAC6	
helix	N...N	O...O	NO	CNC	CNO...C	NO	CNC	CNO...C	
3_{10}	gas-phase	6.57	6.80	1.272	123.1	177.9	1.273	123.0	178.0
3_{10}	PCM/H_2O	6.51	6.74	1.273	123.0	179.8	1.274	123.0	179.2
α	PCM/H_2O	7.97	9.27	1.273	122.6	179.1	1.273	122.5	179.7
3_{10}	X-ray	6.40	6.59	1.276	124.8	178.6	1.279	123.7	177.6

			Φ angle				angle	
	3_{10} gas-phase	3_{10} PCM/H_2O	α PCM/H_2O	3_{10} X-ray	3_{10} gas-phase	3_{10} PCM/H_2O	α PCM/H_2O	3_{10} X-ray
1	59.2	56.8	58.6	57.2	29.9	32.4	29.9	40.3
2	54.1	53.9	50.9	54.6	24.3	24.8	32.3	33.1
3	52.4	51.7	50.2	57.6	33.7	34.2	46.8	24.3
4	55.1	53.8	61.0	51.5	28.1	29.5	47.1	28.3
5	58.2	55.5	64.5	50.5	20.1	25.8	46.2	32.0
6	59.1	58.9	64.3	55.3	31.1	31.6	41.0	39.0

			$NC^{\alpha}C'$ angle				$C^{\beta2}C^{\alpha}C^{\beta1}$ angle	
	3_{10} gas-phase	3_{10} PCM/H_2O	α PCM/H_2O	3_{10} X-ray	3_{10} gas-phase	3_{10} PCM/H_2O	α PCM/H_2O	3_{10} X-ray
1	110.9	110.5	110.7	110.0	110.6	110.5	110.5	110.3
2	111.7	111.2	110.4	111.2	110.5	110.4	110.2	112.4
3	109.2	109.1	108.5	109.8	110.9	110.8	110.6	111.2
4	112.0	114.4	109.9	110.5	110.4	110.2	109.6	111.8
5	112.7	111.9	110.2	111.6	110.1	110.0	109.4	110.9
6	110.0	110.0	108.9	108.7	110.7	110.5	110.2	110.4

helix		HB1	HB2	HB3	HB4	HB5
3_{10}	gas-phase	2.02	2.11	2.05	2.12	2.06
3_{10}	PCM/H_2O	1.96	2.02	2.02	2.04	1.99
α	PCM/H_2O	1.97	2.13	2.18	2.19	-
3_{10}	X-ray	2.22	2.14	2.22	2.18	2.17

Table 3.5: Comparison between the X-ray diffraction and computed geometrical parameters for heptapeptide **1**. (distances in Å and angles in deg). Estimated standard deviations for the crystallographically derived parameters are in the ranges 0.004-0.007 Å 0.3-0.5 deg, and 0.3-0.6 deg for bond distances, bond angles, and torsion angles, respectively.

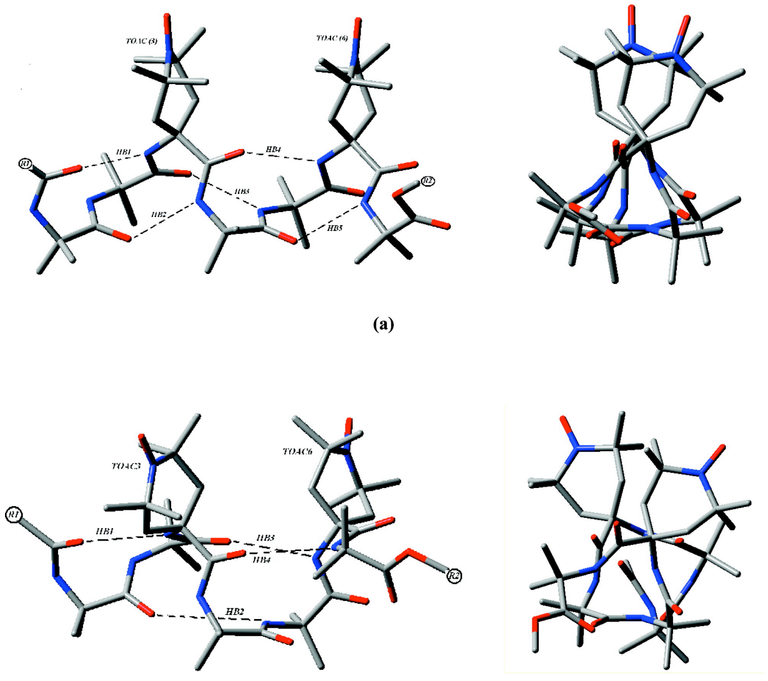

(a)

(b)

Figure 3-34: Optimized structure of heptapeptide **1**: View along (right) and orthogonal (left) the helix axis of the (a) 3_{10}-helix and (b) α-helix secondary structure.

In the 3_{10}-helix the distance (d) between the nitroxide oxygen atoms of the two TOAC residues at relative positions i, $i+3$ is about 6.5 Å, while in the α-helix this distance is significantly longer (8.0 Å). In general, the 3_{10}-helix exhibits $d(i, i+3) < d(i, i+4)$, whereas in the α-helix the opposite holds true. The experimentally observed peptide helices are somewhat distorted from their ideal geometries [181, 182], but the difference in the relative side-chain distances between the 3_{10}- and α-helices persists.

The above 3D-structures have been next used to compute the magnetic tensors in different solvents, including in the case of chloroform and methanol the solvent molecules forming hydrogen bonds with the nitroxide group. Typical optimized structures are shown in Figure 3-35.

Let us recall that the orbitals determining the magnetic properties of non-conjugated nitroxides are strongly localized onto the N-O moiety (Figure 3-36), so that the principal axes of both hyperfine and $\boldsymbol{g}$ tensors are well aligned along the N-O bond (by convention the X-axis) and with the average direction of π-orbitals (Z-axis).

The $\boldsymbol{g}$ tensors computed by last generation density functionals are usually in good agreement with the experiments [19, 87] and have been used without further corrections in the simula-

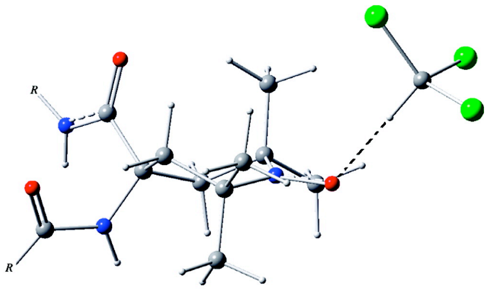

A1

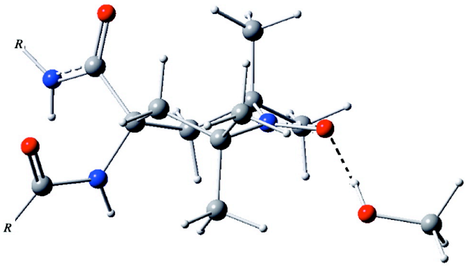

A2

Figure 3-35: Structures of the TOAC-solvent complexes: twist conformation with $CHCl_3$ (***A*1**); twist conformation with methanol (***A*2**). R = peptide chain.

tion of ESR spectra. Table 3.6 shows the values of the principal axes components reported in ppm units relative to the free electron value in order to highlight the difference between the values in different solvents. The most important contribution to $\boldsymbol{g}$ shifts comes from an electronic excitation from the SOMO-1 (an in-plane lone pair, hereafter referred to as n) to the SOMO (an out-of-plane π^* orbital), both of which are sketched in Figure 3-36. The dependence of the $\boldsymbol{g}$ tensor on solvent polarity is related to the selective stabilization of lone pair orbitals by polar solvents: his increases the $n \rightarrow \pi^*$ gap with the consequent reduction of $\boldsymbol{g}$ tensor shifts (especially g_{XX}). Together with this purely electrostatic contribution, formation of solute-solvent H-bonds also concurs to the stabilization of lone pair orbitals and, once again, to a decrease of $\boldsymbol{g}$ tensor shifts. In any case, structural and solvent effects on $\boldsymbol{g}$ are well within experimental uncertainty: thus, constant values of 2.009, 2.006, and 2.003 have been used in the fitting of all spectra for the principal axes of the $\boldsymbol{g}$ tensor. The situation is more complex for nitrogen hyperfine tensors $\boldsymbol{A}$, which can be decomposed into two terms: the isotropic hyperfine term (a_{iso}) and dipolar contributions ($\boldsymbol{B}$). The results reported in Table 3.7 show that the $\boldsymbol{B}$ tensor has the same behaviour as the $\boldsymbol{g}$ tensor and that, to a good

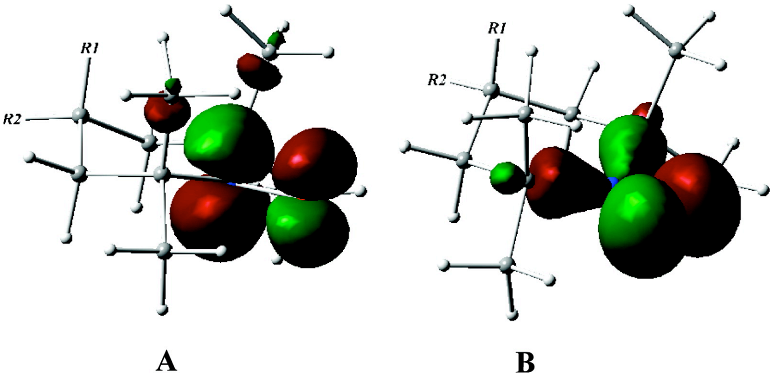

Figure 3-36: Sketch of SOMO (A) and SOMO1 (B) of TOAC (R1 = COOH, R2 = NH2) in two different orientations.

approximation, its principal axes are parallel (B_{ZZ}) or perpendicular (B_{XX}, B_{YY}) to the N-O orbital with $B_{XX} = B_{YY}$. It is well-known that accurate estimates of isotropic hyperfine couplings for nitroxides can be obtained only using very demanding theory levels, like, e.g., quadratic configuration interaction including single and double excitations (QCISD) with purposely tailored basis sets, possibly integrated into an ONIOM-like approach [193]. We have, however, recently developed a new basis set (N06) that, coupled to the PBE0 functional, promises to overcome this problem. Indeed, the computed a_{iso} for the closely related TEMPO (2,2,6,6-tetramethylpiperidine-N-oxyl) radical in cyclohexane (15.23) and in toluene (15.32) are in remarkable agreement with the experimental values (15.28 and 15.40 G, respectively) [194, 195]. The computed values for the chair conformation of TOAC are very close, whereas significantly lower values (12.38 and 12.54 G) are obtained for the twist structure. This is related to the different pyramidality around nitrogen: in particular, the nearly planar arrangement characterizing the twist structure leads to the lack of any contribution of nitrogen *s* orbitals to the orbital formally containing the unpaired electron with the consequent strong reduction of a_{iso}. However, vibrational averaging effects, which are essen-

	g_{XX}	g_{YY}	g_{ZZ}
gas-phase	6829	3787	262
toluene ($\epsilon = 2.3$)	6674	3754	262
chloroform ($\epsilon = 4.9$)	6579 (6349)	3733 (3598)	262 (232)
methanol ($\epsilon = 32$)	6472 (5912)	3709 (3580)	262 (253)
acetonitrile ($\epsilon = 36$)	6470	3709	262

Table 3.6: $\boldsymbol{g}$ tensors (ppm) computed in different solvents. Values in parentheses are obtained including one specific solvent molecule for each N-O moiety (see Figure 3-35).

	B_{XX}	B_{YY}	B_{ZZ}
gas-phase	8.70	8.46	17.16
toluene ($\epsilon = 2.3$)	8.92	8.70	17.62
chloroform ($\epsilon = 4.9$)	9.05 (9.38)	8.85 (9.24)	17.90 (18.62)
methanol ($\epsilon = 32$)	9.19 (9.59)	9.01 (9.48)	18.20 (19.06)
acetonitrile ($\epsilon = 36$)	9.19	9.02	18.21

Table 3.7: Dipolar hyperfine tensors (in Gauss) computed for heptapeptide **1** in different solvents. Values in parentheses are obtained including one specific solvent molecule for each nitroxide moiety (see Figure 3-35).

tially negligible for chair structures, become quite significant for the nearly planar nitroxide moieties characterizing twist structures. Without entering into a detailed description of the effective one-dimensional model we have used to estimate these effects [17, 38, 103, 196] we just mention that a nearly constant vibrational correction of 1.7 G is obtained for all twist structures. It is noteworthy that, after this correction, twist and chair conformations have comparable hyperfine couplings, which show, furthermore, a distinct solvent dependence (see Table 3.8). In particular, solvent polarity and formation of solute-solvent hydrogen bonds concur to the selective stabilization of the nitroxide resonance structure involving at the same time formal charge separation and increased spin density on nitrogen [38]. The final values computed for the different solvents are as follows: 14.3 (toluene), 14.8 (acetonitrile), 15.0 (chloroform), and 15.3 G (methanol), where 1 G = 10^{-4} T. To fine-tune the simulated spectra we set $A_{XX} = A_{YY} = A_{\perp}$ and $A_{ZZ} = A_{\|}$ and then fit the isotropic value $a_{iso} = (2A_{\perp} + A_{\|})$ by keeping constant the anisotropy ratio $R = A_{\perp}/A_{\|} = 0.13$.

Hyperfine and gyromagnetic tensors have a local character and are thus only marginally

	a_{iso}	Δ_{vib}	Δ_{1S}	best calcd	best fit
gas-phase	12.2	1.7			
toluene	12.6	1.7	-	14.3	14.5
chloroform	12.8	1.7	0.58	15.1	15.0
methanol	13.1	1.7	0.61	15.4	15.3
acetonitrile	13.1	1.7	-	14.8	14.8

Table 3.8: Calculated nitrogen isotropic hyperfine couplings (in Gauss) for the optimized 3_{10}-helix of heptapeptide **1** are compared with fitted values (best fit). The final calculated values (best calcd) include electronic values at the energy minimum (a_{iso}), vibrational averaging (Δ_{vib}), and, for protic solvents, the contribution of a single explicit solvent molecule (Δ_{1S}). The last column reports the optimized values of the isotropic hyperfine coupling.

influenced by the long-range interactions modified by conformational changes (e.g. transition from the 3_{10}- to the α-helix). The other magnetic terms (J and spin-spin dipolar interaction) have a long-range character and can provide, in principle, a signature for the different helical structures. The J terms have been calculated from differences between triplet and singlet energies by the so-called broken-symmetry approach [197]. Although the computed J values are slightly different for the 3_{10}- and the α-helix (140.8 and 139.5 G, respectively, at the PBE0/N06 level), this trend does not allow us to gain further structural information, since (as we shall see) all values larger than 130 G are compatible with experimental data.

Usually, the spin-spin dipolar term is calculated by assuming that the two unpaired electrons are localized at the centre of the N-O bonds of the two TOAC residues. Then, the two electrons are considered just as two point magnetic dipoles and the interaction term depends on the distance between the two localized electrons:

$$\boldsymbol{T} = \frac{\mu_0}{4\pi}\frac{g_e^2\beta_e^2}{\hbar r^3}\left[\mathbf{1}_3 - \frac{3}{r^2}\begin{pmatrix} r_X^2 & r_X r_Y & r_X r_Z \\ r_Y r_X & r_Y^2 & r_Y r_Z \\ r_Z r_X & r_Z r_Y & r_Z^2 \end{pmatrix}\right] \tag{3.69}$$

Obviously, this is just a rough approximation which could break down at not too long distances. On the other hand, a complete QM computation is hardly feasible for the large systems we are interested in. Thus, the strong localization of the magnetic orbitals of non-conjugated nitroxides (see Figure 3-36) suggests that, for not too short distances between N-O moieties, a reliable approximation would be to fit the SOMO electron density by linear combinations (with equal weights) of effective nitrogen and oxygen valence Slater orbitals. Then, the tensorial operator $\hat{\boldsymbol{T}}$ has components

$$\hat{T}_{\alpha,\beta} = \frac{r_{1,2}^2\delta_{\alpha,\beta} - 3\left(\boldsymbol{r}_{1,2}\right)_\alpha\left(\boldsymbol{r}_{1,2}\right)_\beta}{r_{1,2}^5} \tag{3.70}$$

where $r_{1,2} = |\boldsymbol{r}_{1,2}| = |\boldsymbol{r}_1 - \boldsymbol{r}_2|$ is the vector between the two electrons, $\alpha, \beta = X, Y, Z$, and $(\boldsymbol{r}_{1,2})_\alpha$ is the component along α of vector $\boldsymbol{r}_{1,2}$. In the present case, only the $T^{(2,0)}$ component (proportional to T_{ZZ} in Cartesian coordinates) contributes significantly to the dipolar tensor. Figure 3-37 shows the trend of $|T^{(2,0)}|$ versus the distance between the two TOAC nitroxides and highlights the position of the 3_{10}-helix and the α-helix with respect to the distance between the TOAC residues. The difference between the point-dipole approximation and the quantum mechanical values of the dipolar tensor is higher in the 3_{10}-helix structure, in which

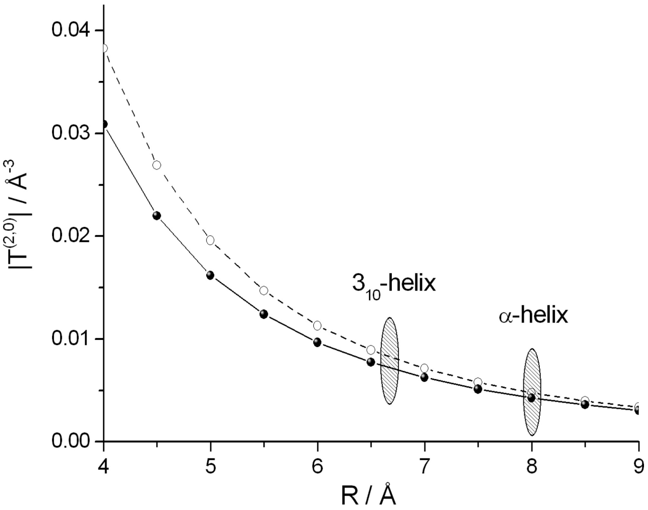

Figure 3-37: Trend of $|T^{(2,0)}|$ versus distance calculated with the point dipole (dashed line) and localized quantum mechanical (solid line) approaches.

the distance between the two nitroxides is lower if compared to that of the α-helix. Details on the calculation are given in appendix B. The rotational dynamics is controlled by the rotational diffusion tensor $\boldsymbol{D}$, which is evaluated with the hydrodynamic approach discussed in Chapter 2. We can write the rotational diffusional tensor (already diagonalized in the molecular frame) in the form $\boldsymbol{D}(T) = D(T)\boldsymbol{d}$, where $D(T) = \mathrm{k_B}T/\xi(T)$ is the translational diffusional coefficient of a sphere of radius R_e at temperature T and $\boldsymbol{d}$ is a diagonal tensor depending only on the molecular geometry, with values $d_{XX} = 1.71 \cdot 10^{16}$, $d_{YY} = 1.83 \cdot 10^{16}$ and $d_{ZZ} = 5.75 \cdot 10^{16}$ m^{-2} for the 3_{10}-helix and $d_{XX} = 1.88 \cdot 10^{16}$, $d_{YY} = 2.01 \cdot 10^{16}$, and $d_{ZZ} = 4.91 \cdot 10^{16}$ m^{-2} for the α-helix. Available viscosity data for the solvents considered [198] is used to calculate the temperature- and solvent-dependent rotational diffusion tensors. The larger difference between the value of the diffusion tensor for the 3_{10}-helix and the α-helix is computed for the ratio of the Z component (d_{ZZ}) and the X component (d_{XX}) of the tensor. For all the temperatures and solvents investigated, this ratio is 3.36 for the 3_{10}-helix and 2.61 for the α-helix. These different values can be explained by simply considering the shape of the two secondary structures illustrated in Figure 3-34. A higher value of the ratio is related to a long and slim shape of the molecule (Figure 3-34b) while a lower value indicates that the molecule is shorter and wider (Figure 3-34a).

Simulated spectra in different solvents exhibit different sensitivities with respect to the magnetic and diffusion calculated parameters. In particular, simulations, as expected, are not

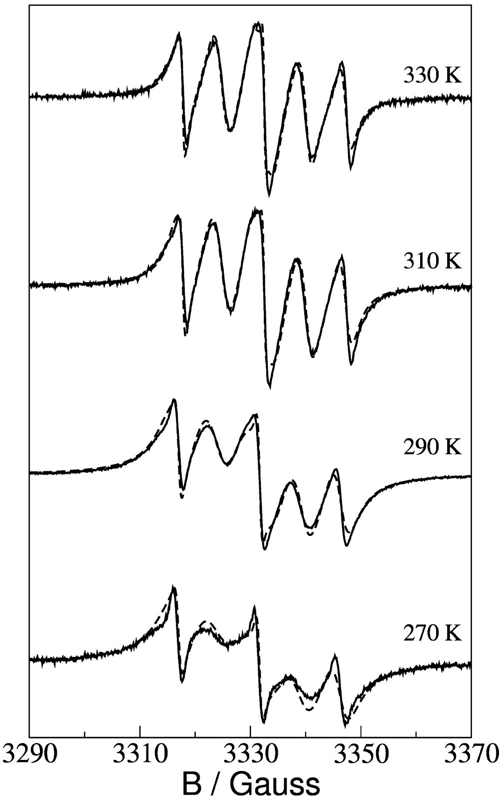

Figure 3-38: Experimental (solid lines) and theoretical (dashed lines) cw-ESR spectra of heptapeptide **1** in MeCN at temperatures 330, 310, 290, and 270 K.

sensitive to changes in the electron exchange interaction J when $J > 130$ G. The dependence on the values of the components of the diffusion tensor $\boldsymbol{D}$ is more significant: variations within a 10% range of the proposed values, calculated according to the hydrodynamic approach, cause a significant change in the intensity and widths of the peaks. Moreover, the spectra dependence on the temperature is perfectly reproduced by the calculated $\boldsymbol{D}$ tensor. Sensitivity upon the dipolar interaction tensor $\boldsymbol{T}$ is also relevant. The spectrum is controlled by the dominant $T^{(2,0)}$ component, which causes noticeable variations when changed within 10%. An overestimation of $\boldsymbol{T}$, corresponding for instance to use of the approximate point dipole formulation, leads to an increase of the width and a decrease of the intensity of all peaks. Finally it is well-known that the general dependence of cw-ESR spectra upon the $\boldsymbol{g}$ and $\boldsymbol{A}$ tensor component values and orientation Euler angles is highly pronounced and no significant adjustment is possible with respect to the calculated values which are in very good agreement with the experimental observations.

The SLE computations were performed for four different solvents: acetonitrile (MeCN),

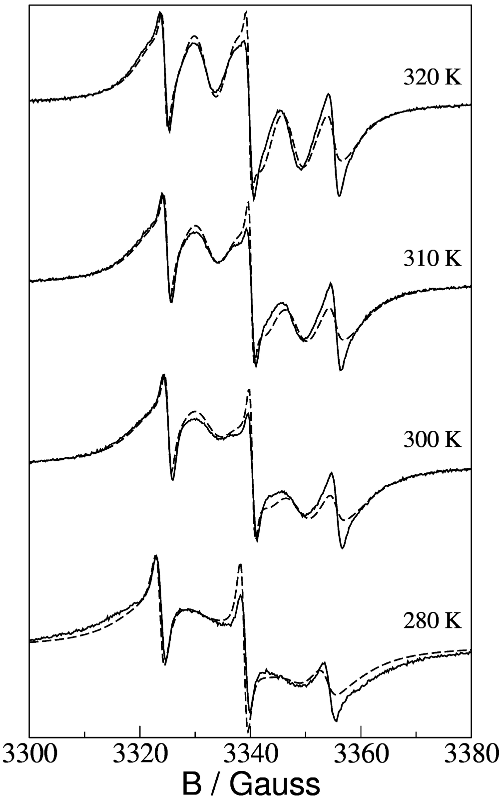

Figure 3-39: Experimental (solid lines) and theoretical (dashed lines) cw-ESR spectra of heptapeptide **1** in methanol at temperatures 320, 310, 300, and 280 K.

methanol, toluene, and chloroform. It is worthwhile to remark that the overall computational protocol has been organized in a novel suite of computational codes which present significant advancements with respect to the existing packages for the interpretation of ESR spectra, namely the integration of the QM and stochastic dynamics parts, the extension to multiple radicals and nuclei, and finally the increased computational efficiency based on a partial on-the-fly evaluation of matrix elements.

For each solvent we examined different temperatures, and at every step a different value of the diffusion tensor was employed owing to the temperature dependence of the viscosity. A common assumption for all solvents is the presence of a monoradical impurity that might arise from the reduction of one of the nitroxide functions. The estimated amount of the impurity is below 4%, a low but still appreciable percentage. It is noteworthy that the optimized values of a_{iso} (the only adjustable parameters in our protocol) are very close to their QM counterparts for all solvents (see Table 3.8).

Figure 3-38 collects four theoretical spectra for the heptapeptide **1** in MeCN and their ex-

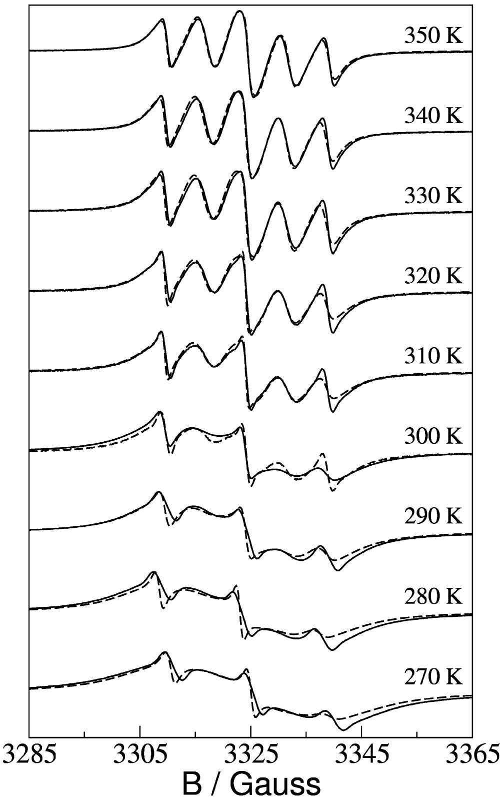

Figure 3-40: Experimental (solid lines) and theoretical (dashed lines) cw-ESR spectra of heptapeptide **1** in toluene at temperatures 350, 340, 330, 320, 310, 300, 290, 280, and 270 K.

perimental counterparts at four different temperatures: 330, 310, 290, and 270 K. From the simulations it appears that in this solvent only the 3_{10}-helix occurs, i.e. $p_\alpha = 0$, $p_{3_{10}} = 98$, $p_{mono} = 2\%$ at all temperatures. Figure 3-39 shows five theoretical and experimental spectra in methanol solution in the temperature range 280 to 320 K. The simulations, which consider that in solution only the α-helix is present, closely reproduce the experimental spectra, $p_\alpha = 97$, $p_{3_{10}} = 0$, $p_{mono} = 3\%$ at all temperatures.

Figure 3-40 collects the simulated and the experimental spectra for a toluene solution in the temperature range 270 to 350 K. At high temperatures (350, 340, 330, 320 K) the experimental spectra are well reproduced using comparable percentages of α-helix and 3_{10}-helix structures, $p_\alpha = 60$, $p_{3_{10}} = 38$, $p_{mono} = 2\%$. At lower temperatures (below 310 K) the experimental spectra are correctly reproduced by progressively increasing the α-helix percentage, with $p_\alpha = 70, 75, 78, 92, 98\%$ at 310, 300, 290, 280, 270 K (and constant $p_{mono} = 2\%$).

Figure 10 shows the spectra for chloroform solutions in the range 290 to 250 K. The experimental spectra are reproduced using only an α-helix structure, $p_\alpha = 96$, $p_{3_{10}} = 0$, p_{mono}

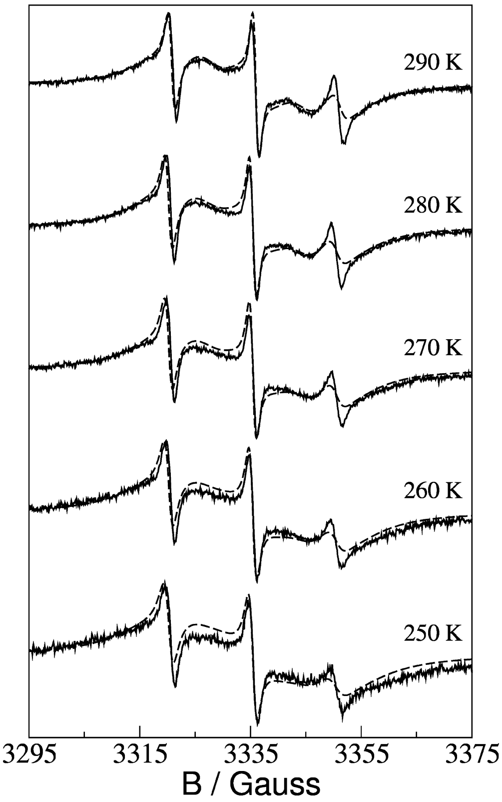

Figure 3-41: Experimental (solid lines) and theoretical (dashed lines) cw-ESR spectra of heptapeptide **1** in chloroform at the temperatures 290, 280, 270, 260, and 250 K.

= 4% at all temperatures. From the available literature data [179] we could expect a high 3_{10}-helix percentage in solution induced by the low polarity of the solvent. However, QM computations show that quite stable hydrogen bonds can be formed between chloroform and both nitroxide and carbonyl groups (see, e.g., Figure 3-35), which, in turn, could lead to a switch from the 3_{10}- to the α-helix [185, 186, 187].

Examples of peptides possessing a main-chain length comparable to that of heptapeptide **1**, and largely [199] based upon C^{α}-tetrasubstituted amino acid residues, able to switch from the 3_{10}- to the α-helical conformation upon increasing medium polarity, have been only recently reported.

Conclusions

We have reported a detailed analysis of the structural and magnetic properties of a double labelled peptide by an integrated computational and experimental strategy. From a chemical point of view, our results provide evidence on the property of Aib-rich peptides changing their conformation from 3_{10}- to α-helix as a function of increasing polarity and hydrogen-bond donor capability of the solvent: α-helix in protic solvents and at low temperature, whereas 3_{10}-helix in aprotic solvents. The X-ray diffractometric analysis reveals that the peptide assumes a 3_{10}-helical conformation in the crystal state. The 3_{10}-helix is very well reproduced by DFT computations in vacuo and in aqueous solution. Our computational results indicate that in aqueous solution the α-helical conformation becomes the deepest conformational minimum when dispersion interactions are taken into account. Computation of magnetic and diffusion tensors and their feeding in a general computational protocol based on the stochastic Liouville equation allowed us to reproduce in a remarkable way the ESR spectra in different solvents and at different temperatures without any adjustable parameter except the relative percentage of 3_{10}- and α-helices. The favourable scaling of our computational protocol with the dimensions of the system and its remarkable performances for both structural and magnetic properties might pave the route for systematic studies of spin labelled peptides and proteins.

3.3.5 Modeling of cw-EPR Spectra of Propagating Radicals in Methacrylic Polymerization at Different Temperatures

We investigate the temperature dependence of the cw-ESR spectra corresponding to the propagating radical responsible of the polymerization of methacrylic monomers. The system can be modelled as a rotator with only one relaxation process, the rotation around the C_α-C_β bond. The simulations clearly indicate that the change of the spectral shape with the temperature is essentially related to the internal flexibility of the radical end.

Introduction

In the last decades, ESR spectroscopy has been a very useful tool to study radical polymerization, [200] allowing a deeper insight in the structure and properties of propagating species, particularly in methacrylic propagating radicals. [200, 201, 202, 203] It has been pointed out the effect of the reaction temperature in these systems not only on the magnitude of the kinetic parameters, [204, 205, 206] but also in the line shape of the spectra obtained at the first steps of the polymerization.

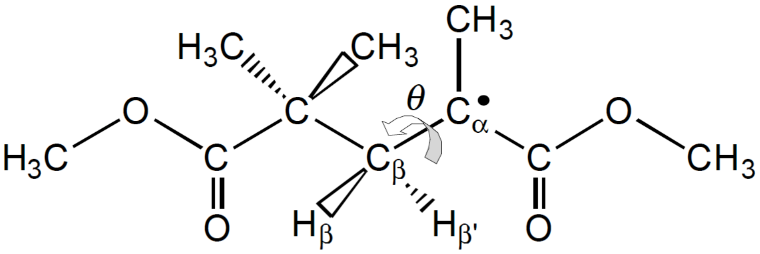

Figure 3-42: Schematic diagram of the methacrylic propagating radical model.

The 13-line spectrum, usually observed in the radical polymerization of methacrylic monomers, is assigned to the propagating radical, resulting from the coupling of the unpaired electron with two methylene and three methyl protons, all in β position to the radical centre (Figure 3-42). The relative peak-to-peak distances in the lines of the spectra deviate from those resulting for a system in fast motional regime. The deviation is more pronounced as the temperature is lowered. This behaviour is not surprising if we take into account that the spectra are a consequence of the internal rotation through the C_α-C_β bond, [207] movement that is expected to be temperature dependent.

The aim of this work is to relate the temperature dependence of the spectral line shape with the internal dynamics at the radical centre by application of the ICA to the simulation of the experimental spectra.

Modelling and interpretation

Simulation of the cw-ESR spectra is based on the implementation and solution of the SLE, so we have to firstly define the main ingredients, i.e. the spin Hamiltonian of the system and the stochastic operator describing the time evolution of the relaxing processes. In ref. [207] it was shown qualitatively that the shape of the spectra is influenced by the internal torsional angle θ, defined in Figure 3-42, describing rotation through the C_α-C_β bond. This fact is due mainly to the high dependency of the hyperfine coupling tensors of the β and β' protons on this torsional angle [208]. The system has been modelled as a flexible rotator with an internal degree of freedom, the torsional angle around the C_α-C_β bond. Furthermore, all magnetic tensors have been found to be nearly isotropic (cfr. next section). This implies that the overall tumbling of the molecule is not coupled to the magnetic properties, so the internal angle θ is the only stochastic variable to be considered.

The magnetic Hamiltonian of the system in our case can be expressed as

$$\hat{\mathcal{H}}\left(\theta\right)/\hbar = \frac{\beta_e}{\hbar} g \boldsymbol{B}_0 \hat{\boldsymbol{S}} + \gamma_e \sum_{n=1}^{5} a_n\left(\theta\right) \hat{\boldsymbol{I}}_n \hat{\boldsymbol{S}} \tag{3.71}$$

where the first term is the Zeeman interaction of the electron spin with the magnetic field $\boldsymbol{B}_0$, and the second term describes the hyperfine interaction of the unpaired electron with the five hydrogen nuclei in β position. We assume that the g-factor is independent on the stochastic variable. Furthermore, for what concerns the hyperfine constants, we consider that only those of the β and β' protons depend on θ, while for the methyl group we use an average value, assuming that its rotation is very fast compared with other relaxation processes in the system.

The spin super-Hamiltonian $\hat{\mathcal{H}}^{\times}$ is usually expressed as the contraction of rank zero of spherical irreducible tensors and tensorial operators of rank zero and two [16, 32]. Due to the isotropy of the magnetic tensors, here the super-Hamiltonian takes the very simple form

$$\hat{\mathcal{H}}^{\times}\left(\theta\right) = \omega_0 F_{g,\,LF}^{(0,\,0)\,*} \hat{A}_{g,\,LF}^{(0,\,0)\,\times} + \sum_{n=1}^{5} \omega_{A_n}\left(\theta\right) F_{A_n,\,LF}^{(0,\,0)\,*} \hat{A}_{A_n,\,LF}^{(0,\,0)\,\times} \tag{3.72}$$

being $\omega_0 = g\beta_e B_0/\hbar$, $F_{g,\,LF}^{(0,\,0)\,*} = F_{A_n,\,LF}^{(0,\,0)\,*} = -\sqrt{3}$, $\hat{A}_{g,\,LF}^{(0,\,0)\,\times} = -\frac{1}{\sqrt{3}}\hat{S}_Z$, $\omega_{A_n} = \gamma_e a_n\left(\theta\right)$ and $\hat{A}_{A_n,\,LF}^{(0,\,0)\,\times} = -\frac{1}{\sqrt{3}}\left[\hat{S}_Z \hat{I}_{Z,n} + \frac{1}{2}\left(\hat{S}_+ \hat{I}_{-,n} + \hat{S}_- \hat{I}_{+,n}\right)\right]$.

To describe the time evolution of the internal torsional angle, we assume that it is subjected to two kinds of motion: *i)* a diffusive motion, which is the rotation about the C$_\alpha$-C$_\beta$ bond, and *ii)* a random walk motion, which can be thought to be originated by the propagation reaction: when a monomer molecule reacts with a propagating radical, the new formed radical may have a different value of the internal angle, generating the random jump.

The time evolution of the probability density $P(\theta, t)$ is

$$\frac{\partial}{\partial t} P\left(\theta, t\right) = -\hat{\Gamma} P\left(\theta, t\right) = -\hat{\Gamma}_D P\left(\theta, t\right) - \hat{\Gamma}_{RW} P\left(\theta, t\right) \tag{3.73}$$

where the subscripts D and RW stand for diffusive and random walk, respectively. The diffusive operator is

$$\hat{\Gamma}_D = -\frac{\partial}{\partial \theta} D_{II}\left(\theta\right) P_{eq}\left(\theta\right) \frac{\partial}{\partial \theta} P_{eq}^{-1}\left(\theta\right) \tag{3.74}$$

where $D_{II}(\theta)$ is the diffusion coefficient and $P_{eq}(\theta)$ is the Boltzmann distribution in the θ space, defined as $P_{eq}(\theta) = \exp\left[-V(\theta)/\mathrm{k_B}T\right]/\langle\exp\left[-V(\theta)/\mathrm{k_B}T\right]\rangle$, being $V(\theta)$ the internal potential.

The random walk operator, in its integrated form, is given by

$$\hat{\Gamma}_{RW} P(\theta,t) = -\int_0^{2\pi} d\theta' \left[P(\theta,t) W(\theta \leftarrow \theta') - P(\theta',t) W(\theta' \leftarrow \theta) \right] \tag{3.75}$$

and its properties depend on the transformation kernel. We take the simplest choice

$$W(\theta \leftarrow \theta') = \omega_{RW} P_{eq}(\theta') \tag{3.76}$$

i.e. the probability of jumping from θ to θ' depends only on the arriving value of the angle and on the jumping frequency ω_{RW}.

The substitution of the kernel (3.76) in the expression of the operator (3.75) reads

$$\hat{\Gamma}_{RW} P(\theta,t) = \omega_{RW} \left[P(\theta,t) - P_{eq}(\theta) \right] \tag{3.77}$$

It is useful to transform the time evolution operator in such a way that it becomes Hermitian; this is achieved by the symmetrization operation $\tilde{\Gamma} = P_{eq}^{-1/2}(\theta)\hat{\Gamma}P_{eq}^{1/2}(\theta)$, that gives

$$\begin{aligned} \tilde{\Gamma}\tilde{P}(\theta,t) &= -P_{eq}^{-1/2}(\theta) \frac{\partial}{\partial\theta} D_{II}(\theta) P_{eq}(\theta) \frac{\partial}{\partial\theta} P_{eq}^{-1/2}(\theta) \tilde{P}(\theta,t) + \\ &\quad -\omega_{RW} \left[\tilde{P}(\theta,t) - P_{eq}^{1/2}(\theta) \int_0^{2\pi} d\theta' P_{eq}^{1/2}(\theta') \tilde{P}(\theta',t) \right] \end{aligned} \tag{3.78}$$

with $\tilde{P}(\theta,t) = P(\theta,t)/P_{eq}^{1/2}(\theta)$.

Finally, the cw-ESR signal is calculated as the spectral density [16]

$$I(\omega-\omega_0) = \frac{1}{\pi}\mathcal{R}e\left\{ \langle\langle vP_{eq}^{1/2}(\theta) \,|\, \left[i(\omega-\omega_0) + \tilde{\mathcal{L}} \right]^{-1} |\, vP_{eq}^{1/2}(\theta)\rangle\rangle \right\} \tag{3.79}$$

where ω is the sweep frequency, and $|\, vP_{eq}^{1/2}(\theta)\rangle\rangle$, called starting vector, is an operator representing the physical observable, i.e. the magnetization along the X-axis; in the current case we have

$$|\, v\rangle\rangle = 2^{-5/2} |\, \hat{S}_X \otimes \mathbf{1}_{I_1} \otimes \mathbf{1}_{I_2} \otimes \mathbf{1}_{I_3} \otimes \mathbf{1}_{I_4} \otimes \mathbf{1}_{I_5} \otimes P_{eq}^{1/2}(\theta)\rangle\rangle \tag{3.80}$$

The basis set that we choose to span the operator and calculate the spectrum is given by the direct product $|\,\Sigma\rangle\rangle = |\,\sigma\rangle\rangle \otimes |\, n\rangle\rangle$ where

$$|\,\sigma\rangle\rangle = |\, p^S q^S, p_1^I q_1^I, p_2^I q_2^I, p_3^I q_3^I, p_4^I q_4^I, p_5^I q_5^I\rangle\rangle \tag{3.81}$$

$$|\, n\rangle\rangle = \frac{1}{\sqrt{2\pi}} e^{-in\theta} \tag{3.82}$$

The spin part, $|\,\sigma\rangle\rangle$, is obtained from the direct product of the transitions spaces [16] of the electron and the five hydrogen atoms.

To calculate the spectrum via the Lanczos algorithm we need to build the matrix representation of the Liouvillean, which is constituted by elements of the type $\langle\langle\Sigma\,|\hat{\mathcal{L}}|\,\Sigma'\rangle\rangle$. They are given in detail in Appendix E.3 together with the evaluation of the projections of the basis on the starting vector.

Different aspects related to the structural, dynamical and magnetic properties of the system under investigation are considered by the SLE just defined. There are seven parameters: five hyperfine coupling constants, the internal diffusion coefficient and the jumping frequency. The ICA protocol gives us the possibility to predict *ab inito* all the parameters but the jumping frequency. The latter has not a clear molecular interpretation so it is consider as a free parameter (the only) to be fitted.

Quantum mechanical calculations According to the results reported in a previous work, [207] a simple system consisting of two monomeric units of methyl methacrylate can be considered as an adequate propagating radical model to reproduce the magnetic properties of the radical centre (Figure 3-42). As above explained, the shape of the spectra depends on the internal torsional angle θ, since the hyperfine coupling tensors of the two β and β' protons vary on this angle [208]. In order to assess quantitatively this dependency, we evaluate the tensors on the structures resulting when varying θ from 0° to 360°. DFT methodology has been employed, specifically the B3LYP functional, which is an hybrid method including the Beckes three parameter exchange functional with the non-local correlation functional of Lee, Yang and Parr. Due to the large size of the analysed system, the computations were performed using two basis sets of contracted Gaussian functions, namely 6-31G* and TZVP [53]. The first one, 6-31G*, is a relatively small basis set including a quality double-ζ plus polarization and a contraction scheme for the second-row elements of (10s4p1d)/[3s2p1d], whereas TZVP is a DFT-optimized valence triple-ζ basis set. The smaller one, 6-31G*, was used to optimize the geometry of the most stable conformation of the radical model, and the TZVP was employed later to obtain the hyperfine tensors as a function of θ. It has been demonstrated that this computational protocol, B3LYP/TZVP//B3LYP/6-31G*, is very adequate to carry out calculations of coupling constants of medium size radicals since

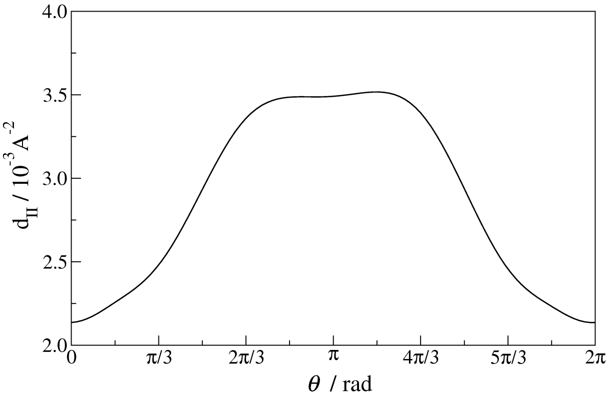

Figure 3-43: Dependence of the reduced internal diffusion coefficient on the internal torsional angle.

it provides accurate values of this property [209, 210]. From these computations, the internal torsional potential is obtained too, which is needed to evaluate the Boltzmann distribution in the θ space. Finally, we obtain also the $\boldsymbol{g}$ tensor of the unpaired electron, which is weakly dependent on θ.

These quantum mechanical calculations reveal a low anisotropy in both Zeeman and hyperfine tensors so, as a rough approximation, we consider them as isotropic. As a consequence, the coupling with overall rotation can be assumed as negligible. The decoupling of spin and global rotational coordinates lead to simplified numerical procedure for solving the resulting SLE, which contains only the internal angle θ as relevant relaxation process, but includes coupling explicitly with all the five hydrogen nuclei that give the main contribution to the shape of the spectrum via hyperfine interaction.

Evaluation of diffusion properties The evaluation of the diffusion properties of the propagating radical model is based on the hydrodynamic approach [36, 57] discussed in Chapter 2. Due to the fact that we are assuming isotropic magnetic tensors, only one dynamical process has to be taken under consideration, i.e. the rotation about the C$_\alpha$-C$_\beta$ bond described by the stochastic variable θ, so from the full diffusion tensor of the molecule, represented by a 7×7 matrix, only the pure internal part, D_{II}, is needed. It is a scalar and, in general, it depends on the geometry, so in principle it has to be considered as a function of the internal angle θ. Figure 3-43 represents the dependence of the reduced internal diffusion coefficient on θ. The reduced coefficient is given as $d_{II} = D_{II}(\pi C R_e \eta / \mathrm{k_B} T)$, which depends only on molecular geometry and not on fluid properties and temperature. As can be

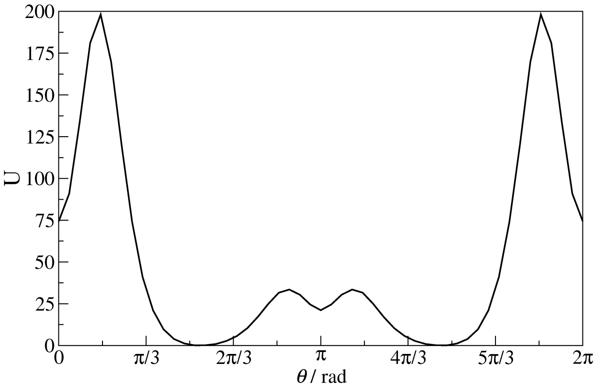

Figure 3-44: Potential energy curve of the propagating radical model as a function of the internal torsional angle θ at 333K ($U = V/\mathrm{k_B}T$), computed at B3LYP/TZVP level.

seen, there is only a little dependence on the internal angle, so we approximate the diffusion coefficient to a constant equal to the value calculated in the minimum energy configuration.

Results and discussion

Torsional potential From the DFT calculations, we extract the internal torsional potential, $V(\theta)$. The computed dependence at 333 K, in $\mathrm{k_B}T$ units, that is $U(\theta) = V(\theta)/\mathrm{k_B}T$, is represented in Figure 3-44. The function is almost symmetric, with two potential wells corresponding to the most stable conformations, located at 96° and 264°. There are two very large barriers ($U \approx 200$) at about 30° and 330° and two other lower, but still large barriers ($U \approx 30$) at about 160° and 200°. This kind of potential implies that the motion about the C_α-C_β bond is confined within the two minima.

The explicit dependence on the torsional angle θ of the potential is obtained expanding the potential over the set of basis functions (3.82). We employ a truncated Fourier sum to represent the potential trend $U(\theta) = \sum_n \epsilon_n e^{-in\theta}$, where $\epsilon_n = \epsilon^*_{-n}$ is assumed to assure that the potential is a real quantity.

Hyperfine coupling constants and g-tensor Figure 3-45 shows the computed isotropic hyperfine coupling constants (hfccs) corresponding to H_β and $\mathrm{H}_{\beta'}$ as functions of the internal torsional angle. According to these calculations, the hyperfine constants of the β and β' protons corresponding to the most stable conformations ($\theta = 96°$ and 264°) are 14.0 and 8.8 G, and the calculated average value corresponding to the protons of the methyl group is 22.5 G. These computed hfccs are in very good agreement with the data obtained from

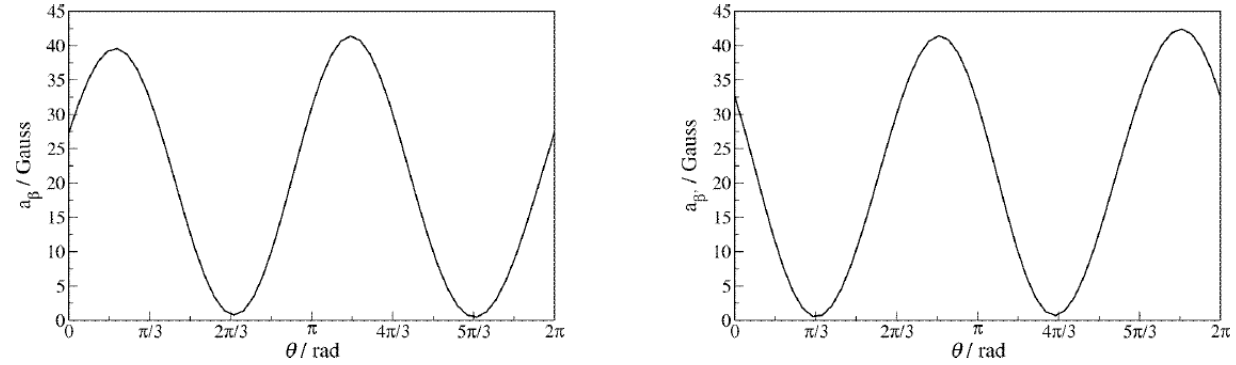

Figure 3-45: Isotropic hyperfine coupling constants of β (left) and β' (right) protons of the propagating radical model as a function of the internal torsion angle , computed at B3LYP/TZVP level.

the experimental spectra [206], which are 14.1, 8.6 and 22.5 G, respectively. Besides, the predicted constants for H_β and $H_{\beta'}$ follow the expected dependence with θ, that is, the well known empirical relation proposed by Heller and McConnell, in which the hfccs of β protons belonging to carbon-center π radicals, such as methacrylic ones, vary with the squared cosine of θ [208]. The agreement between the predicted hfccs by DFT methodology and by Heller and McConnell relation is excellent. These results support the validity of the proposed computational protocol for the calculation and prediction of this magnetic property.

To obtain the explicit dependence of both the coupling constants on θ, we proceed again by expanding over complex exponentials: $a(\theta) = \sum_{n=-4}^{4} a_n e^{-in\theta}$.

Finally, the DFT calculations showed that the $\boldsymbol{g}$-tensor has a weak anisotropy and that it is also independent on the value of the internal angle. Thus, we considered it as an isotropic term, the computed value of which is 2.0046.

Diffusion coefficient The values of the diffusion coefficient, D_{II}, at temperatures in the range 273 - 393 K have been obtained according to the above described hydrodynamic approach, employing an effective radius of 2.0 Å, stick boundary conditions ($C = 6$), and the viscosity of the solution of monomer in toluene at each temperature, $\eta(T)$ (Table 3.9). We performed the calculations on radicals with different chain length, from the dimer till a 100-monomer units system. Figure 3-46 shows how the reduced internal diffusion coefficient changes as the number of monomeric units increases. As we expected, the value of this coefficient reaches a *plateau* and we decided to use this limit value in the calculation of the

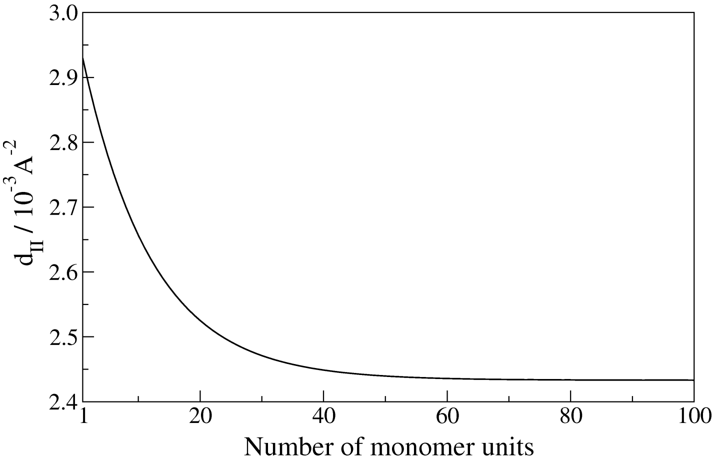

Figure 3-46: Dependence of the reduced internal diffusion coefficient on the number of monomeric units constituting the propagating radical.

spectra.

The values of the diffusion coefficient obtained at the five considered temperatures are gathered in Table 3.9.

Cw-ESR spectra The cw-ESR spectra were simulated according to the defined approach that integrates all the parameters previously computed. The only free parameter, determined via fitting, is the jumping frequency. In fact, we do not really know the origin of the random walk, so it is not possible to calculate this frequency *a priori.* We think that the random walk is related to the propagation reaction, which is taking place during the registration of the spectra. It is plausible that the new radical generated by the addition of a monomer unit, has a different value of the torsional angle than the original one. In this way, the chemical reaction disturbs the relaxation of θ, giving an effective higher relaxation time. The reaction can occur if one reactant encounters the other and the approach of the two molecules is governed by the translational diffusion. This hypothesis is supported by the temperature be-

T / K	η / 10^3 Pa s	D_{II} / 10^8 Hz	ω_{RW} / 10^7 Hz
273	1.667	1.5	1.84
303	1.047	2.6	1.06
333	0.715	4.1	0.61
363	0.520	6.2	0.44
393	0.397	8.8	0.31

Table 3.9: Viscosity of the monomer in toluene solution (η), diffusion coefficient (D_{II}) and jumping frequency (ω_{RW}) at different temperatures.

haviour that we found, reported in Table 3.9. As can be seen, the jumping frequency follows the same temperature dependence that the viscosity.

Figure 3-47 shows the theoretical spectra compared with the experimental ones registered at the beginning of the photopolymerization of TRIS in the temperature range from 273 to 393 K. It is well known that the shape of these spectra changes with monomer conversion due to the increase of the viscosity [207]. In order to avoid this effect, the spectra were registered at the very beginning of the polymerization, when the conversion of monomer into polymer is very low and, thus, the viscosity of the medium has scarcely increased. Therefore, we can assume that the changes in the shape of these spectra are mainly due to the effect that the temperature prompts on the internal rotation.

The experimental 13-lines ESR spectra shown in Figure 3-47 can be interpreted as the result of the hyperfine coupling of the unpaired electron with the methylene protons (β and β') and the three protons of the methyl group, with the overlap of some lines. For comparison sake, spectra have been normalized. The relative peak-to-peak intensities of the lines deviate from the 1:1:1:4:3:3:6:3:3:4:1:1:1 ratio expected for a system in fast motional regime where the internal dynamics does not affect the spectral profile. In particular, the heights of the inner pairs (lines 2, 3, 5, 6, 8, 9, 11 and 12) are lower. As it can be easily seen in this figure, the variation in relative intensities becomes more pronounced when lowering the temperature.

Comparison of simulated and experimental spectra shows that the agreement between experimental and simulated results is reasonably good, qualitatively and even quantitatively, in all the temperature range.

Conclusions

Simulation of the cw-ESR spectra of the propagating radical present during the polymerization of methacrylic monomers at different temperatures have been carried out by using an Integrated Computational Approach that provides the spectral profile solving the Stochastic Liouville Equation. The propagating radical has been modelled as a flexible rotator with an internal degree of freedom, the rotation around the C_α-C_β bond, the motion of which is not purely diffusive but has also a random walk component.

The jumping frequency follows the same temperature dependence that the viscosity, which suggests that the origin of the random walk is related to the propagation reaction.

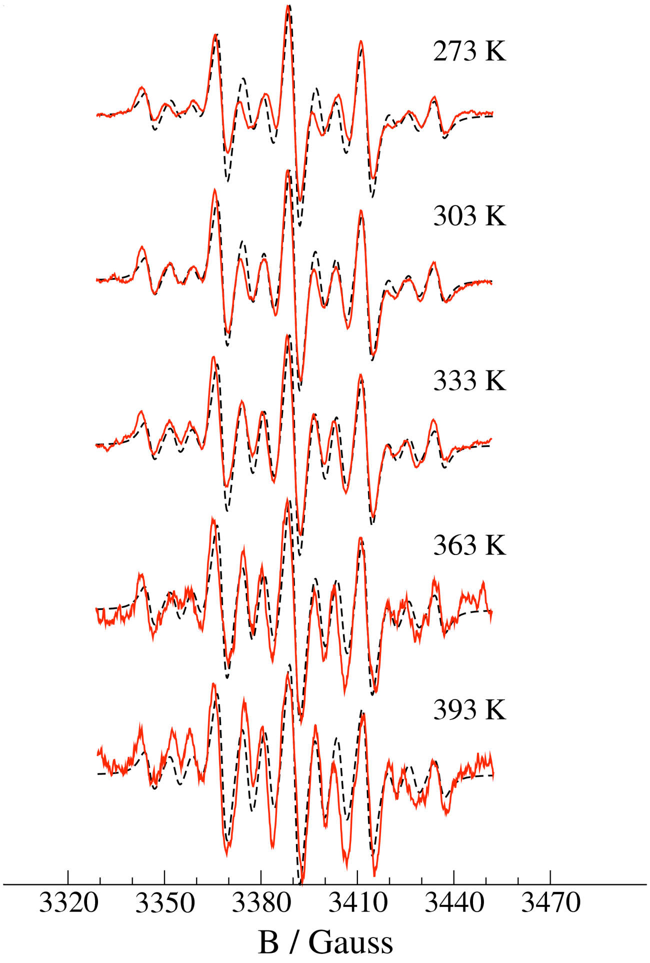

Figure 3-47: Experimental (solid lines) and simulated (dashed lines) spectra of polymerization of TRIS at different temperatures.

Although the employed theoretical model is quite simple (isotropic magnetic tensors and only one relaxing process), it has the main ingredients to describe and interpret the properties of a complex system, as the one investigated in this work. Furthermore, it has to be underlined the accuracy of the methodologies integrated in the ICA to predict magnetic and diffusive parameters that enter in the SLE. This is a very important point in the interpretation of cw-ESR spectra because the parameters have a clear physical molecular interpretation, which is not always ensured if all them are fitted.

The simulated spectra agree well with the experimental ones, qualitatively and even quantitatively, for all the studied range of temperature, which confirms the hypothesis that the internal torsion around the C_α-C_β bond is responsible of the variation in the relative intensities of the spectral lines with temperature.

Chapter 4

Nuclear Magnetic Resonance

Spectroscopic techniques, both magnetic and optical, are widely used in structural and dynamical investigation of microscopic parameters of biomolecules [211] and, in particular, nuclear magnetic resonance (NMR) spectroscopy is an important and powerful experimental technique for characterizing the microdynamics of proteins. Main physical observables are the T_1, T_2 and NOE relaxation parameters of ^{15}N, ^{2}H and ^{13}C nuclei, which are very sensitive to dynamics, i.e. molecular motions have characteristic relaxation times comparable to the nuclear spin relaxations. Isotopic enrichment can be targeted to single residues of the protein, leading to the possibility of understanding localized dynamics (e.g. studying conformational motions specifically in the active site of the protein) and, moreover, comparison of data coming from different residues of the same protein allows to make spatial (structural) considerations.

NMR relaxation data depend on dipolar (^{15}N and ^{13}C) and quadrupolar (^{2}H) interactions, on chemical shift anisotropy and cross-correlation effects. NMR relaxations can be written as functions of the spectral densities of the magnetic interactions, calculated within the theoretical framework describing the dynamics of the system.

A first approach was proposed by Lipari and Szabo [212, 213] with their "Model Free" (MF) analysis. This approach is based on considering the presence of two uncoupled motions in the system: the global tumbling of the protein and the local motion of the probe. The assumption of decoupling leads to an easy formulation for the spectral density, as the sum of spectral densities calculated from two different motions. Simple mathematical expressions and fast calculations come from this approach, together with a number of limitations, leading to a restricted range of validity. The two most important shortcomings of the approach at least in its primitive formulation are: *i)* MF considers an isotropic global tumbling of the protein so that is works well with globular proteins, but not with other molecules having markedly non-spherical shapes; *ii)* fails to reproduce NMR data when the time scales of the motions are similar, i.e. where the decoupling approximation cannot be assumed *a priori*.

An advanced phenomenological model describing two coupled dynamical processes was introduced by Polimeno and Freed [32, 139], originally for the interpretation of electron spin resonance (ESR) of probes in ordered phases like liquid crystals and glasses [31, 130]. The model is known as the slowly relaxing local structure (SRLS) approach, and it is based on a two-body Smoluchowski equation describing the coupled motion of two rigid rotors. SRLS has been applied by Meirovitch et al. [214, 215, 216] to the interpretation of NMR data. Due to the fact that coupled relaxation is taken into account rigorously and because the interaction potential can be interpreted in terms of local ordering imposed by the protein to the probe, the SRLS model has been shown to give good fittings even in that cases that are out of the range of validity of the MF approach.

On the minus side, SRLS is less intuitive than MF and requires some considerable mathematical apparatus. In order to favour the usage of this approach, it is required a simple-to-use implementation that "hides" as much as possible the computational details, letting the user work routinely in a simple way. To this purpose, we developed the C^{++}OPPS (COupled Protein Probe Smoluchowski) package, which is a program aimed to the interpretation of NMR data based on the SRLS model.

C^{++}OPPS implementation takes advantage of the potentiality of C++ for writing fast programs with dynamic allocation of memory. Moreover, thanks to object oriented programming, the classes that build-up the program are easily re-usable and modifiable.

From physico-chemical point of view includes: 1) the possibility of considering full diffusion tensors for both the protein and the probe, 2) potential expansion till fourth rank terms, 3) the possibility to predict the diffusion tensor of the protein via a hydrodynamic model reducing the number of free parameters.

From a strictly computational point of view, parallelization was employed where possible. C^{++}OPPS can run on a local machine (with and without parallelization), or on clusters with access *via* a web interface. Finally, C^{++}OPPS has a Graphical User Interface (GUI) to control the work flow of a calculation in a simple and friendly way.

4.1 Two-body stochastic models

Magnetic relaxation times T_1, T_2 and NOE of ^{15}N, ^{13}C and ^{2}H nuclei, depend on dipolar (^{15}N and ^{13}C) and quadrupolar (^{2}H) interactions, on chemical shift anisotropy and cross-correlation effects. At present C^{++}OPPS includes as spin probe the ^{15}N-^{1}H bond for which, following standard Bloch theory [15], it is possible to express the NMR relaxation times as functions of the spectral densities $J^D(\omega)$ (dipolar interaction) and $J^C(\omega)$ (chemical shift anisotropy):

$$\begin{aligned}
\frac{1}{T_1} &= d^2\left[J^D(\omega_H-\omega_N)+3J^D(-\omega_N)+6J^D(\omega_H+\omega_N)\right]+c^2J^C(-\omega_N)\\
\frac{1}{T_2} &= d^2\left[4J^D(0)+J^D(\omega_H-\omega_N)+3J^D(-\omega_N)+3J^D(\omega_H)+6J^D(\omega_H+\omega_N)\right]+\\
&\quad+\frac{c^2}{3}\left[3J^C(-\omega_N)+4J^C(0)\right]\\
NOE &= 1+d^2\frac{\gamma_H}{\gamma_N}T_1\left[6J^D(\omega_H+\omega_N)-J^D(\omega_H-\omega_N)\right] \qquad (4.1)
\end{aligned}$$

where $d = \mu_0\gamma_H\gamma_N/4\pi r_{NH}^3$, $c = \sqrt{2/15}\omega_N/\delta_{CSA}$, δ_{CSA} is the anisotropy of chemical shift tensor and ω_A is the Larmor frequency of nucleus A.

Spectral densities are calculated within the framework of the theoretical model for the dynamical evolution of the system. As underlined in the introduction section, an advanced approach that is actually available is the so called slowly relaxing local structure (SRLS) model [32, 139]. It consists on a two-body Smoluchowski equation that describes the time evolution of the density probability of two relaxation processes (at different time scales) coupled by an interaction potential. In the application of this model to the description of protein dynamics, the two relaxing processes are interpreted as the slow global tumbling of the whole protein and the relatively fast local motion of the spin probe, the local motion of the ^{15}N-^{1}H bond in our case. Both the processes are described as rigid rotators the motion of which is coupled by a potential correlating their relaxation and that is interpreted as the local ordering that the molecule imposes to the probe.

In this Chapter we give a summary overview on how the SRLS model is applied to the interpretation of NMR data. Although the implementing code is written so that the user

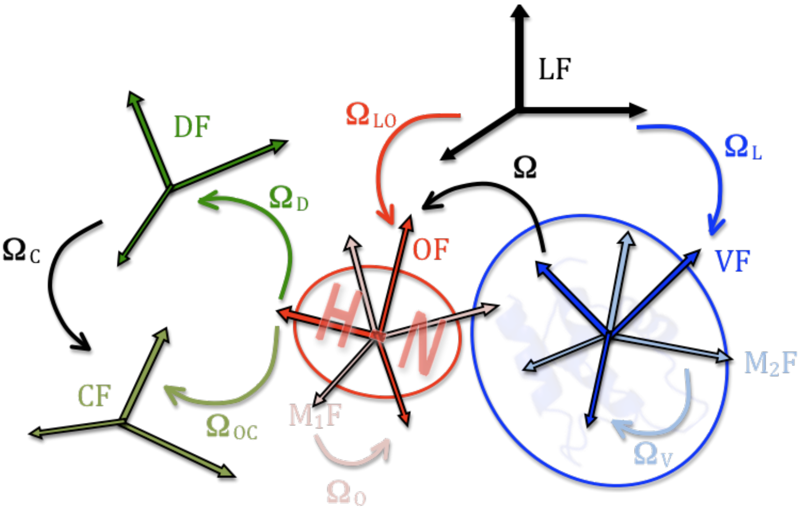

Figure 4-1: Definition of frames and Euler angles in the SRLS model applied to NMR.

does not need to be concerned with technical details, it is of fundamental importance to understand the physical interpretation of the system in order to fully comprehend the input data to pass to the program and to provide a sensible interpretation. Physical data can be classified in dissipative (diffusion tensors) and structural (Euler angles, potential coefficients) parameters. Figure 4-1 shows a schematic picture of the model. It is necessary to introduce a number of reference frames, taking Figure 4-1 as reference:

- LF is the fixed inertial laboratory frame;
- M_1F is the protein fixed frame where the diffusion tensor of the protein, ${}^{M_1}\boldsymbol{D}_1$, is diagonal;
- M_2F is the protein fixed frame where the diffusion tensor of the probe, ${}^{M_2}\boldsymbol{D}_2$, is diagonal;
- VF is the protein fixed frame having the z-axis aligned with the director of the orienting potential;
- OF is the probe fixed frame the z-axis of which tends to be aligned to the director of the potential;
- DF is the probe fixed frame where the dipolar interaction is diagonal;

- CF is the probe fixed frame where the chemical shift tensor is diagonal.

To complete the picture, we need to define the set of Euler angles that transform one frame to the other:

- $\boldsymbol{\Omega}_L$ transform from LF to VF, while $\boldsymbol{\Omega}_{LO}$ transform from LF to OF;
- $\boldsymbol{\Omega}$ transform from VF to OF;
- $\boldsymbol{\Omega}_V$ transform from M$_1$F to VF;
- $\boldsymbol{\Omega}_O$ transform from M$_2$F to OF;
- $\boldsymbol{\Omega}_D$ transform from OF to DF, while $\boldsymbol{\Omega}_{OC}$ transform from OF to DF;
- $\boldsymbol{\Omega}_C$ transform from CF to DF.

The system dynamics is fully described by two independent sets of stochastic Euler angles and in particular our choice is for the set of Euler angles $\boldsymbol{\Omega}_L$, giving the orientation of the protein respectively to the laboratory frame, and $\boldsymbol{\Omega}$, which represent the relative orientation of the probe and the protein. Using this set of stochastic variables, $\boldsymbol{X} = (\boldsymbol{\Omega}, \boldsymbol{\Omega}_L)$, the diffusion operator describing the time evolution of the density probability of the system is

$$\begin{aligned}\hat{\Gamma}(\boldsymbol{X}) &= {}^{O}\hat{\boldsymbol{J}}^{\dagger}(\boldsymbol{\Omega})\,{}^{O}\boldsymbol{D}_2 P_{eq}(\boldsymbol{X})\,{}^{O}\hat{\boldsymbol{J}}(\boldsymbol{\Omega})\,P_{eq}^{-1}(\boldsymbol{X}) + \\ &+ \left[{}^{V}\hat{\boldsymbol{J}}(\boldsymbol{\Omega}) - {}^{V}\hat{\boldsymbol{J}}(\boldsymbol{\Omega}_L)\right]^{\dagger}\,{}^{V}\boldsymbol{D}_1 P_{eq}(\boldsymbol{X})\left[{}^{V}\hat{\boldsymbol{J}}(\boldsymbol{\Omega}) - {}^{V}\hat{\boldsymbol{J}}(\boldsymbol{\Omega}_L)\right]P_{eq}^{-1}(\boldsymbol{X}) \qquad (4.2)\end{aligned}$$

where ${}^{O}\boldsymbol{D}_2$ is the diffusion tensor of the probe in OF, ${}^{V}\boldsymbol{D}_1$ is the diffusion tensor of the protein in VF and the equilibrium distribution, $P_{eq}(\boldsymbol{X})$ is given by

$$P_{eq}(\boldsymbol{X}) = \mathcal{N}\exp\left[-V(\boldsymbol{\Omega}, \boldsymbol{\Omega}_L)/\mathrm{k_B}T\right] \qquad (4.3)$$

with $\mathrm{k_B}$ the Boltzmann constant and T the absolute temperature.
We shall assume that the protein is immersed in an isotropic medium, so the equilibrium distribution is independent on $\boldsymbol{\Omega}_L$ and the total potential is only the interaction potential between the two processes for which we take the following expansion over Wigner matrices:

$$\begin{aligned}-V(\boldsymbol{\Omega})/\mathrm{k_B}T &= c_0^2\mathcal{D}^2_{0\,0}(\boldsymbol{\Omega}) + c_2^2\left[\mathcal{D}^2_{0\,-2}(\boldsymbol{\Omega}) + \mathcal{D}^2_{0\,2}(\boldsymbol{\Omega})\right] + c_0^4\mathcal{D}^4_{0\,0}(\boldsymbol{\Omega}) + \\ &+ c_2^4\left[\mathcal{D}^4_{0\,-2}(\boldsymbol{\Omega}) + \mathcal{D}^4_{0\,2}(\boldsymbol{\Omega})\right] + c_4^4\left[\mathcal{D}^4_{0\,-4}(\boldsymbol{\Omega}) + \mathcal{D}^4_{0\,4}(\boldsymbol{\Omega})\right] \qquad (4.4)\end{aligned}$$

Due to the fact that this is a pure rotational problem, observables are expressed as spectral densities, i.e. Fourier - Laplace transforms of correlation functions of Wigner functions of the absolute probe Euler angles, $\mathbf{\Omega}_{LO} = \mathbf{\Omega} + \mathbf{\Omega}_L$

$$j_{k,k'}(\omega) = \langle \mathcal{D}^{j}_{m\,k}(\mathbf{\Omega}_{LO})\, P_{eq}(\mathbf{\Omega}_{LO}) \,|\, \left(i\omega - \hat{\Gamma}\right)^{-1} |\mathcal{D}^{j'}_{m'\,k'}(\mathbf{\Omega}_{LO})\, P_{eq}(\mathbf{\Omega}_{LO})\rangle \tag{4.5}$$

Considering the symmetry of the magnetic interactions (dipolar and chemical shift anisotropy) contributing to the spin Hamiltonian of the system for ^{15}N-^{1}H probe, only physical observables with $j = j' = 2$ and $m = m' = 0$ have to be considered.

From these spectral densities it is possible to calculate the spectral densities for every magnetic interaction, μ (dipolar, CSA), as

$$J^{\mu}(\omega) = \sum_{k,k'=-2}^{2} \left[\mathcal{D}^{2\,*}_{k\,0}(\mathbf{\Omega}_{\mu})\, \mathcal{D}^{2}_{k'\,0}(\mathbf{\Omega}_{\mu})\right] j_{k,k'}(\omega) \tag{4.6}$$

being $\mathbf{\Omega}_{\mu}$ the set of Euler of angles transforming from OF to the frame where the μ-th magnetic tensor is diagonal.

Calculation of spectral densities $j_{k,k'}(\omega)$ is achieved by spanning the diffusive operator over a proper basis set. In such a way one moves the problem of calculating integrals in eq. (4.5) to a classical linear algebra problem. The basis onto which the operator is spanned is given by the direct product $|\Lambda\rangle = |\lambda_1\rangle \otimes |\lambda_2\rangle = |L_1 M_1 K_1\rangle \otimes |L_2 M_2 K_2\rangle$, where

$$|L_1 M_1 K_1\rangle = \sqrt{\frac{(2L_1+1)}{8\pi^2}}\mathcal{D}^{L_1}_{M_1\,K_1}(\mathbf{\Omega}_L) \tag{4.7}$$

$$|L_2 M_2 K_2\rangle = \sqrt{\frac{(2L_2+1)}{8\pi^2}}\mathcal{D}^{L_2}_{M_2\,K_2}(\mathbf{\Omega}) \tag{4.8}$$

This basis is infinite and to practically solve the problem the expansion have to be truncated at a certain value of the principal numbers L_1 and L_2. For what concerns the basis expansion for the protein ($\{\lambda_1\}$) the truncation is fixed by the symmetry of the physical observables to $L_1 = 2$ and $M_1 = 0$. So only one truncation parameter remains, i.e. L_2. Given a maximum value, $L_{2,MAX}$, the dimension of the basis (in absence of other symmetries) will be

$$N = 5\sum_{i=0}^{L_{2,MAX}} (2i+1)^2 = \frac{5}{3}\left(L_{2,MAX}+1\right)\left(2L_{2,MAX}+1\right)\left(2L_{2,MAX}+3\right) \tag{4.9}$$

It is simpler to work with auto-correlation functions so instead of calculating directly spectral densities in eq. (4.5) we define the function $2C_{k,k'} = \mathcal{D}^{2}_{0\,k} + \mathcal{D}^{2}_{0\,k'}$ and calculate the symmetrised spectral densities

$$j^S_{k,k'}(\omega) = \langle C_{k,k'}(\mathbf{\Omega}_{LO}) P_{eq}(\mathbf{\Omega}_{LO}) | \left(i\omega - \hat{\Gamma}\right)^{-1} | C_{k,k'}(\mathbf{\Omega}_{LO}) P_{eq}(\mathbf{\Omega}_{LO}) \rangle \tag{4.10}$$

and then obtain the $j_{k,k'}(\omega)$ functions as linear combinations of the symmetrised spectral densities:

$$j_{k,k'}(\omega) = \left[2\left(1+\delta_{k,k'}\right) j^S_{k,k'}(\omega) - j^S_{k,k}(\omega) - j^S_{k',k'}(\omega)\right]/10 \tag{4.11}$$

Using the closure relation for the basis $|\Lambda\rangle$, integral in eq. (4.10) can now be re-written in matrix form as

$$j^S_{k,k'} = \boldsymbol{v}^t \left(i\omega\mathbf{1} - \mathbf{\Gamma}\right)^{-1} \boldsymbol{v} \tag{4.12}$$

where

$$(\mathbf{\Gamma})_{i,j} = \langle \Lambda_i | \hat{\Gamma} | \Lambda_j \rangle \tag{4.13}$$

$$(\boldsymbol{v})_i = \langle \Lambda_i | C_{k,k'}(\mathbf{\Omega}_{LO}) P_{eq}(\mathbf{\Omega}_{LO}) \rangle \tag{4.14}$$

Details on evaluation of equations 4.13 and 4.14 are reported in appendix G.
Because of the high dimensions of the basis we employ the Lanczos tridiagonalization [20, 106] an iterative algorithm that creates, at every step n, a tridiagonal symmetric matrix $\boldsymbol{T}_n$, which is an approximation of the matrix associated to the diffusive operator. The transformation between the two matrices is achieved via the orthonormal matrix $\boldsymbol{Q}_n$:

$$\boldsymbol{T}_n = \boldsymbol{Q}^t_n \mathbf{\Gamma} \boldsymbol{Q}_n \tag{4.15}$$

so at a given iteration step n, the approximant $j^S_{k,k',n}(\omega)$ to $j^S_{k,k'}(\omega)$ is given by

$$j^S_{k,k',n}(\omega) = \left(\boldsymbol{Q}^t_n \boldsymbol{v}\right)^t \left(i\omega\mathbf{1}_n + \boldsymbol{T}_n\right)^{-1} \left(\boldsymbol{Q}^t_n \boldsymbol{v}\right) \tag{4.16}$$

and by making use of the orthonormality of $\boldsymbol{Q}_n$ it is possible to see that the last equation reduces to

$$j^S_{k,k',n}(\omega) = \left(i\omega\mathbf{1}_n + \boldsymbol{T}_n\right)^{-1}_{1,1} \tag{4.17}$$

i.e. the n-th approximant to the symmetrised spectral density is the (1,1) element of the inverse of the matrix $(i\omega\mathbf{1}_n + \boldsymbol{T}_n)$. Finally, it can be shown that $j^S_{k,k',n}(\omega)$ can be expressed as a continued fraction

$$j^S_{k,k',n}(\omega) = \cfrac{1}{\alpha_1 - i\omega - \cfrac{\beta_1^2}{\alpha_2 - i\omega - \cfrac{\beta_2^2}{\alpha_3 - i\omega - \cdots}}} \tag{4.18}$$

where $\boldsymbol{\alpha}$ is the n-dimensional vector containing the diagonal of $\boldsymbol{T}_n$ and $\boldsymbol{\beta}$ is the $(n-1)$-dimensional vector containing the sub-diagonal of the tridiagonal matrix.
Just to summarize, the whole procedure that is implemented in C^{++}OPPS is divided in the following steps:

1) build the matrix associated to the diffusive operator $\boldsymbol{\Gamma}$, eq. (4.13);

2) build the starting vector $\boldsymbol{v}$ eq. (4.14);

3) perform Lanczos tridiagonalization to calculate symmetrised spectral densities $j^S_{k,k'}(\omega)$, eq. (4.5);

4) build the spectral densities $j_{k,k'}(\omega)$ as linear combination of the symmetrised ones, eq. (4.11);

5) build the spectral densities of magnetic interactions $J^\mu(\omega)$, eq. (4.6);

6) calculate T_1, T_2 and NOE relaxation times as linear combinations of $J^\mu(\omega)$ functions, eq. (4.1).

4.2 C^{++}OPPS software

C^{++}OPPS is a modular software, a package of programs each having a particular specific task in the work flow of a simulation. The main division is between core programs, written in C/C++, which are aimed to perform the heavy computations, and the graphical user interface (GUI) that is the front-end program that interprets user's decisions and calls the right core programs. A pictorial view of the organization of C^{++}OPPS is given in Figure 4-2. First, a call to the Babel program [108] is required in order to translate the input geometry,

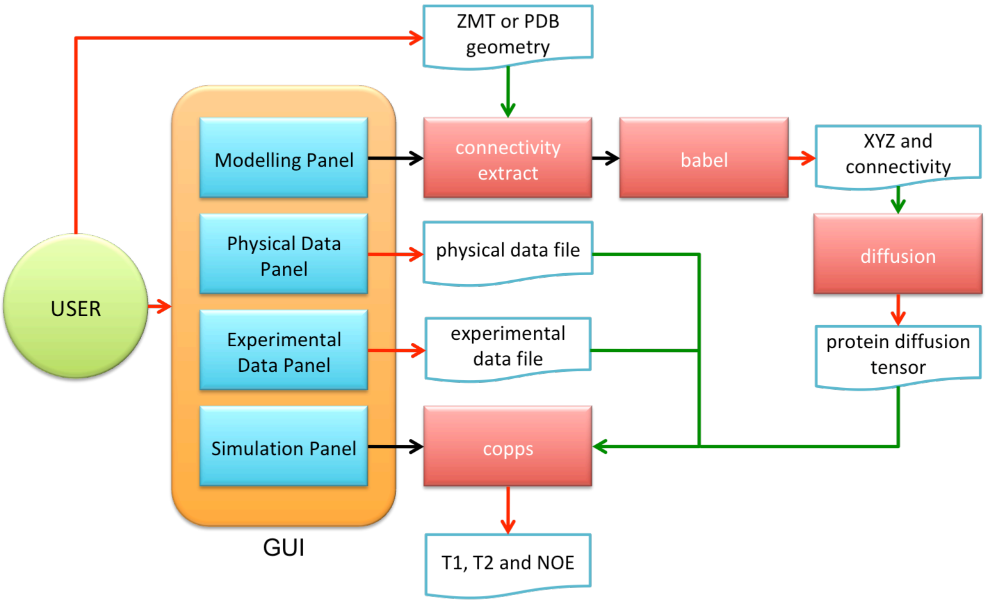

Figure 4-2: Structure of the C^{++}OPPS package. Red arrows represent output, green arrows input and black arrows represent calls to core programs.

given in the usual formats z-matrix (ZMT) or protein data bank (PDB), into Cartesian coordinates and to extract the matrix describing the connectivity among atoms. Figure 4-2 shows (light blue rectangles) that the user is guided in performing the simulation, following a number of steps aimed to the preparation of the whole input informations needed, which will then automatically merged by the interface before calling the last step core program, i.e. the "copps" program that calculates the NMR relaxation data.

The GUI has been written in Java due to the potentialities of such a language in building graphical interfaces and because *i)* Java applications are interpreted, not binary, code so they work on every operating system without the need of recompilation and *ii)* with just a minimal effort it is possible to transform the application into an applet that runs on web browsers.

The core program having the highest requirements of computational resources is "copps" because it has to handle the matrix associated to the diffusive operator. Due to the exponential growth of basis dimensions with the truncation parameter, see eq. (4.9), with relatively small values of $L_{2,MAX}$ the dimensions reach values of $10^4 - 10^5$. Treating such big matrices requires a substantive amount of RAM memory in order to store the matrix elements and a high calculation time for linear algebra operations. To face these problems, the core program

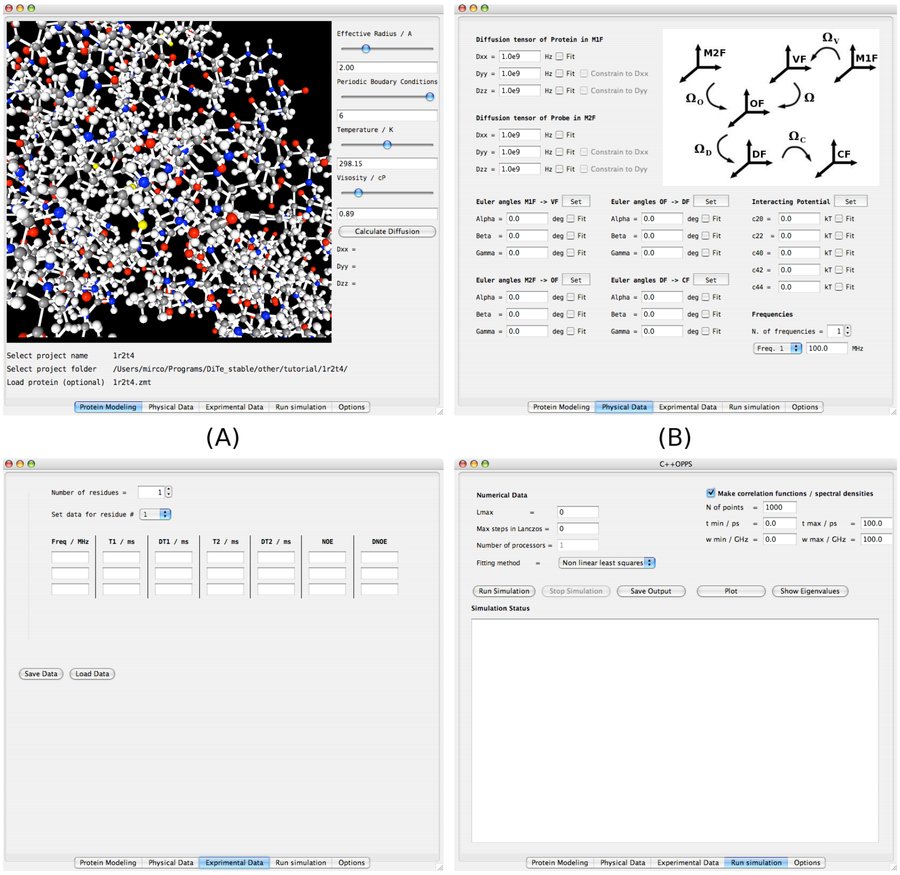

Effective Radius / A = 2.00
Periodic Boudary Conditions = 6
Temperature / K = 298.15
Visosity / cP = 0.89
Dxx =
Dyy =
Dzz =
Select project name 1r2t4
Select project folder /Users/mirco/Programs/DiTe_stable/other/tutorial/1r2t4/
Load protein (optional) 1r2t4.zmt

(A)

Diffusion tensor of Protein in M1F
Dxx = 1.0e9 Hz ☐ Fit
Dyy = 1.0e9 Hz ☐ Fit ☐ Constrain to Dxx
Dzz = 1.0e9 Hz ☐ Fit ☐ Constrain to Dyy

Diffusion tensor of Probe in M2F
Dxx = 1.0e9 Hz ☐ Fit
Dyy = 1.0e9 Hz ☐ Fit ☐ Constrain to Dxx
Dzz = 1.0e9 Hz ☐ Fit ☐ Constrain to Dyy

Euler angles M1F -> VF
Alpha = 0.0 deg ☐ Fit
Beta = 0.0 deg ☐ Fit
Gamma = 0.0 deg ☐ Fit

Euler angles M2F -> OF
Alpha = 0.0 deg ☐ Fit
Beta = 0.0 deg ☐ Fit
Gamma = 0.0 deg ☐ Fit

Euler angles OF -> DF
Alpha = 0.0 deg ☐ Fit
Beta = 0.0 deg ☐ Fit
Gamma = 0.0 deg ☐ Fit

Euler angles DF -> CF
Alpha = 0.0 deg ☐ Fit
Beta = 0.0 deg ☐ Fit
Gamma = 0.0 deg ☐ Fit

Interacting Potential
c20 = 0.0 kT ☐ Fit
c22 = 0.0 kT ☐ Fit
c40 = 0.0 kT ☐ Fit
c42 = 0.0 kT ☐ Fit
c44 = 0.0 kT ☐ Fit

Frequencies
N. of frequencies = 1
Freq. 1 100.0 MHz

(B)

Number of residues = 1
Set data for residue # 1

Freq / MHz	T1 / ms	DT1 / ms	T2 / ms	DT2 / ms	NOE	DNOE

(C)

C++OPPS

Numerical Data
Lmax = 0
Max steps in Lanczos = 0
Number of processors = 1
Fitting method = Non linear least squares

☑ Make correlation functions / spectral densities
N of points = 1000
t min / ps = 0.0 t max / ps = 100.0
w min / GHz = 0.0 w max / GHz = 100.0

Simulation Status

(D)

Figure 4-3: Snapshots of C^{++}OPPS graphical user interface: (A) Modelling Panel, (B) Physical Data Panel, (C) Experimental Data Panel and (D) Simulation Panel.

"copps" has been parallelized under the MPI paradigm, obtaining a code that scales with any number of processors and that can be run on calculation clusters.

In the subsections below a brief description of how C^{++}OPPS GUI works, some details on the parallelization and an overview of the web version of the code will be given.

4.2.1 GUI organization

The graphical user interface of C^{++}OPPS is simply a tagged panel where every panel represents a logical step in the work flow that leads from the definition of the system to the achievement of the NMR data. In every panel users are asked to introduce some data and / or provide informations specific for that panel. The complexity of the problem does not permit to create a "single button" program because the work flow of the simulation is not completely predetermined (e.g. a user can perform a single calculation or a fitting) and a number of decisions have to be taken in the "nodes" of the simulation flow. This fact also implies that the user needs to have an overview, even if not detailed, of the chemical-physical interpretation of the system. Also, this summary knowledge on the theoretical methodology is in general useful in order to give the right interpretation and importance to the numbers returned by the program.

As depicted in Figure 4-2, there are a total of four panels, representing the critical nodes asking to the user to intervene, which are briefly described in what follows.

Initialization of a job - Modelling Panel

Initialization of a simulation and protein modelling are the two tasks handled by the first panel, the Modelling Panel (MP) shown in Figure 4-3A.

C^{++}OPPS works by projects, i.e. every new calculation must be given a name that will be used as a prefix in the names of all the files that will be produced during the simulation. In this first panel a user has the possibility to start a new project or to load an existing one. Here it is possible to specify the geometry of the protein via a ZMT or a PDB file.

C^{++}OPPS integrates the "diffusion" core program for the evaluation of diffusion tensors, which is part of the DITE (DIffusion TEnsor) [34] package described in Section 2.2. If the geometry of the protein has been loaded, its diffusion tensor can be evaluated directly in the Modelling Panel just after the selection of four parameters that are the effective radius of the atoms, the boundary conditions, the viscosity of the fluid and the absolute temperature. These parameters are used to build the elementary friction of the atoms that, in turn, is employed in the calculation of the friction of the molecule. The methodology is based on a hydrodynamic approach, described in Section 2.1. In C^{++}OPPS the protein diffusion tensor is calculated assuming the molecule as a rigid body, so the system has only six degrees of freedom which are the taken as the position of the centre of mass and the three Euler angles defining the orientation with respect to an inertial frame. For a rigid body the diffusion tensor is represented by a 6 × 6 matrix containing the translational, rotational and mixed parts

$$\boldsymbol{D} = \begin{bmatrix} \boldsymbol{D}_{TT} & \boldsymbol{D}_{TR} \\ \boldsymbol{D}_{RT} & \boldsymbol{D}_{RR} \end{bmatrix} \tag{4.19}$$

Here, we are assuming that the response of the system does not depend on the position of the centre of mass of the molecule, so it is possible to project the translational part and remain with only the rotational diffusion tensor, i.e. $\boldsymbol{D} = \boldsymbol{D}_{RR}$. In particular, the "diffusion" core program calculates the diffusion tensor in the frame where the rotational part is diagonal and then the GUI obtains from the output file the principal values of the rotational part and copies them in the Physical Data Panel. The calculation of the diffusion tensor of the protein is optional, but it represents a good opportunity to reduce the number of free parameters, in case of fitting, also because it has been shown that the methodology has a good predictivity for molecules of any size [34].

The actual implementation of C^{++}OPPS includes only the SRLS model for the dynamics of the system, so effectively the modelling of the motion is determined. However, work is being done for the development of new theoretical models for the dynamics that are going to be included in the program and users could select which model to employ directly on the MP.

Definition of microscopic data - Physical Data Panel

As can be seen in the theoretical discussion of SRLS, a number of molecular parameters enter in the definition of the model, i.e. dissipative parameters (diffusion tensors), geometric properties (Euler angles) and the interaction potential between the protein and the probe. C^{++}OPPS offers the possibility to perform a single calculation if the parameters are known, or to perform a Levemberg-Marquardt non-linear least square fitting in order to search for the set of parameters that better reproduces experimental data. In both cases, a choice of the values of the parameters is required; in the case of fitting the program needs an initial guess, i.e. a point where to start searching for the global minimum of the hypersurface in the phase-space of the parameters. The input of the data is done directly on the GUI through the Physical Data Panel (PDP), shown in Figure 4-3B. Just to give a complete view, the full set of parameters that enter in the model are:

- principal values of the diffusion tensor of the protein, ${}^{M_1}\boldsymbol{D}_1$;
- principal values of the diffusion tensor of the probe, ${}^{M_2}\boldsymbol{D}_2$;
- Euler angles $\boldsymbol{\Omega}_V$ that transform from the frame that diagonalizes the protein diffusion tensor ($\mathrm{M_1F}$) to the protein fixed frame (VF) where the orienting potential is defined;

- Euler angles $\mathbf{\Omega}_O$ that transform from the frame that diagonalizes the probe diffusion tensor (M$_2$F) to the probe fixed frame (OF) respect to which the stochastic set of Euler angles $\mathbf{\Omega}$ is defined (describing the relative orientation of the two bodies);
- Euler angles $\mathbf{\Omega}_D$ that transform from OF to DF, where the dipolar interaction is diagonal;
- Euler angles $\mathbf{\Omega}_C$ that transform from DF to CF, where the chemical shift interaction is diagonal;
- the five coefficients of the coupling potential, c_0^2, c_2^2, c_0^4, c_2^4 and c_4^4.

Differently from the older version of COPPS, there is no fixed symmetry for the diffusion tensors, i.e. the three principal values can be all different. However, users have the possibility to decide to add the constraint $D_{xx} = D_{yy}$ so imposing an axial symmetry during the fitting. It is also possible to fit only a multiplicative coefficient of all the three principal values, i.e. only the isotropic part of the diffusion tensor is changed during the fitting.

As shown in Figure 4-3B, a check-box is placed near to every physical parameter giving the possibility to easily choose which parameters have to be fit and which not. In general, the number of free parameters depends on *i)* the physical interpretation of the system, e.g. if the protein - probe interaction is modelled as axial, only the c_0^2 coefficient of the potential will be a free parameter, while the other four coefficients will be fixed to zero; *ii)* the number of experimental data available, i.e. it is not possible to fit a number of parameters greater than the number of experimental points. The second point, together to the problem of physical iterpretability and consistency (not always assured) of fitted parameters and the problem of searching a global minimum in a hypersurface that could present also a number of local minima, are the reasons for which in the last years theoreticians started to move to a new kind of approach that considers the set-up of multi-scale protocols aimed to collect all the theoretical / computational methodologies for the evaluation of the microscopic data, reducing as possible the number of free parameters. This idea has just been applied with success [56, 58, 59, 111, 113, 114] to the interpretation of electron spin resonance spectroscopy of a number of different systems, as discussed in Chapter 3. An analogous protocol for the interpretation of NMR data of proteins is being worked out and is part of the development of C^{++}OPPS. However, a little step forward has been done, with respect to the past, in integrating in C^{++}OPPS the possibility of calculating the diffusion tensor of the protein. Under the philosophy of ”predicting is better than fitting”, if the diffusion tensor of the protein is calculated starting from its structure (in the Modelling Panel), the principal values will automatically set in the PDP and the fit check-boxes will be unchecked. Of course, before running the simulation, users are free to modify the values and / or decide what to fit: the behaviour of the GUI is set to follow the idea of reducing to the minimum the number of fitting parameters, but also to follow user's wills.

Input of experimental data - Experimental Data Panel

The Experimental Data Panel (EPD) node of the work flow requires the intervention of the user only if a fitting calculation has been set in the PDP, i.e. at least one fitting check-box has been checked.

Usually NMR data is collected at different spectrometer frequencies and for a certain number of residues of the protein, depending on the possibility of interpretation of the 2D/3D-NMR spectra.

As can be seen in Figure 4-3C, experimental data is introduced directly on the GUI by filling a table for each residue registered. Note that in the actual implementation, fitting is conducted on the residues separately. Work is in progress to introduce in the algorithm the possibility of running a global multi-residue fitting.

For each residue, it is possible to introduce data collected at up to three different frequencies and, together with the T_1, T_2 and NOE relaxation times, users possibly have to introduce the associated experimental errors, respectively Δ_{T_1}, Δ_{T_2} and Δ_{NOE}, which will be used as weighting factors in determining the chi-squared parameter during the fitting procedure, i.e.:

$$\begin{aligned}\chi^2 \;&=\; \sum_i \left[\frac{\left(T_1^{exp}(\omega_i) - T_1^{theo}(\omega_i)\right)^2}{\Delta^2_{T_1}(\omega_i)} + \frac{\left(T_2^{exp}(\omega_i) - T_2^{theo}(\omega_i)\right)^2}{\Delta^2_{T_2}(\omega_i)} + \right.\\ &\left. + \frac{\left(NOE^{exp}(\omega_i) - NOE^{theo}(\omega_i)\right)^2}{\Delta^2_{NOE}(\omega_i)}\right] \qquad (4.20)\end{aligned}$$

indicating the goodness of the fitting and in particular nearer is χ^2 to zero, more the theoretical NMR relaxation times resemble the experimental ones within the experimental error.

Launching the simulation - Simulation Panel

In the Simulation Panel (SP), a snapshot of which is given in Figure 4-3D, users (optionally) set some numerical parameters and run the simulation. The numerical parameters are:

- $L_{2,MAX}$, see eq. (4.9), which is the maximum rank of the Wigner matrix at which stop the basis expansion for the probe (the expansion for the rotational space of the protein is fixed by the physical properties of the observables);
- the maximum number of iterations in the Lanczos tridiagonalization;
- the number of processors in a parallel calculation.

The first two parameters are defaulted to zero in the GUI, indicating to C^{++}OPPS that their values have to be estimated at runtime, basing on the other input. For both the truncation parameter and the number of Lanczos steps, the selection criteria inside the code are written in order to over-estimate the needed values and so to ensure convergence of the calculation. However, it is always a better practice to take control on these two numbers, especially of the $L_{2,MAX}$ parameter respect to which the convergence of the calculation is more sensible. As can be seen in Figure 4-3D, it is also possible to choose, on the right part of the panel, if the program has to calculate the correlation functions and spectral densities. In particular C^{++}OPPS will return the symmetrised correlation functions and spectral densities, i.e. those for the $C_{k,k'}(\boldsymbol{\Omega}_{LO})$ functions, and the spectral densities $J^{\mu}(\omega)$, where μ indicates dipolar or chemical shift magnetic interactions. Calculation of such functions is based on solving the eigensystem for the $\boldsymbol{T}_n$ tridiagonal matrix *via* the standard TQLI algorithm [217] that returns the eigenvalues, λ_i, and their weights, w_i, so that the correlation functions and the spectral densities are calculated as

$$c(t) = \sum_{i=0}^{n} w_i e^{-\lambda_i t} \tag{4.21}$$

$$j(\omega) = \sum_{i=0}^{n} w_i \frac{1/\lambda_i}{1 + \omega^2/\lambda_i^2} \tag{4.22}$$

The text area in the lower part of the panel reports the job progress and, at the end of calculation, the output of the job is also saved on a file reporting the meaningful physical

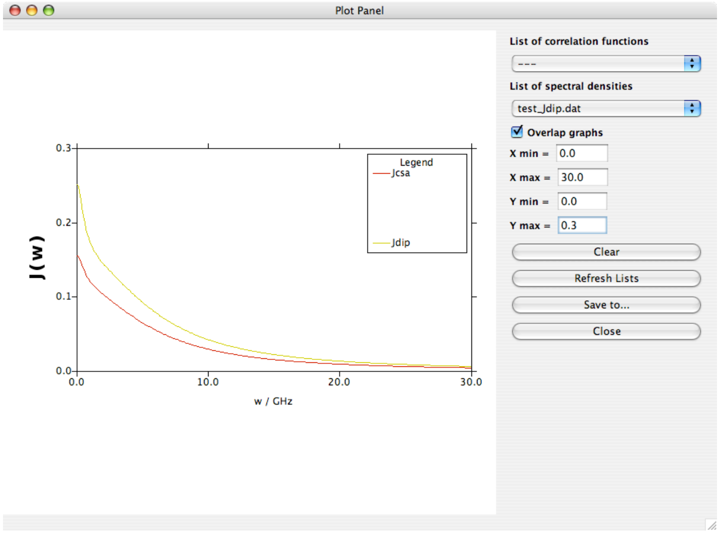

List of correlation functions

List of spectral densities
test_Jdip.dat
☑ Overlap graphs
X min = 0.0
X max = 30.0
Y min = 0.0
Y max = 0.3

Figure 4-4: C^{++}OPPS internal plotting tool for the inspection of the correlation functions and spectral densities.

results, i.e. the values of the fitted parameters, the theoretical T_1, T_2 and NOE data and the order parameters

$$S_0^2 = \langle \mathcal{D}^2_{0\,0}(\mathbf{\Omega}) \rangle \tag{4.23}$$

$$S_2^2 = \left\langle \left[\mathcal{D}^2_{0\,-2}(\mathbf{\Omega}) + \mathcal{D}^2_{0\,2}(\mathbf{\Omega}) \right] \right\rangle \tag{4.24}$$

where $\langle \cdots \rangle$ indicates the average over the $\mathbf{\Omega}$ space.

Correlation functions and spectral densities are produced in a different file and can be plotted directly from the GUI, as shows Figure 4-4, and also saved in PNG graphic format.

4.2.2 Parallelization

As it was outlined above, even small values of the truncation parameter $L_{2,MAX}$ lead to high dimensions of the basis set and technical problems arise when the dimensions reach 10^5 because of the need of a sufficient quantity of RAM memory to store the matrix and because of the exponential increasing of computation time required to complete the simulation, especially for fitting procedures with many free parameters. To face these problems, the most computational heavy parts of the algorithm have been parallelized under the MPI (message passing interface) paradigm, and in particular C^{++}OPPS belongs to the family of the so called ”single program multi processor” (SPMP) programs, i.e. every processor, to which a rank is assigned at runtime, executes the same program but performs different tasks basing on the directives present into the code for its specific rank. Implementation has been carried out so that C^{++}OPPS scales with any number of processors: the work is dynamically distributed among the processors, whichever is their number.

Three are the parts that represent the bottle-necks of the calculation and their time of execution sensibly increases with the dimensions of the basis, so that they require parallelization: the construction of the starting vector, the construction of the matrix associated to the diffusive operator and the matrix vector product inside the Lanczos algorithm.

The construction of the starting vector requires the evaluation of a number of numerical integrals, which are the projections of the physical observables $C_{k,k'}\left(\mathbf{\Omega}_{LO}\right)$ over the basis functions, eq. (4.14). These numerical integrations involve also the evaluation of modified Bessel functions of the first kind, so that they could require a substantial computational effort. If N is the dimension of the basis and N_C the number of $C_{k,k'}$ functions that have to be projected (by using symmetry arguments N_C is reduced from 25 to a maximum of 9), the total number of numerical integrations to perform are $N \times N_C$. Given the number of processors, N_P, the basis functions are equally distributed so that every processor has to calculate only a portion of the numerical integrals, i.e. for every physical observable the number of projections is $N' = N/N_P$. Note that if N_P is not a divisor of N, in the code the reminder of the division, R, will be distributed so that R processors will calculate $N' + 1$ integrals and the other $N_P - R$ processors will handle N' integrations. This is an embarrassingly parallel piece of code, i.e. all the processors work independently. Only at the end every processor scatters its piece of starting vector to the other processors so that all processors have the complete starting vector.

The construction of the matrix is parallelized for two important reasons. The first, very intuitive motivation is to save time, even if in this kind of problems construction of the matrix is quite optimizable and also in a sequential run the building time is not so restrictive. The second and, maybe, more important reason is a memory issue: given the dimension of the basis N, the sparsity of the matrix S and considering that the matrix is symmetric, the number of elements to store are $N_e = S \times N(N + 1)/2$ and the total memory required if numbers are *double* precision is $8 \times N_e$ bytes. As an example, considering $L_{2,MAX} = 25$ (case of very slow motion and / or high interacting potential), one obtains $N = 117130$ and, if $S = 0.1$ (only 10% of the elements are different from zero) the memory required is about 5.5 GBytes, which in general is too much for a dekstop/laptop computer. Parallelization solves the problems with memory because, under the MPI paradigm, the total memory at disposal is the sum of the memory of each processor. In C^{++}OPPS, R processors will build a $(N'+1) \times N$ rectangle of the matrix, while $N_P - R$ processors will build a $N' \times N$ rectangle of the matrix. Due to symmetry, only half of the out of diagonal elements have to be calculated and to balance the computational weight, matrix is built following this standard simple rule: build element $\mathbf{\Gamma}_{i,j}$ if $i + j$ is even or $\mathbf{\Gamma}_{j,i}$ if $i + j$ is odd. Also this part is embarrassingly parallel: no communication between processors is required because calculation of every matrix element is independent on the others and each processor keeps all data required to build its part of the matrix.

Finally, also the matrix vector product in the Lanczos routine is parallelized. When Lanczos tridiagonalization is called, every processor is keeping in memory a rectangular slice of the matrix and the complete starting vector (for each $C_{k,k'}$ function). The iteration step of the Lanczos algorithm contains the multiplication of the matrix with a vector (updated ad every cycle) and a number of linear scaling operations. Our parallelized version of the Lanczos routine implements the parallel matrix vector multiplication followed by an all-to-all scattering so that at the end all processors have in memory the result of the multiplication and, independently, proceed the Lanczos iteration. One single step of the Lanczos algorithm is embarrassingly parallel, but the complete tridiagonalization involves data exchange at every iteration step, so globally the Lanczos algorithm is not embarrassingly parallel.

An analysis of the efficiency of the parallelization is reported in **Appendix A** where it is shown that the building of the matrix is nearly linear scaling, while the Lanczos routine has the worst scalability. Globally the parallelization of C^{++}OPPS ensures an effective gain in computational time within ten processors. An improvement of parallelization efficiency is part of the further work scheduled for the next developments of C^{++}OPPS.

4.2.3 Web implementation

In order to take advantage of the parallelization of C^{++}OPPS, we also developed a cluster version of the program. In this part of the work it came very useful the fact that the GUI

has been written in Java. The passage from an application to an applet was possible with a minimal programming effort. In this way, users that want to run the cluster version work on an interface which has the same appearance of that of the local version and do not have to be concerned about remote computer access because the applet is loaded simply by using any internet browser (Internet Explorer, Firefox, Safari, etc.) on any operating system.
The functionality of local and web interfaces is the same from the point of view of the user. The GUI automatically, and in a completely transparent way, works differently in the case of web or local execution. There are only a couple of small differences that are *i)* a project is created on the server so that, when the simulation is finished, the files have to be downloaded from the server using a dedicated button present only in the web version of the interface; *ii)* each calculation must be submitted to the PBS (portable batch system) queue manager, but also this operation is handled directly from the GUI: users simply have to indicate the number of processors that they want to use before to launch the simulation.

4.3 Case study: AKeco protein

A set of residues of the E. Coli Adenylate Kinase (AKeco) protein has been selected in order to show and test the application of the methodology and of the program to the simulation of real experimental data. In Figure 4-5 are highlighted the chosen residues with different colours. The colour scheme is: yellow for the AMPbd domain, red for the CORE domain, blue for the LID domain and green for the small P-loop. We followed the standard definition in dividing the protein in that domains [214]. For the experimental values see the supporting information of ref. [214].

The diffusion tensor of the protein, in water, was evaluated with slip boundary conditions, effective radius of the spheres of 2.0 Å, room temperature and viscosity of 0.9 cP. With this parameters we obtained ${}^1D_{XX} = 1.11 \cdot 10^7$ Hz, ${}^1D_{YY} = 1.20 \cdot 10^7$ Hz and ${}^1D_{ZZ} = 1.65 \cdot 10^7$ Hz. Because of near axiality of the tensor, in the calculations we assumed the average values $1^D_{XX} = {}^1D_{YY} = 1.15 \cdot 10^7$ Hz.

We imposed an axial orienting potential coupling the two bodies. As underlined above, the first body describes the motion of the protein, while we interpret the second body as the collective local motions in the neighbours of the magnetic probe, the ^{15}N-^{1}H bond. In this

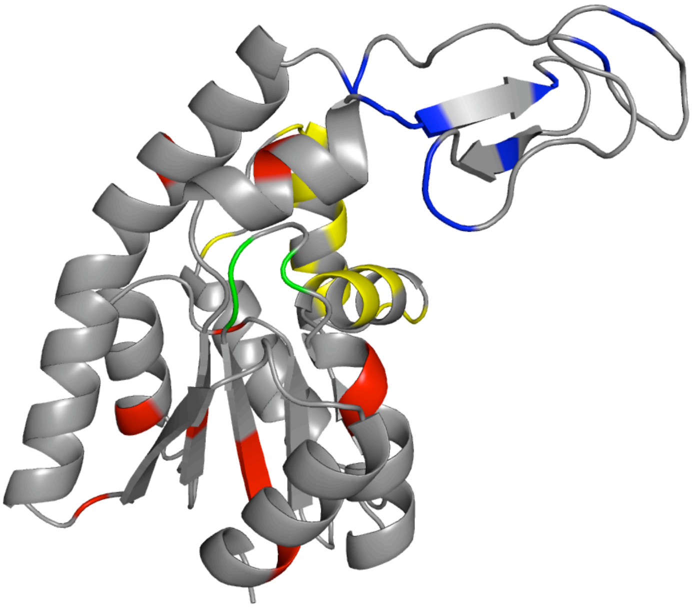

Figure 4-5: Pictorial overview of the distribution of the residues chosen for the calculations. In yellow are the aminoacids belonging to the AMPbd domain, in red those of the CORE domain, in blue the residues of the LID domain and in green those belonging to the small P-loop.

picture we assume, for the second body, a diffusion tensor which is diagonal in a frame having the Z-axis parallel to the ^{15}N-^{1}H bond and the X-axis perpendicular to the peptidic bond plane. Moreover, we consider the tensor to be axially symmetric in such frame. To interpret data we make the further assumption that the coupling potential tends to align the Z-axis of the second body (i.e. of the OF frame), parallel to the direction containing the ^{15}N=^{1}H bond in the equilibrium geometry of the protein. This is reproduced by defining a frame VF having the Z-axis parallel to the ^{15}N-^{1}H bond, which in general is tilted from the M$_1$F, where the diffusion tensor of the protein is diagonal. So, for every residue, we extracted from the geometry of the protein the set of Euler angles that transform from M$_1$F to VF, $\mathbf{\Omega}_1$. We assume that the magnetic tensors are diagonal in the same frame, i.e. $\mathbf{\Omega}_C = (0.0, 0.0, 0.0)$ deg and the constant tilt with respect to the OF $\mathbf{\Omega}_D = (0.0, 18.0, 90.0)$ deg, following ref. [215].

A set of four parameters were considered free and obtained *via* fitting: the parallel and perpendicular components of the diffusion tensor of the second body, ${}^{O}D_{\perp}$ and ${}^{O}D_{\parallel}$, the strength of the axial potential, c_0^2, and a parameter called rate of exchange, R_{ex}, which

Domain	Residue	$^{O}D_{\perp}$ / 10^{7} Hz	$^{O}D_{\parallel}$ / 10^{10} Hz	R_{ex} / Hz	c_0^2	S
AMPbd	32	1.69	10.5	2.95	2.64	0.55
	33	2.04	13.0	1.51	3.65	0.68
	36	1.55	12.7	1.38	2.82	0.58
	41	2.56	5.42	0.277	4.81	0.77
	42	2.54	4.23	0.873	4.80	0.77
	46	2.09	7.02	1.16	4.32	0.74
	48	1.38	7.27	1.30	2.50	0.53
	50	2.23	6.84	1.09	4.69	0.76
	52	2.12	7.09	0.118	4.34	0.74
	53	1.93	5.34	0.882	4.06	0.72
	55	2.36	6.55	1.01	5.13	0.78
	56	2.25	6.29	0.427	4.40	0.74
	60	2.29	5.27	0.196	5.01	0.78
CORE	2	1.29	17.7	1.60	1.77	0.39
	3	1.40	35.1	1.24	2.24	0.49
	16	1.83	11.4	4.21	3.40	0.65
	77	1.32	20.9	1.75	2.06	0.45
	86	1.69	15.6	2.38	2.70	0.56
	97	1.72	19.5	0.54	4.00	0.71
	107	1.33	28.1	2.14	1.83	0.41
	117	1.42	31.5	2.36	2.37	0.51
	170	1.63	8.95	0.898	3.47	0.66
	191	2.20	5.21	0.000	4.27	0.73
	210	1.35	25.4	1.51	3.15	0.62
LID	122	1.70	25.4	6.05	4.16	0.72
	123	1.70	12.4	2.90	3.58	0.67
	126	1.84	15.4	0.000	4.28	0.73
	132	2.58	6.59	0.000	5.38	0.80
	136	2.05	6.87	1.54	5.06	0.78
	137	2.25	6.77	0.000	5.73	0.81
	145	1.64	9.07	1.42	3.53	0.67
	151	1.35	14.7	1.20	3.09	0.62
	158	2.30	3.96	1.49	4.37	0.74
	159	1.79	8.82	0.458	4.28	0.73
P-loop	8	1.84	15.4	0.161	4.33	0.74
	11	1.46	13.5	2.30	2.96	0.60

Table 4.1: Values of the model parameters obtained from fitting.

gives a correction due to a very slow change in configuration of the protein [215]. Table 1 summarizes the values obtained for the 37 residues considered.

Figures 4-6 - 4-8 show the experimental and theoretical values of the T_1, T_2 and NOE at 600.0 MHz, while 800.0 MHz data are reported in Figures 4-9 - 4-11. It can be seen that the overall agreement is good: all the relative errors between theoretical and experimental values are within 5%.

Figure 4-12 plots the values of the order parameters obtained with the standard formula

$$S = \langle \mathcal{D}^2_{0\,0}\left(\boldsymbol{\Omega}_O\right) P_{eq}\left(\boldsymbol{\Omega}_O\right) \rangle \tag{4.25}$$

4.4 Conclusions

Extensive usage of NMR analysis to the investigation of microscopic dynamics is very promising and many experimental measures are available to advanced for interpretative tools. The SRLS model is a phenomenological approach to the problem which is able to give a good physical interpretation in terms of both dynamical and also structural (through the interaction potential) properties. But it is relatively difficult to handle because of the complex mathematical details. C^{++}OPPS provides a framework for applying a complex theoretical methodology to the interpretation of NMR data and it is principally targeted to experimental scientists as a software of routinary usage in the analysis of experimental measurements.

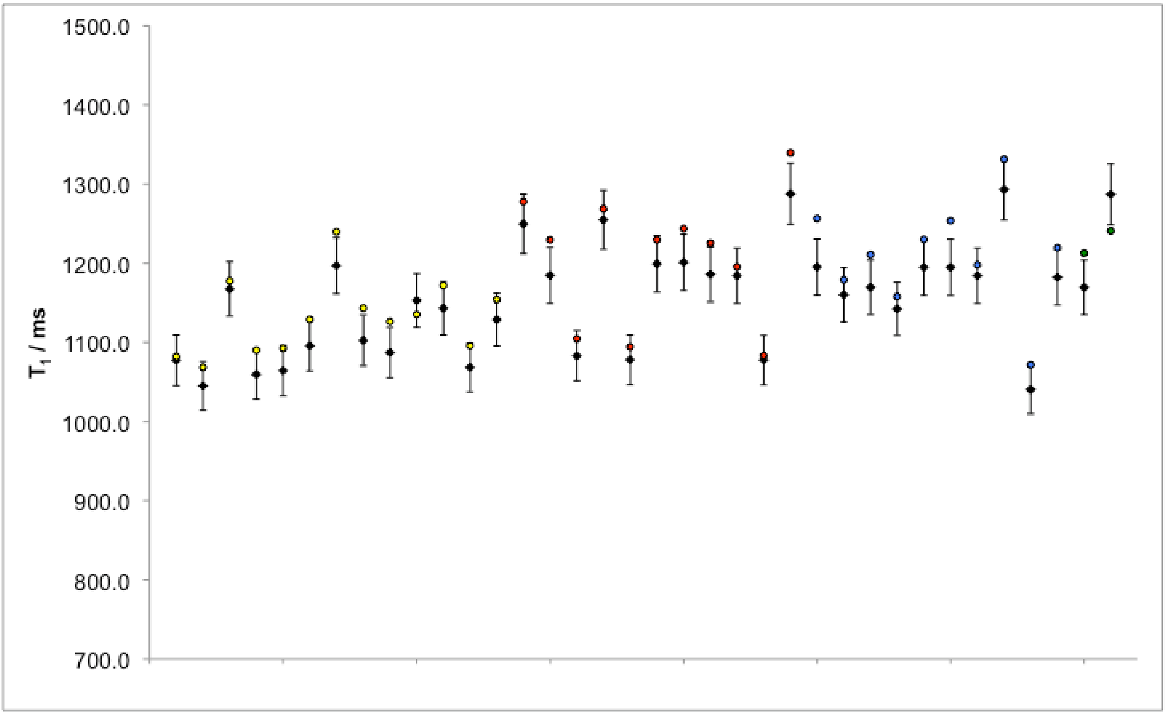

Figure 4-6: Experimental (black rhombi) and theoretical (coloured circles) T_1 values at 600.0 MHz. The values are grouped by domains following the colour scheme described in text.

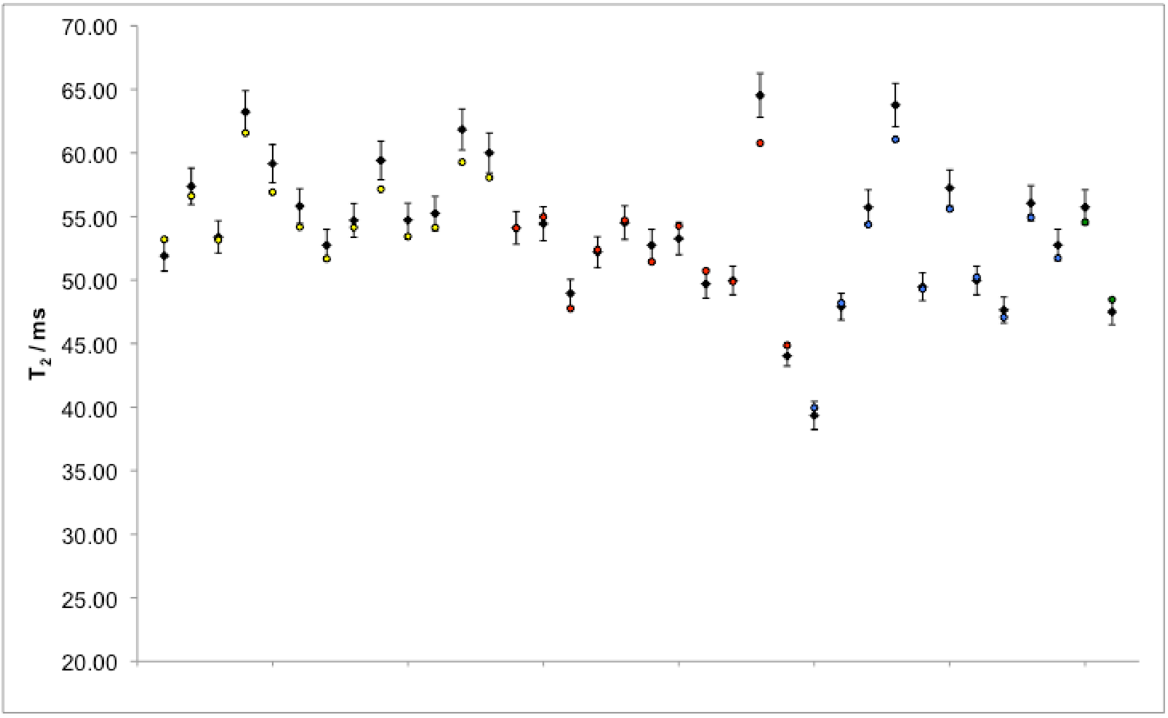

Figure 4-7: Experimental (black rhombi) and theoretical (coloured circles) T_2 values at 600.0 MHz. The values are grouped by domains following the colour scheme described in text.

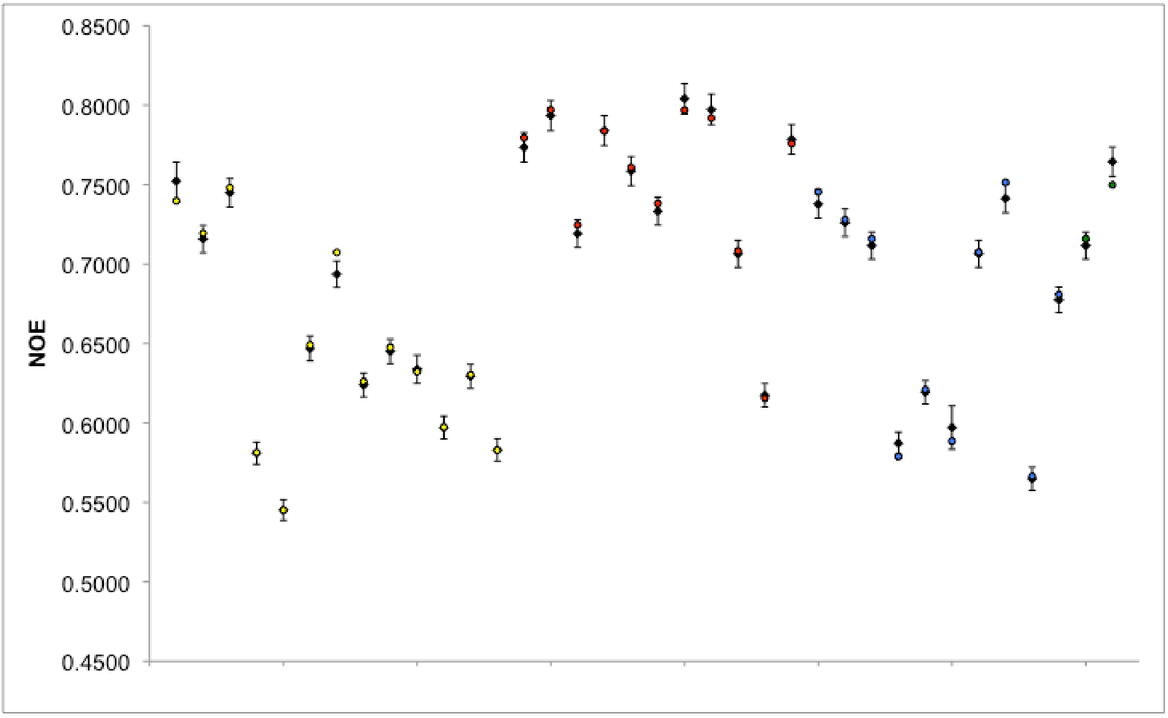

Figure 4-8: Experimental (black rhombi) and theoretical (coloured circles) NOE values at 600.0 MHz. The values are grouped by domains following the colour scheme described in text.

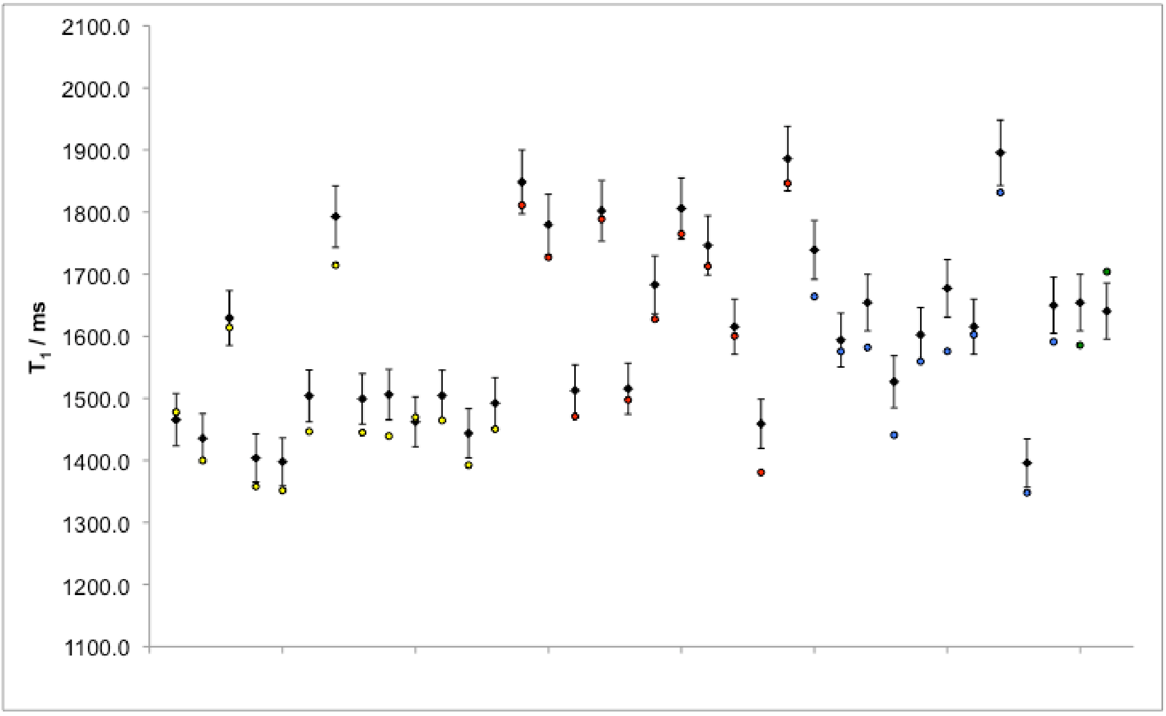

Figure 4-9: Experimental (black rhombi) and theoretical (coloured circles) T_1 values at 800.0 MHz. The values are grouped by domains following the colour scheme described in text.

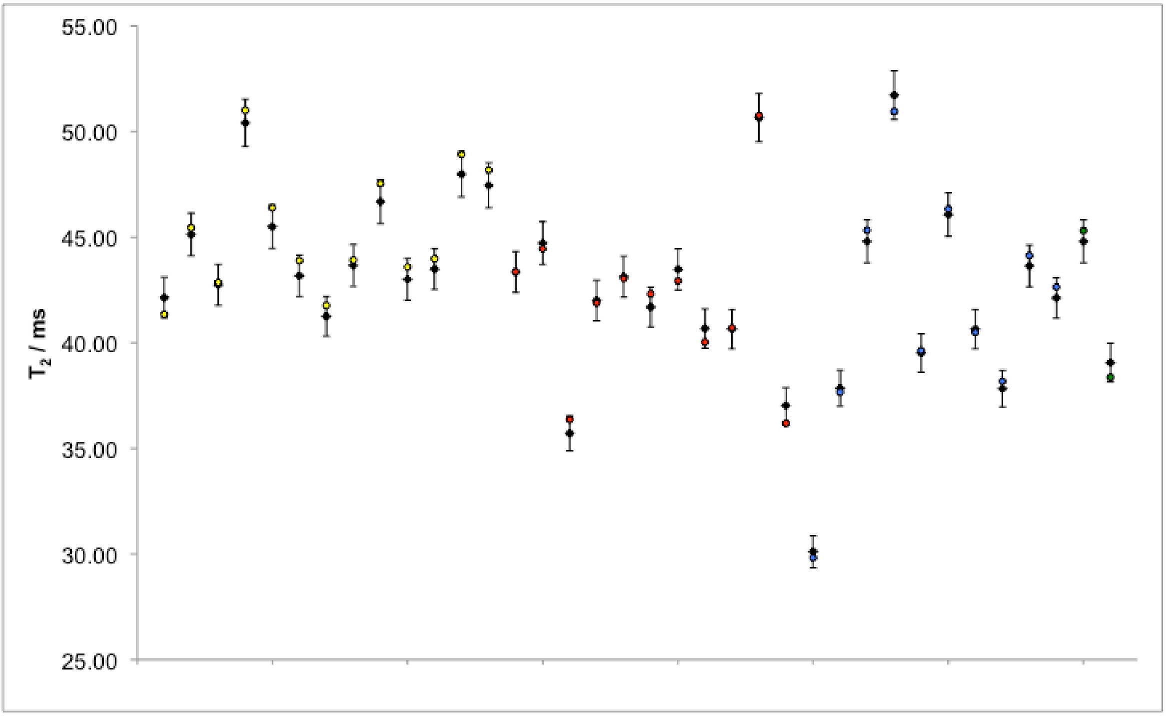

Figure 4-10: Experimental (black rhombi) and theoretical (coloured circles) T_2 values at 800.0 MHz. The values are grouped by domains following the colour scheme described in text.

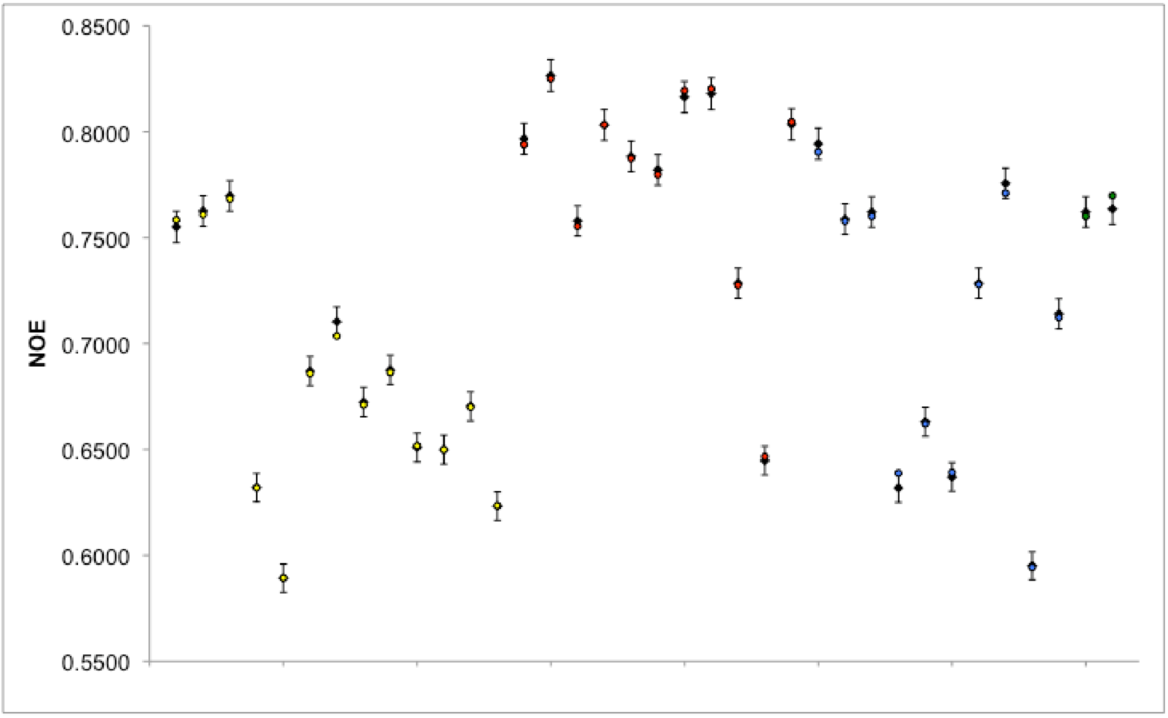

Figure 4-11: Experimental (black rhombi) and theoretical (coloured circles) NOE values at 800.0 MHz. The values are grouped by domains following the colour scheme described in text.

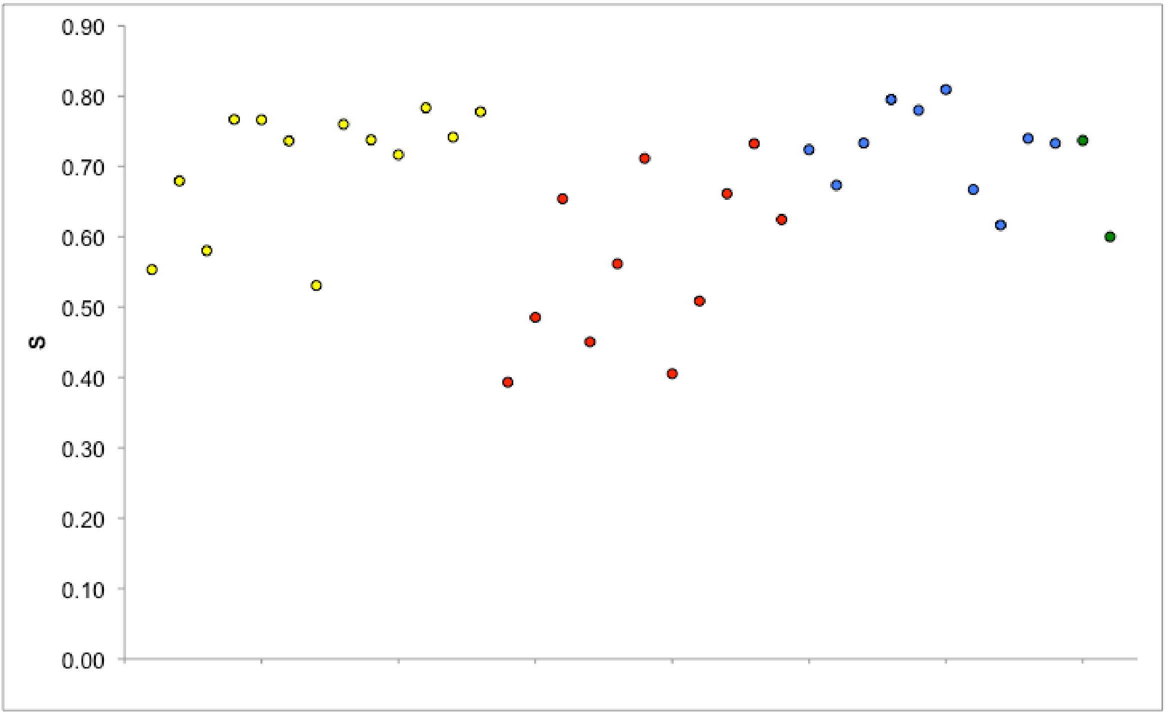

Figure 4-12: Order parameters obtained from fitting. The values are grouped by domains following the colour scheme described in text.

Chapter 5

Conclusions and final remarks

The three years of this doctoral work were dedicated to the development of algorithms and their implementation in the form of integrated software packages (E-SpiReS, C^{++}OPPS, DITE) providing an organized toolbox for gathering information on molecular dynamics from magnetic resonance spectroscopies in solution. The general purpose of the algorithms and the modular structure of the implemented codes, make possible to upgrade the description to new models for molecular dynamics, particularly in the case of complex dynamics in biomolecules.

This research activity shows that a multi-scale physics approach to the interpretation of structural and dynamical properties of complex molecular systems can be very profitable. The main philosophy is, roughly, that it is possible to select a relevant subset of degrees of freedom, from all the molecular details. The "not-relevant" details can be projected and / or treated in an approximated way. This is done for both space and time scales. For example, clearly different spatial scales are used to calculate magnetic tensors and diffusive properties. Structural magnetic properties need the employment of atomistic modelling of the probe and first principles quantum mechanical calculations because electronic structure is required. In the case of dissipative properties one introduces a mesoscopic approach, at a coarse-grained level (e.g. hydrogen atoms are neglected in the calculation). In the hydrodynamic approach the molecular shape is the fundamental parameter; the neglected details are "hidden" into the shape of the molecule.

More pointedly, a "time coarse-graining" approach has been always employed. This is the key point of most modellistic approaches, and therefore at the core of this work. Starting from the hypothesis that a subset of dynamical processes exists having a relevant effect on a given physical observable, one can use ”simple” models to describe complex systems, with good or at least satisfactory results. As an example, the study conducted on the methyl methacrylate polymerization (see Section 3.3.5) demonstrates that a simple dynamical model with only one stochastic coordinate is able to give qualitative and quantitative interpretation of a very complex system such as a polymerizing solution at least for some properties. Moreover, an important fact pointed out by the calculations of cw-ESR spectra of tempo-palmitate in 5-cyanobiphenyl (see Section 3.3.2) is that it is crucial to include all the dynamical details relevant to the experimental time-window in order to reproduce the physical observable. This is clear in Figure 3-25 that shows the importance of using a more detailed description (flexible body) instead of the simple rigid rotator to model the dynamics[1]. This has an important implication on the study of complex molecules: a self-consistent methodology is required in order to guide the recognition and selection of relevant dynamics. In all the cases presented in Chapter 3 we treated substantially simple molecules, for which some chemical insight and the support of QM calculations is sufficient to reach the objective. A future and more ambitious target is the application of stochastic modelling to complex biomolecules, such as proteins, that is to molecules presenting a high number of degrees of freedom leading to a very complex dynamics, characterized by a widespread set of time scales, from fs to μs. As discussed in Chapter 4, where the problem of using NMR to probe proteins dynamics was introduced, an effective and rational methodology to extract relevant dynamics in large biomolecules is still missing. This represents the challenge to be tackled in the next future, which requires not only new computational developments (i.e. ”brute force” approaches, for instance based on massive MD simulations), but also new theoretical methods *ad hoc* developed for large systems, which allow to take into account internal mobility in a cost-effective albeit comprehensive way. The main problems that have to be faced can be summarized as follows:

1. the introduction and implementation of a self-consistent methodology apt to identify and define the relevant motions, e.g. based on the analysis of molecular dynamics trajectories;

---

[1] To quote Einstein: ”Everything should be made as simple as possible, but not simpler.”

2. the development of a theoretical framework to describe the relevant dynamics, formalised in terms of stochastic operators;
3. the introduction of a numerical approach, based on time scales separation, that would have to consider an approximate solution of the dynamical problem due to the general high number of relaxation processes that will enter in the model.

These three major goals represent a possible way to set up a protocol, within a clearly stated framework, aimed at gathering information on molecular mobility from ESR and NMR observables, in large biomolecules.

List of publications

[1] Polimeno, A.; Zerbetto, M.; Franco, L.; Maggini, M.; Corvaja, C. *J. Am. Chem. Soc.* **2006**, *128*, 4734.

[2] Barone, V.; Brustolon, M.; Cimino, P.; Polimeno, A.; Zerbetto, M.; Zoleo, A. *J. Am. Chem. Soc.* **2006**, *128*, 15865.

[3] Zerbetto, M.; Carlotto, S.; Polimeno, A.; Corvaja, C.; Franco, L.; Toniolo, C.; Formaggio, F.; Barone, V.; Cimino, P. *J. Phys. Chem. B* **2007**, *111*, 2668.

[4] Carlotto, S.; Cimino, P.; Zerbetto, M.; Franco, L.; Corvaja, C.; Crisma, M.; Formaggio, F.; Toniolo, C.; Polimeno, A.; Barone, V. *J. Am. Chem. Soc.* **2007**, *129*, 11248.

[5] Zerbetto, M.; Polimeno, A.; Cimino, P.; Barone, V. *J. Chem. Phys.* **2008**, *128*, 24501.

[6] Hermosilla, L.; Sieiro, C.; Calle, P.; Zerbetto, M.; Polimeno, A. *J. Phys. Chem. B* **2008**, *112*, 11202.

[7] Barone, V.; Zerbetto, M.; Polimeno, A. *J. Comp. Chem.* **2009**, *30*, 2–13.

[8] Polimeno, A.; Zerbetto, M.; Meirovitch, E. submitted to Int. J. Quantum Chem.

[9] Zerbetto, M.; Polimeno, A.; Barone, V. submitted to Comp. Phys. Comm.

Appendix A

Sample calculation with DITE

We present in this appendix a tutorial of the DITE program using the case of Calmodulin discussed in Section 2.3.2.

Step 1 - load the PDB file with the geometry (1CFC.pdb file from Protein Data Bank website)

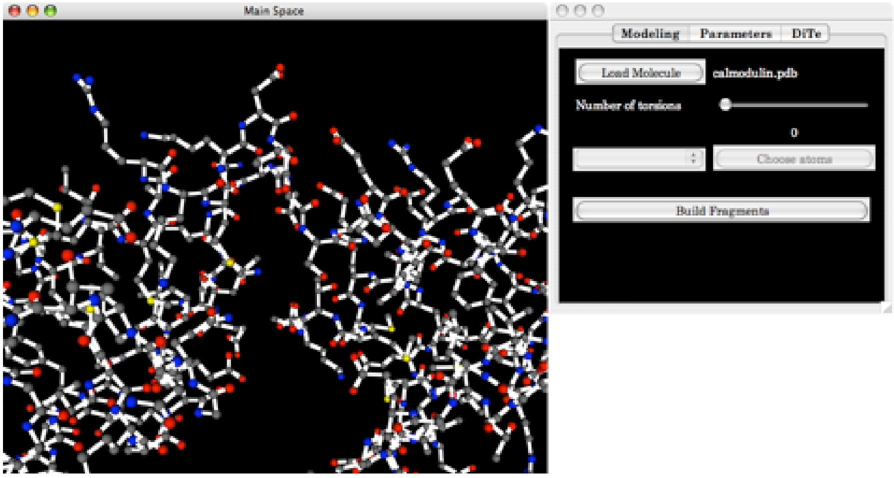

Load Molecule calmodulin.pdb

Number of torsions 0

Figure A-1: Use the left mouse button to rotate the molecule, the right mouse button to translate and the middle button to zoom. If middle button is not available, zoom in/out can be done with keys Z/X.

Step 2 - set the number of torsional angles

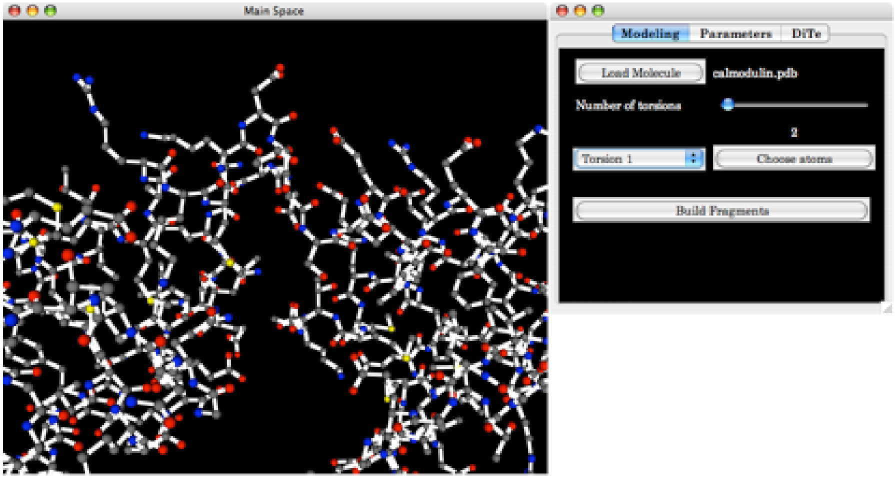

calmodulin.pdb

Number of torsions 2

Torsion 1

Figure A-2: Move the "Number of torsions" bar to the value of 2.

Step 3 - define first torsional angle

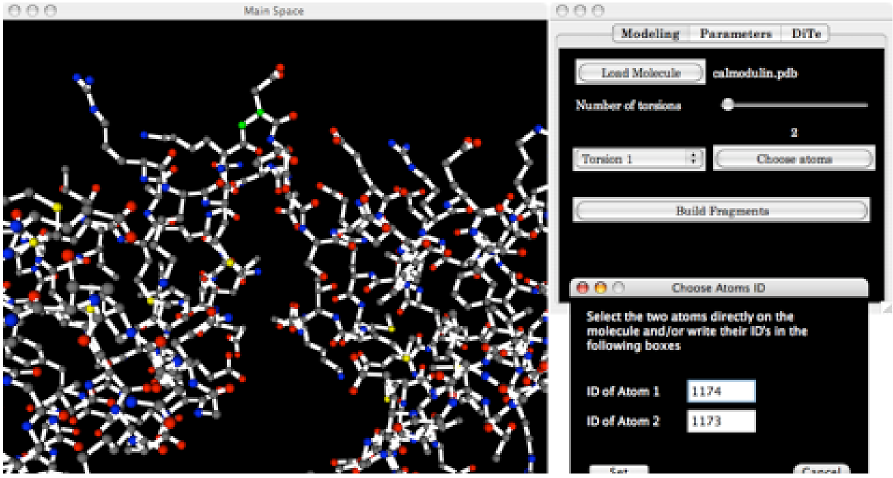

calmodulin.pdb

Number of torsions 2

Torsion 1

Select the two atoms directly on the molecule and/or write their ID's in the following boxes

ID of Atom 1 1174

ID of Atom 2 1173

Figure A-3: Select Torsion 1 in the menu of torsions and click the Choose atoms button. Then select atoms 1174 and 1173 directly on the molecule or by inserting them in the text areas.

Step 4 - define second torsional angle

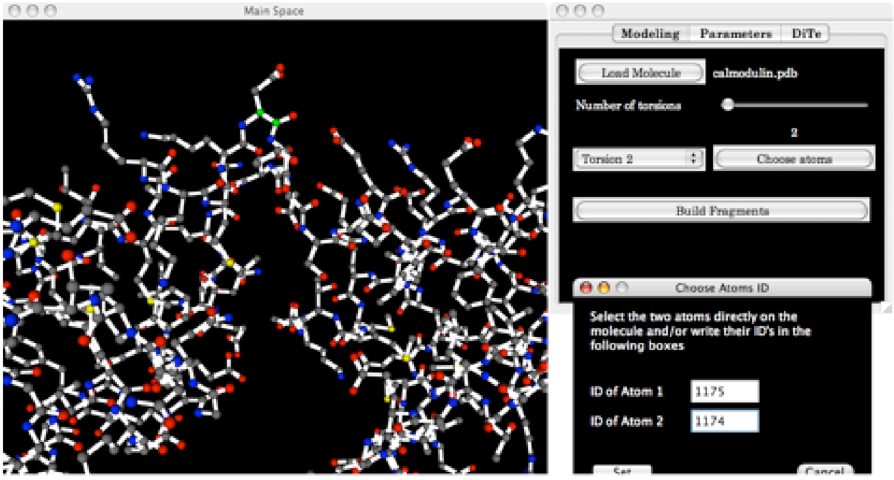

calmodulin.pdb

Number of torsions 2

Torsion 2

Select the two atoms directly on the molecule and/or write their ID's in the following boxes

ID of Atom 1 1175

ID of Atom 2 1174

Figure A-4: Select Torsion 2 in the menu of torsions and click the Choose atoms button. Then select atoms 1175 and 1174 directly on the molecule or by inserting them in the text areas.

Step 5 - build fragments

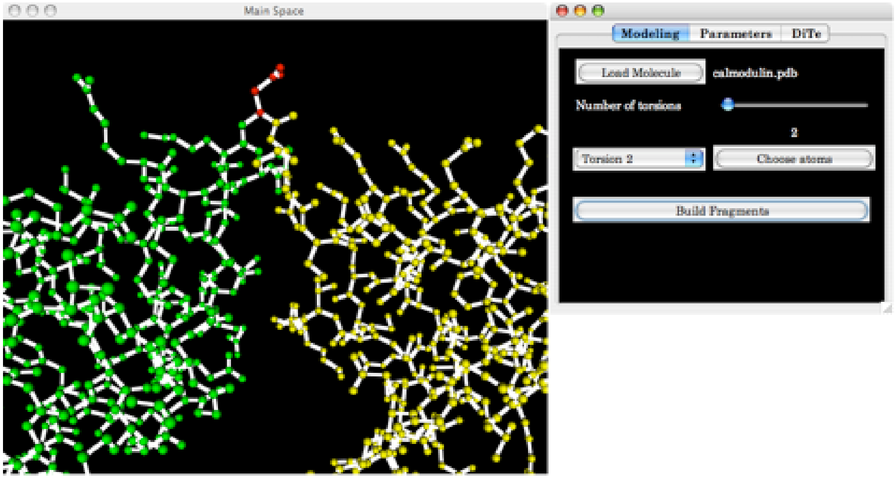

calmodulin.pdb

Number of torsions 2

Torsion 2

Figure A-5: With this operation DITE is informed on the topology of the molecule and assigns a colour code to atoms in order to visibly identify the fragments in which the molecule has been partitioned.

Step 6 - set physical data

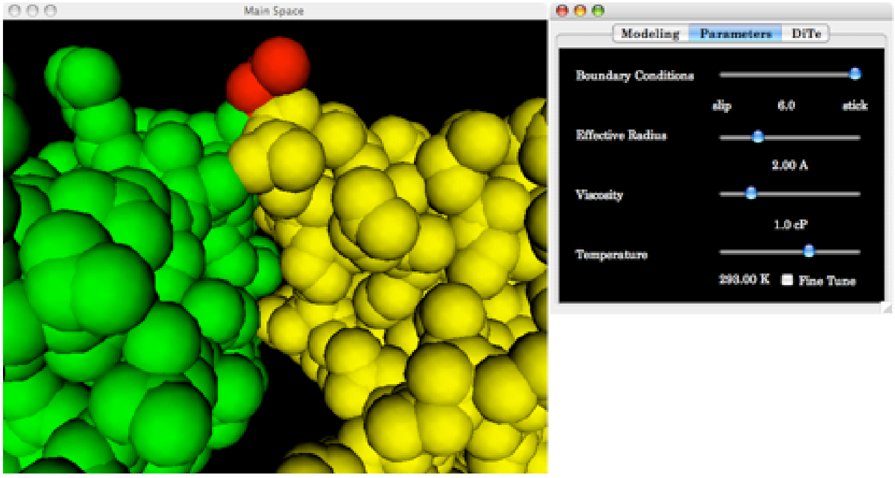

Boundary Conditions slip 6.0 stick

Effective Radius 2.00 A

Viscosity 1.0 cP

Temperature 298.00 K ☐ Fine Tune

Figure A-6: In the Parameters panel one can choose the effective radius of spheres, (R_e), the boundary conditions (C), the viscosity of the fluid (η) and the temperature (T). All these parameters are required in the definition of the translational friction of one sphere given by the Stokes relation $\Xi = \pi C R_e \eta$. The temperature is required in Einstein's relation $D = \mathrm{k_B} T/\Xi$.

Step 7 - set the discretization and sweep for the torsional angles and run simulation

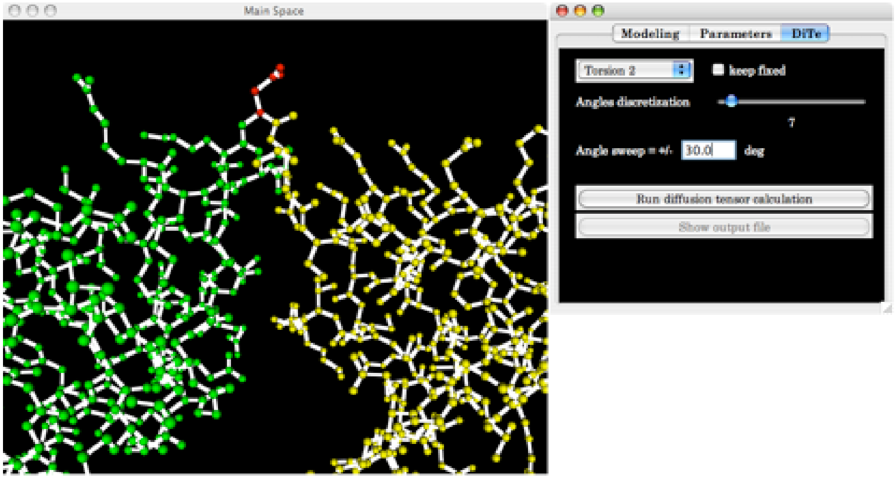

Torsion 2 ☐ keep fixed

Angles discretization 7

Angle sweep = +/- 30.0 deg

Figure A-7: Here we choose 7 points in the range ±30° for a total of 49 configurations. Once the discretization grid is set, the user can run the simulation with the Run diffusion tensor calculation button.

Step 8 - analyse results

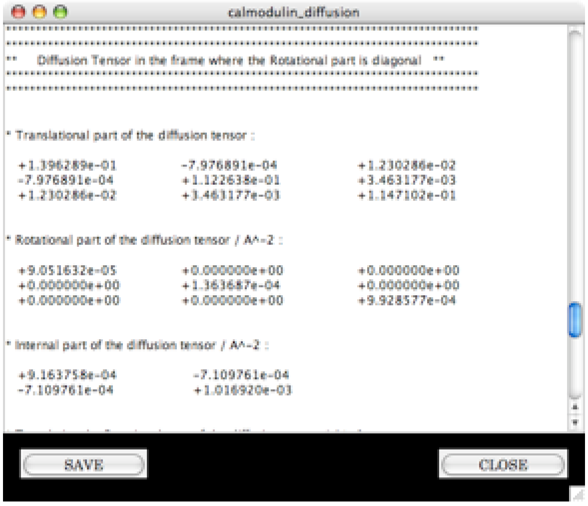

```
****************************************************************************
****************************************************************************
**     Diffusion Tensor in the frame where the Rotational part is diagonal   **
****************************************************************************
****************************************************************************


* Translational part of the diffusion tensor :

  +1.396289e-01          -7.976891e-04            +1.230286e-02
  -7.976891e-04          +1.122638e-01            +3.463177e-03
  +1.230286e-02          +3.463177e-03            +1.147102e-01


* Rotational part of the diffusion tensor / A^-2 :

  +9.051632e-05          +0.000000e+00            +0.000000e+00
  +0.000000e+00          +1.363687e-04            +0.000000e+00
  +0.000000e+00          +0.000000e+00            +9.928577e-04


* Internal part of the diffusion tensor / A^-2 :

  +9.163758e-04            -7.109761e-04
  -7.109761e-04            +1.016920e-03
```

Figure A-8: The ”projectName_diffusion” files contain informations on both friction and diffusion tensors.

Appendix B

Evaluation of dipolar interaction tensor

Let us consider a point in spherical coordinates $\boldsymbol{r} = (r, \theta, \varphi)$ If $\Psi'(\boldsymbol{r})$ and $\Psi''(\boldsymbol{r})$ are the two

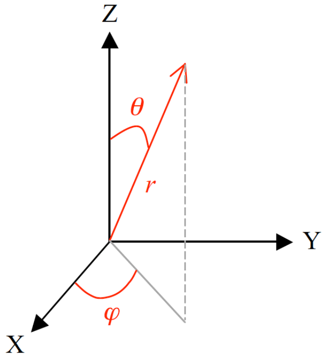

singly occupied molecular orbitals (SOMO) where the two unparied electrons are delocalized, the dipolar tensor is calculated as

$$\boldsymbol{D} = \langle \Psi'(\boldsymbol{r}_1)\Psi''(\boldsymbol{r}_2) - \Psi'(\boldsymbol{r}_2)\Psi''(\boldsymbol{r}_1) \, |\hat{\boldsymbol{D}}| \, \Psi'(\boldsymbol{r}_1)\Psi''(\boldsymbol{r}_2) - \Psi'(\boldsymbol{r}_2)\Psi''(\boldsymbol{r}_1) \rangle \tag{B.1}$$

where the tensor operator $\hat{\boldsymbol{D}}$ has Cartesian components

$$\hat{D}_{\alpha,\beta} = \frac{r_{1,2}^2 \delta_{\alpha,\beta} - 3(\boldsymbol{r}1,2)_\alpha (\boldsymbol{r}1,2)_\beta}{r_{1,2}^5} \tag{B.2}$$

with $r_{1,2} = |\boldsymbol{r}_{1,2}| = |\boldsymbol{r}_2 - \boldsymbol{r}_1|$, $\alpha, \beta = X, Y, Z$ and $(\boldsymbol{r})_\alpha$ representing the α Cartesian component of vector $\boldsymbol{r}$.

The two SOMO orbitals are given as linear combinations of hydrogenic orbitals $\phi_j^i(\boldsymbol{r})$, with i ranging over the number of atoms that contribute to the orbital and j ranging on the number of hydrogenic orbitals of i-th atom giving a contribution to the expansion. This means that the calculation of integral B.1 is a linear combination of integrals over four hydrogenic orbitals:

$$\langle \phi^A_{N_A,L_A,M_A}(\boldsymbol{r}_1 - \boldsymbol{R}_A)\phi^B_{N_B,L_B,M_B}(\boldsymbol{r}_2 - \boldsymbol{R}_B)\,|\hat{\boldsymbol{D}}|\,\phi^C_{N_C,L_C,M_C}(\boldsymbol{r}_1 - \boldsymbol{R}_C)\phi^D_{N_D,L_D,M_D}(\boldsymbol{r}_2 - \boldsymbol{R}_D)\rangle \quad \text{(B.3)}$$

where $\phi^i_{N_I,L_I,M_I}(\boldsymbol{r}_j - \boldsymbol{R}_i)$ is a orbital centred on the i-th atom, occupied by the j-th electron and N, L, M are the three quantum numbers. In the last expression we considered the general case in which all the four atoms are translated from the origin of the reference frame. To be more general, we need to consider also the orientation of orbitals others than s orbitals. So, in the general case that the $\phi_{N,L,M}$ orbital is centred on a frame translated of a vector $\boldsymbol{R} = (R, \Theta, \Phi)$ from the reference frame, and with a relative orientation $\boldsymbol{\Omega} = (\alpha, \beta, \gamma)$, it is possible to apply the transformation:

$$\phi_{N,L,M}(\boldsymbol{r} - \boldsymbol{R}) = \sum_{M'=-L}^{L} \mathcal{D}^L_{M'\,M}(\boldsymbol{\Omega})\phi_{N,L,M'}(\boldsymbol{r} - \boldsymbol{R}) \quad \text{(B.4)}$$

So, in any case, we need to calculate integrals like that given in eq. B.3 because the rotation introduces only corrections to the coefficients of the expansion.
Integration in Cartesian coordinates is computationally heavy and difficult, because it requires an integration over six coordinates. Is is more convenient to express both the orbitals and the operator in spherical coordinates because *i)* it is possible to separate the radial part from the angular part and *ii)* it is easier to make symmetry considerations.

B.1 Expansion of hydrogenic orbitals

In a reference frame the origin of which is the centre of the orbital, the expression of the latter is, in general

$$\phi_{N,M,L}(\boldsymbol{r}) = R_{N,L}(r)Y_{L,M}(\theta, \varphi) \quad \text{(B.5)}$$

with $R_{N,L}$ the radial part and $Y_{L,M}$ the spherical harmonic describing the angular part.
If the orbital is translated of a vector $\boldsymbol{R} = (R, \Theta, \Phi)$, than it is possible to write

$$\phi_{N,L,M}(\boldsymbol{r} - \boldsymbol{R}) = \sum_{l=0}^{\infty}\sum_{m=-l}^{l} \rho^{L,M}_{l,m}(r, \boldsymbol{R})Y_{l,m}(\theta, \varphi) \quad \text{(B.6)}$$

For a Slater type orbital (STO) we have [218]

$$\phi_{N,L,M}(\boldsymbol{r}-\boldsymbol{R}) = \sum_{l=0}^{\infty}\sum_{\lambda=|l-L|}^{(l+L)} \nu_{l,\lambda,L}(r,R) \sum_{m=-l}^{l} \varsigma_{\lambda,L,M,l,m} Y_{\lambda,M-m}(\Theta,\Phi) Y_{l,m}(\theta,\varphi) \tag{B.7}$$

where

$$\begin{aligned}
\varsigma_{\lambda,L,M,l,m} &= \int d\boldsymbol{\omega} Y^{*}_{\lambda,M-m}(\theta,\varphi) Y^{*}_{l,m}(\theta,\varphi) Y_{L,M}(\theta,\varphi) && \text{(B.8)}\\
\nu_{\lambda,l,L}(r,R) &= \frac{2\pi(-)^{l}}{R} \sum_{s=0}^{(l+\lambda+L)/2} \sum_{t=0}^{(l+\lambda+L)/2-s} \Xi_{l,\lambda,L,s,t} \left(\frac{r}{R}\right)^{2t-l-1} \times \\
&\quad \times \int_{|r-R|}^{r+R} dr' \left(\frac{r}{R}\right)^{2s-L+1} R_{N,L}(r') && \text{(B.9)}\\
\Xi_{l,\lambda,L,s,t} &= [(2s)!!(2s-2L-1)!!(2t)!!(2t-2l-1)!! \times \\
&\quad \times (L+l+\lambda-2s-2t)!!(L+l-\lambda-2s-2t-1)!!]^{-1} && \text{(B.10)}
\end{aligned}$$

In the particular case of a $2p_Z = \phi_{2,1,0}(\boldsymbol{r}) = \frac{\alpha^{5/2}}{\sqrt{\pi}} r e^{-\alpha r}\cos(\theta)$ orbital, with $\alpha = Z_{eff}/2a_0$, one has

$$\phi_{2,1,0}(\boldsymbol{r}-\boldsymbol{R}) = \frac{\alpha^{5/2}}{\sqrt{\pi}} \sum_{l=0}^{\infty}\sum_{\lambda=|l-1|}^{(l+1)} \nu_{l,\lambda,1}(r,R) \sum_{m=-\lambda}^{\lambda} \varsigma_{\lambda,1,0,l,m} Y_{l,-m}(\Theta,\Phi) Y_{l,m}(\theta,\varphi) \tag{B.11}$$

with

$$\begin{aligned}
\varsigma_{\lambda,1,0,l,m} &= \int d\boldsymbol{\omega} Y^{*}_{\lambda,-m}(\theta,\varphi) Y^{*}_{l,m}(\theta,\varphi) Y_{1,0}(\theta,\varphi) \\
&= \int d\boldsymbol{\omega} Y_{\lambda,m}(\theta,\varphi) Y_{l,-m}(\theta,\varphi) Y_{1,0}(\theta,\varphi) \\
&= \sqrt{\frac{3(2\lambda+1)(2l+1)}{4\pi}} \begin{pmatrix} \lambda & l & 1 \\ 0 & 0 & 0 \end{pmatrix} \begin{pmatrix} \lambda & l & 1 \\ m & -m & 0 \end{pmatrix} && \text{(B.12)}
\end{aligned}$$

To evaluate $\nu_{l,\lambda,1}(r,R)$ we need to calculate the integral in equation B.9

$$\int_{|r-R|}^{r+R} dr'(r')^{2s-L+1} R_{N,L}(r') = \int_{|r-R|}^{r+R} dr'(r')^{2s+1} e^{-\alpha r'} \tag{B.13}$$

This integral can be solved by parts:

$$\begin{aligned}
\int dr r^{n} e^{-\alpha r} &= -\frac{r^{n}}{\alpha} e^{-\alpha r} + \frac{n}{\alpha}\int dr r^{n-1} e^{-\alpha r} = \\
&= -\frac{r^{n}}{\alpha} e^{-\alpha r} - \frac{n r^{n-1}}{\alpha^{2}} e^{-\alpha r} + \frac{n(n-1)}{\alpha^{2}} \int dr r^{n-2} e^{-\alpha r} = \\
&= -\frac{r^{n}}{\alpha} e^{-\alpha r} - \frac{n r^{n-1}}{\alpha^{2}} e^{-\alpha r} - \frac{n(n-1) r^{n-1}}{\alpha^{3}} e^{-\alpha r} +
\end{aligned}$$

$$\begin{aligned}
&+\frac{n(n-1)(n-2)}{\alpha^3}\int drr^{n-3}e^{-\alpha r} = \ldots = \\
&= -\sum_{\mu=0}^{n}\frac{1}{\alpha^{\mu+1}}\frac{n!}{(n-\mu)!}r^{n-\mu}e^{-\alpha r} \qquad \text{(B.14)}
\end{aligned}$$

So, substitution in eq. B.9 reads

$$\begin{aligned}
\nu_{l,\lambda,1}(r,R) &= \frac{2\pi(-)^{l+1}}{R}\sum_{s=0}^{(l+\lambda+1)/2}\sum_{t=0}^{(l+\lambda+1)/2-s}\Xi_{l,\lambda,1,s,t}\left(\frac{r}{R^{2s}}\right)^{2t-l-1}\times \\
&\times\sum_{\mu=0}^{s2+1}\frac{1}{\alpha^{\mu+1}}\frac{(s2+1)!}{(2s+1-\mu)!}\Big[|r+R|^{2s+1-\mu}e^{-\alpha|r+R|}+ \\
&-|r-R|^{2s+1-\mu}e^{-\alpha|r-R|}\Big] \qquad \text{(B.15)}
\end{aligned}$$

Finally

$$\begin{aligned}
\Xi_{l,\lambda,1,s,t} &= [(2s)!!(2s-3)!!(2t)!!(2t-2l-1)!!\times \\
&\times(l+\lambda-2s-2t+1)!!(l-\lambda-2s-2t)!!]^{-1} \qquad \text{(B.16)}
\end{aligned}$$

B.2 Expression of operator in spherical coordinates

The tensor operator $\hat{\boldsymbol{D}}$ depends on the relative distance of the two electrons. We write its spherical components $\hat{\boldsymbol{D}} = \hat{D}^{(0)} \oplus \hat{D}^{(1)} \oplus \hat{D}^{(2)}$. Because it is a traceless symmetric tensor, only the rank 2 component is not zero. Its expression as function of the Cartesian coordinates is

$$\begin{aligned}
\hat{D}^{(2,0)} &= \sqrt{\frac{3}{2}}\hat{D}_{ZZ} = \sqrt{\frac{3}{2}}\frac{1}{r_{1,2}^3}\left[1-3\frac{(\boldsymbol{r}_{1,2})_Z^2}{r_{1,2}^2}\right] \\
\hat{D}^{(2,\pm1)} &= \mp\left(\hat{D}_{XZ}\pm i\hat{D}_{YZ}\right) = \pm\frac{3}{r_{1,2}^3}\left[\frac{(\boldsymbol{r}_{1,2})_X\boldsymbol{r}_{1,2})_Z \pm i(\boldsymbol{r}_{1,2})_Y\boldsymbol{r}_{1,2})_Z}{r_{1,2}^2}\right] \qquad \text{(B.17)} \\
\hat{D}^{(2,\pm2)} &= \frac{\hat{D}_{XX}-\hat{D}_{YY}}{2}\pm i\hat{D}_{XY} = -\frac{3}{r_{1,2}^3}\left[\frac{(\boldsymbol{r}_{1,2})_X^2-(\boldsymbol{r}_{1,2})_Y^2}{2r_{1,2}^2}\pm i\frac{(\boldsymbol{r}_{1,2})_X(\boldsymbol{r}_{1,2})_Y}{r_{1,2}^2}\right]
\end{aligned}$$

Given the expression of the components of the vector $\boldsymbol{r}_{1,2}$ in spherical coordinates, i.e.

$$\begin{aligned}
(\boldsymbol{r}_{1,2})_X &= r_{1,2}\sin(\theta_{1,2})\cos(\varphi_{1,2}) \\
(\boldsymbol{r}_{1,2})_Y &= r_{1,2}\sin(\theta_{1,2})\sin(\varphi_{1,2}) \qquad \text{(B.18)} \\
(\boldsymbol{r}_{1,2})_Z &= r_{1,2}\cos(\theta_{1,2})
\end{aligned}$$

we obtain

$$\begin{aligned}\hat{D}^{(2,0)} &= \sqrt{\frac{3}{2}}\frac{1}{r_{1,2}^3}\left[1-3\cos^2(\theta_{1,2})\right] = -\sqrt{\frac{24\pi}{5}}\frac{1}{r_{1,2}^3}Y_{2,0}(\theta_{1,2},\varphi_{1,2})\\ \hat{D}^{(2,\pm1)} &= \pm\frac{3}{r_{1,2}^3}\sin(\theta_{1,2})\cos(\theta_{1,2})e^{\pm i\varphi_{1,2}} = -\sqrt{\frac{24\pi}{5}}\frac{1}{r_{1,2}^3}Y_{2,\pm1}(\theta_{1,2},\varphi_{1,2})\\ \hat{D}^{(2,\pm2)} &= -\frac{3}{r_{1,2}^3}\sin^2(\theta_{1,2})e^{\pm i2\varphi_{1,2}} = -\sqrt{\frac{24\pi}{5}}\frac{1}{r_{1,2}^3}Y_{2,\pm2}(\theta_{1,2},\varphi_{1,2})\end{aligned} \tag{B.19}$$

Let's recall the following expansion for the radial component of vector $\boldsymbol{r}_{1,2} = \boldsymbol{r}_2 - \boldsymbol{r}_1 = (r_{1,2}, \theta_{1,2}, \varphi_{1,2})$ [219]

$$\begin{aligned}\frac{1}{r_{1,2}^{L+1}}Y_{L,M}(\theta_{1,2},\varphi_{1,2}) &= \sqrt{\frac{4\pi}{(2L)!}}\sum_{l_1,l_2=0}^{\infty}\sqrt{\frac{(2l_2)!}{(2l_1+1)!}}\frac{r_1^{l_1}}{r_2^{l_2+1}}\times\\ &\times\left[\boldsymbol{Y}_{l_1}(\theta_1,\varphi_1)\otimes\boldsymbol{Y}_{l_2}(\theta_2,\varphi_2)\right]_M^L\end{aligned} \tag{B.20}$$

where it is assumed that $r_1 < r_2$ and $(l_2 - l_1) = L$.

Now, it is possible to express the irreducible spherical components of $\hat{\boldsymbol{D}}$ as a sum of products of a function that depends only on the distance multiplied by a function that depends only on the orientation, i.e.

$$\begin{aligned}\hat{D}^{(2,M)} &= \frac{1}{r_{1,2}^3}Y_{2,M}(\theta_{1,2}\varphi_{1,2})\\ &= \sqrt{\frac{\pi}{6}}\sum_{l_1=0}^{\infty}\sum_{l_2=\max(0,l_1-2)}^{l_1+2}(-)^{l_2}\sqrt{\frac{(2l_2)!}{(2l_1+1)!}}\frac{r_1^{l_1}}{r_2^{l_2+1}}\times\\ &\times\left[\boldsymbol{Y}_{l_1}(\theta_1,\varphi_1)\otimes\boldsymbol{Y}_{l_2}(\theta_2,\varphi_2)\right]_M^2 =\\ &= \sum_{l_1,l_2=0}^{\infty}(-)^{l_2}d_{l_1,l_2}(r_1,r_2)\left[\boldsymbol{Y}_{l_1}(\theta_1,\varphi_1)\otimes\boldsymbol{Y}_{l_2}(\theta_2,\varphi_2)\right]_M^2\end{aligned} \tag{B.21}$$

where $(l_2 - l_1) = 2$.

B.3 Evaluation of four-centers integral

Now that both the expressions for the orbitals and for the operator have been factorized in a radial and angular parts, it is possible to rewrite integral B.3, $I = \langle\phi_A\phi_B\,|\hat{D}^{2,M}|\,\phi_C\phi_D\rangle$, as

$$I = \langle\rho_{l_A,m_A}^{1,0}(r_1,\boldsymbol{R}_A)\rho_{l_B,m_B}^{1,0}(r_2,\boldsymbol{R}_B)\,|d_{l_1,l_2}|\,\rho_{l_C,m_C}^{1,0}(r_1,\boldsymbol{R}_C)\rho_{l_D,m_D}^{1,0}(r_2,\boldsymbol{R}_D)\rangle\times$$

$$
\begin{aligned}
& \times\langle Y_{l_A,m_A}(\boldsymbol{\omega}_1)Y_{l_B,m_B}(\boldsymbol{\omega}_2)\,|\,[\boldsymbol{Y}_{l_1}(\boldsymbol{\omega}_1)\otimes\boldsymbol{Y}_{l_2}(\boldsymbol{\omega}_2)]^2_M\,|\,Y_{l_C,m_C}(\boldsymbol{\omega}_1)Y_{l_D,m_D}(\boldsymbol{\omega}_2)\rangle = \\
= \; & I_r \times I_{\boldsymbol{\omega}}^{(2,M)} \qquad \text{(B.22)}
\end{aligned}
$$

where $\boldsymbol{\omega_i} = (\theta_i, \varphi_i)$ and to keep notation simple we used the Einstein's notation for indexes l_A, m_A, l_B, m_B, l_C, m_C, l_D and m_D, for which the summation limits are given in eq. B.6, and l_1 and l_2 for which the summation limits are given in eq. B.21.

The last equality in eq. B.22 underlines that for each of the five components of $\hat{D}^{(2)}$, the radial part (I_r) is the same. Moreover, calculations of the angular part ($I_{\boldsymbol{\omega}}^{(2,M)}$) can be simplified by using the Wigner-Eckart theorem, i.e.

$$
\begin{aligned}
I_{\boldsymbol{\omega}}^{(2,M)} &= \langle Y_{l_A,m_A}(\boldsymbol{\omega}_1)Y_{l_B,m_B}(\boldsymbol{\omega}_2)\,|\,[\boldsymbol{Y}_{l_1}(\boldsymbol{\omega}_1)\otimes\boldsymbol{Y}_{l_2}(\boldsymbol{\omega}_2)]^2_M\,|\,Y_{l_C,m_C}(\boldsymbol{\omega}_1)Y_{l_D,m_D}(\boldsymbol{\omega}_2)\rangle = \\
&= [(2l_A+1)(2l_B+1)]^{-1/2}\sum_{m_1,m_2} C^{l_A m_A}_{l_C m_C, l_1 m_1} C^{2\,M}_{l_1 m_1, l_2 m_2} C^{l_B m_B}_{l_D m_D, l_2 m_2} \times \\
&\quad \times \langle l_A||\boldsymbol{Y}_{l_1}||l_C\rangle\langle l_B||\boldsymbol{Y}_{l_2}||l_D\rangle \qquad \text{(B.23)}
\end{aligned}
$$

where the reduced matrix elements are [219]

$$
\langle l||\boldsymbol{Y}_L||l'\rangle = \sqrt{\frac{(2L+1)(2l'+1}{4\pi}}C^{l\,0}_{l'\,0,L\,0} \qquad \text{(B.24)}
$$

and $C^{l_3 m_3}_{l_1 m_1, l_2 m_2}$ is a Clebsh - Gordan coefficient, which can be written in terms of 3j symbols as

$$
C^{l_3 m_3}_{l_1 m_1, l_2 m_2} = (-)^{l_1+l_2-m_3}(2l_3+1)^{1/2}\begin{pmatrix} l_1 & l_2 & l_3 \\ m_1 & m_2 & -m_3 \end{pmatrix} \qquad \text{(B.25)}
$$

The integral B.23 becomes

$$
\begin{aligned}
I_{\boldsymbol{\omega}}^{(2,M)} &= \frac{[l_1,l_2,l_A,l_B,l_C,l_D]^{1/2}}{4\pi}\sum_{m_1,m_2}(-)^{m_A+m_B+M}\begin{pmatrix} l_C & l_1 & l_A \\ m_C & m_1 & -m_A \end{pmatrix} \times \\
&\quad \times \begin{pmatrix} l_C & l_1 & l_A \\ 0 & 0 & 0 \end{pmatrix}\begin{pmatrix} l_1 & l_2 & 2 \\ m_1 & m_2 & -M \end{pmatrix}\begin{pmatrix} l_D & l_2 & l_B \\ m_D & m_2 & -m_B \end{pmatrix} \times \\
&\quad \times \begin{pmatrix} l_D & l_2 & l_B \\ 0 & 0 & 0 \end{pmatrix} \qquad \text{(B.26)}
\end{aligned}
$$

where $[l_1, l_2, \ldots, l_n] = (2l_1+1)(2l_2+1)\ldots(2l_n+1)$.

For the first and fourth 3j symbols in the last equation to be different from zero, we must have

$m_1 = m_A - m_C$

$m_2 = m_B - m_D$

so only one term survives in the summation over m_1 and m_2 and we have

$$\begin{aligned} I_{\boldsymbol{\omega}}^{(2,M)} &= \frac{[l_1, l_2, l_A, l_B, l_C, l_D]^{1/2}}{4\pi} (-)^{m_C+m_D} \begin{pmatrix} l_C & l_1 & l_A \\ 0 & 0 & 0 \end{pmatrix} \begin{pmatrix} l_D & l_2 & l_B \\ 0 & 0 & 0 \end{pmatrix} \times \\ &\times \begin{pmatrix} l_C & l_1 & l_A \\ m_C & m_A - m_C & -m_A \end{pmatrix} \begin{pmatrix} l_1 & l_2 & 2 \\ m_A - m_C & m_B - m_D & -M \end{pmatrix} \times \\ &\times \begin{pmatrix} l_D & l_2 & l_B \\ m_D & m_B - m_D & -m_B \end{pmatrix} \end{aligned} \tag{B.27}$$

Considering the symmetries of the 3j symbols, we can impose these constraints to the indexes

$m_A + m_B - m_C - m_D = M$

$l_1 + l_A + l_C =$ even

$l_2 + l_B + l_D =$ even

$|l_1 - l_2| \leq 2 \leq (l_1 + l_2)$

Moreover, eq. B.21 imposes the constraint $(l_2 - l_1) = 2$, so it is possible to write

$$\begin{aligned} I_{\boldsymbol{\omega}}^{(2,M)} &= \frac{[l_1, l_1+2, l_A, l_B, l_C, l_D]^{1/2}}{4\pi} (-)^{m_C+m_D} \begin{pmatrix} l_C & l_1 & l_A \\ 0 & 0 & 0 \end{pmatrix} \begin{pmatrix} l_D & l_1+2 & l_B \\ 0 & 0 & 0 \end{pmatrix} \times \\ &\times \begin{pmatrix} l_C & l_1 & l_A \\ m_C & m_A - m_C & -m_A \end{pmatrix} \begin{pmatrix} l_1 & l_1+2 & 2 \\ m_A - m_C & m_B - m_D & -M \end{pmatrix} \times \\ &\times \begin{pmatrix} l_D & l_1+2 & l_B \\ m_D & m_B - m_D & -m_B \end{pmatrix} \end{aligned} \tag{B.28}$$

with the following new constraints

$m_A + m_B - m_C - m_D = M$

$l_1 + l_A + l_C =$ even

$l_1 + l_B + l_D =$ even

B.4 Calculation of the dipolar tensor in a simple case

We report the calculation of the dipolar tensor for a simple geometry and an approximated expansion of the two SOMO orbitals. This is the evaluation of the dipolar interaction that we used in the spin Hamiltonian of the bi-labelled heptapeptide (see Section 3.3.4.

In what follows we take as reference the image below We have four nuclei placed at the edges

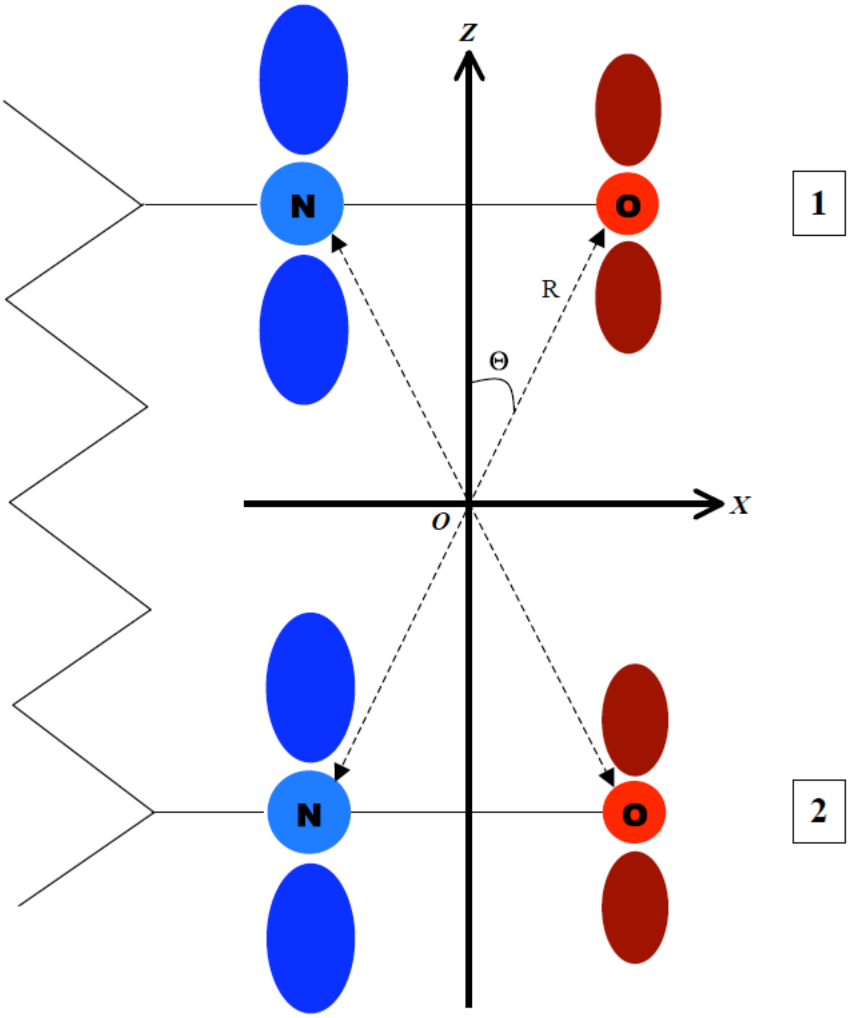

of a rectangle, having spherical coordinates

$\boldsymbol{R}_{N_1} = (R, -\Theta, 0)$

$\boldsymbol{R}_{O_1} = (R, \Theta, 0)$

$\boldsymbol{R}_{N_2} = (R, -\pi + \Theta, 0)$

$\boldsymbol{R}_{O_2} = (R, \pi - \Theta, 0)$

Then, we make the further approximation of considering this simple form for the two SOMO orbitals

$$\Psi' = \frac{1}{\sqrt{2}}\left[\phi_{2,1,0}^{N_1}(\boldsymbol{r} - \boldsymbol{R}_{N_1}) - \phi_{2,1,0}^{O_1}(\boldsymbol{r} - \boldsymbol{R}_{O_1})\right] \tag{B.29}$$

$$\Psi'' = \frac{1}{\sqrt{2}}\left[\phi_{2,1,0}^{N_2}(\boldsymbol{r} - \boldsymbol{R}_{N_2}) - \phi_{2,1,0}^{O_2}(\boldsymbol{r} - \boldsymbol{R}_{O_2})\right] \tag{B.30}$$

i.e., we consider that only the two $2p_Z$ orbitals of a $N - O$ couple contribute to the SOMO, with the same weight. Also, we consider all the four orbitals parallel among them and parallel to the Z-axis of the reference frame in which we are calculating the tensor in order to avoid complications of rotations.

The dipolar tensor is calculated as the expectation value of the operator $\hat{\boldsymbol{D}}$ over the state $|-\rangle = \frac{1}{\sqrt{2}}|\,\Psi'(1)\Psi''(2) - \Psi'2\Psi''(1)\rangle$, so that

$$\boldsymbol{D} = \frac{1}{2}\frac{\mu_0}{4\pi}\frac{g_e^2\beta_3^2}{\hbar}\langle -\,|\hat{\boldsymbol{D}}|\,-\rangle \tag{B.31}$$

In spherical coordinates we have

$$D^{(2,M)} = \frac{1}{2}\frac{\mu_0}{4\pi}\frac{g_e^2\beta_3^2}{\hbar}\langle -\,|\hat{D}^{(2,M)}|\,-\rangle \tag{B.32}$$

Finally, the following symmetry

$$\begin{aligned} D^{(2,-M)} &\propto \langle -\,|\hat{D}^{(2,-M)}|\,-\rangle = (-)^M\langle -\,|\hat{D}^{(2,M)\,*}|\,-\rangle = (-)^M\langle -\,|\hat{D}^{(2,M)}|\,-\rangle^* \propto \\ &\propto (-)^M D^{(2,M)\,*} \end{aligned} \tag{B.33}$$

gives the possibility to calculate only three of the five components.

Appendix C

Sample calculation with E-SpiReS

In this appendix we show how to calculate *ab initio* the cw-ESR spectrum of tempone in water at 298.15 K. This tutorial assumes that the quantum mechanic calculation of magnetic parameters has previously been performed.

Step 1 - launch E-SpiReS and click on "Set Project" button. A window called "Parameter Selector" appears, where all the physical properties of the system under study can be set. Firstly click on "Load Z-Matrix" button to load the molecule.

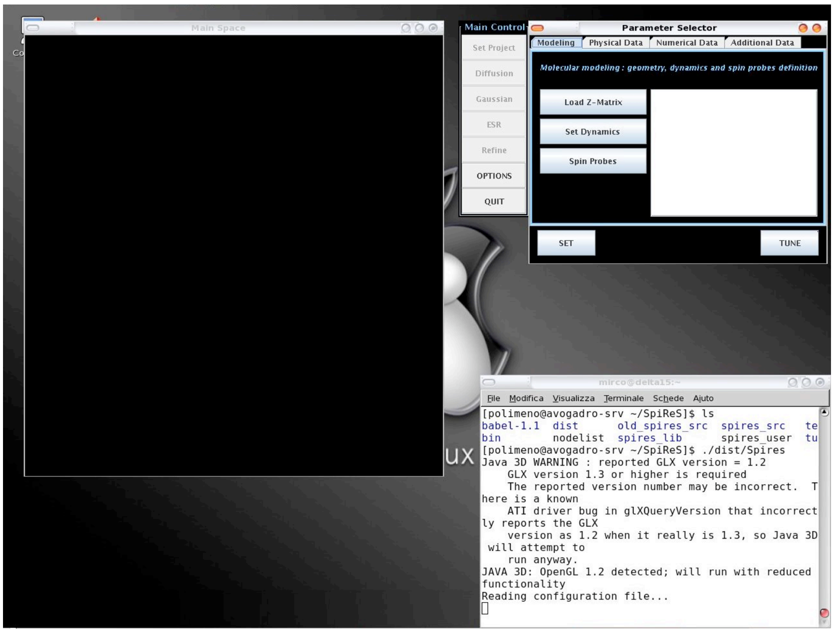

```
[polimeno@avogadro-srv ~/SpiReS]$ ls
babel-1.1  dist      old_spires_src  spires_src   te
bin        nodelist  spires_lib      spires_user  tu
[polimeno@avogadro-srv ~/SpiReS]$ ./dist/Spires
Java 3D WARNING : reported GLX version = 1.2
    GLX version 1.3 or higher is required
    The reported version number may be incorrect.  T
here is a known
    ATI driver bug in glXQueryVersion that incorrect
ly reports the GLX
    version as 1.2 when it really is 1.3, so Java 3D
 will attempt to
    run anyway.
JAVA 3D: OpenGL 1.2 detected; will run with reduced
functionality
Reading configuration file...
```

Step 2 - select the "tempone.zmt" file; the molecule appears in the 3D space in the laboratory frame, LF (also plotted). In the "Parameter Selector" window the Z-matrix is written in the white text area. This area is reactive to mouse clicking, i.e. when a row is clicked, the corresponding atom is highlighted in green.

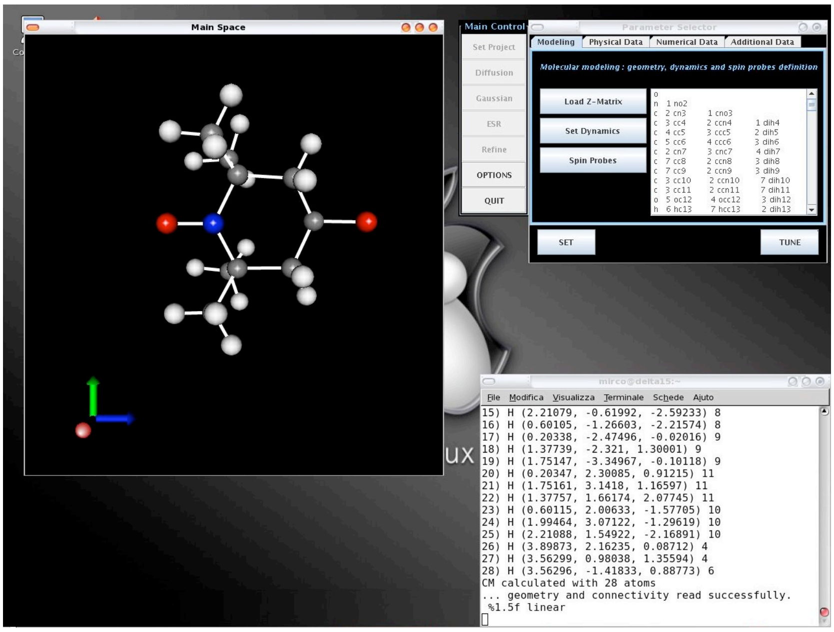

```
o
n  1 no2
c  2 cn3   1 cno3
c  3 cc4   2 ccn4   1 dih4
c  4 cc5   3 ccc5   2 dih5
c  5 cc6   4 ccc6   3 dih6
c  2 cn7   3 cnc7   4 dih7
c  7 cc8   2 ccn8   3 dih8
c  7 cc9   2 ccn9   3 dih9
c  3 cc10  2 ccn10  7 dih10
c  3 cc11  2 ccn11  7 dih11
o  5 oc12  4 occ12  3 dih12
h  6 hc13  7 hcc13  2 dih13
```

```
15) H (2.21079, -0.61992, -2.59233) 8
16) H (0.60105, -1.26603, -2.21574) 8
17) H (0.20338, -2.47496, -0.02016) 9
18) H (1.37739, -2.321, 1.30001) 9
19) H (1.75147, -3.34967, -0.10118) 9
20) H (0.20347, 2.30085, 0.91215) 11
21) H (1.75161, 3.1418, 1.16597) 11
22) H (1.37757, 1.66174, 2.07745) 11
23) H (0.60115, 2.00633, -1.57705) 10
24) H (1.99464, 3.07122, -1.29619) 10
25) H (2.21088, 1.54922, -2.16891) 10
26) H (3.89873, 2.16235, 0.08712) 4
27) H (3.56299, 0.98038, 1.35594) 4
28) H (3.56296, -1.41833, 0.88773) 6
CM calculated with 28 atoms
... geometry and connectivity read successfully.
 %1.5f linear
```

Step 3 - clicking on the "Set Dynamics" button a new window appears. Here one chooses the form of the diffusive operator. Tempone is a small and rigid molecule, so the "One Rigid Body" model is chosen.

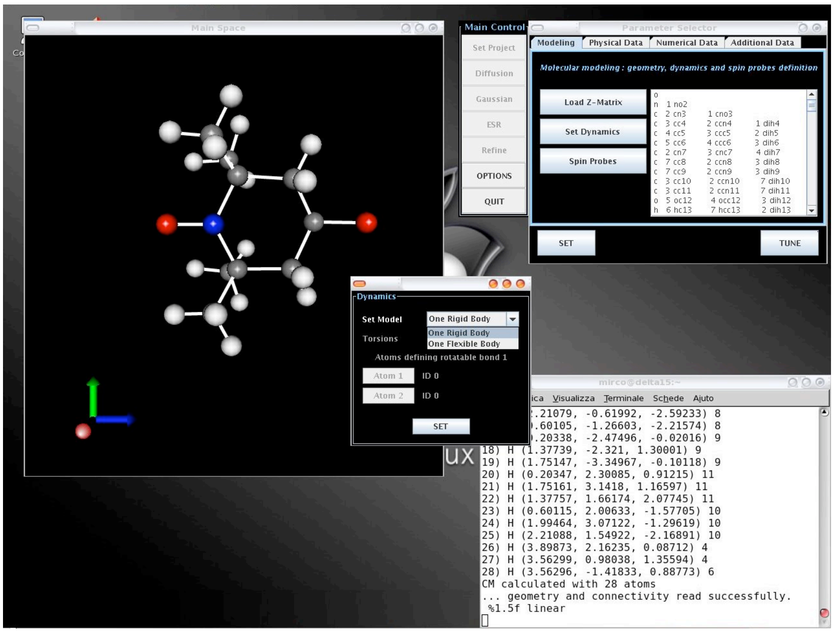

Set Model One Rigid Body

Torsions

Atoms defining rotatable bond 1

Atom 1 ID 0

Atom 2 ID 0

```
o
n  1 no2
c  2 cn3   1 cno3
c  3 cc4   2 ccn4   1 dih4
c  4 cc5   3 ccc5   2 dih5
c  5 cc6   4 ccc6   3 dih6
c  2 cn7   3 cnc7   4 dih7
c  7 cc8   2 ccn8   3 dih8
c  7 cc9   2 ccn9   3 dih9
c  3 cc10  2 ccn10  7 dih10
c  3 cc11  2 ccn11  7 dih11
o  5 oc12  4 occ12  3 dih12
h  6 hc13  7 hcc13  2 dih13
```

```
.21079, -0.61992, -2.59233) 8
.60105, -1.26603, -2.21574) 8
.20338, -2.47496, -0.02016) 9
18) H (1.37739, -2.321, 1.30001) 9
19) H (1.75147, -3.34967, -0.10118) 9
20) H (0.20347, 2.30085, 0.91215) 11
21) H (1.75161, 3.1418, 1.16597) 11
22) H (1.37757, 1.66174, 2.07745) 11
23) H (0.60115, 2.00633, -1.57705) 10
24) H (1.99464, 3.07122, -1.29619) 10
25) H (2.21088, 1.54922, -2.16891) 10
26) H (3.89873, 2.16235, 0.08712) 4
27) H (3.56299, 0.98038, 1.35594) 4
28) H (3.56296, -1.41833, 0.88773) 6
CM calculated with 28 atoms
... geometry and connectivity read successfully.
 %1.5f linear
```

Step 4 - to define the spin Hamiltonian of the molecule choose the "Spin Probes" button. Use the "Choose Atom" button of the first tag of the window to select the N-O bond as probe. The O atom becomes green and a frame appears for the ***g*** tensor.

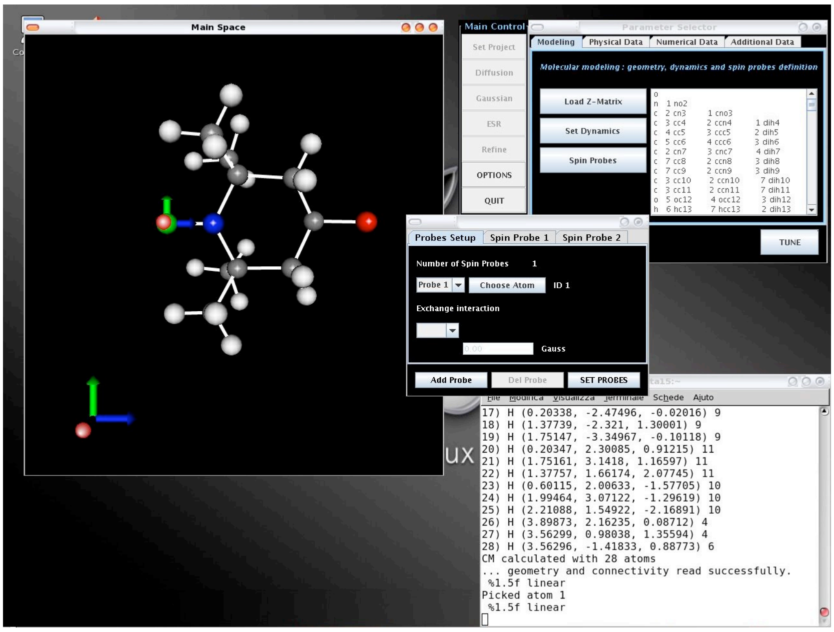

Number of Spin Probes 1

Probe 1 ID 1

```
o
n  1 no2
c  2 cn3     1 cno3
c  3 cc4     2 ccn4     1 dih4
c  4 cc5     3 ccc5     2 dih5
c  5 cc6     4 ccc6     3 dih6
c  2 cn7     3 cnc7     4 dih7
c  7 cc8     2 ccn8     3 dih8
c  7 cc9     2 ccn9     3 dih9
c  3 cc10    2 ccn10    7 dih10
c  3 cc11    2 ccn11    7 dih11
o  5 oc12    4 occ12    3 dih12
h  6 hc13    7 hcc13    2 dih13
```

```
17) H (0.20338, -2.47496, -0.02016) 9
18) H (1.37739, -2.321, 1.30001) 9
19) H (1.75147, -3.34967, -0.10118) 9
20) H (0.20347, 2.30085, 0.91215) 11
21) H (1.75161, 3.1418, 1.16597) 11
22) H (1.37757, 1.66174, 2.07745) 11
23) H (0.60115, 2.00633, -1.57705) 10
24) H (1.99464, 3.07122, -1.29619) 10
25) H (2.21088, 1.54922, -2.16891) 10
26) H (3.89873, 2.16235, 0.08712) 4
27) H (3.56299, 0.98038, 1.35594) 4
28) H (3.56296, -1.41833, 0.88773) 6
CM calculated with 28 atoms
... geometry and connectivity read successfully.
 %1.5f linear
Picked atom 1
 %1.5f linear
```

Step 5 - the second and third tags allow to add spin active nuclei (min 1, max 2) to the probe(s). In the "Spin Probe 1" tag click on "Choose Atom" and select the N atom in the 3D space. The atom becomes green and a reference frame appears for the hyperfine ***A*** tensor; set to 1 the spin number of the nucleus.

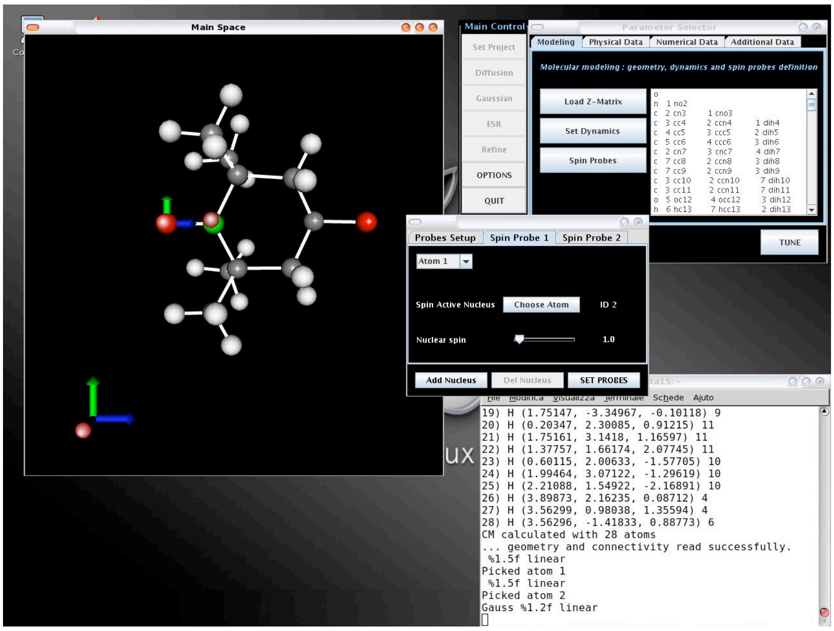

Atom 1

Spin Active Nucleus ID 2

Nuclear spin 1.0

```
o
n  1 no2
c  2 cn3     1 cno3
c  3 cc4     2 ccn4     1 dih4
c  4 cc5     3 ccc5     2 dih5
c  5 cc6     4 ccc6     3 dih6
c  2 cn7     3 cnc7     4 dih7
c  7 cc8     2 ccn8     3 dih8
c  7 cc9     2 ccn9     3 dih9
c  3 cc10    2 ccn10    7 dih10
c  3 cc11    2 ccn11    7 dih11
o  5 oc12    4 occ12    3 dih12
h  6 hc13    7 hcc13    2 dih13
```

```
19) H (1.75147, -3.34967, -0.10118) 9
20) H (0.20347, 2.30085, 0.91215) 11
21) H (1.75161, 3.1418, 1.16597) 11
22) H (1.37757, 1.66174, 2.07745) 11
23) H (0.60115, 2.00633, -1.57705) 10
24) H (1.99464, 3.07122, -1.29619) 10
25) H (2.21088, 1.54922, -2.16891) 10
26) H (3.89873, 2.16235, 0.08712) 4
27) H (3.56299, 0.98038, 1.35594) 4
28) H (3.56296, -1.41833, 0.88773) 6
CM calculated with 28 atoms
... geometry and connectivity read successfully.
 %1.5f linear
Picked atom 1
 %1.5f linear
Picked atom 2
Gauss %1.2f linear
```

Step 6 - in the "Physical Data" tag of the "Parameter Selector" a number of relevant parameters are set. Use the "Frequency", "B Sweep", "Viscosity" and "Temperature" buttons to set the four parameters at, respectively, 8.89 GHz, 75.7 Gauss, 0.89 cP and 298.15 K.

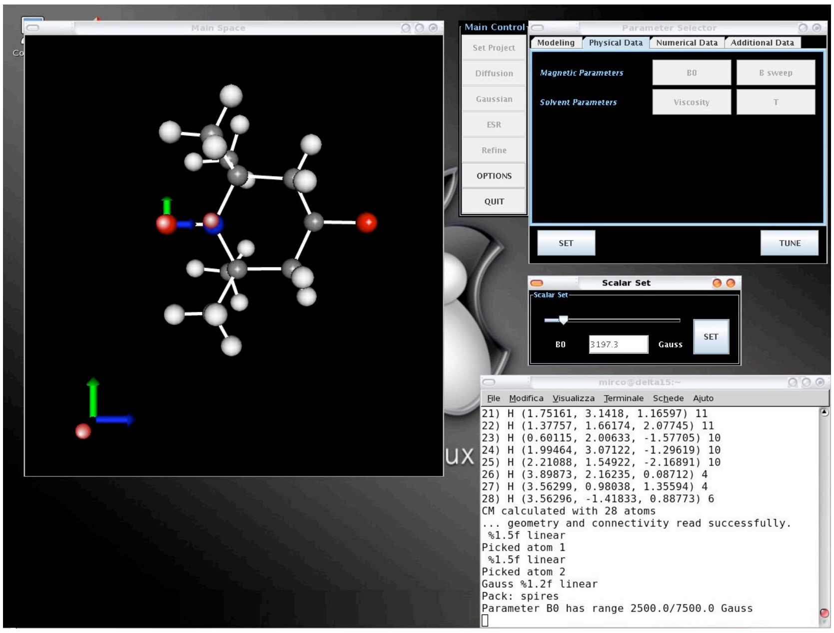

B0 3197.3 Gauss

```
21) H (1.75161, 3.1418, 1.16597) 11
22) H (1.37757, 1.66174, 2.07745) 11
23) H (0.60115, 2.00633, -1.57705) 10
24) H (1.99464, 3.07122, -1.29619) 10
25) H (2.21088, 1.54922, -2.16891) 10
26) H (3.89873, 2.16235, 0.08712) 4
27) H (3.56299, 0.98038, 1.35594) 4
28) H (3.56296, -1.41833, 0.88773) 6
CM calculated with 28 atoms
... geometry and connectivity read successfully.
 %1.5f linear
Picked atom 1
 %1.5f linear
Picked atom 2
Gauss %1.2f linear
Pack: spires
Parameter B0 has range 2500.0/7500.0 Gauss
```

Step 7 - select the "Additional Data" tag to set the intrinsic linewidth to 0.40 Gauss, to take into account the unresolved super-hyperfine coupling of the electron with the twelve surrounding hydrogen atoms.

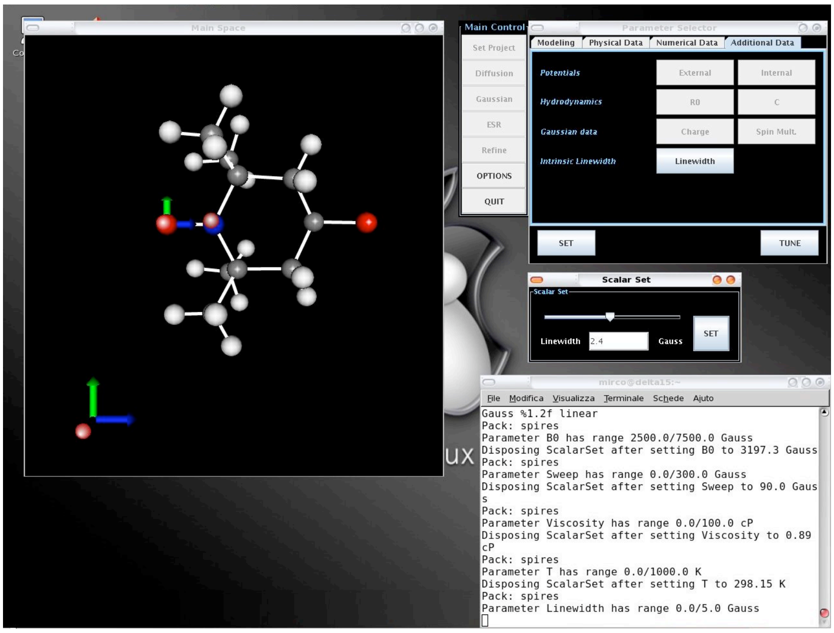

Linewidth 2.4 Gauss

```
Gauss %1.2f linear
Pack: spires
Parameter B0 has range 2500.0/7500.0 Gauss
Disposing ScalarSet after setting B0 to 3197.3 Gauss
Pack: spires
Parameter Sweep has range 0.0/300.0 Gauss
Disposing ScalarSet after setting Sweep to 90.0 Gaus
s
Pack: spires
Parameter Viscosity has range 0.0/100.0 cP
Disposing ScalarSet after setting Viscosity to 0.89
cP
Pack: spires
Parameter T has range 0.0/1000.0 K
Disposing ScalarSet after setting T to 298.15 K
Pack: spires
Parameter Linewidth has range 0.0/5.0 Gauss
```

Step 8 - click the "Diffusion" button in the "Main Control Panel": the diffusion tensor of the molecule is automatically calculated and a new frame appears in the 3D space, i.e. the one that diagonalizes the tensor. The molecule changes its colour: atoms assume different colours if they belong to different fragments.

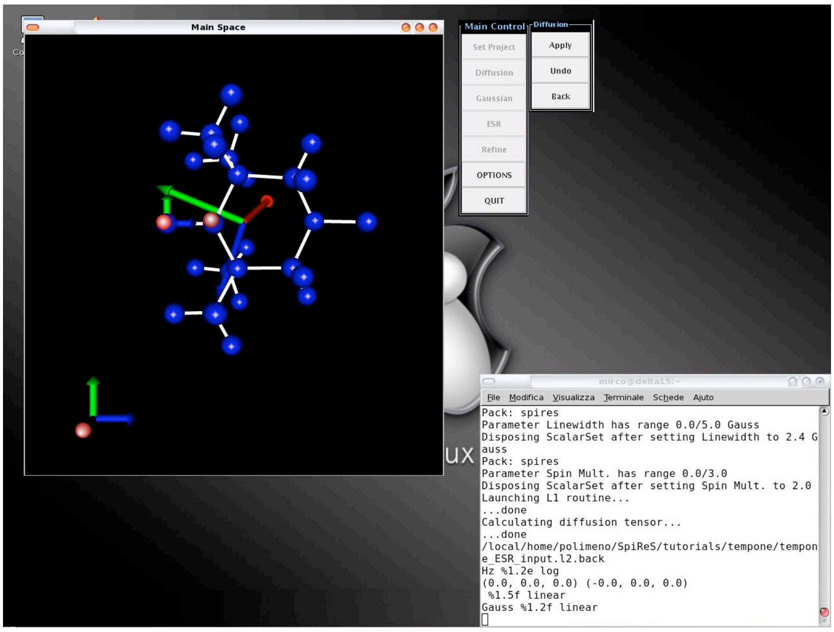

```
Pack: spires
Parameter Linewidth has range 0.0/5.0 Gauss
Disposing ScalarSet after setting Linewidth to 2.4 G
auss
Pack: spires
Parameter Spin Mult. has range 0.0/3.0
Disposing ScalarSet after setting Spin Mult. to 2.0
Launching L1 routine...
...done
Calculating diffusion tensor...
...done
/local/home/polimeno/SpiReS/tutorials/tempone/tempon
e_ESR_input.l2.back
Hz %1.2e log
(0.0, 0.0, 0.0) (-0.0, 0.0, 0.0)
 %1.5f linear
Gauss %1.2f linear
```

Step 9 - to use the magnetic tensors evaluated via QM calculations enter the "Gaussian Environment" and check the "Use output" checkbox. When Gaussian output is loaded, <u>all the tensors</u> are updated.

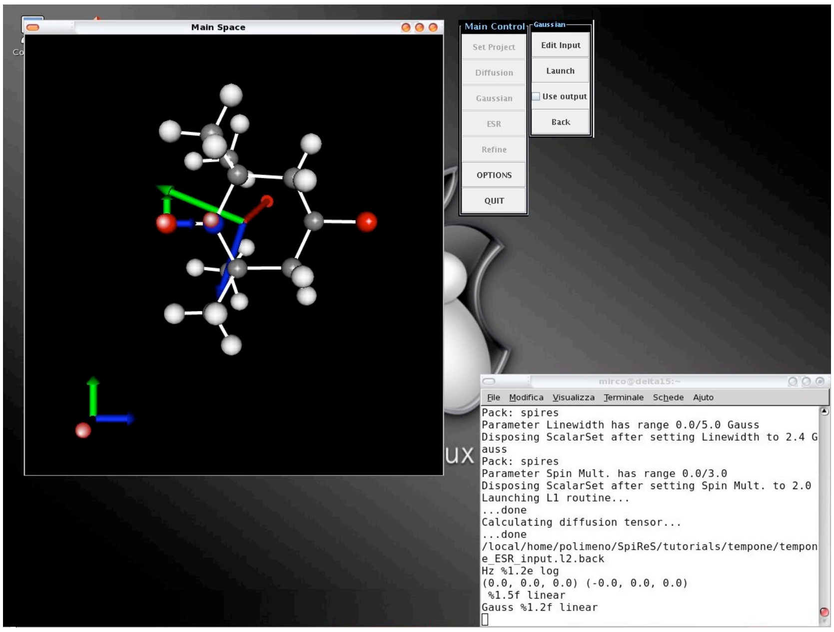

```
Pack: spires
Parameter Linewidth has range 0.0/5.0 Gauss
Disposing ScalarSet after setting Linewidth to 2.4 G
auss
Pack: spires
Parameter Spin Mult. has range 0.0/3.0
Disposing ScalarSet after setting Spin Mult. to 2.0
Launching L1 routine...
...done
Calculating diffusion tensor...
...done
/local/home/polimeno/SpiReS/tutorials/tempone/tempon
e_ESR_input.l2.back
Hz %1.2e log
(0.0, 0.0, 0.0) (-0.0, 0.0, 0.0)
 %1.5f linear
Gauss %1.2f linear
```

Step 10 - tensors can be modified manually in the "Diffusion" environment. Just click on the tensor that needs corrections, and change orientation and / or principal values in the mask. Set the trace of the ***A*** tensor to 16.14 Gauss (the Gaussian '03 package underestimates the value of the coupling of about 2 Gauss). After changes, click the "Apply" button.

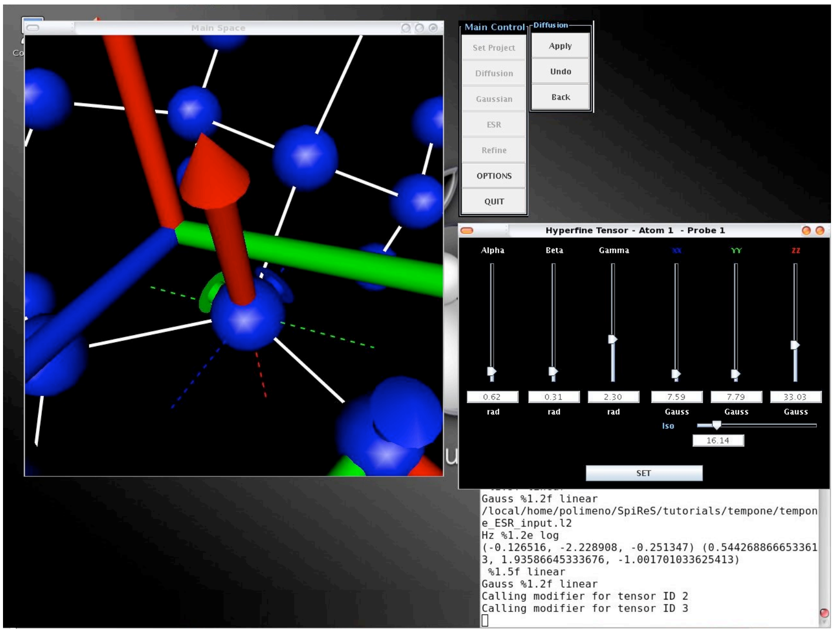

Hyperfine Tensor - Atom 1 - Probe 1

Alpha	Beta	Gamma	XX	YY	ZZ
0.62	0.31	2.30	7.59	7.79	33.03
rad	rad	rad	Gauss	Gauss	Gauss

Iso 16.14

```
Gauss %1.2f linear
/local/home/polimeno/SpiReS/tutorials/tempone/tempon
e_ESR_input.l2
Hz %1.2e log
(-0.126516, -2.228908, -0.251347) (0.544268866653361
3, 1.93586645333676, -1.001701033625413)
 %1.5f linear
Gauss %1.2f linear
Calling modifier for tensor ID 2
Calling modifier for tensor ID 3
```

Step 11 - further adjustments can be obtained by fitting (although, as a general rule, small corrections should be necessary), in the "Refine" environment. In this case we adjust the traces of ***g*** and ***A*** tensors and the intrinsic linewidth, checking the proper boxes.

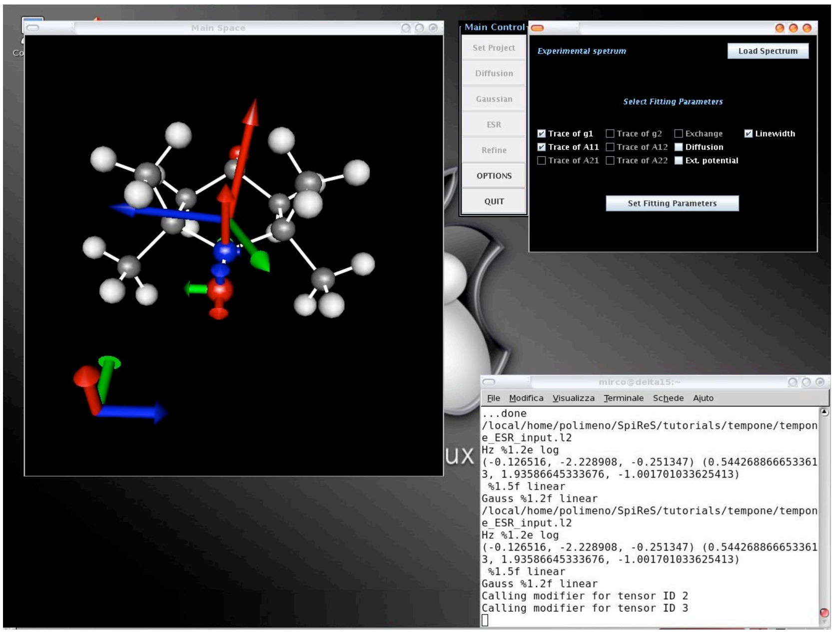

☑ Trace of g1 ☐ Trace of g2 ☐ Exchange ☑ Linewidth
☑ Trace of A11 ☐ Trace of A12 ☐ Diffusion
☐ Trace of A21 ☐ Trace of A22 ☐ Ext. potential

```
...done
/local/home/polimeno/SpiReS/tutorials/tempone/tempon
e_ESR_input.l2
Hz %1.2e log
(-0.126516, -2.228908, -0.251347) (0.544268866653361
3, 1.93586645333676, -1.001701033625413)
 %1.5f linear
Gauss %1.2f linear
/local/home/polimeno/SpiReS/tutorials/tempone/tempon
e_ESR_input.l2
Hz %1.2e log
(-0.126516, -2.228908, -0.251347) (0.544268866653361
3, 1.93586645333676, -1.001701033625413)
 %1.5f linear
Gauss %1.2f linear
Calling modifier for tensor ID 2
Calling modifier for tensor ID 3
```

Step 12 - next we load a reference experimental spectrum, by clicking the "Load Spectrum" button and we choose the *exp.dat* file.

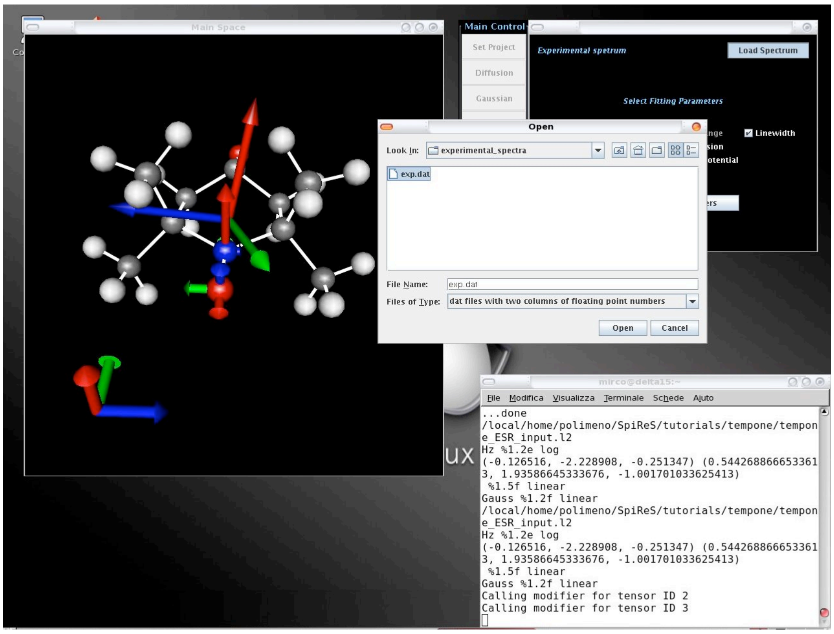

Look In: experimental_spectra

exp.dat

File Name: exp.dat

Files of Type: dat files with two columns of floating point numbers

```
...done
/local/home/polimeno/SpiReS/tutorials/tempone/tempon
e_ESR_input.l2
Hz %1.2e log
(-0.126516, -2.228908, -0.251347) (0.544268866653361
3, 1.93586645333676, -1.001701033625413)
 %1.5f linear
Gauss %1.2f linear
/local/home/polimeno/SpiReS/tutorials/tempone/tempon
e_ESR_input.l2
Hz %1.2e log
(-0.126516, -2.228908, -0.251347) (0.544268866653361
3, 1.93586645333676, -1.001701033625413)
 %1.5f linear
Gauss %1.2f linear
Calling modifier for tensor ID 2
Calling modifier for tensor ID 3
```

Step 13 - now enter in the "ESR" environment and, to refine the parameters, check the "Fit Mode" check box.

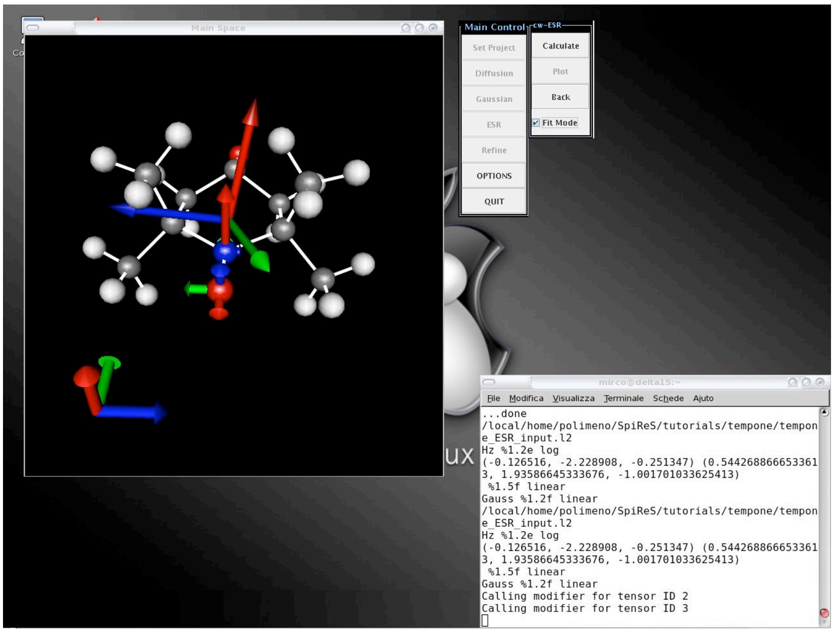

☑ Fit Mode

```
...done
/local/home/polimeno/SpiReS/tutorials/tempone/tempon
e_ESR_input.l2
Hz %1.2e log
(-0.126516, -2.228908, -0.251347) (0.544268866653361
3, 1.93586645333676, -1.001701033625413)
 %1.5f linear
Gauss %1.2f linear
/local/home/polimeno/SpiReS/tutorials/tempone/tempon
e_ESR_input.l2
Hz %1.2e log
(-0.126516, -2.228908, -0.251347) (0.544268866653361
3, 1.93586645333676, -1.001701033625413)
 %1.5f linear
Gauss %1.2f linear
Calling modifier for tensor ID 2
Calling modifier for tensor ID 3
```

Step 14 - by clicking on the "Calculate" button the spectrum is obtained by solving the stochastic Liouville equation.

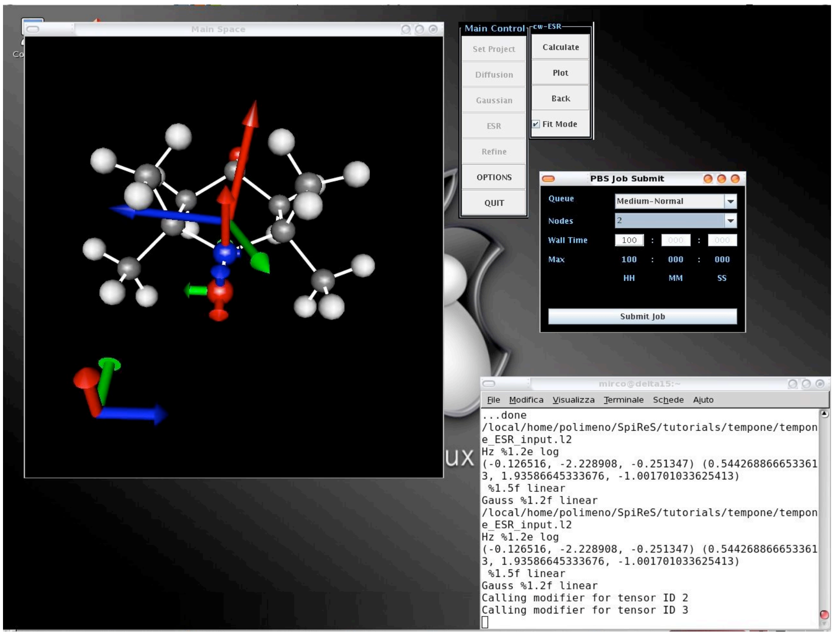

Queue: Medium-Normal
Nodes: 2
Wall Time: 100 : 000 : 000
Max: 100 : 000 : 000
HH MM SS

```
...done
/local/home/polimeno/SpiReS/tutorials/tempone/tempon
e_ESR_input.l2
Hz %1.2e log
(-0.126516, -2.228908, -0.251347) (0.544268866653361
3, 1.93586645333676, -1.001701033625413)
 %1.5f linear
Gauss %1.2f linear
/local/home/polimeno/SpiReS/tutorials/tempone/tempon
e_ESR_input.l2
Hz %1.2e log
(-0.126516, -2.228908, -0.251347) (0.544268866653361
3, 1.93586645333676, -1.001701033625413)
 %1.5f linear
Gauss %1.2f linear
Calling modifier for tensor ID 2
Calling modifier for tensor ID 3
```

Step 15 - after few seconds the calculation ends. In the present case, very small corrections of the refined parameters are obtained. The theoretical (red) and experimental (black) spectra can be visualized by clicking the "Plot" button.

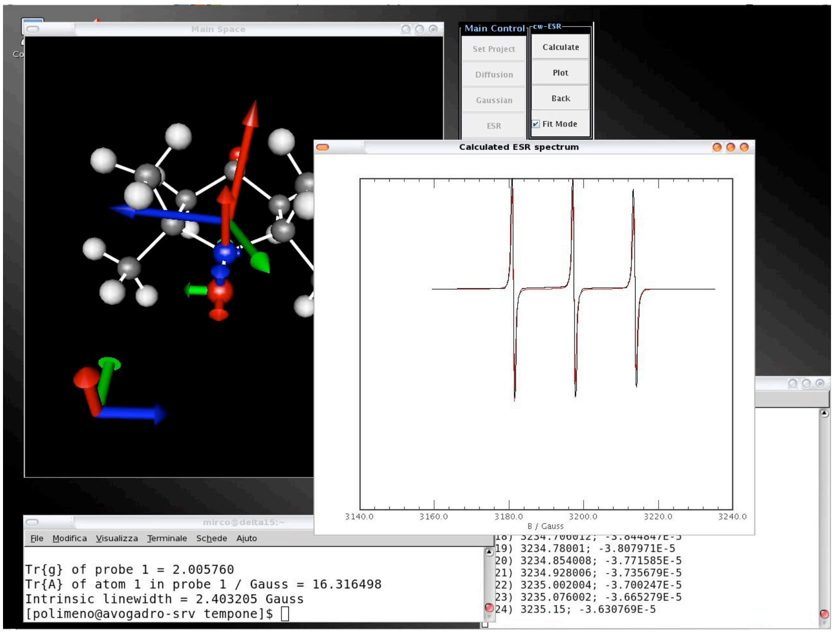

```
Tr{g} of probe 1 = 2.005760
Tr{A} of atom 1 in probe 1 / Gauss = 16.316498
Intrinsic linewidth = 2.403205 Gauss
[polimeno@avogadro-srv tempone]$ 
```

```
19) 3234.78001; -3.807971E-5
20) 3234.854008; -3.771585E-5
21) 3234.928006; -3.735679E-5
22) 3235.002004; -3.700247E-5
23) 3235.076002; -3.665279E-5
24) 3235.15; -3.630769E-5
```

Appendix D

List of libraries

In the implementation of the three software packages developed in this doctoral work, a number of GPL (Gnu Public License) and free libraries has been employed. Here we report a list of such libraries, with a brief description of their function.

E-SpiReS

- BLAS: the Basic Linear Algebra Software library is the most optimized package of routines to handle vector / matrix operations;
- CBLAS: C wrapper for the BLAS library;
- SPBLAS: sparse BLAS library that provides optimized algorithm to store and use sparse matrices;
- CLAPACK 3.0: optimized routines for high level linear algebra operations, such as matrix inversion and diagonalization, which uses BLAS to perform basic linear algebra;
- CQUADPACK: quadrature routine for the calculation of integrals in one variable;
- LEVMAR 2.1.3: routine to perform Levenberg - Marquardt non linear least square fitting;
- MPICH 1.0: message passing interface routine for code parallelization.

C^{++}OPPS

- CMINPACK 1.0.1: C++ routine to perform Levenberg - Marquardt non linear least squares fitting;
- CQUADPACK: quadrature routine for the calculation of integrals in one variable;
- SPARSELIB++ 1.6: C++ library that handles sparse matrices and provides level 1 BLAS routines for basic linear algebra operations and the MV++ basic matrix/vector library; small modifications have been made by us in the library in order to meet the particular demanding of low level control of matrices and vectors construction;
- CLAPACK 3.0: optimized routines for high level linear algebra operations, such as matrix inversion and diagonalization, which uses BLAS to perform basic linear algebra;
- MPICH 1.0: message passing interface routine for code parallelization;
- BESSIK: C++ routine for the evaluation of Bessel functions of first and second kind.

DITE

The following libraries are called by DITE:

- BLAS: the Basic Linear Algebra Software library is the most optimized package of routines to handle vector / matrix operations;
- CLAPACK 3.0: optimized routines for high level linear algebra operations, such as matrix inversion and diagonalization, which uses BLAS to perform basic linear algebra;

Appendix E

Matrix elements of the stochastic Liouville operator

In this appendix we report the explicit expressions for the matrix elements of the Liouvillean $\hat{\mathcal{L}} = i\hat{\mathcal{H}}^{\times} + \hat{\Gamma}$ which are needed to be evaluate in the calculation of cw-ESR spectra. Given the generalized set of coordinates $\boldsymbol{X} = (\boldsymbol{\Omega}, \boldsymbol{q}_{int})$, being $\boldsymbol{\Omega}$ the global orientation of the molecule and $\boldsymbol{q}_{int}$ the set of internal degrees of freedom, the diffusive operator takes the general shape

$$\hat{\Gamma} = -\nabla^{tr}_{\boldsymbol{X}} \boldsymbol{D}(\boldsymbol{X}) P_{eq}(\boldsymbol{X}) \nabla_{\boldsymbol{X}} P^{-1}_{eq}(\boldsymbol{X}) \tag{E.1}$$

where $\nabla_{\boldsymbol{X}}$ is the differentiation operator with respect to $\boldsymbol{X}$, $\boldsymbol{D}$ is the full diffusion tensor (which in general depends on $\boldsymbol{X}$) and $P_{eq}(\boldsymbol{X})$ is the equilibrium distribution, for which we choose a Boltzmann relation

$$P_{eq}(\boldsymbol{X}) = \exp\left[-V(\boldsymbol{X})/\mathrm{k_B}T\right] / \langle \exp\left[-V(\boldsymbol{X})/\mathrm{k_B}T\right] \rangle_{\boldsymbol{X}} \tag{E.2}$$

with $V(\boldsymbol{X})$ the potential acting on the stochastic coordinates, $\mathrm{k_B}$ the Boltzmann constant, T the absolute temperature and $\langle \ldots \rangle_{\boldsymbol{X}}$ indicating integration over the $\boldsymbol{X}$ space.

The spin super Hamiltonian is usually expressed in terms of irreducible spherical tensors

$$\hat{\mathcal{H}}^{\times} = \sum_{\mu} \omega_{\mu} \sum_{l=0,2} \sum_{m,m'=-l}^{l} \mathcal{D}^{l}_{m\,m'}(\boldsymbol{\Omega}) F^{(l,m')\,*}_{\mu,\,MF}(\boldsymbol{q}_{int}) \hat{A}^{(l,m)\,\times}_{\mu,\,LF} \tag{E.3}$$

where μ runs over all the magnetic interactions, $\mathcal{D}^{l}_{m\,m'}(\boldsymbol{\Omega})$ is a Wigner matrix and the explicit expressions for the spherical tensors $F^{(l,m)\,*}_{\mu,\,MF}$ and tensor operators $\hat{A}^{(l,m)\,\times}_{\mu,\,LF}$ are given elsewhere [21].

We span the Liouvillean over the state $|\,\Sigma\rangle\rangle = |\,\boldsymbol{\sigma}\rangle\rangle \otimes |\,LMK\rangle \otimes |\,\boldsymbol{\lambda}\rangle\rangle$, obtained by the direct product of the spin transitions space ($\{\boldsymbol{\sigma}\}$), the space of rigid rotations ($\{LMK\}$) and the space defined by the internal degrees of freedom ($\{\boldsymbol{\lambda}\}$). Then, the matrix elements to be evaluated are

$$\langle\langle\Sigma\,|\hat{\mathcal{L}}|\,\Sigma'\rangle\rangle = i\langle\langle\Sigma\,|\hat{\mathcal{H}}^{\times}|\,\Sigma'\rangle\rangle + \delta_{\boldsymbol{\sigma},\boldsymbol{\sigma}'}\langle LMK,\boldsymbol{\lambda}\,|\hat{\Gamma}|\,L'M'K',\boldsymbol{\lambda}'\rangle \tag{E.4}$$

with

$$\begin{aligned}\langle\langle\Sigma\,|\hat{\mathcal{H}}^{\times}|\,\Sigma'\rangle\rangle \;&=\; \sum_{\mu}\omega_{\mu}\sum_{l=0,2}\sum_{m,m'=-l}^{l}\langle LMK\,|\mathcal{D}^{l}_{m\,m'}|\,L'M'K'\rangle\langle\boldsymbol{\lambda}\,|F^{(l,\,m')\,*}_{\mu,\,MF}|\,\boldsymbol{\lambda}'\rangle\,\times\\ &\quad\times\langle\langle\boldsymbol{\sigma}\,|\hat{A}^{(l,\,m)\,\times}_{\mu,\,LF}|\,\boldsymbol{\sigma}'\rangle\rangle\end{aligned} \tag{E.5}$$

In the following section we give the expressions of the matrix elements to be calculated in the models implemented in E-SpiReS.

E.1 Free rigid rotator

The simplest model is that of a rigid molecule reorienting in an isotropic fluid. Here, the only stochastic variables are the Euler angles $\boldsymbol{\Omega} = (\alpha,\beta,\gamma)$ giving the orientation of the molecule fixed frame (MF) with respect to the inertial laboratory frame (LF). Defining MF as the frame that diagonalizes the rotational diffusion tensor, the diffusive operator takes the simple form

$$\tilde{\Gamma} = \hat{\boldsymbol{J}}^{tr}\boldsymbol{D}\hat{\boldsymbol{J}} = \frac{D_-}{4}\left(\hat{J}_+^2 + \hat{J}_-^2\right) + \frac{D_+}{4}\left(\hat{J}_+\hat{J}_- + \hat{J}_-\hat{J}_+\right) + D_{ZZ}\hat{J}_Z^2 \tag{E.6}$$

where $D^{\pm} = D_{XX} \pm D_{YY}$ and $\hat{\boldsymbol{J}}$ is the angular momentum operator acting on $\boldsymbol{\Omega}$.
The operator is spanned over the basis set

$$|\,LMK\rangle = \sqrt{\frac{2L+1}{8\pi^2}}\mathcal{D}^{L}_{M\,K}(\boldsymbol{\Omega}) \tag{E.7}$$

and matrix elements are easily found to be

$$\begin{aligned}\langle LMK\,|\tilde{\Gamma}|\,L'M'K'\rangle \;&=\; \delta_{L,L'}\delta_{M,M'}\Big\{\delta_{KK'}\Big[D_{ZZ}K^2 + \frac{D_+}{4}\left(c^{-\,2}_{L,K} + c^{+\,2}_{L,K}\right)\Big] +\\ &\quad + \frac{D_-}{4}\left(\delta_{KK'+2}c^{+}_{L,K-2}c^{+}_{L,K-1} + \delta_{KK'-2}c^{-}_{L,K+1}c^{-}_{L,K+2}\right)\Big\}\end{aligned} \tag{E.8}$$

with $c^{+}_{L,K} = \sqrt{L\,(L+1) - K\,(K \pm 1)}$.

The general expressions for the matrix elements of the spin super Hamiltonian are

$$\begin{aligned}\langle\langle \Sigma \,|\hat{\mathcal{H}}^{\times}|\, \Sigma' \rangle\rangle \;&=\; \sqrt{[L, L']}(-)^{M-K}\sum_{\mu,l}\omega_{\mu}\begin{pmatrix} L & l & L' \\ -M & M'-M & M' \end{pmatrix}\times \\ &\times\begin{pmatrix} L & l & L' \\ -K & K'-K & K' \end{pmatrix} F^{(l,\,K'-K)\,*}_{\mu,\,MF}\langle\langle \boldsymbol{\sigma}\,|\hat{A}^{(l,\,M'-M)\,\times}_{\mu,\,LF}|\,\boldsymbol{\sigma}'\rangle\rangle \qquad \text{(E.9)}\end{aligned}$$

Expressions for the reduced matrix elements $\langle\langle \boldsymbol{\sigma}\,|\hat{A}^{(l,\,M'-M)\,\times}_{\mu,\,LF}|\,\boldsymbol{\sigma}'\rangle\rangle$ can be found in the literature [21]. The effective form of the matrix elements of the spin super Hamiltonian depends on the kind of radical, i.e. on the magnetic interactions, μ, that have to be taken into account.

It is also important to evaluate the projections over the basis set of the starting vector, which describes the physical observable. Here that the equilibrium distribution of the stochastic coordinates is a constant, it is possible to write

$$|\,v\rangle\rangle = \mathcal{N}|\,\hat{S}_X \times \mathbf{1}_I\rangle\rangle \qquad \text{(E.10)}$$

where $\mathcal{N}$ is the normalization constant, $\mathbf{1}_I$ the identity operator over the space of nuclear transitions of all N_n nuclei and $\hat{S}_X = \sum_{i=1}^{N_e}\hat{S}_{X,i}$, that is the total X magnetization which is given by the sum of the contributions of all the unpaired electrons (N_e) in the radical. The projections are given by

$$\langle\langle \Sigma\,|v\rangle\rangle = \mathcal{N}\delta_{L,0}\delta_{M,0}\delta_{K,0}\langle\langle \boldsymbol{\sigma}\,|\hat{S}_X\rangle\rangle \qquad \text{(E.11)}$$

where (see ref. [21, 111])

$$\langle\langle \boldsymbol{\sigma}\,|\hat{S}_X\rangle\rangle = \prod_{i=1}^{N_n}\delta_{p^I_i,0}\sum_{j=0}^{N_e!}\mathcal{P}_j\left(\delta_{p^S_1,|1|}\delta_{p^S_2,0}\dots\delta_{p^S_{N_e},0}\right) \qquad \text{(E.12)}$$

being $\mathcal{P}_j(\boldsymbol{x})$ the j-th permutation of indexes in set $\boldsymbol{x}$.

E.2 Flexible rotator in external field

We give here the matrix elements of a rigid rotator coupled with a planar rotator. This model has been introduced in the study of the cw-ESR spectroscopy of tempo-palmitate spin probe in liquid crystal (see section 3.3.2). The diffusion operator is

$$\tilde{\Gamma} = -P_{eq}^{-1/2} \begin{pmatrix} \hat{\boldsymbol{M}} \\ \dfrac{\partial}{\partial\theta} \end{pmatrix}^{\mathrm{tr}} \mathbf{D} P_{eq} \begin{pmatrix} \hat{\boldsymbol{M}} \\ \dfrac{\partial}{\partial\theta} \end{pmatrix} P_{eq}^{-1/2} = \tilde{\Gamma}_{RR} + \tilde{\Gamma}_{II} + \tilde{\Gamma}_{RI} \tag{E.13}$$

where $\tilde{\Gamma}$ acts on $\boldsymbol{X} = (\boldsymbol{\Omega}, \theta)$, i.e. the global orientation $\boldsymbol{\Omega}$ and the internal torsional angle θ; $\hat{\boldsymbol{M}}$ is the infinitesimal rotation operator. The three operators introduced in the last equality of previous equation are give by

$$\tilde{\Gamma}_{RR} = -P_{eq}^{-1/2} \hat{\boldsymbol{M}}^{\mathrm{tr}} \boldsymbol{D}_{RR} P_{eq} \hat{\boldsymbol{M}} P_{eq}^{-1/2} \tag{E.14}$$

$$\tilde{\Gamma}_{II} = -D_{II} P_{eq}^{-1/2} \frac{\partial}{\partial\theta} P_{eq} \frac{\partial}{\partial\theta} P_{eq}^{-1/2} \tag{E.15}$$

$$\tilde{\Gamma}_{RI} = -P_{eq}^{-1/2} \left(\hat{\boldsymbol{M}}^{\mathrm{tr}} \boldsymbol{D}_{RI} P_{eq} \frac{\partial}{\partial\theta} + \frac{\partial}{\partial\theta} \boldsymbol{D}_{IR} P_{eq} \hat{\boldsymbol{M}} \right) P_{eq}^{-1/2} \tag{E.16}$$

where $\boldsymbol{D}_{RR}$, D_{II} and $\boldsymbol{D}_{RI}$ are, respectively, the rotational, internal and coupling parts of the diffusion tensor.

Matrix elements are defined with respect to basis functions $|LMK, n\rangle = |LMK\rangle \times |n\rangle$, with

$$|LMK\rangle = \sqrt{\frac{[L]}{8\pi^2}} \mathcal{D}^L_{M,K}(\boldsymbol{\Omega}) \tag{E.17}$$

$$|n\rangle = \frac{1}{\sqrt{2\pi}} e^{-in\theta} \tag{E.18}$$

Pure rotational operator

By defining the angular momentum operator as $\hat{\boldsymbol{J}} = i\hat{\boldsymbol{M}}$, the pure rotational part of the diffusion operator is $\tilde{\Gamma}_{RR} = \hat{\boldsymbol{J}}^{\mathrm{tr}} \boldsymbol{D}_{RR} \hat{\boldsymbol{J}} + F_{RR}(\boldsymbol{X})$, which has been separated in a operator which is independent on the potential and a function that depends on the potentials.

We express the operator in the molecular frame (MF) where the rotational diffusion tensor $\boldsymbol{D}_{RR}$ is diagonal.

Potential independent part

The potential independent operator is substantially the free rigid rotator

$$\hat{\boldsymbol{J}}^{\mathrm{tr}} \boldsymbol{D}_{RR} \hat{\boldsymbol{J}} = \frac{D^{-}_{RR}}{4} \left(\hat{J}_+^2 + \hat{J}_-^2 \right) + \frac{D^{+}_{RR}}{4} \left(\hat{J}_+ \hat{J}_- + \hat{J}_- \hat{J}_+ \right) + D^{ZZ}_{RR} \hat{J}_Z^2 \tag{E.19}$$

where $D^{\pm}_{RR} = D^{XX}_{RR} \pm D^{YY}_{RR}$. The matrix elements are easily found to be

$$\begin{aligned}
\langle LMK, n|\hat{\boldsymbol{J}}^{\mathrm{tr}}\boldsymbol{D}_{RR}\hat{\boldsymbol{J}}|L'M'K', n'\rangle &= \delta_{n,n'}\delta_{L,L'}\delta_{M,M'} \times \\
&\times \left\{\delta_{KK'}\left[D^{ZZ}_{RR}K^2 + \frac{D^{+}_{RR}}{4}\left(c^{-\,2}_{L,K} + c^{+\,2}_{L,K}\right)\right] + \right. \\
&+ \left. \frac{D^{-}_{RR}}{4}\left(\delta_{KK'+2}c^{+}_{L,K-2}c^{+}_{L,K-1} + \delta_{KK'-2}c^{-}_{L,K+1}c^{-}_{L,K+2}\right)\right\}
\end{aligned} \tag{E.20}$$

with $c^{+}_{L,K} = \sqrt{L\,(L+1) - K\,(K \pm 1)}$.

Potential dependent term

The function that depends on the potential is defined as

$$\begin{aligned}
F_{RR}\left(\boldsymbol{X}\right) &= -P^{-1/2}_{eq}\left(\boldsymbol{X}\right)\hat{\boldsymbol{J}}^{\mathrm{tr}}\boldsymbol{D}_{RR}\hat{\boldsymbol{J}}P^{1/2}_{eq}\left(\boldsymbol{X}\right) = \\
&= -\frac{D^{-}_{RR}}{16}\left[\left(\hat{J}_{+}U\right)^2 + \left(\hat{J}_{-}U\right)^2 - 2\left(\hat{J}^2_{+} + \hat{J}^2_{-}\right)U\right] + \\
&\quad -\frac{D^{+}_{RR}}{8}\left[\left(\hat{J}_{+}U\right)\left(\hat{J}_{-}U\right) - \left(\hat{J}_{+}\hat{J}_{-} + \hat{J}_{-}\hat{J}_{+}\right)U\right] = \\
&= F^{-}_{RR}\left(\boldsymbol{\Omega}\right) + F^{+}_{RR}\left(\boldsymbol{\Omega}\right)
\end{aligned} \tag{E.21}$$

We select an axial external potential $U_{ext}(\boldsymbol{\Omega}) = -\epsilon\mathcal{D}^2_{0\,0}(\boldsymbol{\Omega})$. The following derivatives are provided to write the matrix elements:

$$\hat{J}_{\pm}U_{\mathrm{ext}} = \sqrt{6}\epsilon\mathcal{D}^2_{0,\pm1} \tag{E.22}$$

$$\hat{J}^2_{\pm}U_{\mathrm{ext}} = -2\sqrt{6}\epsilon\mathcal{D}^2_{0,\pm2} \tag{E.23}$$

$$\hat{J}_{\pm}\hat{J}_{\mp}U_{\mathrm{ext}} = -6\epsilon\mathcal{D}^2_{0,0} \tag{E.24}$$

$$\left(\hat{J}_{\pm}U_{\mathrm{ext}}\right)^2 = 6\epsilon^2\sum_{l=0,2,4}[l]\begin{pmatrix} 2 & 2 & l \\ 0 & 0 & 0 \end{pmatrix}\begin{pmatrix} 2 & 2 & l \\ 1 & 1 & -2 \end{pmatrix}\mathcal{D}^l_{0,\pm2} \tag{E.25}$$

$$\left(\hat{J}_{+}U_{\mathrm{ext}}\right)\left(\hat{J}_{-}U_{\mathrm{ext}}\right) = 6\epsilon^2\sum_{l=0,2,4}[l]\begin{pmatrix} 2 & 2 & l \\ 0 & 0 & 0 \end{pmatrix}\begin{pmatrix} 2 & 2 & l \\ 1 & -1 & 0 \end{pmatrix}\mathcal{D}^l_{0,0} \tag{E.26}$$

And the matrix elements are

$$\langle LMK, n|F^{-}_{RR}|L'M'K', n'\rangle = -\delta_{n,n'}\delta_{M,M'}(-)^{(M-K)}\sqrt{[L, L']}\epsilon\frac{D^{-}_{RR}}{8} \times$$

$$\times\sum_l f^-_{RR,l}\begin{pmatrix} L & l & L' \\ -M & 0 & M \end{pmatrix}\left[\begin{pmatrix} L & l & L' \\ -K & 2 & K' \end{pmatrix}+\begin{pmatrix} L & l & L' \\ -K & -2 & K' \end{pmatrix}\right]$$

$$\langle LMK,n|F^+_{RR}|L'M'K',n'\rangle = -\delta_{n,n'}\delta_{M,M'}\delta_{K,K'}(-)^{(M-K)}\sqrt{[L,L']}3\epsilon\frac{D^+_{RR}}{4}\times$$

$$\times\sum_l f^+_{RR,l}\begin{pmatrix} L & l & L' \\ -M & 0 & M \end{pmatrix}\begin{pmatrix} L & l & L' \\ -K & 0 & K \end{pmatrix} \tag{E.27}$$

where

$$f^-_{RR,l} = 3\epsilon[l]\begin{pmatrix} 2 & 2 & l \\ 0 & 0 & 0 \end{pmatrix}\begin{pmatrix} 2 & 2 & l \\ 1 & 1 & -2 \end{pmatrix}+\delta_{l,2}2\sqrt{6} \tag{E.28}$$

and

$$f^+_{RR,l} = \epsilon[l]\begin{pmatrix} 2 & 2 & l \\ 0 & 0 & 0 \end{pmatrix}\begin{pmatrix} 2 & 2 & l \\ 1 & -1 & 0 \end{pmatrix}+\delta_{l,2}2 \tag{E.29}$$

Pure internal operator

The term related to internal dynamics can be written as $\tilde{\Gamma}_{II} = -D_{II}\frac{\partial^2}{\partial\theta^2} + F_{II}(\boldsymbol{X})$. For the case of a generic potential $U_{\text{int}} = -\sum_\nu \chi_\nu|\nu\rangle$ useful expressions for evaluating matrix elements are

$$\frac{\partial U_{\text{int}}}{\partial\theta} = i\sum_{\nu=-1}^{1}\nu\chi_\nu|\nu\rangle \tag{E.30}$$

$$\left(\frac{\partial U_{\text{int}}}{\partial\theta}\right)^2 = -\sum_{\nu,\nu'=-1}^{1}\nu\nu'\chi_\nu\chi_{\nu'}|\nu+\nu'\rangle \tag{E.31}$$

$$\frac{\partial^2 U_{\text{int}}}{\partial\theta^2} = \sum_{\nu=-1}^{1}\nu^2\chi_\nu|\nu\rangle \tag{E.32}$$

Matrix elements of the first term are

$$-D_{II}\langle LMK,n|\frac{\partial^2}{\partial\theta^2}|L'M'K',n'\rangle = \delta_{L,L'}\delta_{M,M'}\delta_{K,K'}\delta_{n,n'}D_{II}n^2 \tag{E.33}$$

Function F_{II} is written explicitly as

$$F_{II}(\theta) = \frac{D_{II}}{4}\left[\left(\frac{\partial U}{\partial\theta}\right)^2 - 2\frac{\partial^2 U}{\partial\theta^2}\right] \tag{E.34}$$

The matrix elements are diagonal in the indexes L, M, K, so that

$$\langle n|F_{II}|n'\rangle = -\frac{D_{II}}{4}\sum_{\nu+\nu'=n-n'} f^{II}_{\nu,\nu'} \tag{E.35}$$

where $f^{II}_{\nu,\nu'} = \nu\nu'\chi_\nu\chi_{\nu'} + 2\delta_{\nu',0}\nu^2\chi_\nu$.

Rotational-internal coupling operator

We define the quantities $D^{\pm}_{RI}(\theta) = \left[D_{XI}(\theta) \mp iD_{YI}(\theta)\right]/2$. The operator that couples the two stochastic coordinates can be written in the following form

$$\tilde{\Gamma}_{RI} = -iP_{eq}^{-1/2}\left(\boldsymbol{X}\right) \sum_{\alpha=\pm,Z} D^{\alpha}_{RI} \left(\frac{\partial}{\partial\theta} P_{eq}\left(\boldsymbol{X}\right)\hat{J}_{\alpha} + \hat{J}_{\alpha} P_{eq}\left(\boldsymbol{X}\right)\frac{\partial}{\partial\theta}\right) P_{eq}^{-1/2}\left(\boldsymbol{X}\right) \tag{E.36}$$

which can be rearranged into:

$$\tilde{\Gamma}_{RI} = 2i \sum_{\alpha=\pm,Z} D^{\alpha}_{RI} \left[\hat{J}_{\alpha}\frac{\partial}{\partial\theta} - \frac{1}{4}\left(\hat{J}_{\alpha}U\right)\frac{\partial U}{\partial\theta}\right] \tag{E.37}$$

The matrix elements for the first term are reported here for the three values of the α index; for $\alpha = \pm 1$ one obtains

$$\langle LMK, n|2iD^{\pm}_{RI}\hat{J}_{\pm}\frac{\partial}{\partial\theta}|L'M'K', n'\rangle = -\delta_{LL'}\delta_{MM'}\delta_{K,K'\pm1}\delta_{n,n'}2D^{\pm}_{RI}c^{\pm}_{L,K\mp1}n \tag{E.38}$$

and for $\alpha = Z$

$$\langle LMK, n|2iD_{ZI}\hat{J}_{Z}\frac{\partial}{\partial\theta}|L'M'K', n'\rangle = -\delta_{LL'}\delta_{MM'}\delta_{K,K'}\delta_{n,n'}2D_{ZI}Kn \tag{E.39}$$

Due to the simple form of the external potential adopted the component $\alpha = Z$ of the potential dependent part is null; only matrix elements derived from $\alpha = \pm 1$ remain:

$$\begin{aligned} &\langle LMK, n| -\frac{i}{2}D^{\pm}_{RI}\left(\hat{J}_{\pm}U\right)\left(\frac{\partial U}{\partial\theta}\right)|L'M'K', n'\rangle = \delta_{M,M'}\delta_{K,K'\pm1}(-)^{M-K} \times \\ \times\quad & \sqrt{[L,L']} \times \sqrt{\frac{3}{2}}\epsilon D^{\pm}_{RI}\begin{pmatrix} L & 2 & L' \\ -M & 0 & M' \end{pmatrix}\begin{pmatrix} L & 2 & L' \\ -K & \pm1 & K\mp1 \end{pmatrix}\left(n-n'\right)\chi_{n-n'} \end{aligned} \tag{E.40}$$

Spin super Hamiltonian

The spin super-Hamiltonian is defined in Eq. (3.54). The matrix elements of the spin super-Hamiltonian are

$$\begin{aligned} &\langle\sigma, LMK, n|\hat{H}^{\times}|\sigma', L'M'K', n'\rangle = (-)^{M-K} \times \\ \times\quad & \sqrt{[L,L']}\sum_{\mu}\omega_{\mu}\sum_{l=0,2}\begin{pmatrix} L & 2 & L' \\ -M & M-M' & M' \end{pmatrix}\begin{pmatrix} L & 2 & L' \\ -K & K-K' & K' \end{pmatrix} \times \\ \times\quad & G_{\mu}^{(l,K-K',n-n')}\langle\langle\sigma|\hat{A}^{(l,M-M')\,\times}_{\mu,LF}|\sigma'\rangle\rangle \end{aligned} \tag{E.41}$$

with

$$G_{\mu}^{(l,m,m')} = \mathcal{D}^{l}_{m,m'}\left(\boldsymbol{\Omega}_{MC}\right)\sum_{m''}\mathcal{D}^{l}_{m',m''}\left(\boldsymbol{\Omega}_{\mu}\right)F_{\mu,\mu F}^{(l,m'')\,*} \tag{E.42}$$

where $\boldsymbol{\Omega}_{MC}$ is the set of Euler angles that transforms MF to a frame, CF, which has the z-axis is parallel to the rotatable bond. $\boldsymbol{\Omega}_{\mu}$ is, instead, the set of Euler angles that transforms from a frame rotated of $(0,0,\theta)$ from CF, to the frame μF that diagonalizes the magnetic tensors.

Starting vector

The starting vector for the system can be written as $|v\rangle\rangle \propto |\hat{S}_x \otimes \mathbf{1}_I \otimes P_{eq}^{1/2}\left(\boldsymbol{X}\right)\rangle\rangle$ and the projection over the basis is

$$\langle\langle\sigma, LMK, n|v\rangle\rangle \propto \langle\langle\sigma|\hat{S}_x\rangle\rangle\langle LMK|P_{eq}^{1/2}\left(\boldsymbol{\Omega}\right)\rangle\langle n|P_{eq}^{1/2}\left(\theta\right)\rangle \tag{E.43}$$

where

$$\begin{aligned}
\langle\langle\sigma|\hat{S}_x\rangle\rangle &= \delta_{|p^S|,1}\delta_{p^I,0} \\
\langle LMK|P_{eq}^{1/2}\left(\boldsymbol{\Omega}\right)\rangle &\propto \delta_{M,0}\delta_{K,0}\sqrt{[L]}\int_0^{\pi} d\beta \sin(\beta)\mathcal{D}^{L}_{0,0}\left(\beta\right)\, e^{\frac{1}{2}\epsilon\mathcal{D}^{2}_{0,0}(\beta)} && \text{(E.44)} \\
\langle n|P_{eq}^{1/2}\left(\theta\right)\rangle &\propto \int_0^{2\pi} d\theta \cos\left(n\theta\right) e^{\chi_1 \cos\left(\theta\right)} && \text{(E.45)}
\end{aligned}$$

Symmetrization

If $\hat{\mathcal{P}}_{Kn}$ is an operator that changes simultaneously sign to K and n, one finds

$$\begin{aligned}
\hat{\mathcal{P}}_{Kn}\langle\langle\sigma, LMK, n|\hat{\mathcal{L}}|\sigma', L'M'K', n'\rangle\rangle &= (-)^{L-L'+K-K'} \times \\
&\times \langle\langle\sigma, LMK, n|\hat{\mathcal{L}}|\sigma', L'M'K', n'\rangle\rangle^{*}
\end{aligned} \tag{E.46}$$

Therefore we introduce the symmetrized basis set

$$|\sigma, LMK, n, j\rangle\rangle_{Kn} = \mathcal{N}e^{-i\frac{\pi}{4}(j-1)}\left(|\sigma, LMK, n\rangle\rangle + j\left(-\right)^{L-K}|\sigma, LM\ -K, -n\rangle\rangle\right) \tag{E.47}$$

where $\mathcal{N} = [2(1+\delta_{K,0}\delta_{n,0})]^{1/2}$; σ, L and M are defined as in the old basis set, while for K, n and j we have

$$\begin{cases} K=0 & n=0 & j=(-)^L \\ K=0 & n>0 & j=\pm 1 \\ K>0 & -N_{max} \leq n \leq N_{max} & j=\pm 1 \end{cases} \tag{E.48}$$

E.3 Planar diffusive rotator with random walk

In one of the case-stadies calculations (see section 3.3.5) we needed to modify the dynamics of the internal torsional angle (planar rotator) adding a random walk contribution to simulate random jumps due to propagation of the polymerization reaction. Here we consider the expressions for the only planar rotator, without coupling it to the rigid body rotator because it is straightforward (see previous section). We also consider that the magnetic tensors are affected by the stochastic variable.

Diffusive operator

The diffusive operator can be written in the convenient form $\tilde{\Gamma}_D = -D_{II}(\partial^2/\partial\theta^2) + F(\theta)$. Given a potential in the general form $U = -\sum_\nu \epsilon_\nu |\,\nu\rangle$, the useful expressions for evaluating matrix elements are

$$\frac{\partial U}{\partial \theta} = i\sum_\nu \nu\epsilon_\nu |\,\nu\rangle \tag{E.49}$$

$$\left(\frac{\partial U}{\partial \theta}\right)^2 = -\sum_{\nu,\nu'} \nu\nu'\epsilon_\nu\epsilon_{\nu'} |\,\nu+\nu'\rangle \tag{E.50}$$

$$\frac{\partial^2 U}{\partial \theta^2} = \sum_\nu \nu^2\epsilon_\nu |\,\nu\rangle \tag{E.51}$$

The matrix elements of the first (potential independent) term are

$$-D_{II}\langle n\,|\frac{\partial^2}{\partial\theta^2}|\,n'\rangle = \delta_{n,n'}D_{II}n^2 \tag{E.52}$$

Function $F(\theta)$ is written explicitly as

$$F(\theta) = \frac{D_{II}}{4}\left[\left(\frac{\partial U}{\partial \theta}\right)^2 - 2\frac{\partial^2 U}{\partial \theta^2}\right] \tag{E.53}$$

and by making use of eqns. (E.50) and (E.51) the matrix elements are

$$\langle n \,| F(\theta) \,| n' \rangle = -\frac{D_{II}}{4} \sum^{f}_{\nu+\nu'=n-n'}{}_{\nu,\nu'} \tag{E.54}$$

where $f_{\nu,\nu'} = \nu\nu' \epsilon_\nu \epsilon_{\nu'} + 2\delta_{\nu',0} \nu^2 \epsilon_\nu$.

Random walk operator

Let's recall the definition of the random walk operator given in section 3.3.5. In its integrated form, the operator is

$$\hat{\Gamma}_{RW} P(\theta, t) = -\int_0^{2\pi} d\theta' \left[P(\theta, t) W(\theta \leftarrow \theta') - P(\theta', t) W(\theta' \leftarrow \theta) \right] \tag{E.55}$$

We make the simplest choice for the transformation kernel:

$$W(\theta \leftarrow \theta') = \omega_{RW} P_{eq}(\theta') \tag{E.56}$$

i.e. the probability of jumping from θ to θ' depends only on the arriving value of the angle and on the jumping frequency ω_{RW}.
The substitution of the kernel (E.56) in the expression of the operator (E.55) reads

$$\hat{\Gamma}_{RW} P(\theta, t) = \omega_{RW} \left[P(\theta, t) - P_{eq}(\theta) \right] \tag{E.57}$$

It is useful to transform the time evolution operator in such a way that it becomes Hermitian; this is achieved by the symmetrization operation $\tilde{\Gamma} = P_{eq}^{-1/2}(\theta) \hat{\Gamma} P_{eq}^{1/2}(\theta)$, that gives

$$\begin{aligned} \tilde{\Gamma} \tilde{P}(\theta, t) = & -P_{eq}^{-1/2}(\theta) \frac{\partial}{\partial\theta} D_{II}(\theta) P_{eq}(\theta) \frac{\partial}{\partial\theta} P_{eq}^{-1/2}(\theta) \tilde{P}(\theta, t) + \\ & -\omega_{RW} \left[\tilde{P}(\theta, t) - P_{eq}^{1/2}(\theta) \int_0^{2\pi} d\theta' P_{eq}^{1/2}(\theta') \tilde{P}(\theta', t) \right] \end{aligned} \tag{E.58}$$

with $\tilde{P}(\theta, t) = P(\theta, t) / P_{eq}^{1/2}(\theta)$.
Evaluation of matrix elements of the random walk operator is straightforward and one gets

$$\langle n \,| \tilde{\Gamma}_{RW} | \, n' \rangle = \omega_{RW} \left[\delta_{n,n'} - \langle n P_{eq}^{1/2}(\theta) \rangle \langle n' P_{eq}^{1/2}(\theta) \rangle \right] \tag{E.59}$$

where the integrals $\langle n P_{eq}^{1/2}(\theta) \rangle$ are evaluated numerically.

Spin super-Hamiltonian

The matrix elements of the spin super-Hamiltonian are

$$\begin{aligned}\langle\langle \Sigma \,|\hat{\mathcal{H}}^{\times}|\, \Sigma'\rangle\rangle &= \delta_{n,n'}\omega_0 F_{g,}^{(0,0)\,*}\langle\langle \sigma \,|\hat{A}_{g,}^{(0,0)\,\times}|\, \sigma'\rangle\rangle \\ &\quad + \sum_{j=1}^{5}\langle n\,|\omega_{A,j}\,(\theta)\,|\,n'\rangle F_{A,j,}^{(0,0)\,*}\langle\langle \sigma \,|\hat{A}_{A,j,}^{(0,0)\,\times}|\, \sigma'\rangle\rangle \end{aligned} \tag{E.60}$$

where the explicit form of the reduced matrix elements $\langle\langle \sigma \,|\hat{A}_{\mu,}^{(0,0)\,\times}|\, \sigma'\rangle\rangle$ $(\mu = g, A)$ is given elsewhere [21] and assuming the truncated Fourier expansion $\omega_{A,j}(\theta) = \sum_{\eta=-4}^{4} \omega_{A,j}^{\eta} e^{-i\eta\theta}$ (with $\omega_{A,j}^{\eta\,*} = \omega_{A,j}^{-\eta}$) the reduced matrix elements that depend on the stochastic variable are

$$\langle n\,|\omega_{A,j}\,(\theta)\,|\,n'\rangle = \sum_{\eta=-4}^{4}\omega_{A,j}^{\eta}\langle n\,|\eta|\,n'\rangle = \omega_{A,j}^{n-n'} \tag{E.61}$$

Starting vector

The projections of the starting vector over the basis functions are given by

$$\langle\langle \Sigma\,|v\rangle\rangle = 2^{-5/2}\langle\langle \sigma\,|\hat{S}_X\rangle\rangle\langle n P_{eq}^{1/2}\,(\theta)\rangle \tag{E.62}$$

where

$$\langle\langle \sigma\,|\hat{S}_X\rangle\rangle = \delta_{|p^S|,1}\delta_{p_1^I,0}\delta_{p_2^I,0}\delta_{p_3^I,0}\delta_{p_4^I,0}\delta_{p_5^I,0} \tag{E.63}$$

$$\langle n\,|P_{eq}^{1/2}\,(\theta)\rangle \propto \int_0^{2\pi} d\theta e^{-in\theta}e^{-U(\theta)/2} \tag{E.64}$$

where the last integral is evaluated numerically.

Appendix F

Sample calculation with C^{++}OPPS

In this appendix we report a step by step example simulation of NMR relaxation times of residues 50 and 165 of E. Coli Adenylate Kinase (Akeco) enzyme in water. The global diffusion tensor of the protein will be obtained from its structure.

First of all, the *4ake.pdb* file must be downloaded from the protein data bank website[1]. The file contains also water molecules that have to be removed, for example with the Pymol program[2].

Place the PDB file with only the structure of the protein in a directory which will represent the job working path (the directory where all the files produced during the calculation will be stored).

Launch C++OPPS and follow these instructions:

1. In the Project Panel, click on "Load protein" and select the PDB file prepared before;

2. In the Project Panel, set:
   Effective Radius = 2.00 Å,
   Periodic Boundary Conditions = 6,
   Temperature = 303.0 K,
   Viscosity = 0.9 cP. Then click on "Calculate Diffusion" button. The GUI will freeze until the diffusion tensor has been calculated and the principal values will appear below the button;

---

[1] File can be found at URL: http://www.rcsb.org/pdb/explore/explore.do?structureId=4AKE

[2] Pymol can be obtained from URL: http://pymol.sourceforge.net/

3. In the Physical Data Panel set the initial guess and fitting parameters as depicted here: Red circles were put for higher clarity on modifications to make. Totally 6 fitting parameter are set: a multiplicative constant of the global diffusion tensor, parallel and perpendicular coefficients of the (axial) diffusion tensor of the probe, the β_D tilt angle between probe molecular frame and dipolar interaction frame, the c_0^2 coefficient of the axial potential and the rate of exchange, R_{ex}.

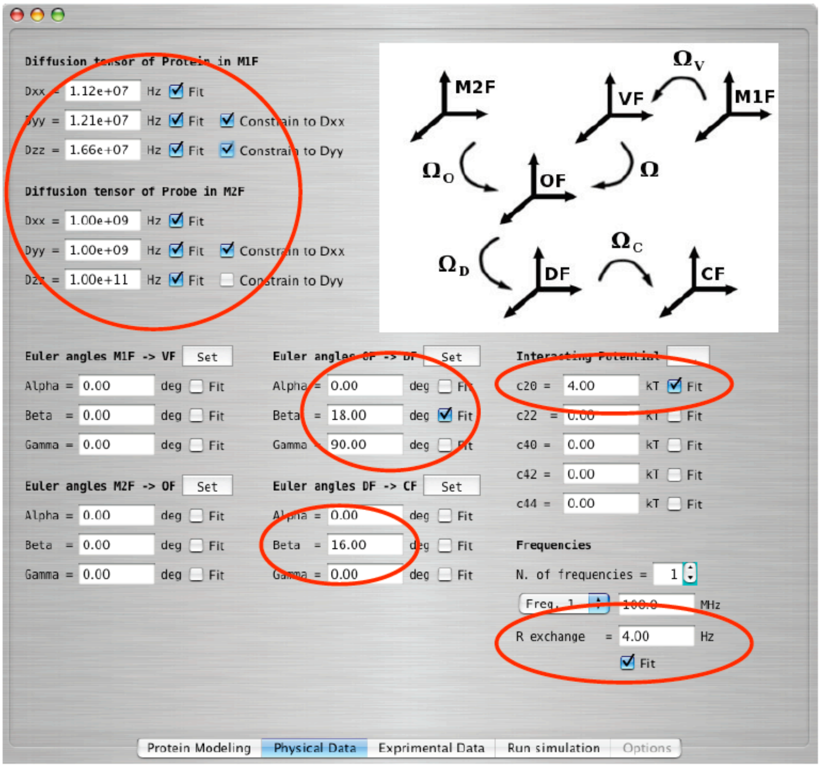

Diffusion tensor of Protein in M1F
Dxx = 1.12e+07 Hz ☑ Fit
Dyy = 1.21e+07 Hz ☑ Fit ☑ Constrain to Dxx
Dzz = 1.66e+07 Hz ☑ Fit ☑ Constrain to Dyy

Diffusion tensor of Probe in M2F
Dxx = 1.00e+09 Hz ☑ Fit
Dyy = 1.00e+09 Hz ☑ Fit ☑ Constrain to Dxx
Dzz = 1.00e+11 Hz ☑ Fit ☐ Constrain to Dyy

Euler angles M1F -> VF
Alpha = 0.00 deg ☐ Fit
Beta = 0.00 deg ☐ Fit
Gamma = 0.00 deg ☐ Fit

Euler angles M2F -> OF
Alpha = 0.00 deg ☐ Fit
Beta = 0.00 deg ☐ Fit
Gamma = 0.00 deg ☐ Fit

Euler angles OF -> DF
Alpha = 0.00 deg ☐ Fit
Beta = 18.00 deg ☑ Fit
Gamma = 90.00 deg ☐ Fit

Euler angles DF -> CF
Alpha = 0.00 deg ☐ Fit
Beta = 16.00 deg ☐ Fit
Gamma = 0.00 deg ☐ Fit

Interacting Potential
c20 = 4.00 kT ☑ Fit
c22 = 0.00 kT ☐ Fit
c40 = 0.00 kT ☐ Fit
c42 = 0.00 kT ☐ Fit
c44 = 0.00 kT ☐ Fit

Frequencies
N. of frequencies = 1
Freq. 1 100.0 MHz
R exchange = 4.00 Hz
☑ Fit

4. In the Experimental Data Panel set to "2" the number of residues. Then input, for each residue, the experimental data by completing the data. Remember that the program accepts a number in the table only if the "Return" key is pressed after the input. The experimental values are [214]:

	Residue 50		
Field	T_1 / ms	T_2 / ms	*NOE*
14.1 T (600.13 MHz)	1102.40 ± 32.20	54.69 ± 1.33	0.6239 ± 0.0075
18.79 T (800.13 MHz)	1499.10 ± 40.50	43.66 ± 0.99	0.6724 ± 0.0069
	Residue 165		
Field	T_1 / ms	T_2 / ms	*NOE*
14.1 T (600.13 MHz)	1274.80 ± 38.20	45.09 ± 0.99	0.7695 ± 0.0092
18.79 T (800.13 MHz)165	1900.70 ± 53.00	37.08 ± 0.86	0.8100 ± 0.0074

5. In the "Simulation Panel" set Lmax to 20 and, if C^{++}OPPS is running in parallelized local mode, the number of processors. Then click the "Run Simulation" button. If the cluster version is being used, user will be asked to decide some properties of the PBS job. Select the "Avogadro_PD" cluster, the "Long-large" queue and 4 processors. Then click on the "Submit" button. Now the simulation in running and periodically the text area in the Simulation Panel will be updated with the current status of the fitting.

This simulation will show that the global diffusion tensor is not changing much during the fitting, so it could be fixed to the predicted one.

Now, run again the simulation, but with only 5 fitting parameters. Just step back to point 3) and set the initial guess as shown below Once the modifications have been done, return to the "Simulation Panel" and run the new simulation.

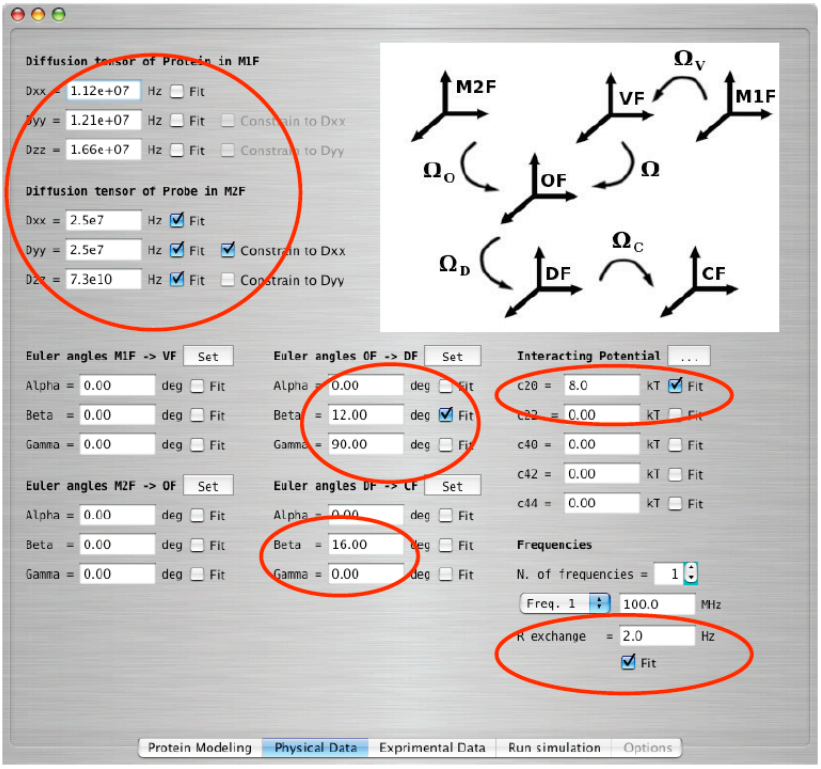
Diffusion tensor of Protein in M1F
Dxx = 1.12e+07 Hz ☐ Fit
Dyy = 1.21e+07 Hz ☐ Fit ☐ Constrain to Dxx
Dzz = 1.66e+07 Hz ☐ Fit ☐ Constrain to Dyy

Diffusion tensor of Probe in M2F
Dxx = 2.5e7 Hz ☑ Fit
Dyy = 2.5e7 Hz ☑ Fit ☑ Constrain to Dxx
Dzz = 7.3e10 Hz ☑ Fit ☐ Constrain to Dyy

Euler angles M1F -> VF
Alpha = 0.00 deg ☐ Fit
Beta = 0.00 deg ☐ Fit
Gamma = 0.00 deg ☐ Fit

Euler angles M2F -> OF
Alpha = 0.00 deg ☐ Fit
Beta = 0.00 deg ☐ Fit
Gamma = 0.00 deg ☐ Fit

Euler angles OF -> DF
Alpha = 0.00 deg ☐ Fit
Beta = 12.00 deg ☑ Fit
Gamma = 90.00 deg ☐ Fit

Euler angles DF -> CF
Alpha = 0.00 deg ☐ Fit
Beta = 16.00 deg ☐ Fit
Gamma = 0.00 deg ☐ Fit

Interacting Potential
c20 = 8.0 kT ☑ Fit
c22 = 0.00 kT ☐ Fit
c40 = 0.00 kT ☐ Fit
c42 = 0.00 kT ☐ Fit
c44 = 0.00 kT ☐ Fit

Frequencies
N. of frequencies = 1
Freq. 1 100.0 MHz
R exchange = 2.0 Hz
☑ Fit

Finally, let's try a third calculation with only three parameters. Together with the global diffusion tensor, also fix the β_D angle to 14° and the exchange rate to 2.5 Hz, so only the axially symmetric diffusion tensor of the probe and the coefficient c_0^2 will be fitted. The starting guess is shown below The three simulations will give the following results:

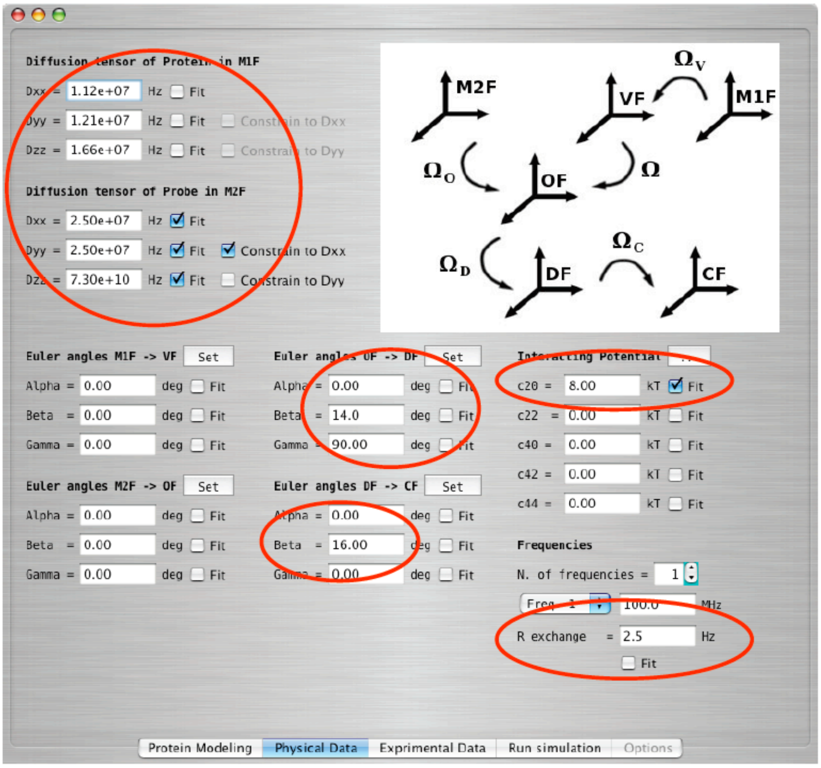

Diffusion tensor of Protein in M1F

Dxx = 1.12e+07 Hz ☐ Fit

Dyy = 1.21e+07 Hz ☐ Fit ☐ Constrain to Dxx

Dzz = 1.66e+07 Hz ☐ Fit ☐ Constrain to Dyy

Diffusion tensor of Probe in M2F

Dxx = 2.50e+07 Hz ☑ Fit

Dyy = 2.50e+07 Hz ☑ Fit ☑ Constrain to Dxx

Dzz = 7.30e+10 Hz ☑ Fit ☐ Constrain to Dyy

Euler angles M1F -> VF Set

Alpha = 0.00 deg ☐ Fit

Beta = 0.00 deg ☐ Fit

Gamma = 0.00 deg ☐ Fit

Euler angles M2F -> OF Set

Alpha = 0.00 deg ☐ Fit

Beta = 0.00 deg ☐ Fit

Gamma = 0.00 deg ☐ Fit

Euler angles OF -> DF Set

Alpha = 0.00 deg ☐ Fit

Beta = 14.0 deg ☐ Fit

Gamma = 90.00 deg ☐ Fit

Euler angles DF -> CF Set

Alpha = 0.00 deg ☐ Fit

Beta = 16.00 deg ☐ Fit

Gamma = 0.00 deg ☐ Fit

Interacting Potential

c20 = 8.00 kT ☑ Fit

c22 = 0.00 kT ☐ Fit

c40 = 0.00 kT ☐ Fit

c42 = 0.00 kT ☐ Fit

c44 = 0.00 kT ☐ Fit

Frequencies

N. of frequencies = 1

Freq 1 100.0 MHz

R exchange = 2.5 Hz

☐ Fit

Fit 1 - 6 parameters fitting

Calculation time is about 6 hours parallelized on 32 processors (about 10 seconds per fit step). The output file reads:

```
Component 1

Parameters:

Protein Dxx = 1.9969e+07 Hz

Protein Dyy = 2.1573e+07 Hz

Protein Dzz = 2.9597e+07 Hz

Probe Dxx = 2.5270e+07 Hz

Probe Dyy = 2.5270e+07 Hz

Probe Dzz = 7.2806e+10 Hz

Beta D = 13.2530 deg

c20 = 7.6581 kT

R exchange = 2.4457 Hz

Relaxation data: Chi square = 0.0000

Fitting procedure terminated for component 1

Final l2 norm of the residual = 0.0000
```

Field/MHz	T_1(th)/ms	T_1(exp)/ms	T_2(th)/ms	T_2(exp)/ms	NOE(th)	NOE(exp)
600.13	1102.40	1102.40	54.69	54.69	0.6239	0.6239
800.13	1499.10	1499.10	43.66	43.66	0.6724	0.6724

```
Exit parameter = 2

Component 2

Parameters:

Protein Dxx = 2.9099e+07 Hz

Protein Dyy = 3.1437e+07 Hz

Protein Dzz = 4.3129e+07 Hz

Probe Dxx = 1.4664e+07 Hz

Probe Dyy = 1.4664e+07 Hz

Probe Dzz = 2.1534e+13 Hz

Beta D = 10.6750 deg

c20 = 12.2089 kT

R exchange = 1.2550 Hz

Relaxation data: Chi square = 0.5006
```

Field/MHz	T_1(th)/ms	T_1(exp)/ms	T_2(th)/ms	T_2(exp)/ms	NOE(th)	NOE(exp)
600.13	1292.41	1274.80	45.13	45.09	0.7719	0.7695
800.13	1878.38	1900.70	37.06	37.08	0.8085	0.8100

```
Fitting procedure terminated for component 2

Final l2 norm of the residual = 0.7075

Exit parameter = 5
```

Fit 2 - 5 parameters fitting

Global diffusion fixed to Hz

Calculation time is about 30 minutes parallelized on 32 processors (about 10 seconds per fit step). The output file reads:

```
Component 1

Parameters:

Probe Dxx = 2.4659e+07 Hz

Probe Dyy = 2.4659e+07 Hz

Probe Dzz = 8.3075e+10 Hz
```

```
Beta D = 18.3082 deg

c20 = 4.1016 kT

R exchange = 3.1302 Hz

Relaxation data: Chi square = 1.1298
```

Field/MHz	T_1(th)/ms	T_1(exp)/ms	T_2(th)/ms	T_2(exp)/ms	NOE(th)	NOE(exp)
600.13	1126.84	1102.40	54.82	54.69	0.6255	0.6239
800.13	1471.24	1499.10	43.59	43.66	0.6714	0.6724

```
Fitting procedure terminated for component 1

Final l2 norm of the residual = 1.0629

Exit parameter = 1

Component 2

Parameters:

Probe Dxx = 1.4262e+07 Hz

Probe Dyy = 1.4262e+07 Hz

Probe Dzz = 3.7507e+11 Hz

Beta D = 16.3966 deg

c20 = 3.2317 kT

R exchange = 2.1360 Hz

Relaxation data: Chi square = 1.9606
```

Field/MHz	T_1(th)/ms	T_1(exp)/ms	T_2(th)/ms	T_2(exp)/ms	NOE(th)	NOE(exp)
600.13	1309.94	1274.80	45.21	45.09	0.7745	0.7695
800.13	1855.85	1900.70	37.00	37.08	0.8079	0.8100

```
Fitting procedure terminated for component 2

Final l2 norm of the residual = 1.4002

Exit parameter = 1
```

Fit 3 - 3 parameters fitting

Global diffusion fixed to Hz

angle fixed to

R exchange fixed to 2.5 Hz

Calculation time is about 15 minutes parallelized on 32 processors (about 10 seconds per fit step). The output file reads:

```
Component 1

Parameters:

Probe Dxx = 3.0475e+07 Hz

Probe Dyy = 3.0475e+07 Hz

Probe Dzz = 1.2749e+11 Hz

c20 = 5.2798 kT

Relaxation data: Chi square = 83.3298
```

Field/MHz	T_1(th)/ms	T_1(exp)/ms	T_2(th)/ms	T_2(exp)/ms	NOE(th)	NOE(exp)
600.13	1059.15	1102.40	48.99	54.69	0.5957	0.6239
800.13	1317.47	1499.10	39.33	43.66	0.6940	0.6724

```
Fitting procedure terminated for component 1

Final l2 norm of the residual = 9.1285

Exit parameter = 1

Component 2

Parameters:

Probe Dxx = 1.1590e+07 Hz

Probe Dyy = 1.1590e+07 Hz

Probe Dzz = 1.5030e+11 Hz

c20 = 1.6331 kT

Relaxation data: Chi square = 5.6361
```

Field/MHz	T_1(th)/ms	T_1(exp)/ms	T_2(th)/ms	T_2(exp)/ms	NOE(th)	NOE(exp)
600.13	1282.81	1274.80	45.41	45.09	0.7876	0.7695
800.13	1876.70	1900.70	36.60	37.08	0.8022	0.8100

```
Fitting procedure terminated for component 2

Final l2 norm of the residual = 2.3740

Exit parameter = 1
```

Appendix G

Evaluation of matrix elements in a two body model

G.1 Diffusive operator

Let us summarize all the reference frames that define the model (cfr as reference Figure 4-1, which is also reported below for clarity)

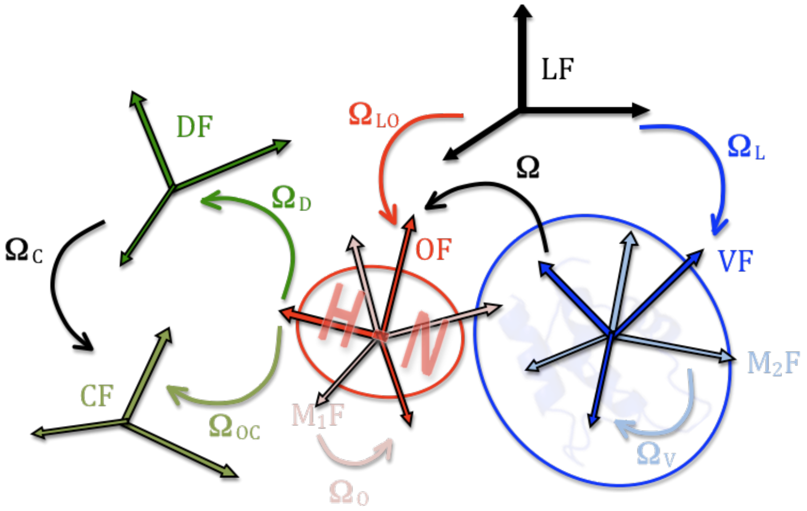

- LF is the laboratory inertial frame;
- B_iF is the frame where the diffusion tensor of the ith body is diagonal. The system is fixed on the ith body;

- VF is the frame fixed on the first body (the generator of the potential) in which is defined the orienting potential;

- OF is a frame fixed on the second body which "feels" the orientation effect;

- μF the reference frame where the magnetic tensor $\boldsymbol{\mu}$ is diagonal.

The sets of Euler angles that transform among the various frames are:

- $\boldsymbol{\Omega}_{LB_1}$ to transform from LF to B_1F;

- $\boldsymbol{\Omega}_{B_1V}$ to transform from B_1F to VF;

- $\boldsymbol{\Omega}_V$ to transform from LF to VF;

- $\boldsymbol{\Omega}_{B_1B_2}$ to transform from B_1F to B_2F;

- $\boldsymbol{\Omega}$ to transform from VF to OF;

- $\boldsymbol{\Omega}_{B_2O}$ to transform from B_2F to OF.

- $\boldsymbol{\Omega}_{B_2\mu}$ to transform from B_2F to μF.

The system is completely described by two stochastic variables and we make the choose $\boldsymbol{X} = (\boldsymbol{\Omega}_V, \boldsymbol{\Omega})$ so that the Smoluchosky operator is written as

$$\begin{aligned}\hat{\Gamma} &= {}^O\hat{J}^\dagger(\boldsymbol{\Omega})^O\boldsymbol{D}_2 P_{eq}(\boldsymbol{q})^O\hat{J}(\boldsymbol{\Omega}) + \\ &+ \left[{}^V\hat{J}(\boldsymbol{\Omega}) - {}^V\hat{J}(\boldsymbol{\Omega}_V)\right]^\dagger {}^V\boldsymbol{D}_1 P_{eq}(\boldsymbol{q}) \left[{}^V\hat{J}(\boldsymbol{\Omega}) - {}^V\hat{J}(\boldsymbol{\Omega}_V)\right]\end{aligned} \tag{G.1}$$

where the right O and V apexes mean that an operator or a tensor are defined in OF or VF and $\boldsymbol{D}_1$ and $\boldsymbol{D}_2$ are the diffusion tensors of the two bodies. Both diffusion tensor ar in general full tensors.

In eq. G.1, $P_{eq}(\boldsymbol{q})$ is the distribution equilibrium of the system. We take the case of isotropic environment so the energy of the system is independent on $\boldsymbol{\Omega}_V$:

$$P_{eq}(\boldsymbol{q}) = P_{eq}(\boldsymbol{\Omega}) = \mathcal{N} \exp\left[-V(\boldsymbol{\Omega})/k_BT\right] \tag{G.2}$$

For the orienting potential we choose

$$\begin{aligned} U(\mathbf{\Omega}) = V(\mathbf{\Omega})/k_BT &= c_0^2\mathcal{D}^2_{0,0}(\mathbf{\Omega}) + c_2^2\left[\mathcal{D}^2_{0,2}(\mathbf{\Omega}) + \mathcal{D}^2_{0,-2}(\mathbf{\Omega})\right] + \\ &\quad + c_0^4\mathcal{D}^4_{0,0}(\mathbf{\Omega}) + c_2^4\left[\mathcal{D}^4_{0,2}(\mathbf{\Omega}) + \mathcal{D}^4_{0,-2}(\mathbf{\Omega})\right] + \\ &\quad + c_4^4\left[\mathcal{D}^4_{0,4}(\mathbf{\Omega}) + \mathcal{D}^4_{0,-4}(\mathbf{\Omega})\right] \end{aligned} \tag{G.3}$$

and foo more convenience let's write the potential as

$$U(\mathbf{\Omega}) = \sum_{\nu=0}^{4}\sum_{\mu=-\nu}^{\nu} \epsilon^\nu_\mu \mathcal{D}^\nu_{0,\mu}(\mathbf{\Omega}) \tag{G.4}$$

where both ν and μ take only even values and $\epsilon^\nu_\mu = (-)^\mu \epsilon^{\nu\,*}_{-\mu}$ to ensure that the potential is real.

We symmetrize the diffusive operator to make it Hermitian:

$$\tilde{\Gamma} = P_{eq}(\mathbf{\Omega})^{-1/2}\hat{\Gamma}P_{eq}(\mathbf{\Omega})^{-1/2} \tag{G.5}$$

Now, we can interpret the operator as composed of a part independent on the potential and a function which depends on the interaction between the two bodies

$$\tilde{\Gamma} = \hat{\mathcal{J}} + F(\mathbf{\Omega}) \tag{G.6}$$

The first part is composed of terms of the type $\hat{\boldsymbol{J}}^\dagger \boldsymbol{D}\hat{\boldsymbol{J}}$, while the explicit form of the function is obtained by remembering that $\tilde{\Gamma}P_{eq}^{1/2} = 0$:

$$F(\mathbf{\Omega}) = -P_{eq}^{-1/2}\hat{\mathcal{J}}P_{eq}^{1/2} \tag{G.7}$$

The operator will be spanned on the space of rotations defined by

$$|\lambda_1, \lambda_2\rangle = |L_1M_1K_1\rangle \times |L_2M_2K_2\rangle \tag{G.8}$$

where

$$|L_1M_1K_1\rangle = \sqrt{\frac{[L_1]}{8\pi^2}}\mathcal{D}^{L_1}_{M_1,K_1}(\mathbf{\Omega}_V) \tag{G.9}$$

$$|L_2M_2K_2\rangle = \sqrt{\frac{[L_2]}{8\pi^2}}\mathcal{D}^{L_2}_{M_2,K_2}(\mathbf{\Omega}) \tag{G.10}$$

and $[L] = 2L + 1$.

In appendix H are reported some properties of the Wigner matrices that will be useful in the calculation of matrix elements.

Potential independent part

The potential independent part of the diffusive operator is made of four terms

$$\hat{\mathcal{J}} = \hat{J}_a + \hat{J}_b + \hat{J}_c + \hat{J}_d \tag{G.11}$$

with

$$\hat{J}_a = {}^{O}\hat{\boldsymbol{J}}^{\dagger}(\boldsymbol{\Omega})^{O}\boldsymbol{D}_2{}^{O}\hat{\boldsymbol{J}}(\boldsymbol{\Omega}) \tag{G.12}$$

$$\hat{J}_b = {}^{V}\hat{\boldsymbol{J}}^{\dagger}(\boldsymbol{\Omega})^{V}\boldsymbol{D}_1{}^{V}\hat{\boldsymbol{J}}(\boldsymbol{\Omega}) \tag{G.13}$$

$$\hat{J}_c = {}^{V}\hat{\boldsymbol{J}}^{\dagger}(\boldsymbol{\Omega}_V)^{V}\boldsymbol{D}_1{}^{V}\hat{\boldsymbol{J}}(\boldsymbol{\Omega}_V) \tag{G.14}$$

$$\hat{J}_d = -\left[{}^{V}\hat{\boldsymbol{J}}^{\dagger}(\boldsymbol{\Omega})^{V}\boldsymbol{D}_1{}^{V}\hat{\boldsymbol{J}}(\boldsymbol{\Omega}_V) + {}^{V}\hat{\boldsymbol{J}}^{\dagger}(\boldsymbol{\Omega}_V)^{V}\boldsymbol{D}_1{}^{V}\hat{\boldsymbol{J}}(\boldsymbol{\Omega})\right] \tag{G.15}$$

It is convenient to change from Cartesian to spherical representation of the operator. In appendix I it is shown how it is possible write the operator as:

$$\hat{\mathcal{J}} = \sum_{l=0,2}\sum_{m=-l}^{l} \hat{J}_a^{(l,m)} + \hat{J}_b^{(l,m)} + \hat{J}_c^{(l,m)} + \hat{J}_d^{(l,m)} \tag{G.16}$$

with

$$\hat{J}_a^{(l,m)} = {}^{O}D_2^{(l,m)}\;{}^{O}\hat{\mathcal{K}}_a^{(l,m)}(\boldsymbol{\Omega}) \tag{G.17}$$

$$\hat{J}_b^{(l,m)} = {}^{V}D_1^{(l,m)}\;{}^{V}\hat{\mathcal{K}}_b^{(l,m)}(\boldsymbol{\Omega}) \tag{G.18}$$

$$\hat{J}_c^{(l,m)} = {}^{V}D_1^{(l,m)}\;{}^{V}\hat{\mathcal{K}}_c^{(l,m)}(\boldsymbol{\Omega}_V) \tag{G.19}$$

$$\hat{J}_d^{(l,m)} = -2\,{}^{V}D_1^{(l,m)}\;{}^{V}\hat{\mathcal{K}}_d^{(l,m)}(\boldsymbol{\Omega},\boldsymbol{\Omega}_V) \tag{G.20}$$

and the specific expressions for the components $D^{(l,m)}$ and the operators $\hat{\mathcal{K}}^{(l,m)}$ are given in appendix I.

A first convenience in employing irreducible spherical tensors and tensorial operators is that the components of the diffusion tensors in OF and VF are easily found

$${}^{O}D_2^{(l,m)} = \sum_{m'=-l}^{l}\mathcal{D}^{l}_{m,m'}(\boldsymbol{\Omega}_{B_2O})\;{}^{B_2}D_2^{(l,m')\,*} \tag{G.21}$$

$${}^{V}D_1^{(l,m)} = \sum_{m'=-l}^{l}\mathcal{D}^{l}_{m,m'}(\boldsymbol{\Omega}_{B_1V})\;{}^{B_1}D_1^{(l,m')\,*} \tag{G.22}$$

Secondly, we will make use of the Wigner-Eckart theorem to evaluate the matrix elements.

Operator $\hat{J}_a$

This operator acts only on λ_2 so matrix elements are diagonal in λ_1 and we have:
for $l = 0$

$$\langle\lambda_2(\mathbf{\Omega})|{}^O\hat{\mathcal{K}}_a^{(0,0)}(\mathbf{\Omega})|\lambda_2'(\mathbf{\Omega})\rangle = -\frac{1}{\sqrt{3}}\delta_{\lambda_2,\lambda_2'}L_2(L_2+1) \tag{G.23}$$

for $l = 2$

$$\begin{aligned}\langle\lambda_2(\mathbf{\Omega})|{}^O\hat{\mathcal{K}}_a^{(2,m)}(\mathbf{\Omega})|\lambda_2'(\mathbf{\Omega})\rangle &= \delta_{L_2,L_2'}\delta_{M_2,M_2'}(-)^{(L_2-K_2)}\sqrt{\frac{(2L_2+3)!}{24(2L_2-2)!}}\times \\ &\times\begin{pmatrix} L_2 & 2 & L_2 \\ -K_2 & m & K_2' \end{pmatrix}\end{aligned} \tag{G.24}$$

In the last equation we made use of the Wigner-Eckart thorem, as explained in Appendix J. Now it is possible to write the matrix element:

$$\begin{aligned}\langle\lambda_1\lambda_2|\hat{J}_a|\lambda_1'\lambda_2'\rangle &= \delta_{\lambda_1,\lambda_1'}\delta_{L_2,L_2'}\delta_{M_2,M_2'}\Bigg[-\delta_{K_2,K_2'}\frac{1}{\sqrt{3}}\,{}^OD_2^{(0,0)}L_2(L_2+1)+ \\ &+(-)^{(L_2-K_2)}\,{}^OD_2^{(2,K_2-K_2')}\sqrt{\frac{(2L_2+3)!}{24(2L_2-2)!}}\times \\ &\times\begin{pmatrix} L_2 & 2 & L_2 \\ -K_2 & K_2-K_2' & K_2' \end{pmatrix}\Bigg]\end{aligned} \tag{G.25}$$

Operator $\hat{J}_b$

Also this operator acts only on λ_2 but it is defined in VF.
For $l = 0$

$$\langle\lambda_2(\mathbf{\Omega})|{}^V\hat{\mathcal{K}}_b^{(0,0)}(\mathbf{\Omega})|\lambda_2'(\mathbf{\Omega})\rangle = -\frac{1}{\sqrt{3}}\delta_{\lambda_2,\lambda_2'}L_2(L_2+1) \tag{G.26}$$

for $l = 2$

$$\begin{aligned}\langle\lambda_2(\mathbf{\Omega})|{}^V\hat{\mathcal{K}}_b^{(2,m)}(\mathbf{\Omega})|\lambda_2'(\mathbf{\Omega})\rangle &= \delta_{L_2,L_2'}\delta_{K_2,K_2'}(-)^{(L_2-M_2)}\sqrt{\frac{(2L_2+3)!}{24(2L_2-2)!}}\times \\ &\times\begin{pmatrix} L_2 & 2 & L_2 \\ -M_2 & -m & M_2' \end{pmatrix}\end{aligned} \tag{G.27}$$

In the last equation we made use of the Wigner-Eckart thorem, as explained in appendix J. Now it is possible to write the matrix element:

$$\begin{aligned}\langle\lambda_1\lambda_2|\hat{J}_b|\lambda_1'\lambda_2'\rangle &= \delta_{\lambda_1,\lambda_1'}\delta_{L_2,L_2'}\delta_{K_2,K_2'}\Bigg[-\delta_{M_2,M_2'}\frac{1}{\sqrt{3}}\,{}^{V}D_1^{(0,0)}L_2(L_2+1)+\\ &+(-)^{(L_2-M_2)}\,{}^{V}D_1^{(2,M_2'-M_2)}\sqrt{\frac{(2L_2+3)!}{24(2L_2-2)!}}\times\\ &\times\begin{pmatrix} L_2 & 2 & L_2\\ -M_2 & M_2-M_2' & M_2'\end{pmatrix}\Bigg]\end{aligned} \tag{G.28}$$

Operator $\hat{J}_c$

This operator is analogous to $\hat{J}_a$, but acting only on λ_1 and defined in VF, so:
for $l=0$

$$\langle\lambda_1(\mathbf{\Omega}_V)|{}^{V}\hat{\mathcal{K}}_c^{(0,0)}(\mathbf{\Omega}_V)|\lambda_1'(\mathbf{\Omega}_V)\rangle = -\frac{1}{\sqrt{3}}\delta_{\lambda_1,\lambda_1'}L_1(L_1+1) \tag{G.29}$$

for $l=2$

$$\begin{aligned}\langle\lambda_1(\mathbf{\Omega}_V)|{}^{V}\hat{\mathcal{K}}_c^{(2,m)}(\mathbf{\Omega}_V)|\lambda_1'(\mathbf{\Omega}_V)\rangle &= \delta_{L_1,L_1'}\delta_{M_1,M_1'}(-)^{(L_1-K_1)}\sqrt{\frac{(2L_1+3)!}{24(2L_1-2)!}}\times\\ &\times\begin{pmatrix} L_1 & 2 & L_1\\ -K_1 & m & K_1'\end{pmatrix}\end{aligned} \tag{G.30}$$

In the last equation we made use of the Wigner-Eckart thorem, as explained in appendix J. Now it is possible to write the matrix element:

$$\begin{aligned}\langle\lambda_1\lambda_2|\hat{J}_c|\lambda_1'\lambda_2'\rangle &= \delta_{\lambda_2,\lambda_2'}\delta_{L_1,L_1'}\delta_{M_1,M_1'}\Bigg[-\delta_{K_1,K_1'}\frac{1}{\sqrt{3}}\,{}^{V}D_1^{(0,0)}L_1(L_1+1)+\\ &+(-)^{(L_1-K_1)}\,{}^{V}D_1^{(2,K_1-K_1')}\sqrt{\frac{(2L_1+3)!}{24(2L_1-2)!}}\times\\ &\times\begin{pmatrix} L_1 & 2 & L_1\\ -K_1 & K_1-K_1' & K_1'\end{pmatrix}\Bigg]\end{aligned} \tag{G.31}$$

Operator $\hat{J}_d$

The spherical tensorial operator $\hat{\mathcal{K}}_d^{(2)}$ acts on both the sub-spaces of the rotations and the Wigner-Eckart theorem would be useful if we employed the coupled representation. Because we are working with the uncoupled representation, it is easier to use the explicit formulas: for $l = 0$

$$\begin{aligned}\langle\lambda_1\lambda_2|{}^V\hat{\mathcal{K}}_d^{(0,0)}|\lambda_1'\lambda_2'\rangle &= -\frac{1}{\sqrt{3}}\delta_{L_1,L_1'}\delta_{M_1,M_1'}\delta_{L_2,L_2'}\delta_{K_2,K_2'}\times\\ &\times\Big[\frac{1}{2}\Big(\delta_{K_1,K_1'-1}\delta_{M_2,M_2'-1}c^-_{L_1,K_1+1}c^-_{L_2,M_2+1}+\\ &+\delta_{K_1,K_1'+1}\delta_{M_2,M_2'+1}c^+_{L_1,K_1-1}c^+_{L_2,M_2-1}\Big)+\\ &+\delta_{K_1,K_1'}\delta_{M_2,M_2'}K_1M_2\Big]\end{aligned}\tag{G.32}$$

for $l = 2$

$$\begin{aligned}\langle\lambda_1\lambda_2|{}^V\hat{\mathcal{K}}_d^{(2,0)}|\lambda_1'\lambda_2'\rangle &= \frac{1}{\sqrt{6}}\delta_{L_1,L_1'}\delta_{M_1,M_1'}\delta_{L_2,L_2'}\delta_{K_2,K_2'}\times\\ &\times\Big[-\frac{1}{2}\Big(\delta_{K_1,K_1'-1}\delta_{M_2,M_2'-1}c^-_{L_1,K_1+1}c^-_{L_2,M_2+1}+\\ &+\delta_{K_1,K_1'+1}\delta_{M_2,M_2'+1}c^+_{L_1,K_1-1}c^+_{L_2,M_2-1}\Big)+\\ &+\delta_{K_1,K_1'}\delta_{M_2,M_2'}2K_1M_2\Big]\end{aligned}\tag{G.33}$$

$$\begin{aligned}\langle\lambda_1\lambda_2|{}^V\hat{\mathcal{K}}_d^{(2,\pm1)}|\lambda_1'\lambda_2'\rangle &= \mp\frac{1}{2}\delta_{L_1,L_1'}\delta_{M_1,M_1'}\delta_{L_2,L_2'}\delta_{K_2,K_2'}\times\\ &\times\Big(\delta_{K_1,K_1'\pm1}\delta_{M_2,M_2'}c^\pm_{L_1,K_1\mp1}M_2+\\ &+\delta_{K_1,K_1'}\delta_{M_2,M_2'\mp1}K_1c^\mp_{L_2,M_2\pm1}\Big)\end{aligned}\tag{G.34}$$

$$\begin{aligned}\langle\lambda_1\lambda_2|{}^V\hat{\mathcal{K}}_d^{(2,\pm2)}|\lambda_1'\lambda_2'\rangle &= \frac{1}{2}\delta_{L_1,L_1'}\delta_{M_1,M_1'}\delta_{L_2,L_2'}\delta_{K_2,K_2'}\delta_{K_1,K_1'\pm1}\delta_{M_2,M_2'\mp1}\times\\ &\times c^\pm_{L_1,K_1\mp1}c^\mp_{L_2,M_2\pm1}\end{aligned}\tag{G.35}$$

and the matrix element will be

$$\langle\lambda_1\lambda_2|\hat{J}_d|\lambda_1'\lambda_2'\rangle = -2\sum_{l=0,2}\sum_{m=-l}^{l}{}^VD_1^{(l,m)}\langle\lambda_1\lambda_2|{}^V\hat{\mathcal{K}}_d^{(l,m)}|\lambda_1'\lambda_2'\rangle\tag{G.36}$$

Potential dependent part

To evaluate the potential dependent function it sufficient to remember that $\tilde{\Gamma}P_{eq}^{1/2} = 0$, so

$$\begin{aligned}F(\mathbf{\Omega}) &= -P_{eq}^{-1/2}(\mathbf{\Omega})\hat{\mathcal{J}}(\mathbf{\Omega},\mathbf{\Omega}_V)P_{eq}^{1/2}(\mathbf{\Omega}) =\\ &= -P_{eq}^{-1/2}(\mathbf{\Omega})\hat{J}_a(\mathbf{\Omega})P_{eq}^{1/2}(\mathbf{\Omega}) - P_{eq}^{-1/2}(\mathbf{\Omega})\hat{J}_b(\mathbf{\Omega})P_{eq}^{1/2}(\mathbf{\Omega}) =\\ &= F_a(\mathbf{\Omega}) + F_b(\mathbf{\Omega})\end{aligned}\tag{G.37}$$

The operators $\hat{J}_c$ and $\hat{J}_d$ do not contribute to $F(\mathbf{\Omega})$ because they contain derivatives with respect to $\mathbf{\Omega}_V$ and the equilibrium distribution probability depends only on $\mathbf{\Omega}$.

To build $F(\mathbf{\Omega})$ it is useful to evaluate some derivatives (all operators act on $\mathbf{\Omega}$ so this dependence will be omitted):

$$\begin{aligned} {}^{O}\hat{J}_Z U &= -\sum_{\nu,\mu} \epsilon_{\nu,\mu} \mu \mathcal{D}^{\nu}_{0,\mu} && \text{(G.38)} \\ {}^{V}\hat{J}_Z U &= 0 && \text{(G.39)} \\ {}^{O}\hat{J}_{\pm} U &= -\sum_{\nu,\mu} \epsilon_{\nu,\mu} c^{\pm}_{\nu,\mu} \mathcal{D}^{\nu}_{0,\mu\pm1} && \text{(G.40)} \\ {}^{V}\hat{J}_{\pm} U &= -\sum_{\nu,\mu} \epsilon_{\nu,\mu} c^{\mp}_{\nu,0} \mathcal{D}^{\nu}_{\mp1,\mu} && \text{(G.41)} \end{aligned}$$

where ν takes the even values from 0 to 4 and μ the even values from $-\nu$ to ν.

From these derivatives one obtains:

$$\begin{aligned} {}^{O}\hat{J}^2_Z U &= \sum_{\nu,\mu} \epsilon_{\nu,\mu} \mu^2 \mathcal{D}^{\nu}_{0,\mu} && \text{(G.42)} \\ {}^{V}\hat{J}^2_Z U &= 0 && \text{(G.43)} \end{aligned}$$

$$\begin{aligned} {}^{O}\hat{J}^2_{\pm} U &= \sum_{\nu,\mu} \epsilon_{\nu,\mu} c^{\pm}_{\nu,\mu} c^{\pm}_{\nu,\mu\pm1} \mathcal{D}^{\nu}_{0,\mu\pm2} && \text{(G.44)} \\ {}^{V}\hat{J}^2_{\pm} U &= \sum_{\nu,\mu} \epsilon_{\nu,\mu} c^{\mp}_{\nu,0} c^{\mp}_{\nu,\mp1} \mathcal{D}^{\nu}_{\mp2,\mu} && \text{(G.45)} \end{aligned}$$

$$\begin{aligned} {}^{O}\hat{J}_{+}{}^{O}\hat{J}_{-} U &= \sum_{\nu,\mu} \epsilon_{\nu,\mu} c^{-}_{\nu,\mu} c^{+}_{\nu,\mu-1} \mathcal{D}^{\nu}_{0,\mu} && \text{(G.46)} \\ {}^{O}\hat{J}_{-}{}^{O}\hat{J}_{+} U &= \sum_{\nu,\mu} \epsilon_{\nu,\mu} c^{+}_{\nu,\mu} c^{-}_{\nu,\mu+1} \mathcal{D}^{\nu}_{0,\mu} && \text{(G.47)} \\ {}^{V}\hat{J}_{+}{}^{V}\hat{J}_{-} U &= {}^{V}\hat{J}_{-}{}^{V}\hat{J}_{+} U = \sum_{\nu,\mu} \epsilon_{\nu,\mu} \nu(\nu+1) \mathcal{D}^{\nu}_{0,\mu} && \text{(G.48)} \end{aligned}$$

$$\begin{aligned} {}^{O}\hat{J}_{Z}{}^{O}\hat{J}_{\pm} U &= \sum_{\nu,\mu} \epsilon_{\nu,\mu} c^{\pm}_{\nu,\mu} (\mu \pm 1) \mathcal{D}^{\nu}_{0,\mu\pm1} && \text{(G.49)} \\ {}^{O}\hat{J}_{\pm}{}^{O}\hat{J}_{Z} U &= \sum_{\nu,\mu} \epsilon_{\nu,\mu} c^{\pm}_{\nu,\mu} \mu \mathcal{D}^{\nu}_{0,\mu\pm1} && \text{(G.50)} \\ {}^{V}\hat{J}_{Z}{}^{V}\hat{J}_{\pm} U &= \mp\sum_{\nu,\mu} \epsilon_{\nu,\mu} c^{\mp}_{\nu,0} \mathcal{D}^{\nu}_{\mp1,\mu} && \text{(G.51)} \end{aligned}$$

$$ {}^{V}\hat{J}_{\pm}{}^{V}\hat{J}_{Z}U = 0 \tag{G.52} $$

$$ \begin{aligned} \left({}^{O}\hat{J}_{Z}U\right)^{2} &= \sum_{\nu,\mu}\sum_{\nu',\mu'}(-)^{\mu-\mu'}\epsilon_{\nu,\mu}\epsilon_{\nu',\mu'}\mu\mu'\sum_{j}[j]\begin{pmatrix} \nu & \nu' & j \\ 0 & 0 & 0 \end{pmatrix}\times \\ &\quad\times\begin{pmatrix} \nu & \nu' & j \\ \mu & \mu' & -(\mu+\mu') \end{pmatrix}\mathcal{D}^{j}_{0,\mu+\mu'} \end{aligned} \tag{G.53} $$

$$ \left({}^{V}\hat{J}_{Z}U\right)^{2} = 0 \tag{G.54} $$

$$ \begin{aligned} \left({}^{O}\hat{J}_{\pm}U\right)^{2} &= \sum_{\nu,\mu}\sum_{\nu',\mu'}(-)^{\mu-\mu'}\epsilon_{\nu,\mu}\epsilon_{\nu',\mu'}c^{\pm}_{\nu,\mu}c^{\pm}_{\nu',\mu'}\sum_{j}[j]\begin{pmatrix} \nu & \nu' & j \\ 0 & 0 & 0 \end{pmatrix}\times \\ &\quad\times\begin{pmatrix} \nu & \nu' & j \\ \mu\pm 1 & \mu'\pm 1 & -(\mu+\mu'\pm 2) \end{pmatrix}\mathcal{D}^{j}_{0,\mu+\mu'\pm 2} \end{aligned} \tag{G.55} $$

$$ \begin{aligned} \left({}^{V}\hat{J}_{\pm}U\right)^{2} &= \sum_{\nu,\mu}\sum_{\nu',\mu'}(-)^{\mu-\mu'}\epsilon_{\nu,\mu}\epsilon_{\nu',\mu'}c^{\mp}_{\nu,0}c^{\mp}_{\nu',0}\sum_{j}[j]\begin{pmatrix} \nu & \nu' & j \\ \mp 1 & \mp 1 & \pm 2 \end{pmatrix}\times \\ &\quad\times\begin{pmatrix} \nu & \nu' & j \\ \mu & \mu' & -(\mu+\mu') \end{pmatrix}\mathcal{D}^{j}_{\mp 2,\mu+\mu'} \end{aligned} \tag{G.56} $$

$$ \begin{aligned} ({}^{O}\hat{J}_{+}U)({}^{O}\hat{J}_{-}U) &= \sum_{\nu,\mu}\sum_{\nu',\mu'}(-)^{\mu-\mu'}\epsilon_{\nu,\mu}\epsilon_{\nu',\mu'}c^{+}_{\nu,\mu}c^{-}_{\nu',\mu'}\sum_{j}[j]\begin{pmatrix} \nu & \nu' & j \\ 0 & 0 & 0 \end{pmatrix}\times \\ &\quad\times\begin{pmatrix} \nu & \nu' & j \\ \mu+1 & \mu'-1 & -(\mu+\mu') \end{pmatrix}\mathcal{D}^{j}_{0,\mu+\mu'} \end{aligned} \tag{G.57} $$

$$ \begin{aligned} ({}^{V}\hat{J}_{+}U)({}^{V}\hat{J}_{-}U) &= \sum_{\nu,\mu}\sum_{\nu',\mu'}(-)^{\mu-\mu'}\epsilon_{\nu,\mu}\epsilon_{\nu',\mu'}c^{-}_{\nu,0}c^{+}_{\nu',0}\sum_{j}[j]\begin{pmatrix} \nu & \nu' & j \\ -1 & 1 & 0 \end{pmatrix}\times \\ &\quad\times\begin{pmatrix} \nu & \nu' & j \\ \mu & \mu' & -(\mu+\mu') \end{pmatrix}\mathcal{D}^{j}_{0,\mu+\mu'} \end{aligned} \tag{G.58} $$

$$ ({}^{O}\hat{J}_{Z}U)({}^{O}\hat{J}_{\pm}U) = -\sum_{\nu,\mu}\sum_{\nu',\mu'}(-)^{\mu-\mu'}\epsilon_{\nu,\mu}\epsilon_{\nu',\mu'}\mu c^{\pm}_{\nu',\mu'}\sum_{j}[j]\begin{pmatrix} \nu & \nu' & j \\ 0 & 0 & 0 \end{pmatrix}\times $$

$$\times \begin{pmatrix} \nu & \nu' & j \\ \mu & \mu' \pm 1 & -(\mu+\mu'\pm 1) \end{pmatrix} \mathcal{D}^{j}_{0,\mu+\mu'\pm 1} \tag{G.59}$$

$$({}^{V}\hat{J}_Z U)({}^{V}\hat{J}_{\pm} U) = 0 \tag{G.60}$$

where $c^{\pm}_{\nu,\mu} = \sqrt{\nu(\nu+1)-\mu(\mu\pm 1)}$ and $[j]=(2j+1)$.

Finally let's recall that

$$P_{eq}^{-1/2}\hat{J}_\alpha \hat{J}_\beta P_{eq}^{1/2} = \frac{1}{4}\left[\left(\hat{J}_\alpha U\right)\left(\hat{J}_\beta U\right) - 2\hat{J}_\alpha \hat{J}_\beta U\right] \tag{G.61}$$

with $\alpha,\beta = \pm, Z$.

Function $F_a(\mathbf{\Omega})$

The first addend of the function F is given by

$$F_a = -\sum_{l,m} {}^{O}D_2^{(l,m)} P_{eq}^{-1/2}\hat{\mathcal{K}}_a^{(l,m)} P_{eq}^{1/2} = -\sum_{l,m} {}^{O}D_2^{(l,m)} F_a^{(l,m)} \tag{G.62}$$

All the components can be written as

$$F_a^{(l,m)} = -\sum_{\mu,\mu'}\sum_{j} f_a^{(l,m)}(\mu,\mu',j)\mathcal{D}^{j}_{0,\mu+\mu'+m} \tag{G.63}$$

with

$$\begin{aligned} f_a^{(0,0)}(\mu,\mu',j) &= -\frac{1}{4\sqrt{3}}\sum_{\nu}\left\{(-)^{\mu-\mu'}[j]\sum_{\nu'}\epsilon_{\nu,\mu}\epsilon_{\nu',\mu'}\begin{pmatrix} \nu & \nu' & j \\ 0 & 0 & 0 \end{pmatrix}\times \right. \\ &\times\left[\begin{pmatrix} \nu & \nu' & j \\ \mu+1 & \mu'-1 & -(\mu+\mu') \end{pmatrix} c^{+}_{\nu,\mu}c^{-}_{\nu',\mu'} + \right. \\ &\left.\left. + \begin{pmatrix} \nu & \nu' & j \\ \mu & \mu' & -(\mu+\mu') \end{pmatrix}\mu\mu'\right]\right\} - \delta_{j,\nu}\delta_{\mu',0}2\epsilon_{\nu,\mu}\nu(\nu+1) \end{aligned} \tag{G.64}$$

$$\begin{aligned} f_a^{(2,0)}(\mu,\mu',j) &= \frac{1}{4\sqrt{6}}\sum_{\nu}\left\{(-)^{\mu-\mu'}[j]\sum_{\nu'}\{\epsilon_{\nu,\mu}\epsilon_{\nu',\mu'}\begin{pmatrix} \nu & \nu' & j \\ 0 & 0 & 0 \end{pmatrix}\times \right. \\ &\times\left[-\begin{pmatrix} \nu & \nu' & j \\ \mu+1 & \mu'-1 & -(\mu+\mu') \end{pmatrix} c^{+}_{\nu,\mu}c^{-}_{\nu',\mu'} + \right. \\ &\left.\left.\begin{pmatrix} \nu & \nu' & j \\ \mu & \mu' & -(\mu+\mu') \end{pmatrix} 2\mu\mu'\right]\right\} + \end{aligned}$$

$$
\begin{aligned}
& +\delta_{j,\nu}\delta_{\mu',0}2\epsilon_{\nu,\mu}\left[\nu(\nu+1)-3\mu^2\right] && \text{(G.65)}\\
f_a^{(2,\pm1)}(\mu,\mu',j) \;=\; & \pm\frac{1}{4}\sum_{\nu}\left[(-)^{\mu-\mu'}[j]\sum_{\nu'}\epsilon_{\nu,\mu}\epsilon_{\nu',\mu'}\mu\, c^{\pm}_{\nu',\mu'}\begin{pmatrix}\nu & \nu' & j\\ 0 & 0 & 0\end{pmatrix}\times\right. \\
& \left.\times\begin{pmatrix}\nu & \nu' & j\\ \mu & \mu'\pm1 & -(\mu+\mu'\pm1)\end{pmatrix}\right]+\delta_{j,\nu}\delta_{\mu',0}\epsilon_{\nu,\mu}c^{\pm}_{\nu,\mu}(2\mu\pm1) && \text{(G.66)}\\
f_a^{(2,\pm2)}(\mu,\mu',j) \;=\; & \frac{1}{8}\sum_{\nu}\left[(-)^{\mu-\mu'}[j]\sum_{\nu'}\epsilon_{\nu,\mu}\epsilon_{\nu',\mu'}c^{\pm}_{\nu,\mu}c^{\pm}_{\nu',\mu'}\begin{pmatrix}\nu & \nu' & j\\ 0 & 0 & 0\end{pmatrix}\times\right. \\
& \left.\times\begin{pmatrix}\nu & \nu' & j\\ \mu\pm1 & \mu'\pm1 & -(\mu+\mu'\pm2)\end{pmatrix}\right]-\delta_{j,\nu}\delta_{\mu',0}2\epsilon_{\nu,\mu}c^{\pm}_{\nu,\mu}c^{\pm}_{\nu,\mu\pm1} && \text{(G.67)}
\end{aligned}
$$

As can be seen from the above equations, we have changed the "natural" order of the indexes, i.e. summation ordered as $\sum_\nu\sum_\mu\sum_{\nu'}\sum_{\mu'}\sum_j$, to the quite "non-natural" order $\sum_\mu\sum_{\mu'}\sum_j\sum_\nu\sum_{\nu'}$. This ordering permits us to write the matrix elements in such a way that the selection rules are evident and all the components $f_a^{(l,m)}$ can be calculated only once, speeding up the algorithm. The matrix element, diagonal in λ_1, is

$$
\begin{aligned}
\langle\lambda_2|F_a|\lambda_2'\rangle \;=\; & -\sum_{l,m}{}^{O}D_2^{(l,m)}\sum_{\mu,\mu',j}f_a^{(l,m)}(\mu,\mu',j)\langle\lambda_2|\mathcal{D}^{j}_{0,\mu+\mu'+m}|\lambda_2'\rangle=\\
=\; & -\delta_{M_2,M_2'}(-)^{M_2-K_2}\sqrt{[L_2,L_2']}\sum_{l,m}{}^{O}D_2^{(l,m)}\sum_{\mu,\mu',j}f_a^{(l,m)}(\mu,\mu',j)\times\\
& \times\begin{pmatrix}L_2 & j & L_2'\\ -M_2 & 0 & M_2\end{pmatrix}\begin{pmatrix}L_2 & j & L_2'\\ -K_2 & \mu+\mu'+m & K_2'\end{pmatrix}=\\
=\; & -\delta_{M_2,M_2'}(-)^{M_2-K_2}\sqrt{[L_2,L_2']}\sum_{l}\sum_{\mu,\mu',j}{}^{O}D_2^{(l,K_2-K_2'-\mu-\mu')}f_a^{(l,K_2-K_2'-\mu-\mu')}(\mu,\mu',j)\times\\
& \times\begin{pmatrix}L_2 & j & L_2'\\ -M_2 & 0 & M_2\end{pmatrix}\begin{pmatrix}L_2 & j & L_2'\\ -K_2 & K_2-K_2' & K_2'\end{pmatrix} && \text{(G.68)}
\end{aligned}
$$

and the variability of the indexes is

$$
\begin{cases}
-4\le\mu\le4\\
max\{-4,(K_2-K_2'-\mu+2)\}\le\mu'\le min\{4,(K_2-K_2'-\mu-2)\}\\
max\{0,|K_2-K_2'-\mu-\mu'|,|L_2-L_2'|\}\le j\le min\{8,(L_2+L_2')\}\\
|\mu|\le\nu\le4\\
max\{|\mu'|,|\nu-j|\}\le\nu'\le min\{4,(\nu+j)\}
\end{cases}
\qquad\text{(G.69)}
$$

which represent the ranges that avoid the explicit zeroes of the $3j$ symbols in the expressions.

Function $F_b(\mathbf{\Omega})$

Analogously, the second addend of the function F is given by

$$F_b = -\sum_{l,m} {}^V D_1^{(l,m)} P_{eq}^{-1/2} \hat{\mathcal{K}}_b^{(l,m)} P_{eq}^{1/2} = -\sum_{l,m} {}^V D_1^{(l,m)} F_b^{(l,m)} \tag{G.70}$$

All the components can be written as

$$F_b^{(l,m)} = -\sum_{\mu,\mu'} \sum_j f_b^{(l,m)}(\mu,\mu',j) \mathcal{D}^j_{-m,\mu+\mu'} \tag{G.71}$$

with

$$\begin{aligned}
f_b^{(0,0)}(\mu,\mu',j) &= -\frac{1}{4\sqrt{3}} \sum_{\nu} \Bigg\{ (-)^{\mu-\mu'} [j] \sum_{\nu'} \epsilon_{\nu,\mu} \epsilon_{\nu',\mu'} \begin{pmatrix} \nu & \nu' & j \\ 1 & 1 & 0 \end{pmatrix} \times \\
&\quad \times \begin{pmatrix} \nu & \nu' & j \\ \mu & \mu' & -(\mu+\mu') \end{pmatrix} c^{-}_{\nu,0} c^{+}_{\nu',0} - \delta_{j,\nu} \delta_{\mu',0} 2 \epsilon_{\nu,\mu} \nu(\nu+1) \\
f_b^{(2,0)}(\mu,\mu',j) &= \frac{1}{\sqrt{2}} f_b^{(0,0)}(\mu',0,j) \\
f_b^{(2,\pm1)}(\mu,\mu',j) &= -\frac{1}{4} \sum_{\nu} \delta_{j,\nu} \delta_{\mu',0} \epsilon_{\nu,\mu} c^{\mp}_{\nu,0} \\
f_b^{(2,\pm2)}(\mu,\mu',j) &= \frac{1}{8} \sum_{\nu} \Bigg[(-)^{\mu-\mu'} [j] \sum_{\nu'} \epsilon_{\nu,\mu} \epsilon_{\nu',\mu'} c^{\mp}_{\nu,0} c^{\mp}_{\nu',0} \begin{pmatrix} \nu & \nu' & j \\ \mp1 & \mp1 & \pm2 \end{pmatrix} \times \\
&\quad \times \begin{pmatrix} \nu & \nu' & j \\ \mu & \mu' & -(\mu+\mu') \end{pmatrix} \Bigg] - \delta_{j,\nu} \delta_{\mu,\mu'} 2 \epsilon_{\nu,\mu} c^{\mp}_{\nu,0} c^{\mp}_{\nu,\mp1}
\end{aligned} \tag{G.72}$$

As can be seen from the above equations, we have changed the "natural" order of the indexes, i.e. summation ordered as $\sum_\nu \sum_\mu \sum_{\nu'} \sum_{\mu'} \sum_j$, to the quite "non-natural" order $\sum_\mu \sum_{\mu'} \sum_j \sum_\nu \sum_{\nu'}$. This ordering permits us to write the matrix elements in such a way that the selection rules are evident and all the components $f_b^{(l,m)}$ can be calculated only once, speeding up the algorithm. The matrix element, diagonal in λ_1, is

$$\begin{aligned}
\langle \lambda_2 | F_b | \lambda_2' \rangle &= -\sum_{l,m} {}^V D_1^{(l,m)} \sum_{\mu,\mu',j} f_b^{(l,m)}(\mu,\mu',j) \langle \lambda_2 | \mathcal{D}^j_{-m,\mu+\mu'} | \lambda_2' \rangle = \\
&= -(-)^{M_2-K_2} \sqrt{[L_2, L_2']} \sum_{l,m} {}^V D_1^{(l,m)} \sum_{\mu,\mu',j} f_b^{(l,m)}(\mu,\mu',j) \times
\end{aligned}$$

$$
\begin{aligned}
& \times \begin{pmatrix} L_2 & j & L_2' \\ -M_2 & -m & M_2' \end{pmatrix} \begin{pmatrix} L_2 & j & L_2' \\ -K_2 & \mu+\mu' & K_2' \end{pmatrix} = \\
= \quad & -(-)^{M_2-K_2} \sum_l \sum_{\mu,\mu',j} {}^V D_1^{(l,M_2'-M_2)} f_b^{(l,M_2'-M_2)}(\mu,\mu',j) \times \\
& \times \begin{pmatrix} L_2 & j & L_2' \\ -M_2 & M_2-M_2' & M_2' \end{pmatrix} \begin{pmatrix} L_2 & j & L_2' \\ -K_2 & K_2-K_2' & K_2' \end{pmatrix}
\end{aligned}
\tag{G.73}
$$

and the variability of the indexes is

$$
\begin{cases}
-4 \le \mu \le 4 \\
max\{-4, (K_2 - K_2' - \mu)\} \le \mu' \le min\{4, (K_2 - K_2' - \mu)\} \\
max\{0, |K_2 - K_2' - \mu - \mu'|, |L_2 - L_2'|\} \le j \le min\{8, (L_2 + L_2')\} \\
|\mu| \le \nu \le 4 \\
max\{|\mu'|, |\nu - j|\} \le \nu' \le min\{4, (\nu + j)\}
\end{cases}
\tag{G.74}
$$

which represent the ranges that avoid the explicit zeroes of the $3j$ symbols in the expressions.

Symmetrization of diffusive operator

The diffusive operator $\tilde{\Gamma}$ is Hermitian and its associated matrix, with the basis set given in eq. (G.8), is Hermitian. It would be desirable to work with a real symmetric matrix in order to simplify the further operations to be done during the Lanczos tridiagonalization. Inspecting the matrix elements one observes that there is a symmetry for the concerted change in sign of the indexes K_1, M_2 and K_2. Precisely, if $\hat{\mathcal{T}}$ is an operator which changes the sign of the three indexes, we have:

$$
\begin{aligned}
& \hat{\mathcal{T}} \langle L_1 M_1 K_1, L_2 M_2 K_2 | \tilde{\Gamma} | L_1' M_1' K_1', L_2' M_2' K_2' \rangle = \\
& = \langle L_1 M_1 - K_1, L_2 - M_2 - K_2 | \tilde{\Gamma} | L_1' M_1' - K_1', L_2' - M_2' - K_2' \rangle \\
& = (-)^{K_1+M_2+K_2} (-)^{K_1'+M_2'+K_2'} \langle L_1 M_1 K_1, L_2 M_2 K_2 | \tilde{\Gamma} | L_1' M_1' K_1', L_2' M_2' K_2' \rangle^*
\end{aligned}
\tag{G.75}
$$

This symmetry permits to introduce a unitary transformation which transforms the Hermitian matrix into a real symmetric one. Instead of applying the transformation to the matrix associated to the diffusive operator we prefer to define a transformed basis. The matrix elements of the operator in the new basis are written as linear combinations of the elements in the original basis. This procedure complicates a little bit the formalism but saves a lot of computational time. The new basis set is

$$|\Lambda\rangle = \mathcal{N} e^{i\frac{\pi}{4}(j-1)} \left(|L_1 M_1 K_1, L_2 M_2 K_2\rangle + js|L_1 M_1 - K_1, L_2 - M_2 - K_2\rangle\right) \tag{G.76}$$

where the indexes L_1, M_1 and L_2 have the same variability of the old base, while for the other indexes we have

$$\begin{cases} K_1 = 0 & K_2 = 0 & M_2 = 0 & j = (-)^{L_1+L_2} \\ K_1 = 0 & K_2 = 0 & 0 < M_2 \leq L_2 & j = \pm 1 \\ K_1 = 0 & 0 < K_2 \leq L_2 & -L_2 \leq M_2 \leq L_2 & j = \pm 1 \\ 0 < K_1 \leq L_1 & -L_2 \leq K_2 \leq L_2 & -L_2 \leq M_2 \leq L_2 & j = \pm 1 \end{cases} \tag{G.77}$$

The other two symbols to be defined are

$$s = (-)^{K_1+M_2+K_2} \tag{G.78}$$

and

$$\mathcal{N} = \left[2\left(1 + \delta_{K_1,0}\delta_{M_2,0}\delta_{K_2,0}\right)\right]^{-1/2} \tag{G.79}$$

It is straightforward to proof that in the new basis the matrix elements of the diffusive operator are

$$\begin{aligned} \langle\Lambda|\tilde{\Gamma}|\Lambda'\rangle &= 2\mathcal{N}\mathcal{N}' \left[\delta_{j,j'} Re\left\{\langle+|\tilde{\Gamma}|+\rangle + j's'\langle+|\tilde{\Gamma}|-\rangle\right\} + \right. \\ &\quad \left. +\delta_{j,-j'}\, j'\, Im\left\{\langle+|\tilde{\Gamma}|+\rangle + j's'\langle+|\tilde{\Gamma}|-\rangle\right\}\right] \end{aligned} \tag{G.80}$$

where $|+\rangle = |L_1 M_1 K_1, L_2 M_2 K_2\rangle$ and $|-\rangle = \hat{\mathcal{T}}|+\rangle$.

G.2 Starting vector

Let's recall that the diffusive operator is spanned over the following basis:

$$|\lambda\rangle = |L_1 M_1 K_1\rangle \otimes |L_2 M_2 K_2\rangle \tag{G.81}$$

with

$$|L_1 M_1 K_1\rangle = \sqrt{\frac{[L_1]}{8\pi^2}} \mathcal{D}^{L_1}_{M_1,K_1}(\mathbf{\Omega}_V) \tag{G.82}$$

$$|L_2 M_2 K_2\rangle = \sqrt{\frac{[L_2]}{8\pi^2}} \mathcal{D}^{L_2}_{M_2,K_2}(\mathbf{\Omega}) \tag{G.83}$$

The starting vector is defined by the physical observable:

$$|v\rangle = \sqrt{\frac{2[J]}{(1+\delta_{K,K'})}} C^J_{M,KK'}(\mathbf{\Omega}_O) P^{1/2}_{eq} \tag{G.84}$$

Using the of properties of Wigner matrices (see appendix H

$$\begin{aligned} C^J_{M,KK'}(\mathbf{\Omega}_O) &= \sum_{M'} \mathcal{D}^J_{M,M'}(\mathbf{\Omega}_V) C^J_{M',KK'}(\mathbf{\Omega}) = \\ &= \frac{1}{2} \sum_{M'} \mathcal{D}^J_{M,M'}(\mathbf{\Omega}_V) \left[\mathcal{D}^J_{M',K}(\mathbf{\Omega}) + \mathcal{D}^J_{M',K'}(\mathbf{\Omega}) \right] \end{aligned} \tag{G.85}$$

Given:

$$P^{1/2}_{eq}(\mathbf{\Omega}_V, \mathbf{\Omega}) = \mathcal{N} e^{-U(\mathbf{\Omega})/2} \tag{G.86}$$

the starting vector can be rewritten as

$$|v\rangle = \sqrt{\frac{[J]}{2(1+\delta_{K,K'})}} \sum_{M'} \mathcal{D}^J_{M,M'}(\mathbf{\Omega}_V) \left[\mathcal{D}^J_{M',K}(\mathbf{\Omega}) + \mathcal{D}^J_{M',K'}(\mathbf{\Omega}) \right] P^{1/2}_{eq}(\mathbf{\Omega}) \tag{G.87}$$

The projection of starting vector on basis is

$$\begin{aligned} \langle v|\lambda\rangle &= \langle v|L_1 M_1 K_1, L_2 M_2 K_2\rangle = \\ &= \sqrt{\frac{[J]}{2(1+\delta_{K,K'})}} \sum_{M'} \langle \mathcal{D}^J_{M,M'} | L_1 M_1 K_1 \rangle \times \\ &\quad \times \left[\langle \mathcal{D}^J_{M',K} P^{1/2}_{eq} | L_2 M_2 K_2 \rangle + \langle \mathcal{D}^J_{M',K'} P^{1/2}_{eq} | L_2 M_2 K_2 \rangle \right] = \\ &= \sqrt{\frac{[J]}{2(1+\delta_{K,K'})}} \sum_{M'} \sqrt{\frac{[L_1]}{8\pi^2}} \int d\mathbf{\Omega}_V \mathcal{D}^J_{M,M'} \mathcal{D}^{L_1}_{M_1,K_1} \times \\ &\quad \times \sqrt{\frac{[L_2]}{8\pi^2}} \left[\int d\mathbf{\Omega} \mathcal{D}^J_{M',K} \mathcal{D}^{L_2}_{M_2,K_2} P^{1/2}_{eq} + \int d\mathbf{\Omega} \mathcal{D}^J_{M',K'} \mathcal{D}^{L_2}_{M_2,K_2} P^{1/2}_{eq} \right] = \\ &= \mathcal{N} \sqrt{\frac{[L_2]}{2(1+\delta_{K,K'})}} \delta_{J,L_1} \delta_{M,M_1} \delta_{K_1,M_2} \times \\ &\quad \times \Bigg[(-)^{M_2-K} \int_0^{\pi} d\beta \sin(\beta) d^{L_1}_{-K_1,-K}(\beta) d^{L_2}_{K_1,K_2}(\beta) \int_0^{2\pi} d\gamma e^{-i(K_2-K)\gamma} e^{-U(\beta,\gamma)/2} + \\ &\quad + (-)^{M_2-K'} \int_0^{\pi} d\beta \sin(\beta) d^{L_1}_{-K_1,-K'}(\beta) d^{L_2}_{K_1,K_2}(\beta) \int_0^{2\pi} d\gamma e^{-i(K_2-K')\gamma} e^{-U(\beta,\gamma)/2} \Bigg] \end{aligned} \tag{G.88}$$

The orienting potential is

$$U(\beta,\gamma) = c_{2,0} \mathcal{D}^2_{0,0} + c_{2,2} \left(\mathcal{D}^2_{0,2} + \mathcal{D}^2_{0,-2} \right) +$$

$$+c_{4,0}\mathcal{D}^4_{0,0}+c_{4,2}\left(\mathcal{D}^4_{0,2}+\mathcal{D}^4_{0,-2}\right)+c_{4,4}\left(\mathcal{D}^4_{0,4}+\mathcal{D}^4_{0,-4}\right) \tag{G.89}$$

and given that

$$\begin{aligned} d^2_{0,-2}(\beta) &= d^2_{0,2}(\beta) && \text{(G.90)}\\ d^4_{0,-2}(\beta) &= d^4_{0,2}(\beta) && \text{(G.91)}\\ d^4_{0,-4}(\beta) &= d^4_{0,4}(\beta) && \text{(G.92)}\\ & && \text{(G.93)} \end{aligned}$$

the coefficients $c_{l,m}$ are real and the potential can be rewritten as

$$U(\beta,\gamma)=-2u_0(\beta)-2u_2(\beta)\cos(2\gamma)-2u_4(\beta)\cos(4\gamma) \tag{G.94}$$

with

$$\begin{aligned} u_0(\beta) &= -\left[c_{2,0}d^2_{0,0}(\beta)+c_{4,0}d^4_{0,0}(\beta)\right]/2 && \text{(G.95)}\\ u_2 &= -c_{2,2}d^2_{0,2}(\beta)-c_{4,2}d^4_{0,2}(\beta) && \text{(G.96)}\\ u_4 &= -c_{4,4}d^4_{0,4}(\beta) && \text{(G.97)} \end{aligned}$$

So we are left to evaluate the following integral:

$$\int_0^\pi d\beta\sin(\beta)d^{L_1}_{-K_1,-K}(\beta)d^{L_2}_{K_1,K_2}(\beta)e^{u_0(\beta)}\int_0^{2\pi}d\gamma e^{-i(K_2-K)\gamma}e^{u_2(\beta)\cos(2\gamma)+u_4(\beta)\cos(4\gamma)} \tag{G.98}$$

The idea is to try to evaluate analytically the integral in γ:

$$\begin{aligned} A(\beta) &= \int_0^{2\pi}d\gamma e^{-i(K_2-K)\gamma}e^{u_2\cos(2\gamma)+u_4\cos(4\gamma)}= && \text{(G.99)}\\ &= \int_0^{2\pi}d\gamma\cos((K_2-K)\gamma)e^{u_2\cos(2\gamma)+u_4\cos(4\gamma)}= && \text{(G.100)}\\ &= \frac{1}{2}\int_0^{4\pi}d\theta\cos(n\theta)e^{u_2\cos(\theta)+u_4\cos(2\theta)}= && \text{(G.101)}\\ &= 2\int_0^{\pi}d\theta\cos(n\theta)e^{u_2\cos(\theta)+u_4\cos(2\theta)} && \text{(G.102)} \end{aligned}$$

where $n=(K_2-K)/2$ and the integral is non zero only for integer values of n.

It seems that it is not possible to give an analytical expression for $A(\beta)$, but it is possible to give an explicit evaluation. The modified Bessel functions of first kind represent the coefficients of the expansion of exponentials of trigonometric functions over cosines, so we can write:

$$e^{u_4 cos(2\theta)} = I_0(|u_4|) + 2\sum_{s=1}^{\infty}(-)^s I_s(|u_4|)cos(2s\theta) \tag{G.103}$$

with $I_n(z)$ a modified Bessel function of first kind of integer order n and argument z. Substituting the last expression in $A(\beta)$ one obtains:

$$\begin{aligned} A(\beta) &= 2\int_0^{\pi} d\theta \cos(n\theta)e^{u_2\cos(\theta)}e^{u_4\cos(2\theta)} = \\ &= 2\int_0^{\pi} d\theta \cos(n\theta)e^{u_2\cos(\theta)}\left[I_0(|u_4|) + 2\sum_{s=1}^{\infty}(-)^s I_s(|u_4|)cos(2s\theta)\right] = \\ &= 2\pi(-)^n I_0(|u_4|)I_n(|u_2|) + 4\sum_{s=1}^{\infty}(-)^s I_s(|u_4|)\int_0^{\pi} d\theta cos(n\theta)cos(2s\theta)e^{u_2 cos(\theta)} = \\ &= 2\pi(-)^n I_0(|u_4|)I_n(|u_2|) + \\ &\quad +2\sum_{s=1}^{\infty}(-)^s I_s(|u_4|)\int_0^{\pi} d\theta\left[cos\left((n-2s)\theta\right) + cos\left((n+2s)\theta\right)\right]e^{u_2 cos(\theta)} = \\ &= 2\pi(-)^n I_0(|u_4|)I_n(|u_2|) + 2\pi(-)^n\sum_{s=1}^{\infty}(-)^s I_s(|u_4|)\left[I_{n-2s}(|u_2|) + I_{n+2s}(|u_2|)\right] \end{aligned} \tag{G.104}$$

As can be seen if the potential does not depend on γ than the integral is $A(\beta) = 2\pi$, while in the case of only $u_4 = 0$ the integral has the explicit "simple" expression $A(\beta) = 2\pi(-)^n I_n(|u_2|)$. In the general case the integral is expressed as an infinite sum of products of modified Bessel functions of first kind.

Let's call $\Delta_n(|u_2|, |u_4|) = (-)^n\sum_{s=1}^{\infty}(-)^s I_s(|u_4|)\left[I_{n-2s}(|u_2|) + I_{n+2s}(|u_2|)\right]$ and $n^{(')} = |K_2 - K^{(')}|/2$, then the projection of the starting vector on the basis is:

$$\begin{aligned} \langle v|\lambda\rangle &= \mathcal{N}\sqrt{\frac{[L_2]}{2(1+\delta_{K,K'})}}\delta_{J,L_1}\delta_{M,M_1}\delta_{K_1,M_2} \times \\ &\quad \times\Big[(-)^{M_2-K+n}\int_0^{\pi} d\beta\sin(\beta)d^{L_1}_{-K_1,-K}(\beta)d^{L_2}_{K_1,K_2}(\beta)I_0(|u_4|)I_n(|u_2|) + \\ &\quad +(-)^{M_2-K}\int_0^{\pi} d\beta\sin(\beta)d^{L_1}_{-K_1,-K}(\beta)d^{L_2}_{K_1,K_2}(\beta)\Delta_n(|u_2|, |u_4|) + \\ &\quad +(-)^{M_2-K'+n'}\int_0^{\pi} d\beta\sin(\beta)d^{L_1}_{-K_1,-K'}(\beta)d^{L_2}_{K_1,K_2}(\beta)I_0(u_4)I_{n'}(|u_2|) + \\ &\quad +(-)^{M_2-K'}\int_0^{\pi} d\beta\sin(\beta)d^{L_1}_{-K_1,-K'}(\beta)d^{L_2}_{K_1,K_2}(\beta)\Delta_{n'}(|u_{|}2, |u_4|)\Big] \end{aligned} \tag{G.105}$$

The starting vector is non zero if $L_1 = J$, $M_1 = M$ and $K1 - M2 = 0$. Due to the global spatial rotational invariance, the two indexes L_1 and M_1 are diagonal in matrix elements, so once the physical observable has be chosen, they can be set equal to, respectively, J and M. Moreover, only functions with $J = 2$ and $M = 0$ will be employed so only basis functions with $L_1 = 2$ and $M_1 = 0$ will contribute to the determination of spectral densities.

By a simple substitution it is possible to change, in the matrix elements, the two indexes K_1 and M_2 with the two linear combinations $M_\pm = K_1 \pm M_2$. This substitution is useful in the case that $\mathbf{\Omega}_V = 0$ and the diffusion tenor ${}^V D_1$ is axial. In this case also M_- becomes diagonal and only basis functions with $M_- = 0$ are needed. Considering the transformation given in eq. (G.76), the representation of the starting vector on the new basis will be in general complex. It is easier to write the Lanczos algorithm is the vector is only real (or only complex), so we define the following observables

$$C^{\pm}_{K,K'} = C^2_{0,KK'} \pm C^{2\,*}_{0,KK'} = \left[\mathcal{D}^2_{0,K} + (-)^K \mathcal{D}^2_{0,-K}\right] \pm \left[\mathcal{D}^2_{0,K'} + (-)^{K'} \mathcal{D}^2_{0,-K'}\right] \tag{G.106}$$

The starting vector for the two observables is

$$|v^\pm\rangle = \mathcal{N}^{\pm}_{KK'} C^{\pm}_{KK'} P^{1/2}_{eq} \tag{G.107}$$

where the normalization constant is

$$\mathcal{N}^{\pm}_{KK'} = \frac{4(1+\delta_{K,K'}) \pm 2(\delta_{K,0} + \delta_{K',0}) \pm 4(-)^{K+K'}\delta_{K,-K'}}{[2]} \tag{G.108}$$

The representation on the basis is given by

$$\begin{aligned}\langle v^\pm|\Lambda\rangle \quad &\propto \quad \mathcal{N}^{\pm}_{KK'}\mathcal{N} e^{i\frac{\pi}{4}(j-1)} \Big(\langle C^{\pm}_{KK'} P^{1/2}_{eq} | L_1 M_1 K_1, L_2 M_2 K_2\rangle + \\ &\qquad + js\langle C^{\pm}_{KK'} P^{1/2}_{eq} | L_1 M_1 - K_1, L_2 - M_2 - K_2\rangle\Big)\end{aligned} \tag{G.109}$$

With some boring passages it is possible to proof that

$$js\langle C^{\pm}_{KK'} P^{1/2}_{eq} | L_1 M_1 - K_1, L_2 - M_2 - K_2\rangle = \pm j \langle C^{\pm}_{KK'} P^{1/2}_{eq} | L_1 M_1 K_1, L_2 M_2 K_2\rangle^* \tag{G.110}$$

implying that

$$\begin{aligned}\langle v^\pm|\Lambda\rangle \quad &\propto \quad \mathcal{N}^{\pm}_{KK'}\mathcal{N} e^{i\frac{\pi}{4}(j-1)} \Big(\delta_{j,\pm 1} Re\left\{\langle C^{\pm}_{KK'} P^{1/2}_{eq} | L_1 M_1 K_1, L_2 M_2 K_2\rangle\right\} + \\ &\qquad + \delta_{j,\mp 1} Im\left\{\langle C^{\pm}_{KK'} P^{1/2}_{eq} | L_1 M_1 K_1, L_2 M_2 K_2\rangle\right\}\Big)\end{aligned} \tag{G.111}$$

Due to the fact that the representation of the starting vector on the new basis is a linear combination of integrals (G.105) only the real part is non zero, i.e. the starting vector $|v^+\rangle$ is non-zero only for $j = 1$ (real vector) and $|v^-\rangle$ is non-zero only for $j = -1$ (imaginary vector):

$$\langle v^+|\Lambda\rangle \propto \mathcal{N}^+_{KK'}\mathcal{N}\delta_{j,1}\langle C^+_{KK'}P^{1/2}_{eq}|L_1M_1K_1, L_2M_2K_2\rangle \quad (G.112)$$

$$\langle v^-|\Lambda\rangle \propto \mathcal{N}^-_{KK'}\mathcal{N}\delta_{j,-1}\langle C^-_{KK'}P^{1/2}_{eq}|L_1M_1K_1, L_2M_2K_2\rangle \quad (G.113)$$

In the equation for $|v^-\rangle$ we omitted the complex i factor because before running the Lanczos tridiagonalization the starting vector is normalized and being the complex i factor is only a scaling factor that is removed in the normalization procedure and the vector, effectively, is real. In the case that D_{YZ} and D_{XY} for both the probe and the cage are zero in the OF and VF, respectively, than only matrix elements with $j = 1$ contribute to the spectral densities.

Appendix H

Properties of Wigner matrices

In this appendix we report some useful properties of Wigner matrices.

Definition

A Wigner matrix is a function of the set of Euler angles $\mathbf{\Omega}$:

$$\mathcal{D}^{L}_{M,K}\left(\mathbf{\Omega}\right)=e^{-iM\alpha}d^{L}_{M,K}\left(\beta\right)e^{-iK\gamma} \tag{H.1}$$

where $d^{L}_{M,K}\left(\beta\right)$ is the so called reduced Wigner matrix. A common formula to calculate its values is:

$$\begin{aligned} d^{L}_{M,K}\left(\beta\right)=\sum_{h}(-)^{h}\frac{[(L+M)!(L-M)!(L+K)!(L-K)!]^{1/2}}{(L+M-h)!(L-K-h)!h!(h+K-M)!}\times \\ \times(\cos\beta/2)^{2L+M-K-2h}(\sin\beta/2)^{2h+K-M} \end{aligned} \tag{H.2}$$

where the summation runs over all values of h for which the arguments of the factorials are non negative.

Symmetry

$$\mathcal{D}^{L\,*}_{M,K}\left(\mathbf{\Omega}\right)=(-)^{M-K}\mathcal{D}^{L}_{-M,-K}\left(\mathbf{\Omega}\right)=\mathcal{D}^{L}_{K,M}(-\mathbf{\Omega}) \tag{H.3}$$

Product

$$\begin{aligned} \mathcal{D}^{L_1}_{M_1,K_1}\left(\mathbf{\Omega}\right)\mathcal{D}^{L_2}_{M_2,K_2}\left(\mathbf{\Omega}\right)=\sum_{L_3}[L_3]\begin{pmatrix} L_1 & L_2 & L_3 \\ M_1 & M_2 & M_3 \end{pmatrix}\times \\ \times\begin{pmatrix} L_1 & L_2 & L_3 \\ K_1 & K_2 & K_3 \end{pmatrix}\mathcal{D}^{L_3\,*}_{M_3,K_3}\left(\mathbf{\Omega}\right) \end{aligned} \tag{H.4}$$

with $|L_1 - L_2| \leq L_3 \leq (L_1 + L_2)$, $M_3 = -(M_1 + M_2)$, $K_3 = -(K_1 + K_2)$ and $[L_3] = 2L_3 + 1$.

Internal product

given *two* Wigner matrices ($\mathbf{\Omega}$ dependence will be omitted):

$$\int d\mathbf{\Omega} \mathcal{D}^{L_1\,*}_{M_1,K_1} \mathcal{D}^{L_2}_{M_2,K_2} = \frac{8\pi^2}{[L_1]} \delta_{L_1,L_2} \delta M_1, M_2 \delta_{K_1,K_2} \tag{H.5}$$

among *three* Wigner matrices:

$$\int d\mathbf{\Omega} \mathcal{D}^{L_1}_{M_1,K_1} \mathcal{D}^{L_2}_{M_2,K_2} \mathcal{D}^{L_3}_{M_3,K_3} = 8\pi^2 \begin{pmatrix} L_1 & L_2 & L_3 \\ M_1 & M_2 & M_3 \end{pmatrix} \begin{pmatrix} L_1 & L_2 & L_3 \\ K_1 & K_2 & K_3 \end{pmatrix} \tag{H.6}$$

Transformation by rotation

give and irreducible spherical tensor $T_a^{(l,\,m)}$ defined in frame a, it's expression in frame b is given by:

$$T_a^{(l,m)} = \sum_k \mathcal{D}^l_{m,k} \left(\mathbf{\Omega}_{a\to b}\right) T_b^{(l,k)} \tag{H.7}$$

where $\mathbf{\Omega}_{a\to b}$ is the set of Euler angles transforming from a to b. The inverse transformation is:

$$T_b^{(l,k)} = \sum_m \mathcal{D}^{l\,*}_{m,k} \left(\mathbf{\Omega}_{b\to a}\right) T_a^{(l,m)} \tag{H.8}$$

Angular momentum operators

a Wigner matrix which depends on a set of Euler angles $\mathbf{\Omega}$ transforming from a frame a to a frame b is an eigenfunction of the angular momentum operators defined on the two frames, and also of their z projections.

In frame a:

$$\begin{cases} {}^a\hat{J}^2 \mathcal{D}^L_{M,K}(\mathbf{\Omega}) = L(L+1)\,\mathcal{D}^L_{M,K}(\mathbf{\Omega}) \\ {}^a\hat{J}_Z \mathcal{D}^L_{M,K}(\mathbf{\Omega}) = -M \mathcal{D}^L_{M,K}(\mathbf{\Omega}) \\ {}^a\hat{J}_\pm \mathcal{D}^L_{M,K}(\mathbf{\Omega}) = -c^\mp_{L,M} \mathcal{D}^L_{M\mp1,K}(\mathbf{\Omega}) \end{cases} \tag{H.9}$$

In frame b:

$$\begin{cases} {}^b\hat{J}^2 \mathcal{D}^L_{M,K}(\mathbf{\Omega}) = L(L+1)\,\mathcal{D}^L_{M,K}(\mathbf{\Omega}) \\ {}^b\hat{J}_Z \mathcal{D}^L_{M,K}(\mathbf{\Omega}) = -K \mathcal{D}^L_{M,K}(\mathbf{\Omega}) \\ {}^b\hat{J}_\pm \mathcal{D}^L_{M,K}(\mathbf{\Omega}) = -c^\pm_{L,K}\, \mathcal{D}^L_{M,K\pm1}(\mathbf{\Omega}) \end{cases} \tag{H.10}$$

with $c^\pm_{L,M} = \sqrt{L(L+1) - M(M\pm1)}$.

Appendix I

Irreducible spherical representation of a Smoluchowski operator

In the SRLS model it is convenient to express the potential independent rotational diffusion operator in its spherical irreducible representation. It is substantially a sum of terms of the type $\hat{\boldsymbol{J}}^{\dagger}\boldsymbol{D}\hat{\boldsymbol{J}}$. It is possible to write this operator, which is expressed in Cartesian coordinates, as the contraction of rank zero of a spherical tensor of rank two, $\boldsymbol{D}^{(2)}$, and a spherical tensor operator of rank two, $\hat{\boldsymbol{\mathcal{K}}}^{(2)}$, i.e.

$$\hat{\boldsymbol{J}}^{\dagger}\boldsymbol{D}\hat{\boldsymbol{J}} = \left[\boldsymbol{D}^{(2)} \otimes \hat{\boldsymbol{\mathcal{K}}}^{(2)}\right]_0^0 \tag{I.1}$$

The contraction is the combination of three components

$$\left[\boldsymbol{D}^{(2)} \otimes \hat{\boldsymbol{\mathcal{K}}}^{(2)}\right]_0^0 = D^{(0)}\hat{\mathcal{K}}^{(0)} \oplus D^{(1)}\hat{\mathcal{K}}^{(1)} \oplus D^{(2)}\hat{\mathcal{K}}^{(2)} \tag{I.2}$$

The component of rank zero gives informations on the isotropic characteristics, the rank one part is linked to the asymmetry and the rank two component contains informations of the anisotropy.

Because the diffusion tensor is symmetric then $D^{(1)} = 0$ so only the components of rank zero and two remain to be considered. Using the standard procedure it is possible to write:

$$D^{(0,0)} = -\frac{1}{\sqrt{3}}\left(D_{XX} + D_{YY} + D_{ZZ}\right) \tag{I.3}$$

$$D^{(2,0)} = \frac{1}{\sqrt{6}}\left(2D_{ZZ} - D_{XX} - D_{YY}\right) \tag{I.4}$$

$$D^{(2,\pm 1)} = \mp\left(D_{XZ} \pm iD_{YZ}\right) \tag{I.5}$$

$$D^{(2,\pm2)} = \frac{D_{XX} - D_{YY}}{2} \pm iD_{XY} \tag{I.6}$$

and

$$\hat{\mathcal{K}}^{(0,0)} = -\frac{1}{\sqrt{3}}\left[\frac{1}{2}\left(\hat{J}_+\hat{J}_- + \hat{J}_-\hat{J}_+\right) + \hat{J}_Z^2\right] \tag{I.7}$$

$$\hat{\mathcal{K}}^{(2,0)} = \frac{1}{\sqrt{6}}\left(3\hat{J}_Z^2 + \sqrt{3}\hat{\mathcal{K}}^{(0,0)}\right) \tag{I.8}$$

$$\hat{\mathcal{K}}^{(2,\pm1)} = \mp\frac{1}{2}\left(\hat{J}_Z\hat{J}_\pm + \hat{J}_\pm\hat{J}_Z\right) \tag{I.9}$$

$$\hat{\mathcal{K}}^{(2,\pm2)} = \frac{1}{2}\hat{J}_\pm^2 \tag{I.10}$$

Operator $\hat{J}_d$ has a little different structure from the other three operators:

$$\hat{J}_d = -{}^V\hat{\boldsymbol{J}}^\dagger(\boldsymbol{\Omega}_V)^V\boldsymbol{D}_1\hat{\boldsymbol{J}}(\boldsymbol{\Omega}) - {}^V\hat{\boldsymbol{J}}^\dagger(\boldsymbol{\Omega})^V\boldsymbol{D}_1\hat{\boldsymbol{J}}(\boldsymbol{\Omega}_V) \tag{I.11}$$

The two angular momentum operators ${}^V\hat{\boldsymbol{J}}(\boldsymbol{\Omega})$ and ${}^V\hat{\boldsymbol{J}}(\boldsymbol{\Omega}_V)$ act on two orthogonal subspaces, so they commute and it is possible to sum the two contributions. The spherical representation of $\hat{J}_d$ is the same of that given in equations I.7-I.10, multiplied by a factor of -2.

Appendix J

Calculation of matrix elements using the Wigner-Eckart theorem

In SRLS model we introduce the irreducible spherical representation of the diffusive operator. This is possible, and useful, because SRLS describes a pure rotational problem. Moreover, we can make use of the Wigner-Eckart theorem [219] to simplify the calculation of matrix elements.

Let us consider two frames a and b; $\mathbf{\Omega}_{a\to b}$ being the set of Euler angles that transforms from a to b. Thanks to the Wigner-Eckart theorem we can write, for the components of the operator $\hat{\mathcal{K}}_a^{(2,m)}$ defined in a:

$$\langle LMK|\hat{\mathcal{K}}_a^{(2,m)}|L'M'K'\rangle = (-)^{L-K}\begin{pmatrix} L & 2 & L' \\ -K & m & K' \end{pmatrix}\langle LM\|\hat{\mathcal{K}}_a^{(2)}\|L'M'\rangle \tag{J.1}$$

so if the reduced matrix element is known, the calculation of all the five matrix elements of the rank 2 tensorial operator simply reduces to the evaluation of five $3j$ symbols.

The calculation of the reduced matrix element is quite simple if one considers the $(2,2)$ component, for which:

$$\langle LMK|\hat{\mathcal{K}}_a^{(2,2)}|L'M'K'\rangle = \delta_{LL'}\delta_{MM'}\delta_{K,K'+2}\frac{1}{2}c^{+}_{L,K-1}c^{+}_{L,K-2} \tag{J.2}$$

From Wigner-Eckart theorem one can independently write:

$$\langle LMK|\hat{\mathcal{K}}_a^{(2,2)}|L'M'K'\rangle = (-)^{L-K}\begin{pmatrix} L & 2 & L' \\ -K & 2 & K' \end{pmatrix}\langle LM\|\hat{\mathcal{K}}_a^{(2)}\|L'M'\rangle \tag{J.3}$$

The last two equations must be equal and this is true only if $L = L'$ and $M = M'$ in the last equation, that is

$$\begin{aligned} \langle LMK|\hat{\mathcal{K}}_a^{(2,2)}|L'M'K'\rangle = \delta_{LL'}\delta_{MM'}\delta_{K,K'+2}(-)^{L-K} \begin{pmatrix} L & 2 & L \\ -K & 2 & K-2 \end{pmatrix} \times \\ \times \langle LM\|\hat{\mathcal{K}}_a^{(2)}\|L'M'\rangle \end{aligned} \tag{J.4}$$

Using the Racah formula for $3j$ symbols one can write

$$\begin{aligned} \begin{pmatrix} L & 2 & L \\ -K & 2 & K-2 \end{pmatrix} = \left[4!\,(L-K)!\,(L+K)!\,(L-K+2)!\,(L+K-2)!\right]^{1/2} \times \\ \times\sqrt{\Delta\,(L,2,L)}\sum_t \frac{(-)^{t+L-K}}{t!\,(2-t)!\,(L-2-K+t)!\,(4-t)!\,(L+K-t)!\,(t-2)!} \end{aligned} \tag{J.5}$$

where $\Delta\,(L,2,L) = 4(2L-2)!/(2L+3)!$ and the summation is over all integers t such that the arguments of the factorials are non-negative.

The formula is different from zero only for $t = 2$, so the $3j$ symbol can be expressed in a simple analytic form

$$\begin{pmatrix} L & 2 & L \\ -K & 2 & K-2 \end{pmatrix} = (-)^{L-K}\sqrt{\frac{3}{2}}\sqrt{\Delta\,(L,2,L)}\left[\frac{(L+K)!\,(L-K+2)!}{(L-K)!\,(L+K-2)!}\right] \tag{J.6}$$

and by expressing

$$\begin{aligned} (L+K)! = (L+K-2)!\,(L+K-1)\,(L+K) \\ (L-K+2)! = (L-K)!\,(L-K+1)\,(L-K+2) \end{aligned} \tag{J.7}$$

one obtains

$$\begin{aligned} \begin{pmatrix} L & 2 & L \\ -K & 2 & K-2 \end{pmatrix} = (-)^{L-K}\sqrt{\frac{3}{2}}\sqrt{\Delta\,(L,2,L)}\times \\ \times\sqrt{(L+K-1)\,(L-K+1)\,(L-K+2)\,(L+K)} \end{aligned} \tag{J.8}$$

After some passages one gets:

$$\sqrt{(L+K-1)\,(L-K+1)\,(L-K+2)\,(L+K)} = c^{+}_{L,K-1}c^{+}_{L,K-2} \tag{J.9}$$

so by comparison the reduced matrix element can be found to be

$$\langle LM\|\hat{\mathcal{K}}_a^{(2)}\|L'M'\rangle = \delta_{LL'}\delta_{MM'}\sqrt{\frac{(2L+3)!}{24\,(2L-2)!}} \tag{J.10}$$

We can make analogous considerations for the operator defined in b, $\hat{\mathcal{K}}_b^{(2,m)}$. Remembering that the action of shift operators ${}^b\hat{J}_\pm$ have the opposite behaviour of the shift operators in a, it can be found that

$$\langle LMK|\hat{\mathcal{K}}_b^{(2,m)}|L'M'K'\rangle = (-)^{L-M} \begin{pmatrix} L & 2 & L' \\ -M & -m & M' \end{pmatrix} \langle LK\|\hat{\mathcal{K}}_b^{(2)}\|L'K'\rangle \tag{J.11}$$

with

$$\langle LK\|\hat{\mathcal{K}}_b^{(2)}\|L'K'\rangle = \delta_{LL'}\delta_{KK'}\sqrt{\frac{(2L+3)!}{24\,(2L-2)!}} \tag{J.12}$$

Appendix K

Parallelization analysis

In both E-SpiReS and C^{++}OPPS three parts are parallelized: the building of the matrix, that building of the starting vector and the matrix vector multiplication in the Lanczos algorithm. In this appendix we present a short analysis on the efficiency of the parallelization taking as reference a calculation performed with C^{++}OPPS in the case of basis dimension $N = 8855$ and rhombic potential. Figures K-1, K-2 and K-3 show, respectively, the calculation time, speed-up and efficiency of parallelization as functions of the number of processors. The trends of the three routines and of the global execution are reported as function of the number of processors. The speed-up, S_P, of a calculation is defined as

$$S_P = \frac{t_1}{t_P} \tag{K.1}$$

where t_1 is the calculation time for a sequential run (one processor), while t_P is the calculation time for a parallel run with N_P processors. Efficiency, percent, is given by

$$E_P = 100\frac{S_P}{N_P} \tag{K.2}$$

The speed-up parameter is an index of how faster runs a parallel calculation on N_P processors with respect to the sequential execution. Efficiency, instead, is an index of how efficient is the speed-up normalized by the number of processors and it indicates how much is the parallelization efficient, i.e. how much processors are occupied in calculations with respect to the time spent in communications. In the ideal case of linear scaling, the efficiency would remain constant at 100%. In the real case of deviation from linearity, efficiency decays while increasing the number of processors.

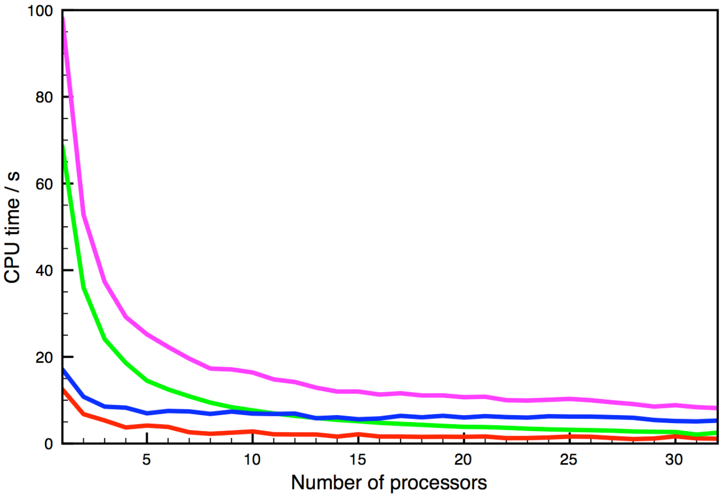

Figure K-1: CPU time as function of the number of processors for $N = 8855$ calculated for the starting vector building routine (red line), matrix building routine (green line), Lanczos algorithm (blue line) and the total simulation (magenta line).

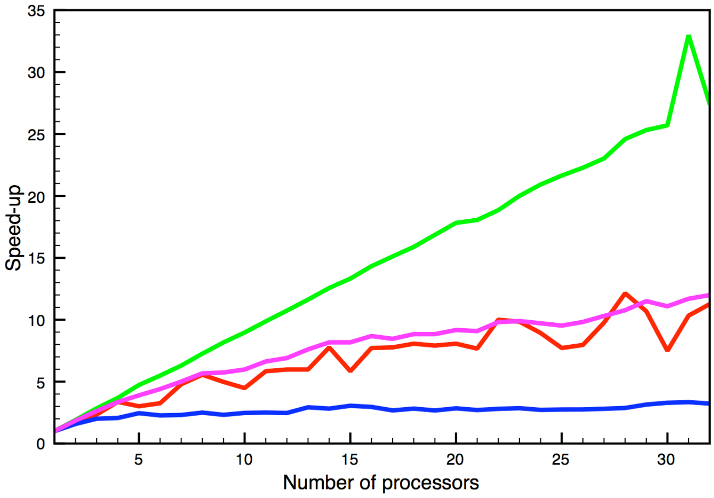

Figure K-2: Speed-up of calculation as function of the number of processors for $N = 8855$ calculated for the starting vector building routine (red line), matrix building routine (green line), Lanczos algorithm (blue line) and the total simulation (magenta line).

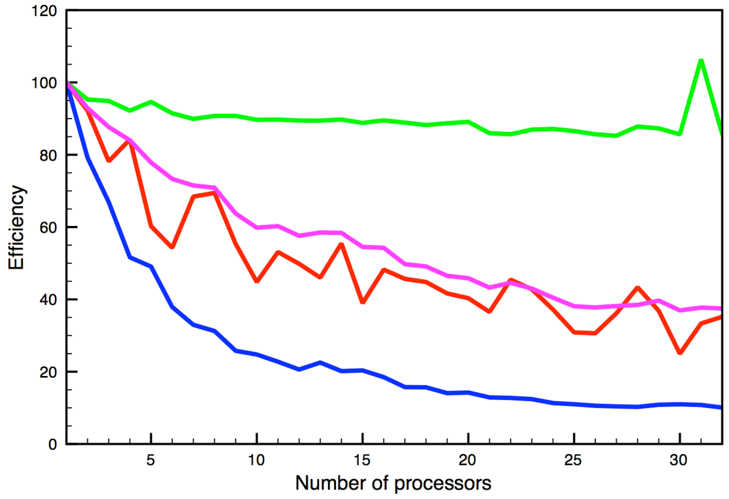

Figure K-3: Efficiency of parallelization as function of the number of processors for $N = 8855$ calculated for the starting vector building routine (red line), matrix building routine (green line), Lanczos algorithm (blue line) and the total simulation (magenta line).

From Figure K-2 it can be seen that the speed-up is not linear with the number of processors. Part of this deviation should be attributed to the fact that work is not well balanced during the evaluation of the starting vector. Moreover, there is a not embarrassingly parallel part in the algorithm: the Lanczos routine. This is due by the fact that before any new iteration data exchange among processors is required. In particular, the scaling stays quite linear while the time required for the matrix vector multiplication is lower than that required for the communication of results. Increasing the number of processors, N_P, the computational weight of the multiplication decreases as $1/N_P$ while the communication time grows as $N_P \log_2(N_P)$ because scattering is done with a binary tree. An estimation of computational time for a given dimension N of the basis is

$$t(N, N_P) \propto \frac{N(N+1)}{N_P + 0.3} + 2NN_P \log_2(N_P) \tag{K.3}$$

In the examined case of $N = 8855$ the minimum is located around 32 processors with an estimated speed-up of 11 - 12.

To conclude we can say that the matrix build up has been well parallelized, with an efficiency that remains to about 70% independently on the number of processors. The less efficient routine, in parallelization, is the Lanczos algorithm and a better parallelization is part of the future work that will be done on the code.

Bibliography

[1] Ryabov, Y. E.; Geragthy, C.; Varshney, A.; Fushman, D. *J. Am. Chem. Soc.* **2006**, *128*, 15432.

[2] Osiecki, J. H.; Ullman, E. F. *J. Am. Chem. Soc.* **1968**, *90*, 1078.

[3] Awaga, K.; Inabe, T.; Yokoyama, T.; Maruyama, Y. *Molecular Crystals and Liquid Crystals* **1993**, *232*, 79.

[4] Gorini, L.; Caneschi, A.; Menichetti, S. *Synlett* **2006**, 948.

[5] Balog, M.; Kálai, T.; Jekö, J.; Berente, Z.; Steinhoff, H. J.; Engelhard, M.; Hideg, K. *Tetrahedron Letters* **2003**, *44*, 9213.

[6] Hubbell, W. L.; Mchaourab, H. S.; Altenbach, C.; Lietzow, M. *Structure* **1996**, *4*, 1996.

[7] Steinhoff, H. J. *Frontiers in Bioscience* **2002**, *7*, 2002.

[8] Kay, L. E. *Nat. Struct. Biol.* **1998**, *5*, 513.

[9] Ishima, R.; Torchia, D. A. *Nature Structural Biology* **2000**, *7*, 740.

[10] Chatfield, D. C.; Szabo, A.; Brooks, B. R. *J. Am. Chem. Soc.* **1998**, *120*, 5301.

[11] Pfeiffer, S.; Fushman, D.; Cowburn, D. *J. Am. Chem. Soc.* **2001**, *123*, 3021.

[12] Lienin, S. F.; Bremi, T.; Brutsher, B.; Brüschweiler, R.; Ernst, R. R. *J. Am. Chem. Soc.* **1998**, *120*, 9870.

[13] Choy, W. Y.; Kay, L. E. *J. Biom. NMR* **2003**, *25*, 325.

[14] Skrynnikov, N. R.; Millet, O.; Kay, L. E. *J. Am. Chem. Soc.* **2002**, *124*, 6449.

[15] Abragam, A. *The Principles of Nuclear Magnetism*; Oxford University Press: London, 1961.

[16] Schneider, D. J.; Freed, J. H. *Advances in Chemical Physics* **1989**, *73*, 387.

[17] Barone, V.; Subra, R. *The Journal of chemical physics* **1996**, *104*, 2630–2637.

[18] Jolibois, F.; Cadet, J.; Grand, A.; Subra, R.; Rega, N.; Barone, V. *J. Am. Chem. Soc.* **1998**, *120*, 1864.

[19] Barone, V.; Carbonniere, P.; Pouchan, C. *J. Chem. Phys.* **2005**, *122*, 224308.

[20] Moro, G.; Freed, J. H. *Large-Scale Eigenvalue Problems, Mathematical Studies Series*; Elsevier: New York, 1986; Vol. 127.

[21] Meirovitch, E.; Igner, D.; Igner, E.; Moro, G.; Freed, J. H. *J.Chem.Phys.* **1982**, *77*, 3915–3938.

[22] Uhlenbeck, G. E.; Ornstein, L. S. *Phys. Rev.* **1930**, *36*, 823.

[23] Kramers, H. A. *Physica* **1940**, *7*, 284.

[24] Chandrasekhar, S. *Rev. Mod. Phys.* **1943**, *15*, 1.

[25] Wang, M. C.; Uhlenbeck, G. E. *Rev. Mod. Phys.* **1945**, *17*, 323.

[26] Haken, H. *Rev. Mod. Phys.* **1975**, *47*, 67.

[27] van Kampen, N. G. *Stochastic processes in physics and chemistry*; Elsevier: North-Holland, 1981.

[28] Schuss, Z. *Theory and Applications of Stochastic Differential Equations*; Wiley: New York, 1980.

[29] Risken, H. *The Fokker-Planck Equation*; Springer - Verlag: Berlin, 1989.

[30] Sastry, V. S. S.; Polimeno, A.; Crepeau, R. H.; Freed, J. H. *J. Chem. Phys.* **1996**, *107*, 5753.

[31] Earle, K. A.; Moscicki, J. K.; Polimeno, A.; Freed, J. H. *J. Chem. Phys.* **1997**, *106*, 9996.

[32] Polimeno, A.; Freed, J. H. *J. Phys. Chem.* **1995**, *99*, 10995.

[33] Zerbetto, M.; Polimeno, A.; Barone, V. submitted to Comp. Phys. Comm.

[34] Barone, V.; Zerbetto, M.; Polimeno, A. *J. Comp. Chem.* **2009**, *30*, 2–13.

[35] Moro, G. *Chem. Phys.* **1987**, *118*, 167.

[36] Moro, G. *Chem. Phys.* **1987**, *118*, 181.

[37] Polimeno, A.; Zerbetto, M.; Meirovitch, E. submitted to Int. J. Quantum Chem.

[38] Improta, R.; Barone, V. *Chem. Rev.* **2004**, *104*, 1231.

[39] Barone, V.; Polimeno, A. *Chem. Soc. Rev.* **2007**, *26*, 1724.

[40] Improta, R.; Barone, V.; Santoro, F. *Angew. Chem.* **2007**, *46*, 405.

[41] Allen, M. P.; Tildesley, D. J. *Computer Simulation of Liquids*; Clarendon: Oxford, 1987.

[42] Filson, D. P.; Bloomfield, V. A. *Biochemistry* **1967**, *6*, 1650.

[43] Bloomfield, V. A.; Dalton, W. G.; Holde, K. E. *Biopolymers* **1967**, *5*, 135.

[44] Bloomfield, V. A. *Science* **1968**, *161*, 1212.

[45] De La Torre, J. G.; Bloomfield, V. A. *Q. Rev. Biophys.* **1981**, *14*, 81.

[46] De La Torre, J. G.; Huertas, M. L.; Carrasco, B. *J. Mag. Reson. B* **2000**, *147*, 138.

[47] De La Torre, J. G.; Huertas, M. L.; Carrasco, B. *Biophys. J.* **2000**, *78*, 719.

[48] Ortega, A.; De La Torre, J. G. *J. Am. Chem. Soc.* **2005**, *127*, 12764.

[49] Cossi, M.; Rega, N.; Scalmani, G.; Barone, V. *J. Comp. Chem.* **2003**, *24*, 669.

[50] Scalmani, G.; Rega, N.; Cossi, M.; Barone, V. *J. Comp. Meth. Sci. Eng.* **2002**, *2*, 159.

[51] Yamakawa, H. *J. Chem. Phys.* **1970**, *53*, 436.

[52] Rotne, J.; Prager, S. *J. Chem. Phys.* **1969**, *50*, 4831.

[53] A., J. et al. *Gaussian 03, Revision C.02*, note: Gaussian, Inc., Wallingford, CT, 2004.

[54] Anderson, E.; Bai, Z.; Bischof, C.; Blackford, S.; Demmel, J.; Dongarra, J.; Du Croz, J.; Greenbaum, A.; Hammarling, S.; McKenney, A.; Sorensen, D. *LAPACK Users' Guide*, 3rd ed.; Society for Industrial and Applied Mathematics: Philadelphia, PA, 1999.

[55] Tjandra, N.; Feller, S. E.; Pastor, R. W.; Bax, A. *J. Am. Chem. Soc.* **1995**, *117*, 12562.

[56] Carlotto, S.; Cimino, P.; Zerbetto, M.; Franco, L.; Corvaja, C.; Crisma, M.; Formaggio, F.; Toniolo, C.; Polimeno, A.; Barone, V. *J. Am. Chem. Soc.* **2007**, *129*, 11248.

[57] Barone, V.; Polimeno, A. *Phys. Chem. Chem. Phys.* **2006**, *8*, 4609.

[58] Barone, V.; Brustolon, M.; Cimino, P.; Polimeno, A.; Zerbetto, M.; Zoleo, A. *J. Am. Chem. Soc.* **2006**, *128*, 15865.

[59] Zerbetto, M.; Carlotto, S.; Polimeno, A.; Corvaja, C.; Franco, L.; Toniolo, C.; Formaggio, F.; Barone, V.; Cimino, P. *J. Phys. Chem. B* **2007**, *111*, 2668.

[60] Dionne, K. E. *Biophys. J.* **1976**, *16*, 705.

[61] Donkers, R. L.; Leaist, D. G. *J. Phys. Chem. B* **1997**, *101*, 304.

[62] Gaab, K. M.; Bardeen, C. J. *Phys. Rev. Lett.* **2004**, *93*, 056001–1.

[63] Fioroni, M.; Diaz, M. D.; Burger, K.; Berber, S. *J. Am. Chem. Soc.* **2002**, *124*, 7737.

[64] Yuan, P.; Richmond, M. G.; Schwartz, M. *Inorg. Chem.* **1991**, *30*, 588.

[65] Levine, Y. K.; Partington, P.; Roberts, G. C. K. *Mol. Phys.* **1973**, *25*, 497.

[66] Tombolato, F.; Ferrarini, A.; Freed, J. H. *J. Phys. Chem. B* **2006**, *110*, 26248.

[67] Tombolato, F.; Ferrarini, A.; Freed, J. H. *J. Phys. Chem. B* **2006**, *110*, 26260.

[68] Müller, C. W.; Schlauderer, C. J.; Reinstein, J.; Schulz, G. E. *Structure* **1996**, *4*, 147.

[69] Pfeiffer, M.; Rink, T.; Gerwert, K.; Oesterhelt, D.; Steinhoff, H. J. *J. Mol. Biol.* **1999**, *287*, 163171.

[70] Steinhoff, H. J.; Suess, B. *Methods* **2003**, *29*, 188195.

[71] Barone, V. *J. Chem. Phys.* **1994**, *101*, 10666.

[72] Barone, V. *Theor. Chem. Acc.* **1995**, *91*, 113.

[73] Barone, V. *Advances in Density Functional Theory, part I*; World Science Publishing Co.: Singapore, 1995; Vol. 287.

[74] Feller, D.; Davidson, E. R. *J. Chem. Phys.* **1988**, *88*, 5770.

[75] Engels, B.; Eriksson, L. A.; Lunell, S. *Advances in Quantum Chemistry*; Academic Press: San Diego, 1996; Vol. 27, p 297.

[76] Perera, S. A.; Salemi, L. M.; Bartlett, R. J. *J. Chem. Phys.* **1997**, *106*, 4061.

[77] Al Derzi, A. R.; Fau, S.; Bartlett, R. J. *J. Phys. Chem. A* **2003**, *107*, 6656.

[78] McConnell, H. M. *J. Chem. Phys.* **1963**, *39*, 1910.

[79] McConnell, H. M. *Proc. R. A. Welch Found. Conf. Chem. Res.* **1967**, *11*, 144.

[80] Stone, A. J. *Proc. R. Soc. London Series A, Mathematical and Physical Sciences* **1963**, *271*, 424.

[81] Stone, A. J. *Mol. Phys.* **1964**, *7*, 311.

[82] Adamo, C.; Barone, V.; Subra, R. *Theoretical Chemistry Accounts: Theory, Computation, and Modeling (Theoretica Chimica Acta)* **2000**, *104*, 207.

[83] Neese, F. *J. Chem. Phys.* **2001**, *115*, 11080.

[84] Ditchfield, R. *Mol. Phys.* **1974**, *27*, 789.

[85] Cheeseman, J. R.; Trucks, G. W.; Keith, T. A.; Frisch, M. J. *J. Chem. Phys.* **1996**, *104*, 5497.

[86] Malkina, O. L.; Vaara, J.; Schimmelpfennig, B.; Munzarova, M.; Malkin, V. G.; Kaupp, M. *J. Am. Chem. Soc.* **2000**, *122*, 9206.

[87] Ciofini, I.; Adamo, C.; Barone, V. *J. Chem. Phys.* **2004**, *121*, 6710.

[88] Nillson, J. A.; Eriksson, L. A.; Laaksonen, A. *Mol. Phys.* **2001**, *99*, 247.

[89] Nonella, M.; Mathias, G.; Tavan, P. *J. Phys. Chem. A* **2003**, *107*, 8638.

[90] Asher, J. R.; Doltsinis, N. L.; Kaupp, M. *Magn. Reson. Chem.* **2005**, *43*, S237.

[91] Pavone, M.; Benzi, C.; De Angelis, F.; Barone, V. *Chem. Phys. Lett.* **2004**, *395*, 120.

[92] Pavone, M.; Cimino, P.; De Angelis, F.; Barone, V. *J. Am. Chem. Soc.* **2006**, *128*, 4338.

[93] Pavone, M.; Sillanpaa, A.; Cimino, P.; Crescenzi, O.; Barone, V. *J. Phys. Chem. B* **2006**, *110*, 16189.

[94] Koseki, S.; Schmidt, M. W.; Gordon, M. S. *J. Phys. Chem.* **1992**, *96*, 10768.

[95] Fermi, E. *Zeitschrift fr Physik A Hadrons and Nuclei* **1930**, *60*, 320.

[96] Frosch, R. A.; Foley, H. M. *Phys.Rev.* **1952**, *88*, 1337–1349.

[97] Tomasi, J.; Mennucci, B.; Cammi, R. *Chem. Rev.* **2005**, *105*, 2999.

[98] Barone, V.; Cossi, M.; Tomasi, J. *J. Chem. Phys.* **1997**, *107*, 3210.

[99] Benzi, C.; Cossi, M.; Improta, R.; Barone, V. *J. Comp. Chem.* **2005**, *26*, 1096.

[100] Cossi, M.; Scalmani, G.; Rega, N.; Barone, V. *J. Chem. Phys.* **2002**, *117*, 43.

[101] Barone, V.; Grand, A.; Minichino, C.; Subra, R. *J. Chem. Phys.* **1993**, *99*, 6745.

[102] Barone, V.; Adamo, C.; Brunel, Y.; Subra, R. *J. Chem. Phys.* **1996**, *105*, 3168.

[103] Barone, V. *Chem. Phys. Lett.* **1996**, *262*, 201.

[104] Pavone, M.; Benzi, C.; abd V. Barone, F. D. A. *Chem. Phys. Lett.* **2004**, *395*, 120.

[105] Crescenzi, O.; Pavone, M.; de Angelis, F.; Barone, V. *J. Phys. Chem. B* **2005**, *109*, 445.

[106] Moro, G.; Freed, J. H. *J. Chem. Phys.* **1981**, *74*, 3757–3773.

[107] Borbat, P. P.; Costa-Filho, A. J.; Earle, K. A.; Moscicki, J. K.; Freed, J. H. *Science* **2001**, *291*, 266.

[108] Guha, R.; Howard, M. T.; Hutchison, G. R.; Murray-Rust, P.; Rzepa, H.; Steinbeck, C.; Wegner, J. K.; Willighagen, E. L. *Journal of Chemical Information and Modeling* **2006**, *46*, 991, The Open Babel Package, version 2.0.1 http://openbabel.sourceforge.net/.

[109] Gropp, W.; Lusk, E.; Doss, N.; Skjellum, A. *Parallel Computing* **1996**, *22*, 789–828.

[110] Gropp, W. D.; Lusk, E. *User's Guide for* `mpich`*, a Portable Implementation of MPI*; Mathematics and Computer Science Division, Argonne National Laboratory, 1996, ANL-96/6.

[111] Polimeno, A.; Zerbetto, M.; Franco, L.; Maggini, M.; Corvaja, C. *J. Am. Chem. Soc.* **2006**, *128*, 4734.

[112] Polimeno, A.; Carlotto, S.; Zerbetto, M.; Toniolo, C.; Huber, M. in preparation.

[113] Zerbetto, M.; Polimeno, A.; Cimino, P.; Barone, V. *J. Chem. Phys.* **2008**, *128*, 24501.

[114] Hermosilla, L.; Sieiro, C.; Calle, P.; Zerbetto, M.; Polimeno, A. *J. Phys. Chem. B* **2008**, *112*, 11202.

[115] Luckhurst, G. R. *Spin Labeling, Theory and Applications*; Berliner, L. J.: Academic Press: New York, 1976; pp 133–181.

[116] Meier, P.; Blume, A.; Ohmes, E.; Neugebauer, F. A.; Kothe, G. *Biochemistry* **1982**, *21*, 526.

[117] Miick, S. M.; Martinez, G. V.; Fiori, W. R.; Todd, A. P.; Millhauser, G. L. *Nature* **1992**, *359*, 653.

[118] Eaton, S. S.; Eaton, G. R.; Berliner, L. J. *Biological Magnetic Resonance*; Eaton, S. S., Eaton, G. R., Berliner, L. J.: Kluwer/Plenum Press: New York, 2000; Vol. 19.

[119] Millhauser, G. L. *Biochemistry* **1995**, *34*, 3873.

[120] Millhauser, G. L. *Biochemistry* **1995**, *34*, 10318.

[121] Toniolo, C.; Valente, E.; Formaggio, F.; Crisma, M.; Pilloni, G.; Corvaja, C.; Toffoletti, A.; Martinez, G. V.; amd Glenn L. Millhauser, M. P. H.; George, C.; Flippen-Anderson, J. L. *J. Pept. Sci.* **1995**, *1*, 45.

[122] Hanson, P.; Millhauser, G.; Formaggio, F.; Crisma, M.; Toniolo, C. *J. Am. Chem. Soc.* **1996**, *118*, 7618.

[123] Mazzoni, M.; Franco, L.; Corvaja, C.; Zordan, G.; Menna, E.; Scorrano, G.; Maggini, M. *ChemPhysChem* **2002**, *3*, 527.

[124] Vasavada, K. V.; Schneider, D. J.; Freed, J. H. *J. Chem. Phys.* **1987**, *86*, 647.

[125] Mazzoni, M.; Franco, L.; Ferrarini, A.; Corvaja, C.; Zordan, G.; Scorrano, G.; Maggini, M. *Liquid Crystals* **2002**, *29*, 203.

[126] Trahanovsky, W. S. *Oxidation in Organic Chemistry*; Academic Press: New York, 1978; p 267.

[127] *Tinker Molecular Modeling homepage.* `http://dasher.wustl.edu/tinker/`.

[128] Miller, J. S.; Epstein, A. J. *Angewandte Chemie International Edition in English* **1994**, *33*, 385–415.

[129] Brown, P. J.; Capiomont, A.; Gillon, B.; Schweizer, J. *Journal of Magnetism and Magnetic Materials* **1979**, *14*, 289.

[130] Sastry, V. S. S.; Polimeno, A.; Crepeau, R. H.; Freed, J. H. *J. Chem. Phys.* **1996**, *107*, 5773.

[131] Vecchi, I.; Arcioni, A.; Bacchiocchi, C.; Tiberio, G.; Zanirato, P.; Zannoni, C. *J. Phys. Chem. B* **2007**, *111*, 3355.

[132] Meirovitch, E.; Freed, J. . H. *J. Phys. Chem.* **1984**, *88*, 4995.

[133] Arcioni, A.; Bacchiocchi, C.; Vecchi, I.; Venditti, G.; Zannoni, C. *Chem. Phys. Lett.* **2004**, *396*, 433.

[134] Freed, J. H. *Electron Spin Relaxation in Liquids*; Plenum Press: New York, 1972; p 387.

[135] Freed, J. H. *Spin Labeling. Theory and Applications*; Academic Press: New York, 1976; p 53.

[136] Schneider, D. J.; Freed, J. H. *Biological Magnetic Resonance. Spin Labeling*; Plenum Press: New York, 1989; Vol. 8.

[137] Arcioni, A.; Bacchiocchi, C.; Grossi, L.; Nicolini, A.; Zannoni, C. *J. Phys. Chem. B* **2002**, *206*, 9245.

[138] Morsy, M. A.; Oweimreen, G. A.; Hwang, J. S. *J. Phys. Chem.* **1996**, *100*, 8331.

[139] Polimeno, A.; Freed, J. H. *Adv. Chem. Phys.* **1993**, *83*, 89.

[140] Benzi, C.; Cossi, M.; Barone, V. *J. Chem. Phys.* **2005**, *123*, 194909.

[141] Adamo, C.; Barone, V. *J. Chem. Phys.* **1999**, *110*, 6158.

[142] Chandrasekhar, S. *Liquid Crystals*, 2nd ed.; University Press: Cambridge, 1992.

[143] De Gennes, P. G.; Prost, J. *The Physics of Liquid Crystals*, 2nd ed.; Oxford University Press: New York, 1993.

[144] Vertogen, G.; de Jeu, W. H. *Thermotropic Liquid Crystals, Fundamentals*; Springer-Verlag: Berlin, 1993.

[145] Leslie, F. M. *Quart. J. Mech. Appl. Math.* **1966**, *19*, 357.

[146] Leslie, F. M. *Adv. Liq. Cryst.* **1979**, *4*, 1.

[147] Ericksen, J. L. *Trans. Soc. Rheol.* **1961**, *5*, 23.

[148] Ericksen, J. L. *Adv. Liq. Cryst.* **1976**, *2*, 233.

[149] Caneschi, A.; Chiesi, P.; David, L.; Ferraro, F.; Gatteschi, D.; Sessoli, R. *Inorg. Chem.* **1993**, *32*, 1445.

[150] Caneschi, A.; Ferraro, F.; Gatteschi, D.; le Lirzin, A.; Novak, M. A.; Rentschler, E.; Sessoli, R. *Adv. Mater.* **1995**, *7*, 476.

[151] Caneschi, A.; Ferraro, F.; Gatteschi, D.; le Lirzin, A.; Rentschler, E. *Inorganica Chimica Acta* **1995**, *235*, 159.

[152] Pillet, S.; Souhassou, M.; Pontillon, Y.; Caneschi, A.; Gatteschi, D.; Lecomte, C. *New J. Chem.* **2001**, *25*, 131.

[153] Liang, Z.; Lou, Y.; Freed, J. H.; Columbus, L.; Hubbell, W. L. *J. Phys. Chem. B* **2004**, *108*, 17649.

[154] Möbius, K.; Savitsky, A.; Wegener, C.; Plato, M.; Fuchs, M.; Schnegg, A.; Dubinskii, A. A.; Grishin, Y. A.; Grigor'ev, I. A.; Khn, M.; Duch, D.; Zimmermann, H.; Steinhoff, H. J. *Magn. Reson. Chem.* **2005**, *43*, S4.

[155] Barone, V.; Polimeno, A. Manuscript in preparation.

[156] Favro, L. D. *Phys. Rev.* **1960**, *119*, 53.

[157] Hubbard, P. S. *Phys. Rev. A* **1972**, *6*, 2421.

[158] Fixman, M.; Rider, K. *J. Chem. Phys.* **1969**, *51*, 2429.

[159] Franci, M. M.; Pietro, W. J.; Hehre, W. J.; Binkley, J. S.; Gordon, M. S.; DeFrees, D. J.; Pople, J. A. *J. Chem. Phys.* **1982**, *77*, 3654.

[160] Scalmani, G.; Barone, V.; Kudin, K. N.; Pomelli, C. S.; Scuseria, G. E.; Frisch, M. J. *Theoretical Chemistry Accounts: Theory, Computation, and Modeling (Theoretica Chimica Acta)* **2004**, *111*, 90.

[161] Rega, N.; Cossi, M.; Barone, V. *J. Chem. Phys.* **1996**, *105*, 11060.

[162] Tedeschi, A. M.; D'Errico, G.; Busi, E.; Basosi, R.; Barone, V. *Phys. Chem. Chem. Phys.* **2002**, *4*, 2180.

[163] di Matteo, A.; Adamo, C.; Cossi, M.; Barone, V.; Rey, P. *Chem. Phys. Lett.* **1999**, *310*, 159.

[164] Adamo, C.; di Matteo, A.; Rey, P.; Barone, V. *J. Phys. Chem. A* **1999**, *103*, 3481.

[165] Assael, M. J.; Dalaouti, N. K.; Dymond, J. H. *Int. J. Thermophys.* **2000**, *21*, 291.

[166] Barlow, A. J.; Lamb, J.; Matheson, A. J. *Proc. R. Soc. London.Series A, Mathematical and Physical Sciences (1934-1990)* **1966**, *292*, 322.

[167] Koch, W.; Holthousen, W. C. *A Chemist's Guide to Density Functional Theory*; Wiley-VCH: Weinheim, 2000.

[168] Brancato, G.; Rega, N.; Barone, V. *The Journal of chemical physics* **2006**, *125*, 164515.

[169] Gustavsson, T.; Banyasz, A.; Lazzarotto, E.; Markovitsi, D.; Scalmani, G.; Frisch, M. J.; Barone, V.; Improta, R. *J. Am. Chem. Soc.* **2006**, *128*, 607.

[170] Improta, R.; Santoro, F.; Barone, V. *Theor. Chem. Acc.* **2007**, *117*, 1073.

[171] Santoro, F.; Improta, R.; Lami, A.; Bloino, J.; Barone, V. *The Journal of chemical physics* **2007**, *126*, 084509.

[172] Brancato, G.; Barone, V.; Rega, N. *Theoretical Chemistry Accounts: Theory, Computation, and Modeling (Theoretica Chimica Acta)* **2007**, *117*, 1001.

[173] Tsvetkov, Y. D. *Biological Magnetic Resonance*; Kluwer Academic/Plenum Publishers: New York, 2004; Vol. 21, p 385.

[174] Jeske, G.; Pannier, M.; Spiess, H. W. *Biological Magnetic Resonance*; Kluwer Academic/Plenum Publishers: New York, 2000; Vol. 19, pp 493–512.

[175] Borbat, P. P.; Freed, J. F. *Biological Magnetic Resonance*; Kluwer Academic/Plenum Publishers: New York, 2000; Vol. 19, p 383.

[176] Karle, I. L.; Balaram, P. *Biochemistry* **1990**, *29*, 6747.

[177] Toniolo, C.; Crisma, M.; Formaggio, F.; Peggion, C. *Peptide Science* **2001**, *60*, 396.

[178] Improta, R.; Barone, V.; Kudin, K. N.; Scuseria, G. E. *J. Am. Chem. Soc.* **2001**, *123*, 3311.

[179] Toniolo, C.; Crisma, M.; Formaggio, F. *Peptide Science* **1998**, *47*, 153.

[180] Crisma, M.; Deschamps, J. R.; George, C.; Flippen-Anderson, J. L.; Kaptein, B.; Broxterman, Q. B.; Moretto, A.; Oancea, S.; Jost, M.; Formaggio, F.; C.Toniolo, *J. Pept. Res.* **2005**, *65*, 564.

[181] Barlow, D. J.; Thornton, J. M. *J. Mol. Biol.* **1988**, *201*, 601.

[182] Tonlolo, C.; Benedetti, E. *Trends in Biochemical Sciences* **1991**, *16*, 350.

[183] Armen, R.; Alonso, D. O. V.; Daggett, V. *Prot. Sci.* **2003**, *12*, 1145.

[184] Bolin, K. A.; Millhauser, G. L. *Acc. Chem. Res.* **1999**, *32*, 1027.

[185] Smythe, M. L.; Huston, S. E.; Marshall, G. R. *J. Am. Chem. Soc.* **1995**, *117*, 5445.

[186] Smythe, M. L.; Nakaie, C. R.; Marshall, G. R. *J. Am. Chem. Soc.* **1995**, *117*, 10555.

[187] Marshall, G. R.; Hodgkin, E. E.; anf G. D. Smith, D. A. L.; Zabrocki, J.; Leplawy, M. T. *Natl. Acad. Sci. U.S.A.* **1990**, *87*, 487.

[188] Smythe, M. L.; Huston, S. E.; Marshall, G. R. *J. Am. Chem. Soc.* **1993**, *115*, 11594.

[189] Fiori, W. R.; Miick, S. M.; Millhauser, G. L. *Biochemistry* **1993**, *32*, 11957.

[190] Zhang, L.; Hermans, J. *J. Am. Chem. Soc.* **1994**, *116*, 11915.

[191] Paterson, Y.; Rumsey, S. M.; Benedetti, E.; Nemethy, G.; Scheraga, H. A. *J. Am. Chem. Soc.* **1981**, *103*, 2947.

[192] Cremer, D.; Pople, J. A. *J. Am. Chem. Soc.* **1975**, *97*, 1354.

[193] D'Amore, M.; Improta, R.; Barone, V. *J. Phys. Chem. A* **2003**, *107*, 6264.

[194] Lucarini, M.; Pedulli, G. F. *Chem. Phys. Phys. Chem.* **2002**, *3*, 789.

[195] Aurich, H. G.; Hahn, K.; Stork, K.; Weiss, W. *Tetrahedron* **1977**, *33*, 969.

[196] Barone, V. *J. Phys. Chem.* **1995**, *99*, 11659.

[197] Improta, R.; Kudin, K. N.; Scuseria, G. E.; Barone, V. *J. Am. Chem. Soc.* **2002**, *124*, 113.

[198] *Handbook of Chemistry and Physics*, 64th ed.; Raton, B., Ed.; CRC Press: Florida, 1983; p. F-39.

[199] Bellanda, M.; Mammi, S.; Geremia, S.; Demitri, N.; Randaccio, L.; Broxterman, Q. B.; Kaptein, B.; Pengo, P.; Pasquato, L.; Scrimin, P. *Chemistry - A European Journal* **2007**, *13*, 407–416.

[200] Kamachi, M. *Polymer Physics* **1987**, 207.

[201] Kamachi, M. *Journal of Polymer Science Part A: Polymer Chemistry* **2002**, *40*, 269.

[202] Yamada, B.; Westmoreland, D. G.; Kobatake, S.; Konosu, O. *Progress in Polymer Science* **1999**, *24*, 565.

[203] McCaffrey, V. P.; Harbron, E. J.; Forbes, M. D. E. *Macromol.* **2005**, *38*, 3342.

[204] Kajiwara, A.; Maeda, K.; Kubo, N.; Kamachi, M. *Macromol.* **2003**, *36*, 526.

[205] García, N.; Guzmán, J.; Riande, E.; García, F.; na, J. L. D. L. P.; Calle, P.; Jimeno, M. L. *Journal of Polymer Science Part A: Polymer Chemistry* **2000**, *38*, 3883.

[206] García, N.; Guzmn, J.; Riande, E.; Calle, P.; Sieiro, C. *Polymer* **2001**, *42*, 6425.

[207] Hermosilla, L.; Calle, P.; Sieiro, C.; Garca, N.; Tiemblo, P.; Guzmn, J. *Chem. Phys.* **2007**, *340*, 237.

[208] Heller, C.; McConnell, H. M. *J. Chem. Phys.* **1960**, *32*, 1535.

[209] Hermosilla, L.; Calle, P.; Garcia de la Vega, J. M.; Sieiro, C. *J. Phys. Chem. A* **2005**, *109*, 1114.

[210] Hermosilla, L.; Calle, P.; Garcia de la Vega, J. M.; Sieiro, C. *J. Phys. Chem. A* **2005**, *109*, 7626.

[211] Palmer III, A. G. *Annu. Rev. Biophys. Biomol. Struct.* **2001**, *20*, 129.

[212] Lipari, G.; Szabo, A. *J. Am. Chem. Soc.* **1982**, *104*, 4546.

[213] Lipari, G.; Szabo, A. *J. Am. Chem. Soc.* **1982**, *104*, 4559.

[214] Shapiro, Y. E.; Kahana, E.; Tugarinov, V.; Liang, Z.; Freed, J. H.; Meirovitch, E. *Biochemistry* **2002**, *41*, 6271.

[215] Meirovitch, E.; Polimeno, A.; Freed, J. H. *J. Phys. Chem. B* **2006**, *110*, 20615.

[216] Meirovitch, E.; Polimeno, A.; Freed, J. H. *J. Phys. Chem. B* **2007**, *111*, 12865.

[217] Press, W. H.; Teukolsky, S. A.; Vetterling, W. T.; Flannery, B. P. *Numerical Recipes in C: The Art of Scientific Computing*; Cambridge University Press: New York, NY, USA, 1992.

[218] Silverstone, H. J.; Moats, R. K. *Phys. Rev. A* **1977**, *4*, 1731.

[219] Varshalovich, D. A.; Moskalev, A. N.; Khersonskii, V. K. *Quantum Theory of Angular Momentum*; World Scientific: Singapore, 1988.